UNIVERSITY OF SOUTHAMPTON

Faculty of Engineering and the Environment

National Centre for Advanced Tribology at Southampton

WS_2 NANOPARTICLES AS LUBRICANT ADDITIVES

Vlad Bogdan Niste

PhD Thesis

October 2015

UNIVERSITY OF SOUTHAMPTON

ABSTRACT

FACULTY OF ENGINEERING AND THE ENVIRONMENT

National Centre for Advanced Tribology at Southampton

Doctor of Philosophy

WS_2 NANOPARTICLES AS LUBRICANT ADDITIVES

Vlad Bogdan Niste

Due to their excellent tribological properties and potential to replace problematic lubricant additives currently in use, WS_2 nanoparticles (NPs) have spurred considerable interest from academia and industry over the last two decades to decipher their mechanism of action.

To elucidate the mechanism, this study carried out tribological tests at high pressures and low/high temperatures (40 and 100ºC) and investigated the tribofilm generated on the wear track and its wear and friction properties. It was found that WS_2 NPs react with the metal substrate at high temperatures to form a chemical tribofilm covered with squashed NPs. The generation of this tribofilm accounts for their excellent tribological properties.

By investigating the chemical and mechanical properties of the tribofilm, it was possible to explain the tribological properties of WS_2 NPs. Based on chemical analysis results, a layered structure was proposed for the chemically formed tribofilms. The large amount of tungsten compounds in the composition may explain the excellent mechanical properties of the tribofilm, as revealed by nanoindentation tests.

The importance of base oil polarity was investigated. It was found that the efficiency of the NPs is reduced in polar oils, because the oil molecules can compete with the nanoadditive by adsorbing on the metal surface in the tribological contact and impeding the formation of the tribofilm.

To investigate which type of WS_2 NPs (2H or IF) performs better in tribological applications and if other tungsten dichalcogenides (IF-WSe_2) are also potential candidates as nanoadditives, tribological tests and analysis of the wear tracks were performed. 2H-WS_2 showed superior friction and wear reducing properties in high-pressure high-temperature contacts.

The tribological performance of 2H-WS_2 NPs was compared to that of popular conventional additives, e.g. antiwear zinc dialkyldithiophosphates (ZDDPs) and organic friction modifiers (OFMs). At the end of three hour tests, 2H-WS_2 NPs and ZDDP+OFM mixtures showed similar antiwear properties, but 2H-WS_2 NPs induced a significant reduction of the friction coefficient in the mixed and boundary lubrication regimes.

The ability of 2H-WS_2 NPs to inhibit hydrogen permeation in high strength bearing steel used in fuel cells and wind turbines was also investigated. Thermal desorption spectroscopy revealed that the chemical tribofilm generated on the wear tracks can significantly reduce the concentration of hydrogen and water in the steel substrate after rolling contact fatigue tests performed in high-temperature high-pressure conditions.

Table of contents

LIST OF FIGURES

LIST OF TABLES

LIST OF ACRONYMS

AES	Auger electron spectroscopy
AFM	atomic force microscopy
Ag	silver
Al	aluminium
API	American Petroleum Institute
AW	antiwear
C	carbon
Ca	calcium
Cl	chlorine
COF	coefficient of friction
CS_2	carbon disulphide
Cu	copper
DLS	dynamic light scattering
DVLO	Derjaguin, Landau, Verwey and Overbeek theory
EDX	energy-dispersive X-ray spectroscopy
EHD/EHL	elastohydrodynamic regime
EP	extreme pressure
Fe	iron
FeS	iron sulphide
FIB	focused ion beam
FM	friction modifier
FTIR	Fourier transform infrared spectroscopy
Ga	gallium
H	hydrogen
H_3O^+	hydronium ion
H_{ads}	adsorbed hydrogen
HD	hydrogen damage
HE	hydrogen embrittlement
HEDE	hydrogen enhanced decohesion theory
HELP	hydrogen enhanced localised plasticity theory
HRSEM	high resolution scanning electron microscopy
HRTEM	high resolution transmission electron spectroscopy
IF	inorganic fullerene-like

JCPDS	Joint Committee on Powder Diffraction Standards
JSPS	Japan Society for the Promotion of Science
K	potassium
K_2MoO_4	potassium molybdate
Mg	magnesium
Mn	manganese
Mo	molybdenum
MoDDP	molybdenum dialkyldithiophosphate
MoDTC	molybdenum dithiocarbamate
MoO_2	molybdenum dioxide
MoO_3	molybdenum trioxide
MoS_2	molybdenum disulphide
MTM	mini traction machine
N	nitrogen
Na	sodium
NaCl	sodium chloride
$NaNO_2$	sodium nitrite
Ni	nickel
NP	nanoparticle
NTA	nitrilotriacetic acid
O	oxygen
OA	oleic acid
OFM	organic friction modifier
P	phosphorous
P_2S_5	phosphorous pentasulphide
PAO	polyalphaolefin
PPG	polypropylene glycol
PSD	particle size distribution
PTFE	polytetrafluoroethylene
PV	load x velocity
RCF	Rolling contact fatigue
REACH	Registration, Evaluation, Authorisation & restriction of Chemicals
S	sulphur
SAPS	sulphated ash, phosphorous and sulphur
SD	standard deviation

SEM	scanning electron microscopy
Si	silicon
SIMS	secondary ion mass spectrometry
SLIM	spacer layer imaging method
SRR	slide roll ratio
STEM	scanning transmission electron spectroscopy
TDS	thermal desorption spectroscopy
TEM	transmission electron spectroscopy
TLK	terrace ledge kink
W	tungsten
WDTC	tungsten dithiocarbamate
WEA	white etching area
WEC	white etching crack
WO_3	tungsten trioxide
WS_2	tungsten disulphide
XPS	X-ray photoelectron spectroscopy
XRD	X-ray diffraction
ZDDP	zinc dialkyldithiophosphate
Zn	zinc
ZnDTC	zinc dithiocarbamate

NOMENCLATURE

A_{1g}, E^{1}_{2g}	WS_2 absorption bands in Raman	m^{-1}
α	pressure viscosity coefficient	Pa^{-1}
dC/dx	concentration gradient	$mol/m^3/m$
D	diffusion coefficient	m^2/s
E'	reduced Young’s modulus	Pa
E_a	activation energy	J
E_A, E_B	elastic moduli of bodies A and B	Pa
E_{diff}	diffusion energy	J
E_s	saddle point energy	J
E_{trap}	trap energy	J
ΔG	Gibbs free energy	J
$\bar{G}$	materials parameter	dimensionless
γ	surface tension	N/m
h	film thickness	m
h_0	minimum film thickness	m
h_c	central film thickness	m
η	viscosity	Pa s
J	flux	$mol/m^2/s$
L	contact length	m
λ	lambda ratio	dimensionless
M/z	molecular mass per charge	kg/mol
μ	friction coefficient	dimensionless
ν_A, ν_B	Poisson’s ratio of bodies A and B	dimensionless
p	pressure	Pa

R'_x	reduced radii of contact	m
R_a	average roughness	m
R_{ax}, R_{bx}	radius of curvature of bodies A and B	m
R_q	root-mean-square-roughness	m
Sw	specific surface area	m^{-1}
σ	composite surface roughness	m
T	temperature	K
U, V, w	velocity in the x, y and z directions	m/s
$\bar{U}$	speed parameter	dimensionless
W	applied load	N
$\bar{W}$	load parameter	dimensionless
ζ	zeta potential	V

AUTHOR'S DECLARATION

I, Vlad Bogdan Niste, declare that this thesis and the work presented in it are my own and have been generated by me as the result of my own original research.

WS_2 NANOPARTICLES AS LUBRICANT ADDITIVES

I confirm that:

1. This work was done wholly or mainly while in candidature for a research degree at this University;
2. Where any part of this thesis has previously been submitted for a degree or any other qualification at this University or any other institution, this has been clearly stated;
3. Where I have consulted the published work of others, this is always clearly attributed;
4. Where I have quoted from the work of others, the source is always given. With the exception of such quotations, this thesis is entirely my own work;
5. I have acknowledged all main sources of help;
6. Where the thesis is based on work done by myself jointly with others, I have made clear exactly what was done by others and what I have contributed myself;
7. Parts of this work have been published as:

Journal publications:

[1] V. B. Niste, H. Tanaka, M. Ratoi, J. Sugimura, WS_2 nanoadditized lubricant for applications affected by hydrogen embrittlement, *RSC Adv.*, 2015, **5**(51), 40678-40687.

[2] M. Ratoi, V. B. Niste, J. Zekonyte, WS_2 nanoparticles – potential replacement for ZDDP and friction modifier additives, *RSC Adv.*, 2014, **4**(41), 21238-21245.

[3] M. Ratoi, V. B. Niste, H. Alghawel, A. Suen, K. Nelson, The Impact of Organic Friction Modifiers on Engine Oil Tribofilms, *RSC Adv.*, 2014, **4**, 4278-4285.

[4] M. Ratoi, V. B. Niste, J. Walker, J. Zekonyte, Mechanism of action of WS_2 lubricant nanoadditives in high-pressure contacts, *Tribol. Lett.*, 2013, **52**(1), 81–91.

Conference publications:

[1] M. Ratoi, V. B. Niste, H. Tanaka, J. Sugimura, WS_2 nanoadditized lubricant for applications affected by hydrogen embrittlement. *Hydrogenius & I^2CNER Tribology Symposium* (Fukuoka, Japan, 2015).

[2] V. B. Niste, M. Ratoi, H. Tanaka, J. Sugimura, F. Xu, Y. Zhu, Tribological behaviour of Al-WS_2 composites against steel. *6th UK-China Symposium on Nanomaterials and Tribology* (Southampton, UK, 2014).

[3] V. B. Niste, H. Tanaka, M. Ratoi, J. Sugimura, Effect of lubrication conditions on permeation of hydrogen into bearing steel. *STLE 69th Annual Meeting & Exhibition* (Lake Buena Vista, Florida, 2014).

[4] M. Ratoi, V. B. Niste, J. Zekonyte, WS_2 nanoparticles - potential replacement for ZDDP and friction modifier additives. *19th International Colloquium Tribology – Industrial and Automotive Lubrication* (Esslingen, Germany, 2014).

[5] V. B. Niste, M. Ratoi, B. Mellor, The mechanism of inorganic fullerene-like WS_2 nanoparticles. *IMechE 21st Mission of Tribology Research: Capturing the Future of UK Research* (London, UK, 2012).

[6] V. B. Niste, M. Ratoi, B. Mellor, The mechanism of IF-WS_2 nanoparticles. *The 1st Postgraduate Engineering Sciences Conference* (Southampton, UK, 2012).

[7] M. Ratoi, V. B. Niste, Mechanism of IF-WS_2 nanoadditives. *4th UK-China Symposium on Lubrication and Chemical Aspects of Wear* (Southampton, UK, 2012).

[8] V. B. Niste, M. Ratoi, B. Mellor, Feasibility of using nanoparticles as lubricant additives. *9th Annual Tribo-UK Conference in Tribology* (Southampton, UK, 2012).

[9] M. Ratoi, V. B. Niste, Functionalised IF-WS_2 NPs as lubricant additives. *18th International Colloquium Tribology – Industrial and Automotive Lubrication* (Esslingen, Germany, 2012).

Signed:

Date:

ACKNOWLEDGEMENTS

I would like to express my deepest gratitude towards my supervisors, Dr Monica Ratoi and Dr Brian Mellor, for their support and patience throughout my studies. They have shared a wealth of information and always helped direct the research onto its optimal course, while also providing guidance and support in aspects far outreaching academic boundaries.

The experimental work presented in Chapter 6 was performed at Kyushu University, Japan and was possible due to a one year fellowship awarded by JSPS (Japan Society for the Promotion of Science), which is gratefully acknowledged. I would also like to thank Prof Joichi Sugimura, Dr Hiroyoshi Tanaka and Ms Yoshie Kurono for their kind advice and help with the experimental work during this period.

I would like to acknowledge the Royal Society of Chemistry for providing funding to attend the 69th STLE Annual Meeting & Exhibition 2014, where parts of this research have been presented.

Parts of the experimental work presented in this project were performed at EPSRC facilities across the UK. The following are gratefully acknowledged for their help in carrying out the analyses, along with their support in interpreting the data: Dr John Walker (University of Southampton) – FIB/SIMS analysis; Dr Jurgita Zekonyte (University of Southampton) – nanoindentation; Dr Naoko Sano (Newcastle University) – XPS analysis; Dr Benjamin Johnson (University of Leeds) – XPS analysis; Dr David Morgan (Cardiff University) – XPS analysis; Dr Fredrik Hage (SuperSTEM Laboratory) – STEM analysis; Dr Ian MacLaren (Glasgow University) – TEM analysis; Ms Chao Ma (University of Southampton) – TEM analysis; Dr Mark Light (University of Southampton) – XRD analysis. I am also very grateful to Dr Ekaterina Vasilyeva (Saint-Petersburg State Polytechnical University) for supplying the IF-WS_2 and IF-WSe_2 NPs.

I would like to thank my friends here in the UK, Japan and at home for their continuous support and company. They have all contributed to a unique experience during these memorable four years.

My gratitude also extends towards my family for the patience and encouragement offered throughout this period spent abroad.

1. INTRODUCTION

1.1 Overview and project objectives

The majority of tribological applications employ lubricants containing various additives in order to prevent the contact between moving surfaces and to reduce friction and wear. Zinc dialkyldithiophosphates (ZDDPs) are the most popular antiwear additives and have been used extensively in the past ~70 years due to their unparalleled efficiency in reacting with the metal substrate and forming a protective tribofilm. However, ZDDPs and their reaction products are not environmentally friendly and they are known to poison catalyst systems. Therefore, many studies have attempted to find cleaner alternatives for these traditional additives.

Nanoparticles (NPs) are very attractive novel lubricant additives because of their nanoscale size, which allows them to penetrate contacts of diverse geometries, fill the gaps between contact asperities and ultimately form a protective boundary film, persistent under high pressure. For this reason, a vast array of NPs have been used in published research to investigate their effect on friction or wear in tribological contacts.

Tungsten disulphide (WS_2) NPs have received particular interest because, apart from being highly effective in reducing friction and wear between moving parts, they are inert, non-toxic, non-magnetic and have high resistance to oxidation and thermal degradation. Their positive influence is especially visible in mixed or boundary lubrication regimes when the most severe wear and damage occur.

A large amount of published research has investigated the mechanism of action of WS_2 NPs, with the aim of applying this knowledge for designing novel lubricants for specific applications. However, a consensus has not been achieved and many proposed hypotheses are still being debated. This project aims to offer a comprehensive study of the properties of WS_2 NPs in a range of practical conditions for a better understanding of their behaviour in tribological contacts.

WS_2 NPs are known to be very efficient at reducing friction between moving components. However, some studies show that they are also capable of acting as antiwear and extreme pressure additives and reduce wear of the metal surfaces in the contact. This project will also investigate the ability of WS_2 NPs to generate a chemical tribofilm in the contact and will compare the tribological performance of WS_2 NPs to both friction modifiers (i.e. organic friction modifiers (OFM)) and antiwear additives (i.e. ZDDP).

High strength steels are susceptible to hydrogen embrittlement, which occurs as a consequence of the permeation of atomic hydrogen into the substrate. Several studies have shown that antiwear lubricant additives can reduce the concentration of atomic hydrogen in bearing steel due to the formation of a sacrificial tribofilm. Therefore, this study will also assess the capability of the WS_2 NP-generated tribofilm to inhibit the formation and permeation of atomic hydrogen into bearing steel.

Apart from reducing friction and wear, lubricant additives must also have good dispersability in the base oil and their dispersions must be stable over time. Although they are excellent additives, WS_2 NPs are difficult to functionalize due to their chemically inert surfaces, which leaves them vulnerable to particle agglomeration and collapse of the colloid. New functionalization methods are required in order to take advantage of the remarkable properties of this nanoadditive. The project also addresses this aspect and investigates the approaches reported in the literature to functionalize WS_2 NPs.

The main objectives of the project are summarized below:

- To investigate the mechanism of action of WS_2 NPs in tribological contacts;
- To compare the tribological properties of three tungsten dichalcogenide NPs (2H-WS_2, IF-WS_2 and IF-WSe_2) in order to assess their potential as lubricant nanoadditives;
- To compare the tribological properties of 2H-WS_2 nanoadditives with conventional additive formulations containing an antiwear additive (i.e. ZDDP) and an OFM;
- To investigate the ability of 2H-WS_2 NPs to reduce hydrogen generation and permeation in bearing steel during rolling contact fatigue tests;
- To obtain stable dispersions of 2H-WS_2 NPs in base oil, which can be employed in tribological applications.

1.2 Thesis structure

The thesis is divided into 8 chapters.

Chapter 2 presents a literature review of the main aspects involved in the use of WS_2 NPs as lubricant additives. The four separate sections discuss the basic principles of tribology, the main additives currently used in tribological applications, the effects of hydrogen on high-strength bearing steel and the functionalization of WS_2 NPs.

Chapter 3 describes the techniques used in the present study. A broad range of physical, chemical and mechanical characterisation techniques were performed in order to investigate the properties of the WS_2 NPs and the tribofilms generated on the wear tracks.

Chapter 4 contains the experimental results obtained using 2H-WS_2 NP dispersions under different testing conditions in the Mini Traction Machine in a point contact. The mechanism of action for the nanoadditive is investigated at low/high temperatures and in both polar/nonpolar base oils. A comparison is made with the results obtained using similar dichalcogenide nanoadditives, such as IF-WS_2 and IF-WSe_2 NPs.

Chapter 5 describes the experimental tests performed for the comparison of the tribological properties of 2H-WS_2 NPs with conventional lubricant formulations, such as mixtures of antiwear ZDDP and an OFM.

Chapter 6 contains the experimental results and discussion concerning the effect of 2H-WS_2 NPs on the reduction of hydrogen permeation in bearing steel during rolling contact fatigue tests.

Chapter 7 presents the most important conclusions of the project.

Chapter 8 suggests further work to be carried out related to this project.

2. LITERATURE REVIEW

2.1 INTRODUCTION

This chapter discusses the main aspects related to the use of WS_2 nanoparticles (NPs) as lubricant additives in high-pressure contacts. The fundamental tribological concepts are presented in Section 2.2, with a focus on the conditions encountered in elastohydrodynamic and boundary contacts, specific for high-pressure applications such as bearings or gears. Section 2.3 discusses the main additives currently used in tribological applications, along with their strengths and limitations, and some of the existing research and advantages of using new lubricant additives such as WS_2 NPs. Section 2.4 describes the importance of the effects of hydrogen on high-strength bearing steel, along with arguments for the use of WS_2 nanoadditives in order to reduce hydrogen permeation in steel. The chapter concludes in Section 2.5 with a discussion on the challenges of WS_2 NP functionalization, which is required in order to achieve a stable lubricant dispersion suitable for use in tribological applications.

2.2 TRIBOLOGY OF LUBRICATED CONTACTS

2.2.1 Introduction

Tribology is the ‘science and technology of interacting surfaces in relative motion and of related subjects’. It derives from the word ‘*tribos*’ (rubbing) and deals with the principles of friction, lubrication and wear [1-4].

Although tribology is a relatively new field compared to other engineering disciplines, the problems of friction and wear have always been of interest. Some basic tribological principles have been observed ever since the earliest years of recorded history: 5000 years ago, Sumerians and Egyptians used various devices to reduce friction in sliding and rolling contacts. Examples include transporting heavy stones by using rolling bodies and oils as lubricants or simple bearings for pottery wheels and chariots [1-5].

In the 15th century, Leonardo da Vinci conducted many experiments investigating the friction coefficient on inclined planes and wear of bearing materials. He discovered the proportionality between the normal and friction forces and formulated the laws of dry friction.

In 1883 Beauchamp Tower was studying journal bearing-type setups when he discovered that the oil inside was under considerable pressure. Osborne Reynolds published a theoretical approach to hydrodynamic lubrication in 1886 and explained the pressure distribution inside a bearing [2]. He used Tower’s detailed data to provide experimental confirmation of hydrodynamic lubrication. At the same time (1882), Heinrich Hertz calculated the contact stresses and deformation between elastic solids. In just a few years the foundations of tribology as a modern subject were set [6, 7].

In the following years, with the development of advanced instrumentation that allows for microscopic-scale analysis, more knowledge was acquired and tribology was finally recognized as a distinct field of science in 1967.

The objective of tribology in most applications is to reduce both friction and wear with the use of lubrication. Less wear leads to a longer lifetime for components, while less friction leads to the reduction of the magnitude of forces applied. There are some exceptions to this situation, when high friction is desired (brakes, clutches, tyres), when high wear is preferred (pencils, chalk) or when both friction and wear are needed (erasers) [1].

Presently, lubricants are complex mixtures containing a large number of additives performing different functions. Some of these additives are not environmentally friendly or poison exhaust catalysts, but efficient replacements are yet to be found [8].

Many researchers have been investigating the possibility of using NPs as lubricant additives, although there are a number of issues to be addressed, such as the thermodynamic instability of NP colloids and the compatibility with the base oil and the additive package [9-11]. In order to be a suitable candidate for tribological applications, a nanoadditive such as WS_2 must show colloidal stability in the base oil and its mechanism of action should impart it with good tribological properties without interfering with other additives in the lubricant [12, 13].

This section presents the main concepts used to describe tribological contacts and an overview of the possible advantages of using WS_2 NPs in lubricated contacts.

2.2.2 Friction and material surfaces

Friction is the force that acts against the relative motion of two surfaces in contact. It is a dissipative force – an irreversible process in which energy from a system is lost in the form of heat to another system. Friction therefore represents the dissipation of energy between the surfaces [14, 15].

The coefficient of friction ($\boldsymbol{\mu}$ or COF) is a dimensionless scalar with an empirical value for every material contact. It is defined as the ratio of the friction force and the normal load on the surface. This model offers a good approximation for most physical systems. However, it relies on the assumption that atoms make contact across the whole surface. In reality, because surfaces usually have a very complex texture at the microscopic level, other factors such as adhesion and deformation of the surfaces make it impossible to directly derive $\boldsymbol{\mu}$ as a specific materials constant. Therefore, the friction coefficient is typically measured experimentally.

Solid surfaces

Except for very few materials (e.g. mica sheets), surfaces are ‘rough’ at the atomic level and have a very complex form with many defects. Depending on their size, these imperfections have a strong influence on the chemistry and mechanics of the surfaces and the lubricant in between, e.g. atomic imperfections lead to an active surface, capable of adsorbing lubricant/additive molecules [16].

Most surfaces consist of atomic terraces and are thus quasi-planar surfaces, as shown in Figure 2.1 (a). Furthermore, some gaps can appear due to missing atoms, or extra atoms can populate the surface. Such a model has been presented in the literature as a 'terrace ledge kink' (TLK) model. In addition to this, most surfaces will be contaminated with various impurities, e.g. metal surfaces have additional oxygen atoms as part of oxides on the surface, small molecules (i.e. water, oxygen) adsorbed or other contaminants.

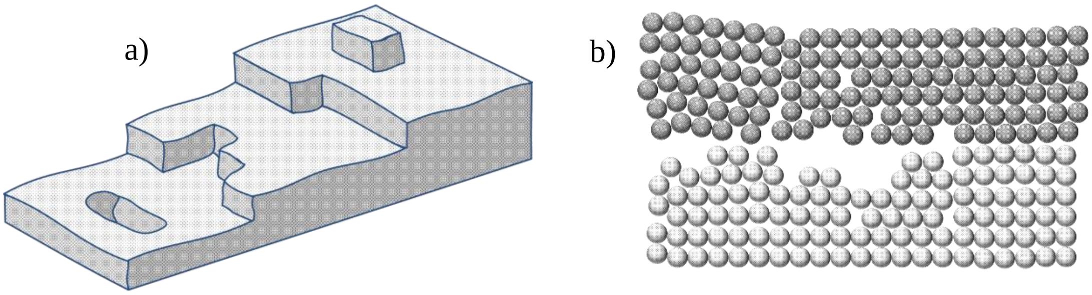

Figure 2.1 a) The terrace ledge kink model, b) atomic-scale contact between surfaces [adapted from 1]

It is obvious that the contact between surfaces will be influenced by these imperfections. Figure 2.1 (b) shows that some surface atoms may have fewer neighbouring atoms and therefore, these atoms are less bonded to the substrate and are subjected to different mechanical conditions. It is believed this arrangement also facilitates reactions between the lubricant/additive and the substrate once these molecules are adsorbed. Without these catalytic sites, most surfaces would be virtually inert to chemical reactants [17].

Solid contact

Due to the complex nature of surfaces, two bodies that come into contact only touch at a few high peaks called asperities. They represent just a small fraction of the apparent contact area, as shown in Figure 2.2 (a). The contact pressures at these points are very high and can lead to plastic deformation, which increases the size of the contact area until it is sufficient to balance the load [18].

The real contact between asperities is very important in predicting the magnitude of the friction force and the friction coefficient. Rougher surfaces allow peaks and valleys to interlock, impeding the relative motion of the surfaces and therefore increasing the friction coefficient. In lubricated contacts, this behaviour is encountered in mixed or boundary lubrication regimes, which are discussed in Section 2.2.3. The severity of the interactions is generally reduced by using friction modifiers, which adsorb or react with the active surfaces and form thin layers. When both surfaces are covered with friction modifier molecules, the asperities slide over each other more easily, reducing the friction coefficient, while the film is sustained by strong lateral attractions between the nonpolar carbon chains of the FM molecules. Depending on the contact pressure, films may eventually be penetrated or gradually removed from the contact [1, 2, 19-22].

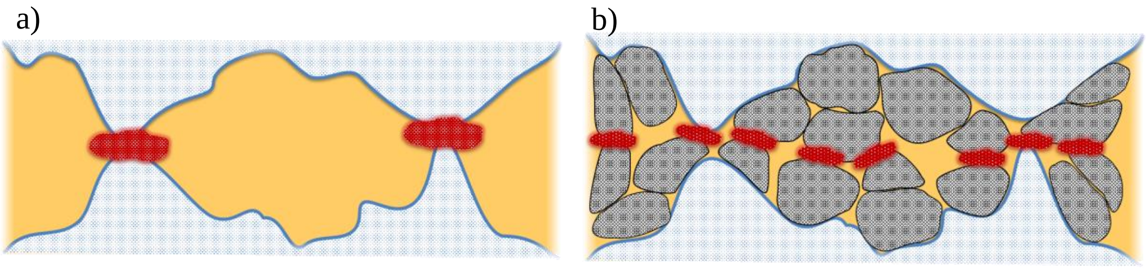

Figure 2.2 a) True contact between surfaces at the nanoscale, b) NPs infiltrate asperities and increase contact area, reducing local contact pressures between asperities [adapted from 1]

Particular interest has been shown for NPs due to their nanoscale size, which allows them to infiltrate contacts of diverse geometries, fill the gaps between contact asperities (increase real contact area and therefore decrease contact pressures between asperities) and ultimately form a protective boundary film, persistent under high pressure, as shown schematically in Figure 2.2 (b). It has been proposed that the size of the NPs should be equal to or smaller than the surface roughness in order to infiltrate the contact efficiently [9-11, 23].

2.2.3 Lubrication

Lubricated friction occurs when a lubricant film separates two moving surfaces. The lubricant creates a film that helps carry the load between the opposing surfaces.

Depending on how the load is carried, three main ***lubrication regimes*** were initially proposed: boundary, mixed and hydrodynamic (HD) [1-4, 24]. Literature usually differentiates between them according to the ratio of the lubrication film thickness with respect to the surface roughness. The theory was initially designed for *conformal contacts*, where the load is spread on the surface and the contact pressures are thus relatively low (e.g. disc-on-disc). However, in *counter-formal contacts* (e.g. ball-on-disc), the surface geometry causes the loads to be carried by a limited area, generating very high pressures in the contacts, sufficient to induce greater elastic deformation of the contacting surfaces. Elastohydrodynamic (EHD or EHL) lubrication was proposed to explain the mechanism of lubrication in such contacts. Figure 2.3 shows the lubrication regimes and the variation of the friction coefficient.

For experimental purposes, a *'Stribeck curve'* (Figure 2.3) will illustrate the variation of the friction coefficient with ($\boldsymbol{\eta U/W}$), where $\boldsymbol{\eta}$ is the viscosity of the lubricant, $\boldsymbol{U}$ is the speed and $\boldsymbol{W}$ is the applied load.

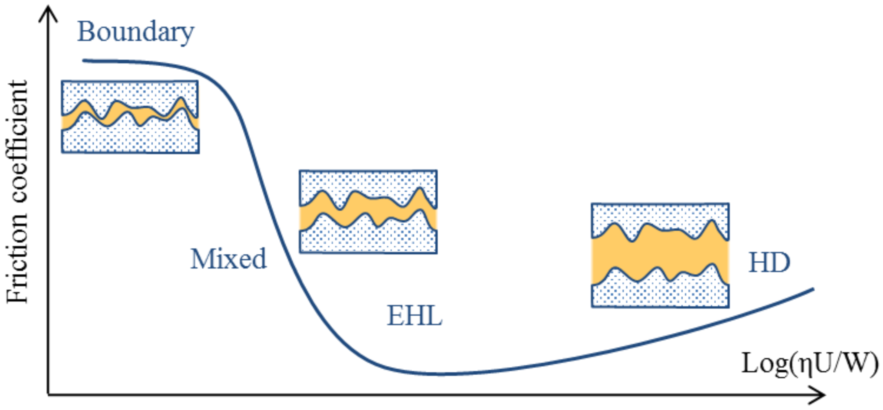

Figure 2.3 Stribeck curve and lubrication regimes

Hydrodynamic (HD) regime

In the HD regime the surfaces are completely separated by the lubricant film and the load is fully supported by the lubricant due to viscous forces. With increase of ($\boldsymbol{\eta U/W}$), which shows the capability of the lubricant to form a separating film, friction will continue to increase with a gentle slope. The regime describes lubrication for systems where the contact pressures are relatively low and have a negligible effect on the viscosity of the lubricant. Additives in the lubricant have little effect on the tribological properties of the base oil, unless they influence viscosity.

Mixed regime

In the mixed regime the size of the material asperities is similar to that of the protecting film. The opposing surfaces are moving closer, interactions between them begin to appear and the friction coefficient increases sharply with the decrease of ($\boldsymbol{\eta U/W}$). The hydrodynamic film still supports part of the load, although boundary lubrication mechanisms are also important in this condition.

Boundary and extreme-pressure (EP) regime

In this regime the load is carried by the asperities on the contacting surfaces, the friction being highest and independent of the ($\boldsymbol{\eta U/W}$) parameter. This regime is the most damaging to the surfaces and precautions are usually taken to avoid it. In contacts where boundary and EP lubrication inescapably occur, it is countered by the use of lubricant additives capable of physisorption, chemisorption or reaction with the material surface, depending on the loading conditions and temperature in the contact: in low-temperature applications the regime is termed boundary, while in high-pressure high-temperature contacts the regime is traditionally referred to as EP lubrication.

In *low-temperature* applications (up to about 100-150ºC) boundary lubrication is performed with adsorbed thin layers of surfactant molecules (friction modifiers) such as organic acids, alcohols and amines, often termed ‘oiliness additives’ [19-22]. These adsorb onto the surface by either physisorption or chemisorption. *Physisorption* is a reversible process that occurs at lower temperatures and involves the formation of Van der Waals forces between the polar groups of the additive and the metal surface. There is a critical temperature above which molecules possess enough energy to desorb back into the lubricant. *Chemisorption* is usually irreversible and entails a reaction of the additive molecules with the substrate. The effect of these surfactant molecules on friction increases with carbon chain length and decreases with the degree of molecule branching (the packing of branched molecules is restricted) [1, 25]. Both adsorption mechanisms require the presence of an oxide layer or contaminants on the substrate, as the fresh metal surface is extremely active and leads to the decomposition of the organic additive molecules [26, 27].

Boundary lubrication can also be performed using inorganic layered materials with weak Van der Waals interlayer bonding, such as graphite or metal dichalcogenides (molybdenum disulphide, tungsten disulphide, tungsten diselenide etc.). These additives are physisorbed onto the substrate and shear under sliding conditions with very low friction coefficients [9, 19, 20, 28]. WS_2 has been successfully used as a friction modifier in dry contacts yielding remarkable results (COF as low as 0.03 [29, 30]). However, the impediment to using WS_2 in lubricants has long been the difficulty in obtaining stable dispersions of the additive [31-34].

In *high-pressure high-temperature* contacts EP lubrication is enhanced by active chemicals that react with the metal substrate to form sacrificial films which display a controlled wear rate. The additive reaction is favoured by the formation of fresh catalytic sites (‘nascent surfaces’) during rubbing which leads to the build-up of thick tribofilms. The thickness of the films depends on the reactivity of the additives towards the metal substrate. EP additives are usually organic compounds containing mainly sulphur (S), phosphorous (P), chlorine (Cl) or organometallic complexes [1, 19]. The importance of the presence of S in EP molecules is discussed in Section 2.3.3.2. ‘Mild’ EP additives (‘antiwear’ additives (AW)) usually contain metals or P and generate lower-friction films resistant at medium slide-roll ratios (the ratio of the sliding speed to the entrainment speed) and moderate loads. Since the reactivity of these additives is lower, the chemical reaction is assisted by high local contact pressures [8]. ‘Active’ EP additives mostly contain S, which forms sacrificial films suitable for applications with high slide-roll ratios, high loads and unexpected shock loading [35]. These additives are more reactive and an application-specific balance must be found to avoid either the generation of thin, inefficient films or corroding the substrate and generating large amounts of wear. S is the most commonly used element because it offers the greatest lubricating effect for the least amount of corrosive wear, followed by P and Cl. However, the explanation for this variation has not yet been found [1].

WS_2 has a layered structure with W atoms packed in between sheets of S atoms exposed to the environment. This configuration suggests that under severe conditions (high temperatures and pressures), WS_2 NPs will react with the metal substrate and act as an AW/EP additive [36-38]. This is further discussed in Section 2.3.3.2.

The effect of boundary and AW/EP additives on the Stribeck curve is shown in Figure 2.4. The reduction in friction in the boundary regime is directly related to the efficiency of the additive to adsorb/react in the contact. The small increase in friction in the mixed regime is expected due to the formation of the rough tribofilm [8, 39, 40].

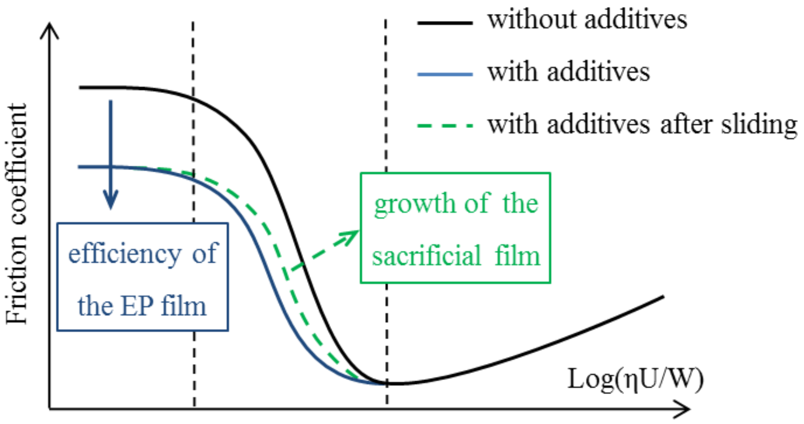

Figure 2.4 The influence of boundary and EP additives on the shape of the Stribeck curve

Elastohydrodynamic (EHL) lubrication appears in *counter-formal contacts*. The surface geometry causes the load to be carried by a limited area, generating very high pressures in the contacts (e.g. ball on flat). These are sufficient to influence the lubricant viscosity and cause elastic deformation of the solid surface, as shown in Figure 2.5 (a).

When two elastic bodies come into contact, their surfaces are deformed and the size of the contact area is a function of the load applied. Knowing the real contact area is important in determining the pressures inside the contact. This problem can be approached using the theory of elasticity and was first solved for two static elastic spheres by Hertz [41]. However, the pressure distribution inside an elliptical EHL contact (e.g. between balls and raceways in ball bearings) changes when the surfaces move relative to each other.

A diagram of the EHL contact and the corresponding pressure distribution is presented in Figure 2.5, along with an interferometry image of the EHL contact between a ball and a silica coated glass disc. A film constriction is formed at the outlet of the contact with a corresponding pressure peak due to the flow of the lubricating oil through the contact, whose viscosity is increased by the large contact pressures [1, 42]. The central film thickness value (h_c) decreases towards the outlet to a minimum film thickness h_0, which dictates the severity of the lubrication regime, as shown schematically in the profile view of the contact shown in Figure 2.5 (b). Due to the circular shape of contact, the constriction in a point contact is curved and forms a 'horseshoe' constriction, as shown in Figure 2.5 (c).

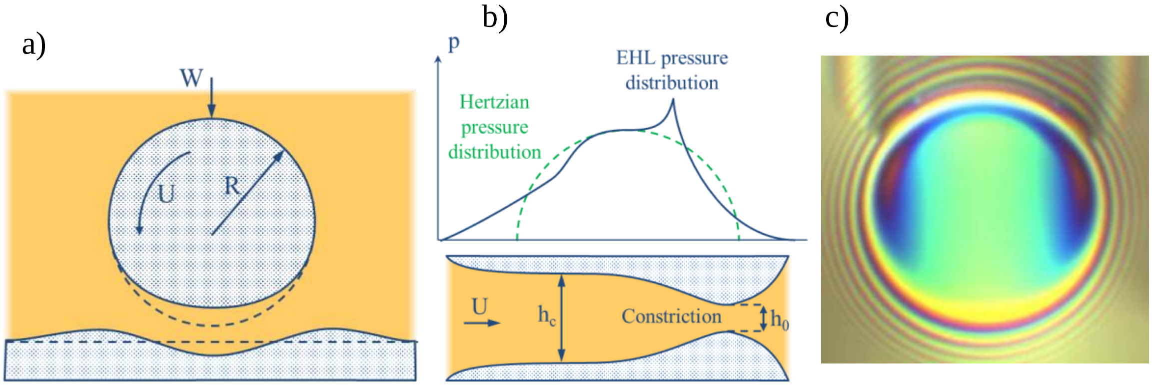

Figure 2.5 a) Schematic of an EHL contact (exaggerated deformation) [adapted from 1], b) pressure distribution in an EHL contact [adapted from 1], c) interferometry image of an EHL contact [reproduced with permission from 43]

The Reynolds equation (2.1) can be used to describe the flow of the lubricant in a tribological contact. This can be simplified according to the specific flow conditions in order to obtain the pressure distribution profile in different applications (journal bearings, thrust bearings, gears etc.).

$$\frac{\partial}{\partial \mathrm{x}}\left(\frac{h^3}{\eta}\frac{\partial p}{\partial x}\right)+\frac{\partial}{\partial \mathrm{y}}\left(\frac{h^3}{\eta}\frac{\partial p}{\partial y}\right)=6\left(U\frac{\partial h}{\partial x}+V\frac{\partial h}{\partial y}\right)+12\,(w_2-w_1)\quad \mathbf{(2.1)}$$

p – fluid pressure [Pa]

h – film thickness [m]

η – fluid viscosity [Pa s]

U, V, w – velocities in the x, y and z directions [m/s]

Dowson/Higginson and Hamrock/Dowson have calculated the minimum film thickness h_0 for line and point contacts in an EHL contact [1, 2]:

$$\frac{h_0}{R'_x}=2.65\ \bar{U}^{\,0.7}\ \bar{G}^{\,0.54}\ \overline{W_L}^{\,-0.13}\qquad -\text{line contact}\quad \mathbf{(2.2)}$$

$$\frac{h_0}{R'_x}=3.63\ \bar{U}^{\,0.68}\ \bar{G}^{\,0.49}\ \bar{W}^{\,-0.073}\left(1-e^{-0.7\,(R'y/R'x)^{0.64}}\right)\quad -\text{point contact}\ \ \mathbf{(2.3)}$$

where $\bar{\boldsymbol{G}}, \bar{\boldsymbol{W}}$ and $\bar{\boldsymbol{U}}$ are the *materials*, *load* and *speed* parameters:

$$\bar{U}=\frac{U\,\eta_0}{E'R'_x}\ ;\quad \bar{G}=\alpha\,E';\quad \overline{W_L}=\frac{W}{E'R'_x\,L}\ \text{(line)}\ ;\quad \bar{W}=\frac{W}{E'R'^2_x}\ \text{(point)}$$

$$\frac{2}{E'}=\frac{1-\nu_A^2}{E_A}+\frac{1-\nu_B^2}{E_B}\quad ;\quad \frac{1}{R'_x}=\frac{1}{R_{ax}}+\frac{1}{R_{bx}}$$

E' – reduced Young's modulus [Pa]

$\boldsymbol{\nu_A}$, $\boldsymbol{\nu_B}$ – Poisson's ratio of bodies A and B

$\boldsymbol{E_A}$, $\boldsymbol{E_B}$ – elastic moduli of bodies A and B

$\boldsymbol{R'_x}$ – reduced radii of contact [m]

$\boldsymbol{R_{ax}}$, $\boldsymbol{R_{bx}}$ – radius of curvature of bodies A and B in the ***x*** direction [m]

α – pressure viscosity coefficient [Pa^{-1}]

As seen in equations 2.2 and 2.3, the minimum film thickness is mainly dependent on the viscosity of the lubricant and the speed of the surfaces. Because the film thickness is largely independent of the applied load, experiments usually yield Stribeck curves that show the variation of the friction coefficient ***μ*** with (***ηU***).

In EHL conditions the contact between asperities is expected to have a marginal contribution to the overall friction coefficient induced between the surfaces. Primarily, ***μ*** accounts for the large shear forces created in the highly compressed lubricant, which displays a non-Newtonian behaviour due to the high EHL contact pressures.

The two opposing surfaces can experience a sliding motion against each other (i.e. the overall speed in the contact is U_a-U_b), a rolling motion (i.e. the entrainment speed is (U_a+U_b)/2) or a combination of the two. The slide roll ratio (SRR) defines the amount of rolling and sliding present in the contact as the ratio of the sliding speed to the entrainment velocity. The SRR is an important parameter, as it affects the severity of the conditions in the tribological contact and can promote the activity of AW/EP lubricant additives [1, 2].

Due to the fact that surfaces are rough, the ***specific film thickness*** (rather than the minimum film thickness) is usually used to characterise lubrication in rubbing contacts [1-4, 44, 45]. This is also known as *the dimensionless* $\boldsymbol{\lambda}$ *ratio* and is defined as the ratio of the calculated minimum film thickness, $\boldsymbol{h_0}$, to the composite surface roughness $\boldsymbol{\sigma}$. This ratio can be seen as the relative separation of surfaces.

$$\boldsymbol{\lambda = \frac{h_0}{\sigma} = \frac{h_0}{\sqrt{R_{q1}^2 + R_{q2}^2}}} \qquad \mathbf{(2.4)}$$

where $\boldsymbol{h_0 = f\left(\frac{U \cdot \eta}{W}\right)}$

A Stribeck curve can alternately be plotted as the friction coefficient against the $\boldsymbol{\lambda}$ ratio, to show the mixed lubrication regime in the range 1 < $\boldsymbol{\lambda}$ < 3 (Figure 2.6).

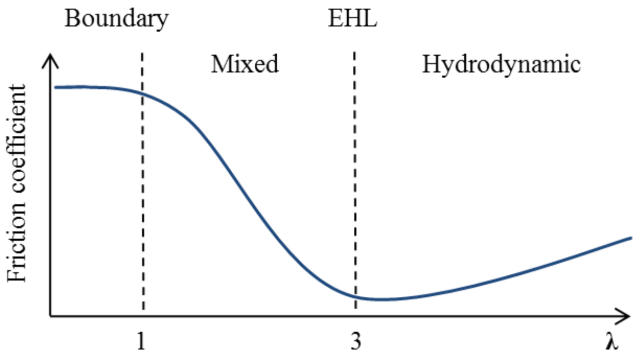

Figure 2.6 Stribeck curve plotted against $\boldsymbol{\lambda}$

Micro-elastohydrodynamic lubrication

When the calculated film thickness in EHL contacts is similar to the surface roughness ($\boldsymbol{\lambda} \approx 1$), the boundary regime is traditionally used to describe the lubrication of moving components. However, many machine elements operate well in these conditions without the occurrence of wear. To explain this, *micro-EHL* lubrication proposes that elastic deformation of asperities takes places, resulting in EHL lubrication between individual asperities. This pushes the onset of the mixed and boundary regimes to lower values of $\boldsymbol{\lambda}$ (e.g. depending on loading conditions, to as little as ~0.2) [1, 2, 46-48].

Temperature plays an important role in EHL and micro-EHL lubrication, especially in sliding contacts. As the viscosity of the lubricant increases towards the maximum pressure peak, frictional energy is dissipated as heat inconsistently across the contact. The temperature difference between the surfaces and the centre of the lubricant film can be in excess of 60ºC, enough to induce large changes in the oil viscosity (lubricant thinning) and reduce the thickness of the lubricating film [1, 2]. Increased temperature near contacting asperities can also lead to *thermoelastic instabilities* – high temperatures cause thermal expansion of asperities, which further decreases the contact surface and results in even higher pressures and temperatures. Lubricant additives must show improved resistance to oxidation due to the temporary increase in frictional energy (flash temperatures). The structure of WS_2 NPs (discussed in Section 2.3.3.1) provides them with high thermal stability, recommending them as possible additive candidates for EHL contacts [49].

The main differences between the friction regimes are summarised in Table 2.1.

Table 2.1 Lubrication regimes [adapted from 50]

Regime	h_0 (μm)	μ	Film formation	Contact geometry
Dry	0.001 – 0.01	0.4 – 0.8	No lubricant	Variable
Boundary / EP	0.001 – 0.05	0.08 – 0.3	Lubricant reacts with surface	Variable
EHL	0.1 – 1	0.03 – 0.1	Lubricant dragged into contact	Counter-formal
Hydrodynamic	1 - 100	0.007 – 0.01	Lubricant dragged into contact	Conformal

In the boundary and EP regime, friction is highest and dependent only on the interactions between asperities or the strength of the high-pressure non-Newtonian film covering the interface. Therefore, antiwear and EP additives are used to reduce the friction coefficient and to prevent excessive wear of materials. Friction drops towards a minimum in the EHL regime (valid for counter-formal geometries), remaining constant, unvarying with the film thickness. In practice, viscous forces in the fluid lead to a gradual increase in friction.

2.2.4 Wear

Wear represents the loss or sideways displacement of material from a solid surface. It is the result of the mechanical action of another surface and it is greatly influenced by the roughness in the contact area. A sliding motion can generate more wear with the increase of the surface roughness. There are many types of wear, depending on the mechanism involved: abrasive wear, erosive wear, adhesive wear, corrosive wear, surface fatigue and fretting wear [1].

Abrasive wear is the most active type of wear and produces the largest costs to the industry. Therefore, it has been intensely studied to determine its mechanism and ways to prevent it. Abrasive wear occurs when a body is loaded against a material of the same hardness or higher. The harder material causes loss of material on the softer surface. There are two types of abrasive wear: two-body abrasion and three-body abrasion (Figure 2.7). The two-body abrasive wear model involves asperities and immobile grits passing over the opposing surface like a cutting tool. In the three-body abrasive wear model, the grits are free to move, leading to a slower material removal process [51, 52].

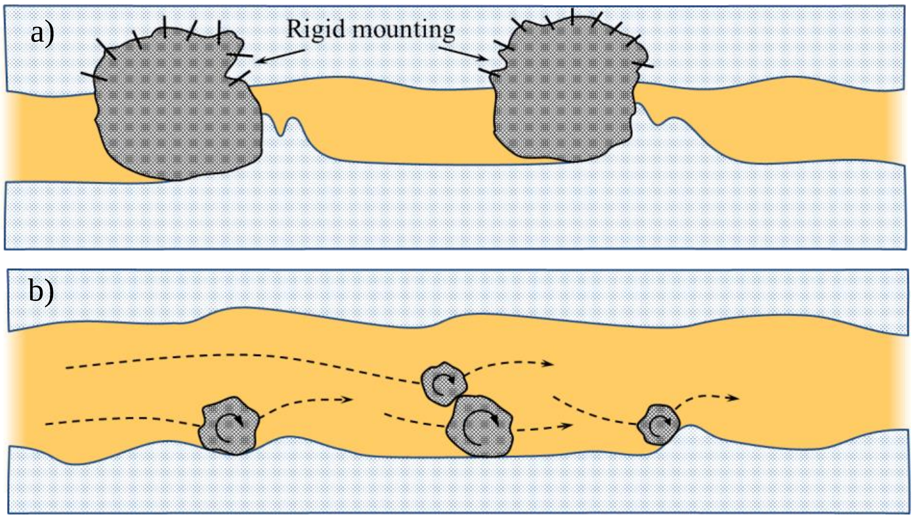

Figure 2.7 a) Two and b) three body abrasion [adapted from 1]

In lubricated contacts, abrasive wear occurs in the mixed regime (to a lesser degree) and in the boundary and EP regime. In order to prevent metal asperity contact and the generation of hard debris, antiwear and EP additives are commonly used to initiate a chemical reaction with the substrate and generate sacrificial films on the metal 'nascent surfaces'. The most common antiwear additives currently in use are zinc dialkyldithiophosphates (ZDDP), which generate thick, glassy phosphate films in the contact. The disadvantage is the formation of phosphorous- and sulphur-containing volatile compounds that decrease the life of exhaust catalysts and possess environmental issues [8, 53, 54]. As opposed to this, WS_2 does not contain organic sulphur in its structure and the possibility of releasing volatile components during tribofilm formation is very low.

Failure to provide lubrication between surfaces can lead to ***adhesive wear***. This is a serious form of wear, as most solids adhere on contact (and particularly metals). Solids in normal contacts are protected by layers of adsorbed gases, water or oils and a layer of oxide for most metals. However, under high loads and sliding, these protective films are removed and reactive 'nascent surfaces' are exposed. When metals come under direct contact in these conditions, the atoms bond by electron transfer between surfaces (the nature of the metallic bond allows electrons to move in different types of lattices as long as the atoms are sufficiently close) [1, 55]. Adhesion is strongest between metals of the same material (i.e. steel to steel), but generally, very high adhesion occurs between most metal surfaces. Adhesion is usually followed by transfer of material to the harder body, as shown in Figure 2.8.

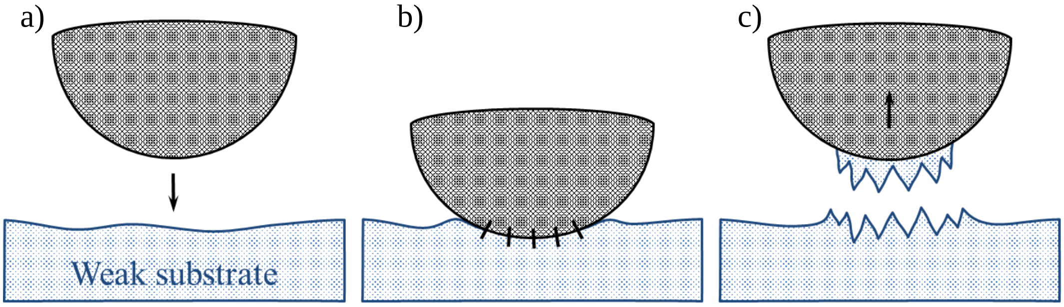

Figure 2.8 Transfer of material due to adhesion of two surfaces [adapted from 1]

The combination of adhesion and a sliding movement produces a very large amount of plastic deformation. Transfer layers are formed on the harder material and have a high impact on wear, because the transferred material is work hardened in the process and can wear the surface itself. In order to avoid adhesive wear and the large, varying friction coefficients associated with it, formation of oxide or contaminant layers are encouraged and lubricants/lubricant additives are employed to keep the bodies apart.

Corrosive wear is due to reactions of the substrate with different chemical reagents (e.g. EP additives, a reactive lubricant, water or air). In boundary and AW/EP lubricated contacts, corrosion is induced purposely by generating a protective film on the surface in order to prevent abrasive and adhesive wear. However, aggressive corrosion can lead to severe loss of material and a balance should be found between a large sacrificial film thickness (corrosion due to a very active AW/EP lubricant) and a small tribofilm thickness (which may not offer sufficient boundary protection and allow adhesion). The film formation is a dynamic process controlled by its generation (chemical reaction kinetics) and removal (wear) rates, which depend on the reactivity of the EP additive and the operating conditions (temperature, time, load, slide-roll ratio etc.) [56-58].

WS_2 NPs have a high thermal stability and strong bonding within individual layers, preventing them from being too reactive. When asperities are in contact, high pressures and temperatures are generated that can help initiate the formation of a S-based sacrificial film on the surface only where it is needed, as discussed further in Section 2.3.3.2.

Fatigue wear occurs when asperities that are subjected to high local stresses and deformation generate cracks in the substrate. Wear generated by this type of mechanism is determined by crack initiation, growth and fracture. The typical mechanism begins with the initiation of a crack at a weak point on the surface (stress raising defect). As the crack grows, it can develop secondary cracks or merge with other cracks. When it resurfaces, a wear particle is formed and released from the surface.

In ***rolling contacts*** such as bearings, the loads are concentrated over a small area and therefore rolling elements operate in EHL conditions. Rolling contact fatigue (RCF) displays a number of particularities due to the cyclic loading conditions and the large contact pressures: characteristic pressures are in the order of one to a few GPa, but they are expected to be substantially higher in local contacts between asperities [1, 2]. Due to the magnitude of the stress, cracks form in the material at the surface or subsurface. Material imperfections in the steel such as inclusions are preferential crack initiators, along with weak grain boundaries or local zones with high residual stresses [59].

With the continuous increase in bearing steel strength, a new type of failure was observed in rolling elements related to the presence of atomic hydrogen in the material [60]. Hydrogen embrittlement occurs in high-strength steel early in the life of the component, with the formation of white etching areas (WEA) associated with white etching cracks (WEC) [61], as discussed in Section 2.4.4. A number of studies have suggested the importance of understanding the mechanisms of hydrogen permeation into the material, which could provide a direct way of preventing embrittlement and RCF failure [62, 63]. WS_2 NP additives are a possible solution to embrittlement due to their ability to form tribofilms on the steel substrate, which are efficient at preventing hydrogen permeation [64].

2.2.5 Summary

In order to reduce friction and wear, most tribological systems use a lubricant film to prevent the contact between surfaces. The thickness of this film dictates the lubrication regime and the magnitude of the friction forces. The friction coefficient is measurable and can be plotted as a Stribeck curve to show its behaviour in different lubricating conditions. It is desirable to obtain the smallest value possible for $\boldsymbol{\mu}$, as this usually leads to reduced energy costs and wear of the surfaces. Therefore, most engineering applications try to avoid dry or boundary lubrication and focus on providing hydrodynamic (conformal contacts) and elastohydrodynamic (counter-formal contacts) lubrication conditions.

Local contact pressures between asperities are significantly higher than the nominal pressure due to the rough nature of surfaces. However, nanoparticle additives can infiltrate contacts, fill the gaps between asperities and reduce contact pressures.

Boundary and EP additives interact with the surface and reduce friction and wear by forming tribofilms of various thicknesses. Boundary additives such as carboxylic acids adsorb onto the substrate and are very efficient in low temperature applications, while inorganic layered materials can reduce friction due to their weak, interlayer shearing forces. EP additives are particularly reactive towards the fresh catalytic surfaces generated during rubbing in high-pressure, high-temperature contacts and generate thick tribofilms. Sulphur based molecules show the highest efficiency at generating chemical tribofilms for the amount of corrosion produced, although the reactivity of the additives should not be too high.

WS_2 NPs have a layered structure with weak, interlayer Van der Waals forces and strong bonding within individual layers, which provide them with high thermal stability and low shear strength. WS_2 has been successfully used as a friction modifier in dry lubrication, but tests in oil lubricated conditions are affected by their colloidal instability. Furthermore, high-temperature tests have not been performed to investigate their EP properties. The next sections provide more information about the current understanding of the mechanism of action of WS_2 and details concerning the challenges of obtaining stable WS_2 dispersions in lubricants.

2.3 ADDITIVES IN LUBRICATION

2.3.1 Introduction

A lubricant film present between solid surfaces can greatly reduce friction and wear. The extent of these improvements is dictated by the properties of the lubricant. The use of a simple base oil (e.g. mineral oil) is sufficient for some applications, but new technologies require more sophisticated geometries, greater loads and higher contact pressures. The properties of a lubricant can be improved by the use of additives. These are chemical compounds mixed with the base fluid, which impart special properties to lubricants. Two of the most important types of additives are *friction modifiers* (FM) and *antiwear* (AW) additives.

Zinc dialkyldithiophosphates (ZDDPs) have been used in engine oils for more than 70 years and are probably the most successful AW additives ever discovered. In addition to being good antioxidants, they reduce wear by rapidly forming relatively thick sacrificial boundary tribofilms with a hardness characteristic of soft polymeric materials [8, 39, 65]. However, ZDDP molecules contain organic Zn, S and P, which are generally toxic and poisonous to the exhaust catalyst in automotive applications [53, 54]. Furthermore, the formation of the tribofilms is accompanied by high friction and therefore, FM additives must be added to overcome this inconvenience.

NPs have attracted increasing interest in tribological applications due to their ability to infiltrate asperities (increasing the real contact area) and cover the surfaces with a thin boundary film. When the surface chemistry of the particles is matched with the chemistry of the steel surface, stable dispersions of NPs can act as friction modifiers, antiwear additives or both [9, 11, 66].

WS_2 NPs have a layered structure, similar to other inorganic layered materials such as graphite or MoS_2, which allows them to exfoliate under shear, giving them excellent friction reducing properties [12, 23]. MoS_2 has a very similar structure to WS_2 and shows EP behaviour due to the reaction of S atoms with the metal substrate. However, the EP properties of WS_2 have not been thoroughly investigated, possibly due to the higher thermal stability of WS_2, which was expected to render the particles chemically inactive [67].

This section describes the properties of the main types of additives currently in use in tribological applications. The structure of WS_2 is also discussed in order to explain their remarkable properties as nanoadditives. The discussion will emphasise the possibility of using WS_2 NPs as FM and/or AW additives.

2.3.2 Base oils

Base oils are obtained by refining crude oil (mineral oils) or by manufacturing using chemical processes (i.e. synthetic oils) and they provide the basic lubricating properties: separate the moving surfaces, remove heat and wear particles and minimize friction [68-71].

Viscosity (**η**) is one of the most important physical properties of a base oil and quantifies the resistance of the fluid to flow. The dynamic (absolute) viscosity is the resistance to relative shearing motion (internal resistance) and is measured in [Pa s] or [P] (poise). The kinematic viscosity quantifies the fluid flow due to gravity and is measured in [m^2/s] or [S] (Stokes) [1, 2]. The relation between the two is given by:

$$kinematic\ viscosity = \frac{dynamic\ viscosity}{density} \quad (\mathbf{2.5})$$

The viscosity of a base oil decreases with temperature and this behaviour affects the overall performance of the lubricant. ***The viscosity index (VI)*** is defined as the susceptibility of a lubricant to changes in viscosity with temperature, with higher VIs indicating smaller changes in viscosity and better performing oils:

$$VI = 100 \times \frac{L-U}{L-H} \quad (\mathbf{2.6})$$

U – viscosity of the sample at 40ºC
L – viscosity at 40ºC of a standard oil with a VI=0
H – viscosity at 40ºC of a standard oil with a VI=100
– the standard oils are selected to have the same viscosity at 100ºC as the oil sample.

According to the composition and VIs of the refined base oils, they are categorized by the American Petroleum Institute (API) into 5 major groups [2, 72, 73].

Mineral oils are obtained from crude oil and comprise Groups I, II and III, according to the severity of the refining process and subsequent viscosity/temperature properties and oxidation stability. Branched paraffins (alkanes) are the most desired type of molecules in refined mineral oils due to their increased chemical stability.

Synthetic oils are created by chemical processes from various feedstocks. They are more expensive to produce than mineral oils, but usually have improved thermal and oxidative stability, wider temperature performance ranges and higher VIs [2, 74].

- Group IV (synthetic hydrocarbon) oils are usually polymeric compounds with a hydrocarbon base. The large majority of these oils are polyalphaolefins (PAOs).
- Group V oils account for the rest of the oils which cannot be placed in the previous groups. They are carboxyl esters, phosphate esters and polyglycols.

Due to their superior performance, synthetic oils were used throughout this study. The polarity of the oil is expected to influence its interaction with the substrate and the additives. Therefore, both a nonpolar Group IV PAO and a polar Group V polypropyleneglycol (PPG) were used to investigate the mechanism of WS_2 and its interactions with the base oil and metal substrate.

2.3.3 Classic additives

2.3.3.1 Friction modifiers

Friction modifiers (FMs) reduce friction between lubricated moving parts, directly increasing fuel economy. There are mainly two types of FMs: amphiphilic organic molecules with a polar head group and a long hydrophobic chain (e.g. carboxylic fatty acids, glycerol monooleate and phosphate esters) and inorganic layered structures bound by Van der Waals forces (e.g. graphite, MoS_2, WS_2, WSe_2) [68, 69]. The former can physically adsorb (the polar heads adsorb on the polar metal substrates while the long carbon chains keep the surfaces apart) or chemically react with the contact surfaces. The latter exfoliate under shear, penetrate contacts of diverse geometries, fill the gaps between contact asperities and ultimately form a protective boundary film, persistent under high pressure. FMs are most efficient in low- or medium-loaded surface contacts [1].

Carboxylic fatty acids and salts of fatty acids are often called '*oiliness additives*'. Oiliness refers to the friction reducing capacity and is a joint property of both lubricant and metal substrate [21]. Fatty acid derivatives have been developed over the last 100 years to reduce boundary friction of mineral oil lubricated contacts and their mechanism of action has been a topic of great interest in recent research. Current understanding of their mechanism involves the adsorption/reaction of molecules on the substrate and formation of dense monolayers (2 nm thick) or thick reacted viscous layers [21, 22, 75].

Organic acids have a polar carboxylic group (-COOH) and a long hydrophobic carbon chain. The adsorption of the molecule is governed by the interaction between the acidic group with the metal substrate and the formation of polar bonds. For noble metals such as platinum and silver, which are unreactive and are not protected by an oxide layer, the lubrication mechanism is based on the direct physisorption onto the metal. However, most metals are covered in a thin oxide layer and other impurities and the FM molecules adsorb onto these protective layers, as shown schematically in Figure 2.9 (a).

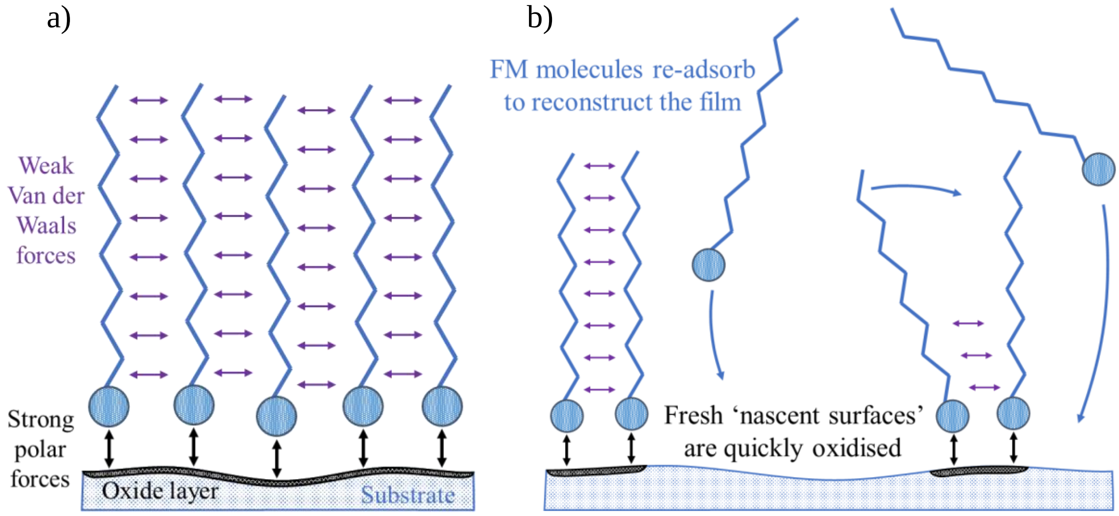

Figure 2.9 a) Physisorption of FM molecules on the metal substrate [adapted from 1], b) re-adsorption of FM molecules after partial removal during sliding [adapted from 1]

Carboxylic acids and their salts are also capable of reacting with the substrate, leading to chemisorbed molecules and a thicker tribofilm. It has been shown that a 2:1 mixture of metal oleate and oleic acid can form thick boundary films (10 nm+) on the substrate if the metal has a lower redox potential than iron (i.e. if the metal is after Fe in the electrochemical series). These are believed to consist primarily of insoluble Fe (II) oleate generated by the redox reaction between the metal oleate and iron from the nascent steel surface [22]. The chemisorption of FMs is usually irreversible and films can even resist washing with solvents. However, if the oxide protective layer on the metal surface is removed during sliding and active catalytic surfaces are exposed, the carboxylic molecules are decomposed due to the very high reactivity of the 'nascent surfaces' [16, 26]. However, these 'nascent surfaces' are quickly oxidized and the film is regenerated (unless the conditions are detrimental, i.e. experiments performed in vacuum).

The strength of the FM film is governed by the molecule bonding to the substrate, but also by the large number of weak Van der Waals intermolecular forces between the C chains, which are arranged in a compact layer. Therefore, the strength of the film depends on the number of Van der Waals interactions, which is proportional to the length of the C chain, as also highlighted in Figure 2.9 (a). For adequate lubrication, the minimum chain length was found to be 9 C atoms, while the most used compounds have a chain length of ~18 C atoms [76]. Molecule branching is also an important factor for the adsorption strength of the FM (i.e. branched hydrocarbon chains occupy a larger area on the substrate and thus have a smaller number of Van der Waals bonds with adjacent molecules [25]).

During sliding of the asperities, the film may be partially removed. The efficiency of the film is considered to depend on its ability to regenerate. The rate limiting process (i.e. the slowest step) is the re-adsorption of the free FM molecules from the lubricant into the incomplete film, as shown schematically in Figure 2.9 (b) [77].

Due to their good FM properties and their ability to adsorb on surfaces, carboxylic acids have also been used to functionalize different NPs (e.g. silver [78], silica [79], ceria [80], copper sulphide [81], lead sulphide [82] etc.). The interactions at the surface of functionalized particles are similar, i.e. the FM molecules adsorb forming compact films, while the hydrophobic carbon chains interact with the oil via Van der Waals forces, preventing the agglomeration of NPs and keeping them suspended as a colloid (this is further discussed in Section 2.5.3).

Transition metal dichalcogenides, such as ***molybdenum disulphide (MoS_2)*** and ***tungsten disulphide (WS_2)***, are some of the most efficient compounds at reducing friction [9, 83-88]. The first recorded use of MoS_2 was by early prospectors in the 1600s, who used it to lubricate the axles of wagons. Since then, it has been used as a lubricant or additive to lubricants, with records of patents dating back to 1927. The coefficient of friction of surfaces covered in metal dichalcogenides is 0.002-0.05 in dry conditions, but increases up to ~0.2 in humid environments [89].

Both MoS_2 and WS_2 crystals have a hexagonal structure and are composed of a layer of molybdenum/tungsten atoms packed in between two layers of sulphur, as shown in Figure 2.10 [1, 88-90]. The metal has a trigonal prismatic coordination sphere accommodating six sulphide ligands, while each sulphur atom has a pyramidal configuration and a pair of free electrons occupying the space in between the sulphide layers. The bonding in the individual layers is very strong, especially for WS_2, conferring the compounds excellent thermal resistance (i.e. the properties of MoS_2 are unaffected up to ~350-400ºC, while WS_2 is stable up to ~500ºC [87, 89]). Lubrication relies on the low shear slippage between the S atoms, which are only bound by weak Van der Waals forces (Figure 2.11). The properties of the lamellar structure are intrinsic and no external form of moisture is required, as opposed to other common FMs such as graphite (the mechanism of action of graphite is also based on the weak Van der Waals forces between individual carbon layers, but it is not as effective in dry conditions, as water molecules are needed to promote the shearing between layers [86, 87, 91]).

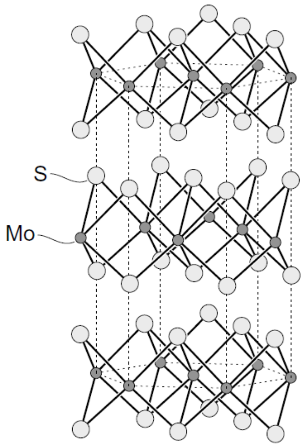

Figure 2.10 Structure of MoS_2 [reproduced with permission from 1].

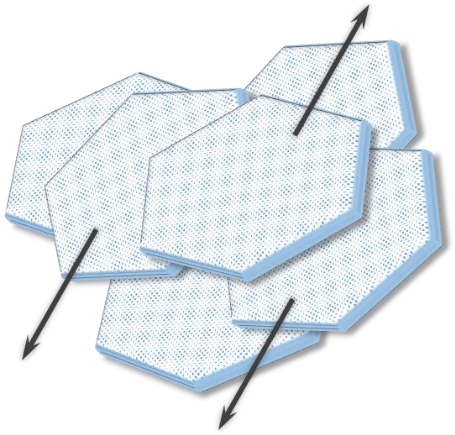

Figure 2.11 Lubrication with WS_2 by low interlayer shear [adapted from 92].

Unfortunately, MoS_2 and WS_2 are not soluble in organic solvents (and therefore oils), so they can be used only as fine dispersions, greases or as oil soluble complexes. Molybdenum-containing complexes have been developed, such as molybdenum (VI) dialkyldithiophosphate (Mo-DDP) [93] and molybdenum dithiocarbamate (Mo-DTC) [94, 95]. These compounds react with the steel substrate and form MoS_2 sheets in the contact [96-108], which is responsible for very low friction coefficients even in dry conditions. The initiation of the chemical reaction requires temperature (at least 70ºC) and in mild conditions leads to the formation of 10-25 nm sized MoS_2 in the contact [96]. MoDTC was found to form MoS_2 more readily than MoDDP, and only at asperity contacts, where temperatures and pressures are higher [97-99]. MoDTC is more effective when used with ZDDP, a synergistic effect observed by many researchers and explained by the positive influence of ZDDP on the formation of MoS_2 [106-112]. However, the chemical interactions also lead to the generation of other compounds, such as various molybdenum oxides, including MoO_2 and MoO_3 [86, 88, 100-103, 113]. Some researchers have reported that MoO_3 has short Mo-O bond lengths and high decohesion energy, indicating it is not a good FM [114, 115]. Research has also shown that MoO_2 is very abrasive [88].

Corresponding organic tungsten compounds have also been synthesized. Tungsten dithiocarbamate (WDTC) added to oil in a concentration of 0.5% w/w was observed to give better antiwear protection than MoDTC/MoDTP [116, 117]. However, the antiwear mechanism has not been investigated. The chemical interactions with the substrate are expected to be similar to MoDTC, with some small differences: if the formation of WO_3 on the track is observed, friction should be lower. Tungsten oxides are reported to have very low decohesion energy and therefore, WO_3 should not be abrasive [114, 115].

Unfortunately, there are many downsides to using organic molybdenum/tungsten compounds. They are expensive and their synthesis is complex and involves problematic compounds (e.g. P_2S_5 and CS_2) which are very toxic. Because of this, their use in conventional lubricants is limited [8, 9, 54].

2.3.3.2 Antiwear additives

Antiwear additives (AW) are chemicals that are added in order to prevent or reduce metal-metal contacts in moving applications. They accomplish this by reacting with the metal surface and providing a protective low shear strength film that wears off over time.

Zinc dithiophosphates (ZDDPs) are by far the most common antiwear additives [94, 118-121] and have been studied and used for more than half a century. They find applications in virtually all current engine oils. Aside from their antiwear property, ZDDPs also exert an antioxidant action in the oil. The general structure of ZDDP is shown in Figure 2.12.

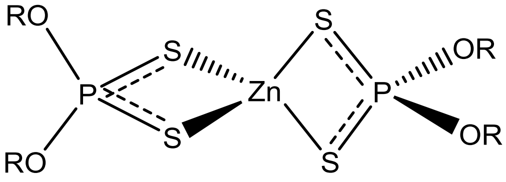

Figure 2.12 The structure of ZDDP [adapted from 122]

The generation of ZDDP tribofilms on steel surfaces and their nature has been the focus of many published studies [8]. It has been shown that they form only on the rubbing tracks and that they are dependent on temperature. The minimum temperature required to start the generation of an AW tribofilm is ~60ºC. On steel, tribofilms can rapidly grow in thickness to 50-150 nm and show an uneven, pad-like distribution (typically 5 to 20 μm across), separated by deep fissures. A two layer model was proposed, where a soft polyphosphate film covers a more rigid sulphide-rich layer (zinc or iron sulphide) chemisorbed onto the steel surface [39]. Organic compounds and unreacted ZDDP are found on the surface of the tribofilm, as presented in Figure 2.13. The chemistry of the ZDDP oil solution was reported to affect the chemical make-up, thickness and mechanism of formation of the antiwear film [123]. The antiwear films formed by ZDDP have high boundary friction coefficients in the range of 0.11 to 0.14, which are maintained up to much higher sliding speeds than is normally the case (i.e. the Stribeck curve is shifted to the right, as previously discussed in Section 2.2.3 and shown in Figure 2.4). This is thought to be due to the unusual morphology of the reaction film [124].

Immersion of steel in heated ZDDP formulations leads to the generation of ZDDP *thermal films* [8]. Temperatures in excess of 100ºC can promote the formation of ~10 nm thin films on the surface of steels, but their thickness can increase with temperature to values of ~200 nm. Tribological experiments carried out on thermal films showed that they resist for at least 12 h in base oil, indication of an AW behaviour.

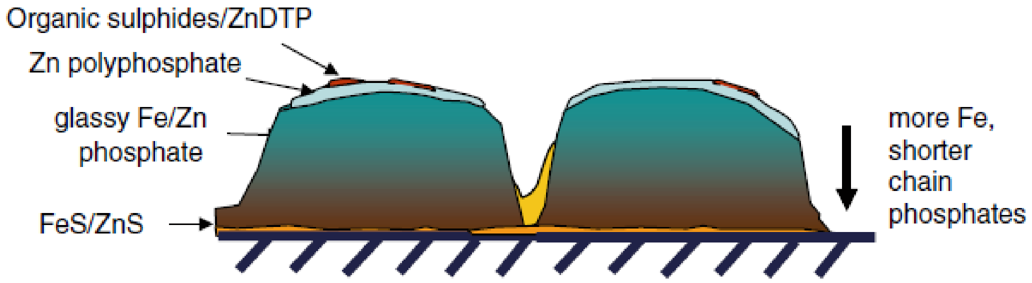

Figure 2.13 Diagram of a ZDDP pad structure and composition [reproduced with permission from 8]

To reduce the high boundary friction of the ZDDP tribofilms, it is necessary to use efficient FMs when formulating lubricants. However, both antiwear and friction modifier additives work by reacting or adsorbing on the lubricated contact surface. Since these two types of additives are used together, it is important to understand the mechanism of action for generating the tribofilm and how these additives interact during this process. In most cases, the selection of optimal additive combinations for lubricant formulation primarily depended upon trial and error or past experience, rather than knowledge of fundamental chemical interactions [56].

Published work investigating the interaction between ZDDP and FMs mainly focuses on ZDDP and MoDTC, which have been shown to synergize well and reduce both wear and friction [106-112]. However, the downside of using MoDTC alone or in combination with ZDDP in oils is the formation of Mo oxides, which are responsible for high friction [86, 88, 102, 113]. One study which investigated the synergism between ZDDP and MoDTC reported that there is a competitive adsorption on the rubbing steel surface between ZDDP and MoDTC, which results in a thinner ZDDP tribofilm [125].

Another study which investigated organic FMs (OFMs) proposed a different mechanism of action, in which OFM additives form a friction-reducing film not on the ferrous surface, but on the zinc phosphate. Therefore, it was recommended that FMs be tested and optimized for effectiveness on the ZDDP films [126].

However, it was later shown that OFMs can greatly influence the reaction of ZDDP with the substrate and consequently, the kinetics, thickness, composition and tribological properties of the tribofilm generated in the rubbing contact [56]. Depending on their chemical composition, some effective OFMs can react with the wear track in rubbing contacts to generate their own tribofilms, which have growth kinetics and thickness comparable to the ZDDP tribofilms. It was also found that in a ZDDP/OFM mixture, the OFM can reduce overall friction, but can also hinder the formation of a thick antiwear tribofilm.

In a tribological contact, tribofilm formation is a dynamic process controlled by its generation (chemical reaction kinetics) and removal (wear) rates, which depend on the reactivity of the additives (towards the substrate and between themselves) and the operating conditions (temperature, time, load, slide-roll ratio etc.) [56-58]. This is especially the case for antiwear and OFM additive mixtures, which compete to react/adsorb on the rubbing ferrous substrates. The generation of tribofilms is the result of the simultaneous interaction of these two additives with the surface of the wear track.

ZDDP has also been investigated in combination with WS_2 [127]. These authors observed a synergistic effect between the two additives tested in PAO oil at 100ºC, i.e. the ZDDP/WS_2 mixture generated ~5 times less wear than 1% w/w ZDDP and ~25% less friction than 1% w/w WS_2. It was concluded that WS_2 enhances the antiwear properties of ZDDP, while ZDDP protects WS_2 particles from oxidation and increases their friction reducing properties.

Aside from high friction, the other drawback of ZDDP additives, as their name suggests, is their zinc, sulphur and phosphorous content. As the lubricant deteriorates, many toxic compounds are released in the oil and can pollute the environment or poison the catalyst in the exhaust filter (e.g. phosphorous oxides, sulphur oxides, metallic ash and volatile compounds such as mercaptides, alkyl sulphides, hydrogen sulphide and low molecular weight olefins) [8, 54]. A lot of research has been directed in trying to find an alternative to this drawback in recent years, but no additive has been found to rival their antiwear properties conferred by the sulphur and phosphorous atoms.

As discussed in Section 2.2.3, sulphur and phosphorous are present in most EP additive compounds, generating sacrificial films resistant under moderate (P and Cl) or high loads (S). The importance of S in EP molecules was identified when chemical analysis techniques became sufficiently accurate to measure the composition of the tribofilms generated on the wear tracks. It was noted that the amount of S present directly correlates with the antiwear behaviour of the film, particularly when S is found as metal sulphides [97, 128-132]. It was also observed that increasing loads and temperatures generate a higher concentration and degree of S penetration in the film [97, 128]. The presence of S can usually be recorded in the top few tens of nanometres [128, 129]. The formation of the tribofilm is described in the literature [56, 57, 129, 130] as a two-step process: a) the initial adsorption/chemisorption of additive molecules on the substrate and b) the reaction of the molecules with the metal surface under the combined effect of shear and temperature, with the generation of various S-containing compounds, which can diffuse into the tribofilm. The growth of the EP film is a dynamic competition between the rate of the chemical reaction (i.e. generation of S compounds) and the rate of removal from the surface (by abrasive action, dissolution into the lubricant or diffusion into the bulk metal).

The presence of S in the structure of transition dichalchogenides such as WS_2 and MoS_2 enables these additives to display an EP behaviour under favourable conditions. Some studies have analysed the chemical composition of the wear tracks generated by MoS_2 and found traces of elemental Mo, which can occur by the following chemical reaction [86, 88, 113, 133-136]:

$$MoS_2 + 2Fe \xrightarrow{720°C} 2FeS + Mo$$

This reaction with the Fe substrate was found to occur above 720ºC, leading to the formation of elemental Mo and iron sulphide. Such temperatures are possible at asperity contacts and therefore, the iron sulphide formed on the asperities can prevent metal contact and seizure. It was proposed that the tribological properties of MoS_2 are due to both a mechanical effect (i.e. acting as an efficient FM and separating the surfaces) and a chemical effect (i.e. acting as an EP additive by the formation of iron sulphides in the contact) [113, 133].

Due to the similar structure, it is expected that WS_2 will perform similarly in loaded contacts. However, WS_2 has higher thermal stability and may undergo a chemical reaction only in high-pressure high-temperature conditions. Therefore, this study will investigate the behaviour of WS_2 at different temperatures.

2.3.4 Nanoparticle additives

2.3.4.1 Applications of NPs as lubricant additives

Increasing attention has recently been given to NPs in many research fields. In tribology, NPs have been employed as solid lubricants, oil dispersions or coating inclusions. There are many advantages associated with using NPs as lubricant additives. Their small size allows them to penetrate tribological contacts and fill the gaps between asperities, as shown in Figure 2.2 [23]. They are also usually larger than simple additive molecules and provide better separation between surfaces. They have large specific surface areas, which give them very different properties compared to the corresponding bulk material, such as higher strength and hardness [137]. Depending on the chemical composition of the NPs, their synthesis can also be focused on more environmentally-friendly compounds. NPs can enhance different lubricant properties, such as load-carrying capacity, friction-reducing ability and antiwear properties [9, 12, 13, 89, 92, 138].

The use of NPs is paramount in *space applications*, where the presence of fluid lubricants is impractical. Another potential application is for *wind turbines*, which are being developed as a viable alternative energy source, but are expensive due to their short lifecycles. Although gearboxes usually have a designed lifetime of 20 years, wind turbines are often serviced at shorter intervals and incur high repair costs and revenue loss due to down times [139, 140]. Gearboxes and turbine lubrication are some of the most important areas where NPs can improve the tribological properties of materials.

IF-WS_2 NPs have been recently added to mineral oils and greases for use in *engines* and *compressors* in various applications such as automotive, marine and heavy duty vehicles. Their efficiency is competitive with other common FM/AW additives [141-144].

The concept of '*green tribology*' was recently introduced and mainly refers to environmentally-friendly lubrication systems and the tribology of renewable-energy applications [145]. Current additives contain various elements or chemical groups (e.g. S, P, Cl or metals in organic complexes), which release toxic compounds or greenhouse gasses upon degradation. As a consequence, successive regulations constantly require the reduction of the Zn, S and P content in lubricants and fuels. Although it may be impossible to eliminate the use of all these elements, it may be feasible to use NPs or compounds with a reduced impact on the environment. Most of the NPs that have been investigated contain simple elements and are more environmentally-friendly [54]. Furthermore, the synthesis of NPs is usually focused on simple reactants, unlike existing additives (i.e. ZDDP), which require toxic chemicals such as P_2S_5 and CS_2 [9]. Used in green lubricants (i.e. lubricants manufactured, used and disposed in an environmentally responsible manner), NPs have the potential to replace toxic additives in future lubrication technologies [54].

An interesting application can be found in the newly developed *hydrogen technologies* [146, 147]. Hydrogen can be converted into electricity and vice-versa using highly efficient green technologies. Many hydrogen fuel cells are being used in vehicle prototypes around the world that offer an environmentally-friendly alternative to fossil fuels. In hydrogen environment applications, moving or sensitive components such as bearings, valves or seals are subject to high-pressure hydrogen gas. Hydrogen is a small atom that can permeate through the superficial layers of steel and cause hydrogen embrittlement under certain circumstances, which ultimately affects the reliability of the components [60-64]. The permeation of hydrogen occurs predominantly inside tribological contacts due to the dissociation of the hydrogen molecules on the catalytic metal ‘nascent surfaces’ [63, 64]. NPs with EP behaviour (i.e. generate a chemical tribofilm on the substrate) can create a barrier which protects against the dissociation and permeation of hydrogen in the metal [148]. By reducing the negative effect of hydrogen permeation into steel, NPs can pave the way for a clean and efficient hydrogen-based economy in the future. The potential use of WS_2 NPs to reduce hydrogen embrittlement is covered in more detail in Section 2.4.

2.3.4.2 Challenges associated with using NPs

The use of NPs introduces a number of challenges – they have a very large specific surface area, which gives them a large surface energy. Therefore, nanoparticles are thermodynamically unstable and their dispersions are susceptible to agglomeration. In order to prevent this, functionalization is required [31-34]. These aspects are addressed in detail in Section 2.5.3.

The risk and safety aspects associated with nanotechnology research constitute a sensitive topic due to the use of nanosize constituents [149, 150]. Therefore, handling, mixing, storage of NPs and NP dispersions, as well as the disposal of the waste oil dispersions have to be carefully considered to avoid possible health risks associated with the exposure to NPs.

The main routes of exposure during the manufacturing, use and disposal of NPs are by inhalation and skin contact and therefore, adequate protective measures should always be implemented to avoid possible health risks. Combustible NPs (e.g. metals and metal oxides) also present a higher fire and explosion risk, which can be avoided by using special production and storage measures.

However, when dispersed in a fluid, the risk of inhaling NPs is much diminished (this could only take place through inhalation of aerosolized droplets produced by vigorous mixing). As nanoadditives, NPs such as WS_2 are dispersed in oils or greases in small concentrations (up to ~1 % w/w). They can be supplied to the consumer as dispersion concentrates to be mixed in oils/greases or as a ready to use product. When NPs are dispersed in oil/grease, health risks are reduced to a minimum, confining any environmental and health issues to the manufacturing stage. Engine oils containing nanoadditives can be disposed of similarly to standard waste lubricants, i.e. collected at petrol stations in ‘used lubricant’ drums and incinerated or recycled. Nanomaterial powder waste should always be collected in specific drums and treated as hazardous industrial waste that is incinerated or disposed via landfill.

The life-cycle assessment with regards to the accumulation and ecotoxicology of by-products is also an important aspect of an environmentally friendly lubricant. About 50 % of a lubricant can be recycled into an oil of up to Group II quality [20]. New environmentally-friendly regulations such as REACH (Registration, Evaluation, Authorisation & restriction of CHemicals) have imposed severe limits for re-refining processes of oils, which now typically involve distillation and hydrotreatment. These technologies can easily separate and inactivate WS_2 and corresponding inorganic by-products [20]. It is also expected that WS_2 nanoadditized lubricants will benefit from an extended service life due to their superior tribological properties.

2.3.5 The use of WS_2 NPs in tribological applications

A large amount of published research has shown that many different types of NPs can help reduce friction or wear if dispersed in a base oil and therefore, they are proposed to be alternatives to problematic additives currently in use (e.g. ZDDP) [9, 54].

The main types of NPs studied in the literature are metals, metal oxides and metal sulphides. The list is not exhaustive and includes additional compounds such as boron nitride, carbonates, borates and nanosized graphite or diamond [9, 12, 92, 138]. The behaviour of NPs can generally be divided in two categories: a) most of the NPs are hard and display a friction reducing effect, but are abrasive and increase the wear of the substrate; b) metal sulphides show AW properties, but have varying FM properties [151-159]. Nonetheless, all NPs must be functionalized in order to obtain stable colloidal dispersions in oil, as discussed in Section 2.5.3.

Compared to other NPs investigated in the literature, WS_2 nanoparticles have excellent friction reducing properties. Studies show that by using WS_2 dispersions in oil, very low friction coefficients can be generated (as discussed in Sections 2.3.5.1 and 2.3.5.2). The properties of WS_2 NPs have not been investigated at high temperatures, but the presence of S in their structure should also enable them to have AW properties. The absence of reactive metals (tungsten compounds are very inert) and organic S or P in the structure make WS_2 NPs and their by-products relatively environmentally-friendly and easily disposable.

WS_2 is already used in space applications due to the high inertness of the material and has several other advantages over the additives currently used in lubricants. Apart from being highly effective in reducing friction and wear between moving parts [12, 37, 38, 160-163], they are inert, non-toxic, non-magnetic and have high resistance to oxidation and thermal degradation [49]. Their positive influence is especially visible in the mixed or boundary lubrication regimes [164] when the most severe wear and damage occur.

WS_2 NPs exist in two forms: 2H and IF. In 2H-WS_2, the layers are flat and present ‘dangling bonds’ (edge effects that can cause deterioration of the nanoparticle through oxidation or burnishing) [12], while in IF-WS_2 (inorganic fullerene-like WS_2) NPs, the layers are rounded up to form closed, ‘onion-like’ cages [29]. From the tribological point of view, it has been reported that under high PV (load x velocity) conditions, as encountered in most engineering applications, 2H-WS_2 outperform IF-WS_2 NPs, while in relatively low PV, IF are better [165]. Manufacturing IF-WS_2 NPs involves higher temperatures and they are also more difficult to functionalize due to their structure. For these reasons, 2H-WS_2 NPs could be more convenient to employ as lubricant nanoadditives in high pressure tribological applications.

2.3.5.1 2H-WS_2 NPs

WS_2 has a layered structure, with W atoms confined in a trigonal prismatic coordination sphere (Figure 2.14). In an acidic environment, each of the sulphur atoms at the edges of these layers has one hydrogen atom bonded (so called 'dangling bond') and are subject to oxidation. For this reason, this structure has been named 2H-WS_2. This structure is maintained regardless of the size of the particle and is responsible for very low friction coefficients (e.g. 0.002-0.05 in dry lubrication and 0.06 in boundary lubrication [89, 92]).

Hexagonal 2H-WS_2 can be synthesized directly from the elements by heating at temperatures above 700ºC [90]. WS_2 is a stoichiometric compound (i.e. it does not form compounds of the type $WS_{2\pm x}$ like other transition metals such as molybdenum).

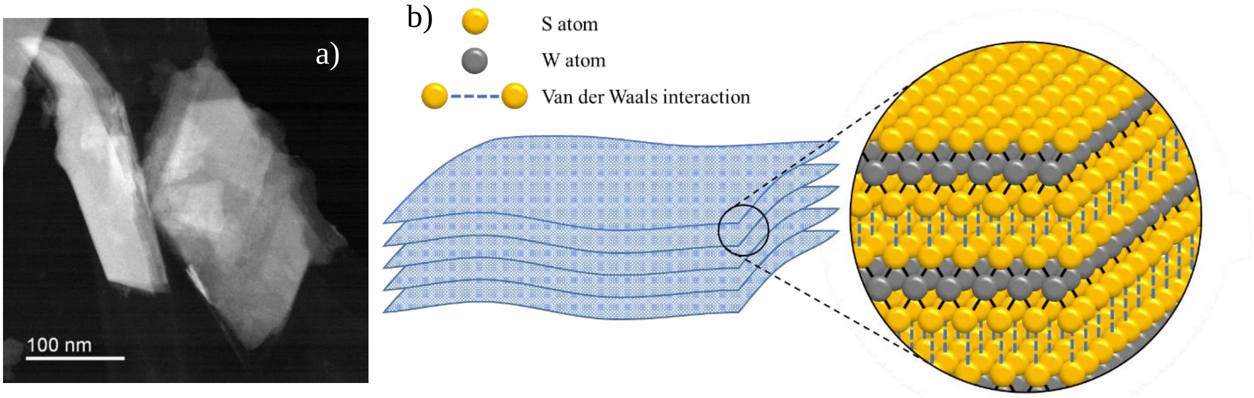

Figure 2.14 The layered structure of 2H-WS_2: a) TEM image and b) schematic showing the layers and atomic arrangement

Because IF and 2H-WS_2 NPs possess a layered morphology similar to graphite and other transition metal dichalcogenides (such as MoS_2), which exfoliate under shear and therefore reduce friction, their tribological properties have also been investigated. Techniques such as TEM and Raman analysis were employed to show that delaminated 2H-WS_2 sheets adhere to the wear track to form a tribofilm [10, 36, 166] and ascribed their superior tribological properties to this mechanism of action. However, this mechanism can only explain the friction reducing properties of WS_2 NPs and not their excellent antiwear properties, effective over a wide range of loads.

An important aspect is that most investigations of the tribological properties of WS_2 NPs have been carried out at room temperature, except for two studies which tested the NPs at 75ºC [164] and 80ºC [167]. However, the authors did not report the presence of a tribofilm on the wear track.

2.3.5.2 Inorganic Fullerene-like WS_2 NPs

An interesting type of additive has been introduced with the synthesis of *inorganic fullerene-like (IF) NPs*. They are hollow, multi-layered spherical particles (as shown in Figure 2.15) that do not have ‘dangling bonds’ [9, 12, 23]. In this case, the edge effects are no longer present and the particles are more inert to chemicals [92].

IF-WS_2 NPs have attracted particular interest because of the high thermal resistance to oxidation and degradation of tungsten compounds [49]. The IF-WS_2 nanoparticles are highly inert to many chemical reagents and do not seem to oxidize easily. Annealing of the NPs has been obtained at 450ºC, but this only cleanses the surface of impurities, without degrading their tribological properties [67]. This allows the use of WS_2 NPs in applications with a very large range of temperatures.

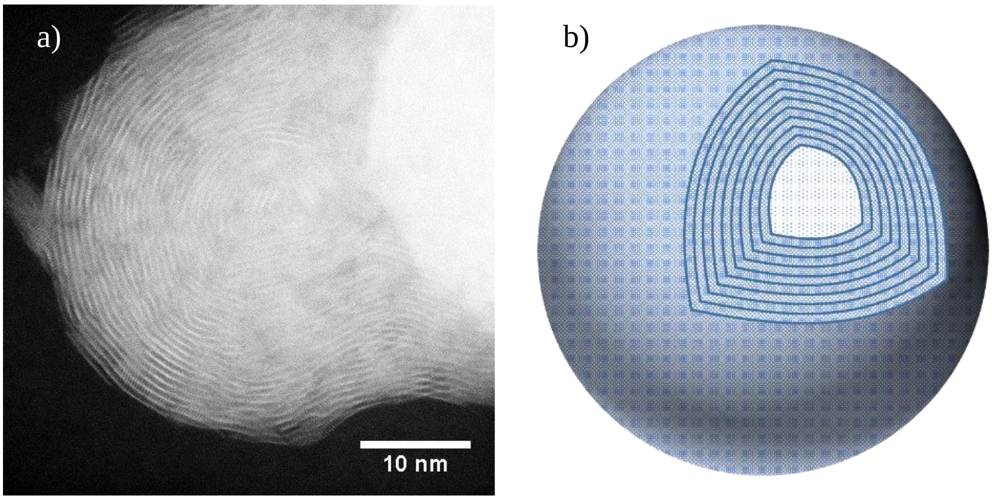

Figure 2.15 Structure of IF-WS_2 NPs: a) an HRTEM image and b) schematic of IF layers

Large amounts of IF-WS_2 NPs are usually obtained by chemical reduction from tungsten compounds (e.g. tungsten trioxide, tungsten hexacarbonyl) in the presence of sulphur vapour or hydrogen disulphide at high temperatures (800-1000ºC) [168-174]. Other important methods include reduction from ammonium tetra thiotungstate to tungsten trisulphide and subsequent reduction with hydrogen at 800-1100ºC [171] and solvothermal synthesis in solution (i.e. reduction from ammonium tetra thiotungstate with sodium borohydride at 190ºC [38, 175]). All methods produce nano-sized IF-WS_2 additives capable of significantly reducing friction and wear (i.e. a COF as low as 0.03-0.04 in boundary lubrication [10, 36, 92, 160-162, 164, 166, 174, 176]).

A large number of research studies have attempted to explain the mechanism of action of IF-WS_2 NPs by proposing many hypotheses [10, 36, 83, 165, 166, 177, 178].

One of the first attempts to explain the mechanism of action stipulated their potential to act as rolling nano ball bearings. Under low loads, the shear force between the inner and outer closed layers of the NPs was not considered to be high enough to exfoliate them, as in the case of the flat layered structures, such as graphite and 2H-WS_2 [165]. This hypothesis was investigated by Golan [179] who used Multiple Beam Interferometry in the surface force apparatus to show that there was no evidence for ’rolling friction’ and the low values of the coefficient of friction can be explained by the friction-induced transfer of layers of WS_2 to the lubricated contact surfaces. However, some recent studies [10, 178], which investigated the rolling mechanism of IF NPs in HRSEM and TEM-AFM in high and respectively low pressure contacts showed that well crystallized, spherically shaped IF NPs can reduce friction through a rolling mechanism. These studies were carried out on atomically smooth silica wafers [10] and the question arises whether in real contact conditions, in which nanoparticles could get trapped or jammed between the surface asperities, the rolling motion is still enabled.

Another attempt to explain the friction reducing mechanism of WS_2 NPs was ascribed to the general ability of NPs to fill the asperity valleys of the contact surfaces due to their nanosize [177]. Thus, in order to be effective, NPs have to be smaller than the asperities and the gap between the contacting surfaces. However, this condition would seem to imply that IF-WS_2 NPs with an average size of 120 nm, as used in these studies, cannot be effective in the boundary and even mixed lubrication regimes, where the gaps are usually smaller than 100 nm. Therefore, this simple hypothesis fails to explain their friction reducing ability.

In view of overcoming the thermodynamic instability of WS_2 NP colloids, two studies investigated the boundary lubrication mechanism of IF-WS_2 NPs coated with trioctylamine and methyltrioctylammoniumchloride (200 nm diameter) under high loads at 25°C [37, 38]. The authors claimed that the mechanism may be ascribed to a tribochemical reaction film, but their X-ray photoelectron spectroscopy (XPS) data of the wear tracks only shows the presence of Fe, C, O and N (from the functionalization groups). Another study, which also used XPS analysis to investigate the wear track generated by WS_2 NPs at room temperature, found small concentrations of tungsten oxide (1.4 at. %), tungsten sulphide and iron oxides [36].

IF-WS_2 NPs have excellent tribological properties. The nature of their surfaces makes them heat resistant and inert to chemicals. However, their dispersions are not stable in time and this inertness is responsible for the difficulty encountered in trying to functionalize them with different dispersants. The mechanism of IF-WS_2 is still debated and their properties still need to be investigated. For this reason, the present study will investigate the tribological properties of WS_2 at different temperatures in order to explore the possibility of a chemical reaction on the steel wear track, which could explain the AW/EP properties of the NPs. Based on the similarity with MoS_2, WS_2 NPs are expected to form a tribofilm containing WO_3 and elemental W. As opposed to Mo oxides, WO_3 is not abrasive due to the long bond lengths and low decohesion energy between layers [114, 115]. Furthermore, tungsten compounds have high hardness and the tribofilm is likely to have very good AW properties.

The only difference between 2H-WS_2 and IF-WS_2 NPs is in the arrangement of the layers, which in IF-WS_2 are rounded up to form closed, ‘onion-like’ cages. The edge effects are no longer present and the particles are more inert to chemicals. However, obtaining such structures involves higher temperatures (i.e. higher manufacturing costs) and also reduces their sensitivity to functionalization. For these reasons, it is easier to study 2H-WS_2 NPs in order to investigate the mechanism of action of WS_2.

IF-WSe_2 NPs

A similar type of NPs have been synthesized containing selenium (Se) instead of S [180, 181]. The IF-WSe_2 structure shows a similar layered morphology with low shear strength between the individual sheets and it is expected that the tribological properties are similar to those of IF-WS_2 NPs. However, Se is a larger atom compared to S and induces higher strain in the IF structure. Furthermore, Se is less reactive that S and thus the synthesis of IF-WSe_2 NPs is slower and allows the formation of more dislocations in the NP [180]. For these reasons the IF structures have a faceted shape compared to the smoother shape of the IF-WS_2 NPs. These defects in the structure, along with the low reactivity of WSe_2, may influence the tribological properties of the NPs, but few studies have investigated these NPs. This study has therefore investigated the tribological properties of IF-WSe_2 NPs and compared them with 2H- and IF-WS_2.

2.3.6 Summary

Lubricant properties can be improved by using various additives. Common friction modifiers such as carboxylic acids, Mo and W dichalcogenides or graphite can help reduce friction between moving components by adsorbing onto the substrates and the formation of thin boundary layers. Antiwear additives such as ZDDP or Mo- and W-DDP can prevent wear of the surfaces by reacting with the steel and generating a sacrificial tribofilm. However, many of the additives currently in use are either complex and/or toxic and give rise to environmental issues.

Many types of NPs have been shown to possess good tribological properties and are believed to be possible candidates to replace the problematic additives still in use today. The main advantage of NPs is their size, which allows them to penetrate asperities of different geometries and to provide a smoothing effect.

WS_2 NPs possess the inertness required for industrial applications. They show outstanding tribological performance in comparison to any other additive and their mechanism of action may depend on a combination of both FM and AW properties. This study will investigate the properties of WS_2 NPs at different temperatures to verify this mechanism.

2H-WS_2 NPs have similar properties to IF-WS_2 NPs, such as the same chemical composition, low friction coefficients, stability to oxidative and thermal degradation, but they are easier to functionalize due to the edge effects. These properties recommend them as the best candidates for use as lubricant nanoadditives. Understanding the way they reduce friction and wear, as well as finding a feasible and effective method of functionalizing the surface with surfactants, can lead to a new generation of lubricant additives able to solve some of the current lubrication challenges.

2.4 HYDROGEN DAMAGE IN HIGH-STRENGTH STEELS

2.4.1 Introduction

Hydrogen damage (HD) describes a wide range of failure modes that occur when a metallic component is subjected to the combined action of hydrogen and applied stress. The phenomena related to HD have been studied for many decades due to the extensive array of applications in which materials suffer from this type of failure [182].

The negative impact of hydrogen on materials was observed as early as 1875, when it was reported that in the presence of hydrogen or acids, materials show a decrease in toughness and breaking strain at room temperature [60]. Further work indicated that applying stress above a certain threshold causes the degradation of mechanical properties, manifested as reduced load-carrying capacity and fracture below the yield strength, usually in a brittle mode. Consequently, the process has been termed hydrogen embrittlement (HE) [183, 184].

Modern research describes a large number of ways in which hydrogen damages different materials: hydrogen environment embrittlement, hydrogen stress cracking, loss in tensile ductility, hydrogen attack, blistering, microperforation, hydride formation etc. However, although these are often collectively termed HE, several do not show the classical features of embrittlement. HE describes just some of the failure modes induced by the presence of hydrogen in the material [185].

The amount of hydrogen responsible for HD can be minute due to the small size and high mobility of the hydrogen atoms in the material. Under loading conditions, hydrogen moves to the region of highest stress, where it accumulates and induces a change in the material (e.g. a microcrack). As the defect grows, hydrogen follows the high stress location until final fracture occurs [62, 186].

The exact mechanism of HD is still debated in the literature. Unfortunately, a large amount of work in the field has been carried out on commercial materials with microstructures which are difficult to characterize in detail (impurity distribution, defect density etc.) and thus experiments show the response of the material to a variety of competing phenomena without addressing them in particular. Nevertheless, the three generally accepted conditions for the occurrence of HD refer to the material (metal susceptibility to hydrogen permeation/embrittlement), stress (loading, temperature etc.)

and the presence of hydrogen in the substrate [62, 63], as depicted schematically in Figure 2.16. To prevent HD it is required to remove at least one of these factors. For a specific steel in a given application (such as a high-strength steel in a bearing), the only factor which can be influenced is the presence of hydrogen in the substrate.

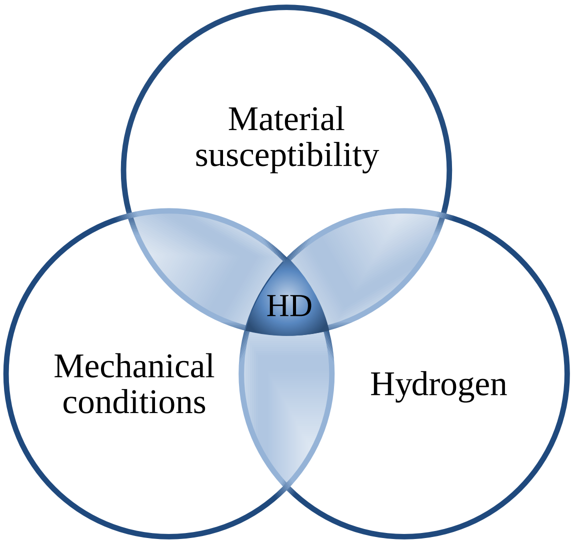

Figure 2.16 Conditions required for hydrogen damage

Bearing applications require the use of high-strength steels, which are susceptible to HE. For this reason, some studies have employed lubricant additives (i.e. passivators and EP additives) to induce the generation of sacrificial films on the steel surface, in order to prevent the generation and permeation of hydrogen into bearing steel [148].

This section reviews the mechanism of hydrogen permeation into high-strength bearing steel and HE and the solutions that have been proposed to deter this. The experimental part of this study will show how the chemical tribofilm generated by the WS_2 NPs on the wear track can reduce the formation and permeation of atomic hydrogen into steel.

2.4.2 Hydrogen sources and entry into metals

In order to initiate HD, hydrogen atoms must permeate (diffuse) through the material to a location of high stress. There are many sources of atomic and molecular hydrogen described in the literature, usually grouped into *internal* and *environmental* hydrogen. The action of this hydrogen on the substrate is similar, the only difference between them being the provenance of hydrogen [62, 185].

The internal hydrogen relates to the residual hydrogen retained in the material during production. Melting, casting, acid cleaning, welding or surface treating can introduce small amounts of hydrogen, which are often eliminated by a subsequent heating operation. Standard quality steel produced by modern manufacturing techniques usually contains less than 1 ppm hydrogen trapped in the material. This amount is generally sufficiently small to be harmless on its own [62, 182].

Environmental hydrogen refers to hydrogen gas (in hydrogen applications such as fuel cells) or hydrogen generated as a direct interaction with the environment (i.e. corrosion, the interaction with electrolytes or the decomposition of water/lubricant molecules on the fresh catalytic surfaces formed on the substrate during service) [62, 64]. In order to initiate HD, environmental hydrogen must undergo a preliminary step of entry (adsorption and absorption) into the metal.

The hydrogen molecule is too large to permeate through the metal lattice and induce HD. Entry into the substrate occurs as atomic hydrogen, which is small enough to reside permanently or temporarily in the lattice or at different defects in the structure, such as voids, dislocations and grain boundaries [182, 187]. The formation of atomic hydrogen is the result of the decomposition of molecular hydrogen or hydrogen-containing molecules (e.g. water and lubricants) [64, 182, 188-194]. These reactions are thermodynamically favoured on the catalytic 'nascent surfaces' created during sliding conditions [1]. This is a critical step where lubricant additives can interfere with the HD process, as discussed in Section 2.4.5. EP additives such as WS_2 can generate a thick tribofilm and prevent the formation of catalytic 'nascent surfaces' responsible for the formation of atomic hydrogen [148, 188, 189].

The process of hydrogen entry into the material has been described in both gas and liquid phases by many researchers, but there is still a degree of uncertainty about the exact mechanisms [195].

Solid-gas interactions

In hydrogen applications, materials are often exposed to an atmosphere containing hydrogen gas (H_2) and the entry of hydrogen can be described by a succession of general solid-gas interactions: physisorption, chemisorption and absorption [63].

During *physisorption* the hydrogen gas molecules form a multi-layered fluid on the surface of the material. Although this step is in competition with the reverse process of desorption, it is fast (generally instantaneous) and it has a low activation energy.

Chemisorption involves the dissociation of the adsorbed hydrogen molecule and formation of chemical bonds between surface atoms and hydrogen. The interaction is short ranged (only monolayers are formed) and slow (requires larger activation energy).

The adsorbed hydrogen atom (H_{ads}) is finally *absorbed* into the material, either as a neutral atom (H) or as an ion (H^+ or H^-), though the exact nature is still debated. The process is in competition with the reaction between two adjacent atoms, leading to the regeneration of the hydrogen molecule and desorption into the environment.

Solid-liquid interactions

When the metal component is immersed in a solution/lubricant, the boundary interface and the chemical reactions involved are more complex, as water and lubricant molecules can adsorb and decompose on the surface in a loaded contact and generate atomic hydrogen. Alternatively, hydrogen containing electrolytes (particularly in acidic solutions) can discharge atomic hydrogen into the material. Both these processes can generate a large amount of hydrogen, usually orders of magnitude higher than hydrogen absorbed through a solid-gas interface [63, 195].

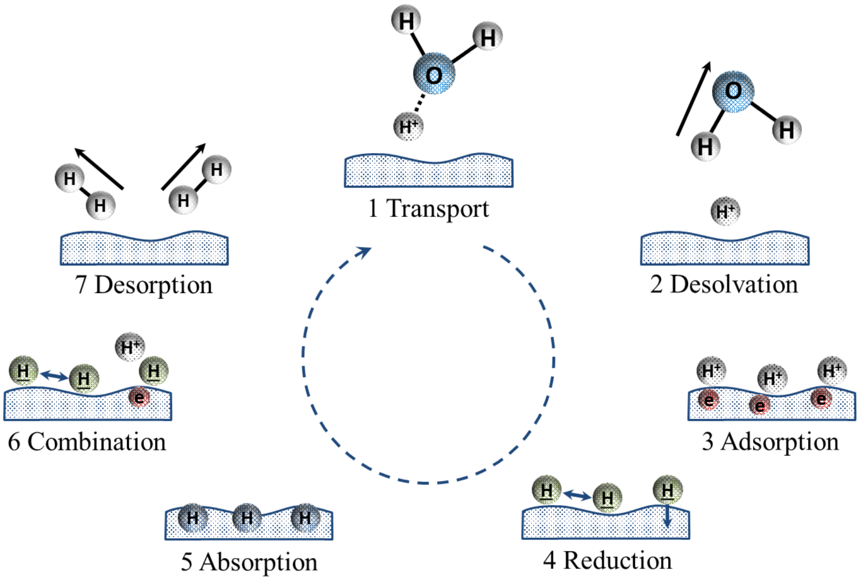

Figure 2.17 Hydrogen generation, entry and evolution at an aqueous solid-liquid interface [adapted from 195]

Figure 2.17 shows a schematic of hydrogen atom formation, entry and evolution in an acid solution. The hydronium ion (H_3O^+) can transport a hydrogen ion (H^+) to the surface (1) and desorb back into the solution as a water molecule (2). The H^+ ion is adsorbed on the surface (3) and by accepting an electron (4) it is reduced and adsorbed as a neutral atom (H_{ads}).

H_{ads} is absorbed into the material (5) in a similar manner to the absorption at the solid-gas interface. The competing process is the formation of a hydrogen molecule by either the reaction of two adjacent H_{ads} or between H_{ads} and another free H^+ plus an electron (6). In this case, the molecules will desorb and be released back into the solution (7).

The process described above can occur on both 'nascent surfaces' and passivated surfaces, and is highly dependent on the amount of hydrogen ions present in the solution. However, in high pressure/temperature conditions, the aqueous or oil based lubricant molecules are mainly decomposed on the highly energetic catalytic sites and atomic hydrogen is produced and adsorbed on the surfaces. The mechanism of entry into the material is similar to steps 5-7 described in Figure 2.17, but is largely dependent on the amount of fresh 'nascent' surfaces created in the contact. Chemically reactive EP additives can inhibit the formation and permeation of hydrogen and therefore the extent of HD by efficiently competing with other molecules for adsorption on the substrate and by rapidly generating a protective film, which is also wear resistant and reduces the exposure of the metallic surface.

In all of the mechanisms described above, a large amount of the environmental hydrogen adsorbed (H_{ads}) is released back into the solution/lubricant. The fraction that is absorbed and the rate of its entry process depend on external conditions (temperature, hydrogen concentration, load) and the complex interactions between hydrogen and the material structure. These aspects are further discussed in Section 2.4.3 [182, 195].

2.4.3 Hydrogen diffusion and interactions with metals

Another important requirement for the occurrence of HD is the material susceptibility to hydrogen permeation. Hydrogen diffusion through metals is directly linked to its interactions with the metal atoms and defects in the material and thus, to the condition of the studied sample. The microstructure ultimately determines the solubility, transport (diffusion) and trapping of hydrogen atoms at particular low-energy locations in the lattice.

Solubility is the ability of the material to dissolve a solute (in this case hydrogen). It is the result of an equilibrium between absorption and evolution processes and therefore, the external conditions are an important factor (e.g. stress/contact pressure, temperature, hydrogen concentration in hydrogen applications). In steel, hydrogen can be found in normal interstitial sites or trapped in microstructural imperfections. Interstitial sites between atoms have a very small available volume and are not favourable positions for hydrogen. Therefore, steel usually solves a very small amount of atomic hydrogen (in the ppm range), but this is enough to induce HD since hydrogen atoms easily diffuse through most materials and accumulate in preferential locations [195, 196].

Hydrogen diffusion is the transport of atoms through the material lattice due to a concentration gradient. The process is comparable to heat transfer and a similar equation was therefore generated by Fick (2.7). However, further research pointed to some discrepancies due to hydrogen trapping (e.g. delayed initial rate).

$$\boldsymbol{J = -D\frac{dC}{dx}} \qquad (\mathbf{2.7})$$

J – flux [mol/m^2/s]

D – diffusion coefficient (diffusivity) [m^2/s]

dC/dx – concentration gradient over distance [mol/m^3/m]

The diffusivity (represented by D) is the ease of movement of hydrogen atoms in a matrix and is directly related to the velocity of the diffusing particles through the material. For a specific material it is dependent on the operating temperature, stress/contact pressure and the atomic structure. As an example, hydrogen diffusivity is lower in fcc (austenite) than bcc (ferrite) or bct (martensite) microstructures, due to the closer packing of atoms [196, 197].

Hydrogen trapping

Experiments on hydrogen diffusion rates in iron and steels show a lower initial value (a delay in diffusion), which has been attributed to hydrogen trapping by different imperfections in the material [185]. As hydrogen atoms travel through the lattice, they are confined at low-energy locations.

Figure 2.18 illustrates the diffusion and trapping of hydrogen atoms in a sample. An atom requires a minimum amount of energy (E_{diff}) to diffuse through the lattice. The metal atoms near a defect may have a different bonding energy in the lattice associated with a saddle point energy (E_S). Depending on the type of defect, this energy may be smaller/larger than the diffusion energy. The trapping sites are attractive to hydrogen and have a lower potential well (E_{trap}). The energy required for an atom to escape the trap is E_a.

Due to the random motion of atoms, these energy barriers can be overcome with a certain temperature-dependent probability. The larger the energy barrier, the smaller the probability of exiting the trap and the longer the amount of time an atom is trapped. This has led to the description of reversible and irreversible trapping sites. If the residence time in the trap at a certain temperature is similar to the normal 'relaxation' time for a hydrogen atom to diffuse through the material (small E_{trap}, or $E_a \approx E_{diff}$), the trap is reversible (low interaction energy) and a potential trigger for HD. Irreversibly trapped hydrogen has a low probability of escaping (large E_{trap}, or $E_a >> E_{diff}$) and atoms are less likely to move towards a region of high stress during operation to cause HD. However, at higher temperatures, enough energy could be made available for hydrogen atoms to make these traps reversible [62, 63, 182, 195].

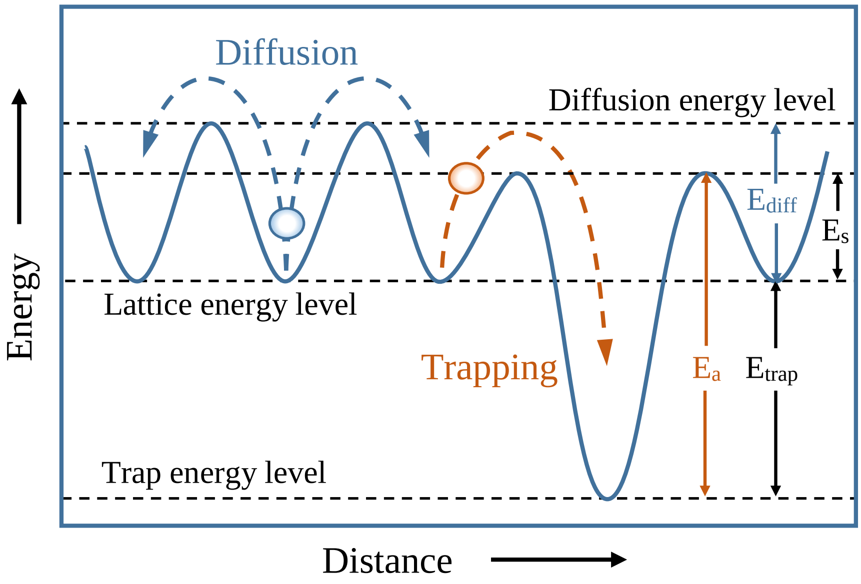

Figure 2.18 Hydrogen diffusion and trapping in the material [adapted from 196]

Figure 2.19 shows the possible locations of hydrogen in the material. Hydrogen can be absorbed in the normal lattice (a), adsorbed at the surface (b) sub-surface (c) and confined at the main microstructural defects acting as hydrogen traps.

Vacancy/void defects ((f) in Figure 2.19) are the simplest type of traps. Hydrogen atoms are attracted by the open volume of the defect (in the sense that the time spent inside is considerably longer) and chemisorb onto the metal atoms in a similar manner as to a free surface. The bond energy is therefore quite large and voids are usually irreversible traps at normal temperatures.

Grain boundaries ((d) in Figure 2.19) are also preferential sites for hydrogen adsorption, but the binding energy associated with them is small, allowing hydrogen atoms to move easily. Due to this they are reversible traps at normal temperatures.

Hydrogen atoms are also attracted by the strain field near dislocations (e in Figure 2.19), fall into a lower energy state and are trapped. However, the binding energy is small and they are therefore treated as reversible traps.

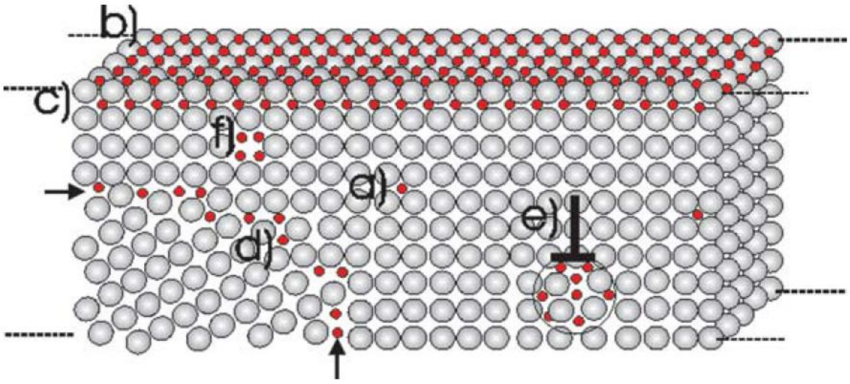

Figure 2.19 Hydrogen trapping at different trap sites [reproduced with permission from 198]

Impurities are different atoms or compounds present in the material, as a result of the manufacturing process. They create second phase particles in the matrix (precipitates and inclusions such as sulphides and oxides), which form chemical bonds with hydrogen (strong bonds, leading to irreversibly bound hydrogen), especially at grain boundaries, affecting the overall mechanical properties of the metal [196].

Sulphur and phosphorous present even in very small concentrations are known to promote HD. This is due to the high affinity of these atoms for hydrogen, which results in the formation of chemical bonds and retention of hydrogen in the material. This also explains why these elements, known to be poisonous for catalysts (which are involved in hydrogenation reactions) have been identified to promote hydrogen permeation in the material. The elements in the V-A and VI-A periodic groups such as arsenic, antimony, selenium and tellurium and their compounds, cyanides, antimony etc. were also found to have this effect [63, 186, 195, 196]). Consequently, the presence of these elements is not desired in steels and their concentration is usually controlled during manufacturing.

There are also elements that have an opposite behaviour. Tungsten has been found to decrease the hydrogen permeation rate and diffusivity in steels. Steels containing 0-2 w/w % W have been investigated between 10 and 70ºC and the hydrogen permeation rate and diffusivity were found to be proportional to the content of W in the steel [197, 199]. This indicates that hydrogen permeation may be inhibited by employing WS_2 nanoadditives in lubricants, which can to generate a tribofilm rich in W and WO_3.

2.4.4 Hydrogen embrittlement

As shown in Figure 2.16, HD occurs when stress is applied to a susceptible material that contains absorbed hydrogen, and the time to failure depends on the severity of the conditions. The rate of the process is influenced by temperature (higher temperatures can stimulate HD by allowing higher hydrogen mobility, but high strength steels are more susceptible to HD at ambient temperatures, i.e. there appears to be an optimum temperature for hydrogen permeation in the range of -50ºC to +100ºC [193]), load (HD is promoted by high stress), strain rate (higher rates impede hydrogen transport and HD) and microstructure (the martensitic structures of high strength steels are more susceptible to HD) [62, 63, 200].

The ASM Handbook [185] describes the general types of HD encountered. These can be divided in a few major processes, dependent on the observed failure mode. Some of them involve a material phase transformation and are easier to understand and describe (e.g. blistering, cracking, hydrogen attack and hydride formation), while hydrogen embrittlement is a more complex phenomenon and its mechanism is still debated.

Embrittlement does not involve a phase transformation and is therefore more difficult to investigate. Hydrogen atoms diffuse to regions of high stress in the materials and promote crack initiation and growth, leading to failure in a brittle manner. There are a number of theories concerning the formation of these cracks, but there is still no consensus at the present [63, 185, 195, 196].

Some of the initially proposed theories for HE have been later associated with the other types of HD observed. The *pressure theory* proposed the accumulation of molecular hydrogen at voids and other surfaces in the material and is now considered the predominant mechanism for hydrogen blistering and cracking. The *hydrogen attack* theory suggested that hydrogen atoms induce surface and internal decarburisation at high operating temperatures and is presently considered responsible for the failures bearing the same term. Similarly, the *hydride formation* theory was proposed as the main mechanism for many transition metals, as hydride precipitation was detected at the crack tip. However, the three main theories that specifically address HE in steels refer to surface adsorption, decohesion and enhanced localised plasticity [182].

The *surface adsorption theory* suggests that hydrogen atoms diffuse to the surfaces of the crack tip and reduce the free energy and work of fracture. However, it has a number of shortfalls and fails to explain why other atoms (such as oxygen) do not have the same effect.

The *hydrogen enhanced decohesion theory* (HEDE) is based on the assumptions that hydrogen atoms diffuse towards regions of high stress near cracks and that they reduce the bonding between atoms in the lattice as shown schematically in Figure 2.20. The mechanism occurs in the material lattice just ahead of the crack tip and leads to crack propagation in a discontinuous mode, with a propagation rate dependent on the mobility of hydrogen. It was later proposed that this mechanism occurs only up to a few atomic distances ahead of the crack tip and that the cracking process is continuous [196].

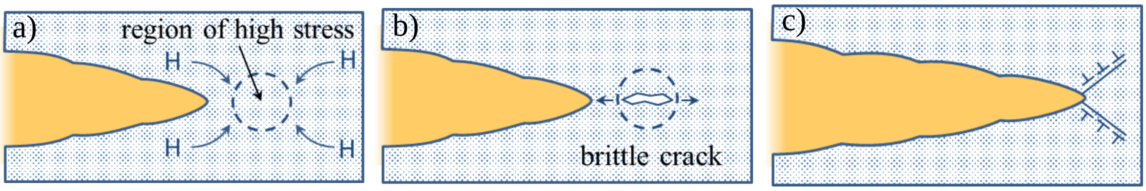

Figure 2.20 HEDE theory: a) hydrogen atoms diffuse to the region of high stress in front of the crack tip; b) a small brittle crack is formed; c) the crack propagates due to the merger of the crack fronts [adapted from 196]

The *hydrogen enhanced localised plasticity theory* (HELP) suggests that hydrogen promotes the formation and movement of dislocations in the plastic region near the crack tip. Hydrogen localises in this plastic region and crack propagation occurs at a rate dependent on the material microstructure, stress intensity and local hydrogen concentration, i.e. hydrogen only assists the deformation process which is permitted by the specific combination of microstructure and loading conditions, allowing it to take place at lower stresses. Depending on the magnitude of the stress intensity factor (K), the possible mechanisms are microvoid coalescence (Figure 2.21 (a), high K), quasi-cleavage (Figure 2.21 (b), intermediate K), intergranular fracture and (Figure 2.21 (c), low K) and intergranular fracture with assistance from hydrogen (Figure 2.21 (d)). Diffusion along the grain boundaries is expected to be faster than through the grains. However, the microvoid coalescence and quasi-cleavage fracture modes are kinetically faster at high K values.

These mechanisms have been the subject of a substantial amount of research and it is evident that each is influenced by many factors in the substrate. Therefore, HE is more likely the result of a combination of different mechanisms and that the operating conditions are responsible for the predominance of a singular failure mode.

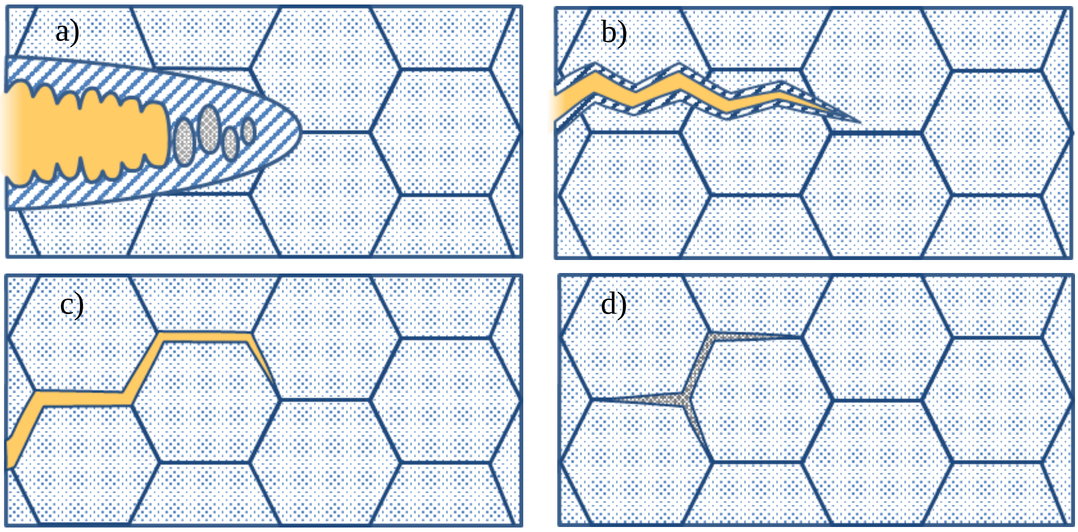

Figure 2.21 Fracture modes according to HELP theory: a) microvoid coalescence; b) quasi-cleavage; c) intergranular fracture; d) intergranular fracture with assistance from hydrogen [adapted from 196]

Hydrogen embrittlement in rolling element bearings

Bearings typically undergo a large number of loading cycles during their lifetime and therefore, the steels used in bearing applications must have a distinct set of mechanical properties: high rolling contact fatigue resistance, high strength, high resistance to wear, high shakedown limit (the maximum contact pressure the material can support in the elastic range), minimum inclusion content etc. As a result of these requirements, the most commonly used steel in bearings is the 52100 type, which is a high-strength martensitic high carbon chrome alloy, containing carbon (0.9-1.1 %), chromium (1.3-1.6 %), manganese (0.2-0.5 %), silicon (≤0.35 %), sulphur (≤0.05 %), phosphorous (≤0.05 %) and iron (balance) [59].

The desired microstructure and hence properties are obtained by austenitisation (heating above 850ºC to obtain an austenite microstructure with a face centred cubic (fcc) crystal structure), quenching (rapid cooling to form a martensitic structure with body centred tetragonal (bct) crystal structure) and subsequent tempering (to achieve the required hardness). The resulting microstructure contains tempered martensite, retained austenite and different carbides, along with the crystal defects and second phase particles. The low solubility of hydrogen atoms in the martensitic structure leads to the diffusion of hydrogen atoms towards trapping sites and makes the 52100 bearing steel particularly susceptible to hydrogen embrittlement under static loads at ambient temperature [59].

Widely used in moving components, rolling element bearings eventually suffer from a type of surface damage known as rolling contact fatigue (RCF) [201-203]. RCF is characterized by the damage of the steel surface due to the formation of fatigue cracks, which initiate at inclusions and other defects in the steel and propagate in the direction of the overall stress (Figure 2.22 (a)).

However, due to increasing demands on operating conditions for rolling elements, some applications such as wind turbine gearboxes or automotive powertrains display an unusually short service life, which some authors have associated with accumulation of hydrogen in the material. Investigations have shown that if the local concentration of hydrogen is in excess of ~1 ppm the tribological components display a different type of surface damage [59, 64].

This mechanism differs from the classic RCF and includes the formation of a peculiar type of white etching areas (WEA) associated with white etching cracks (WEC). WEAs are characterized by two phases: an ultrafine ferrite grain structure several tens of nanometres in diameter [204, 205] with increased hardness (30-50% higher compared to the bulk matrix) and an amorphous-like phase near the cracks [61]. The mechanism of WEA formation is much disputed. One possible mechanism is that dislocations introduced by the shear stresses involved in RCF refine the microstructure by dissolving the carbides and form an ultrafine grain size recrystallized structure. WECs are wide discontinuous sub-surface three-dimensional network cracks that have their origin at or near the surface (0-150 μm), where the maximum shear stress is located, and propagate in the over-rolling direction (Figure 2.22 (b)).

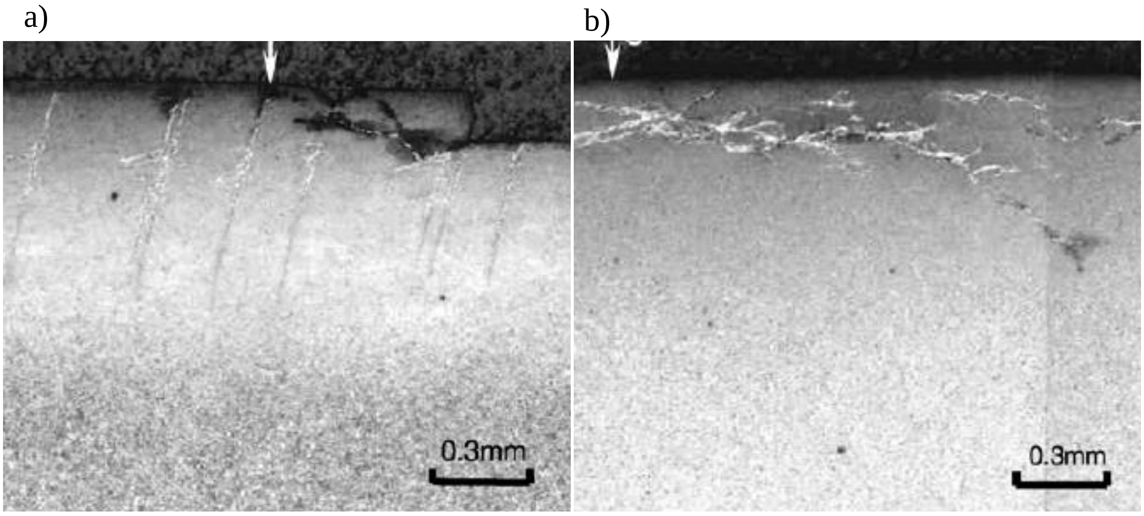

Figure 2.22 Section through a SCM420 JIS (4118 ASTM) wear track which shows: a) typical damage in a sample with a long RCF life, b) typical damage in a sample subjected to HE with a short RCF life [reproduced with permission from 64]

The mechanism of the failure mode involving WEC formation in rolling element bearings is not fully understood, but hydrogen embrittlement and stress concentration (especially at inclusions) are believed to be important factors. Proponents of the stress concentration mechanism have reported that WECs are formed as a result of the WEA caused by the sliding between the ball and the bearing ring (race) and depends on the testing conditions. They have shown that WECs are initiated at the interface between the amorphous and fine granular phases inside WEA and between WEA and the matrix [61]. Hydrogen-assisted fatigue reported in fuel cells using hydrogen as a source of energy was shown to lead to WECs or accelerate classic RCF [139, 190, 194, 206-211].

Although the mechanism of WEC formation is still debated, HE has been identified as a major consequence of the hydrogen permeation and local accumulation in the contacts and represents an extra challenge for tribological parts in fuel cells that are normally subjected to high stresses.

In a hydrogen atmosphere, the RCF life of rolling element bearings was reported to decrease with increasing concentration of hydrogen permeated into the bulk material. Higher operating temperatures lead to increased concentrations of hydrogen, which infer that high-temperature operating bearings, as found in wind turbine gearboxes, are more affected. For this reason, some research studies recommend that the lubricant temperature in wind turbine gearboxes be maintained below 75 - 90ºC to reduce hydrogen permeation and extend bearing life [212-214].

2.4.5 Reducing embrittlement in high-strength steels

The process of HE is largely influenced by the microstructure of the material and the operating conditions, but only begins with the absorption of atomic hydrogen in the metal component. A large number of studies have focused on measuring the amount and type of hydrogen present in the material at the time of failure in order to understand the mechanism and propose ways of reducing the concentration of hydrogen.

The main techniques developed for the measurement of hydrogen concentration are based on heating or melting the sample and analysing the properties of the desorbed gases: mass, thermal conductivity, IR vibrations or neutron scattering.

Thermal desorption spectroscopy (TDS) is a very efficient way of quantifying the presence of hydrogen in a material. The technique is performed by heating the sample under a constant heating rate in order to induce desorption of all gaseous species, which are then analysed by a mass spectrometer. By recording the temperature during the analysis, TDS also allows the measurement of the adsorption energy of hydrogen in the material. Therefore, it is possible to determine the type of traps/defects that are responsible for HE in a certain sample. This is done by heating the samples with different heating rates, causing hydrogen to diffuse with different speeds, giving an indication of the bonding energy of atoms [215-220].

The concentration of internal hydrogen in steel can usually be kept to a minimum by carefully manufacturing and treating the material prior to service: using vacuum melting techniques, gas/flux shielded welding, pickling (acid cleaning) with weaker acids or in combination with inhibitors, baking etc.

The generation of environmental hydrogen is linked to the operating conditions and may sometimes be more difficult to prevent, but several solutions have been proposed in the literature, as detailed below.

Steel composition

Steels with a tensile strength below 1040 MPa are generally not affected by HE. Steels with a carbon content between 0.4 and 0.8 % C are less susceptible to embrittlement [203, 221-223], although such steels have lower strength and their mechanical properties are inferior (i.e. reduced load bearing capacity).

A higher chromium content in the steel can also offer resistance against hydrogen permeation due to the formation of chromium oxides that passivate the surface (i.e. fewer ‘nascent surfaces’ are exposed, leading to a smaller amount of atomic hydrogen generated in the contact). Stainless steel (>10.5 %Cr) has a longer RCF life [148, 192-194, 224, 225], but in some cases a large amount of adhesive wear is observed (the high adhesive nature of stainless steel leads to the failure of a percentage of components), making this steel unsuitable for applications where direct contact cannot be eliminated (e.g. contacts operating in the mixed lubrication regime) [148].

The use of metal coatings

One possible solution is to use a coating able to reduce the permeation of hydrogen atoms. Previous research showed that a thin layer of nickel electrodeposited on the steel substrate can effectively reduce hydrogen permeation due to its very small coefficient of hydrogen diffusion as compared to the coefficient of diffusion through steel [64]. A number of other sacrificial coatings have been proposed [195] and although hydrogen embrittlement was reduced for steel immersed in aqueous solutions, tribological tests have not been conducted to verify the properties of the coatings.

However, there are a number of drawbacks associated with coatings. Most of them are only effective in dry conditions due their different chemical affinity for the additives in oil (i.e. lubricant additives may be less reactive towards the coating than to the steel surface). Additionally, coatings might not have the mechanical properties required for the contact (i.e. they may deform/crack). Furthermore, the coatings may interfere with the steel baking – the electrodeposition process introduces internal hydrogen in the steel which must be removed through baking, but the coating may hinder the desorption of hydrogen atoms [62].

Case carburising

A reduced wear rate of the materials can influence HE by delaying the formation of active catalytic sites available to generate atomic hydrogen. Better wear resistance was reported for case carburised steels along with a small improvement in RCF life, though the process was not recommended as a robust solution to embrittlement due to its costly and lengthy nature [203, 221, 226, 227].

The use of passivators and conventional antiwear additives

Steels are normally covered in thin oxide films, but they are removed during operation and fresh metal sites are generated that act as catalysts for the decomposition of water/oil molecules and the generation of atomic hydrogen. Previous studies have investigated the possibility of using a range of oils and additives to reduce hydrogen generation and permeation into the steel and to increase the life of the material.

The mechanism involves the deactivation of the catalytic action of fresh steel surfaces formed during sliding and can be achieved with the use of lubricant additives which chemically interact with the ‘nascent surfaces’. There are two types of additives capable of reducing hydrogen permeation into steel: passivators (by quickly oxidizing the fresh surfaces) and AW/EP additives (by forming sacrificial phosphate and sulphide tribofilms to reduce wear and the occurrence of catalytic sites) [148, 188, 189, 228].

The amount of hydrogen generated in vacuum conditions by various types of base oils employed to lubricate a ball-on-disc sliding test was found to be proportional to the wear width measured at the end of the test and therefore depends on the lubricity of the oil [188]. The addition of antiwear additives such as *MoDTC* and *ZnDTC* in the base oils can reduce the hydrogen concentration in the substrate by as much as 50 %, due to the rapid generation of a thick chemical tribofilm, which produced smaller wear tracks [148]. Passivators such as *sodium nitrite* ($NaNO_2$) can have an even greater effect on the hydrogen permeation, reducing it by two thirds compared to the base oil. However, its antiwear properties are less effective and its use results in increased wear. Furthermore, it is known to react with amines to form carcinogenic nitrosoamines [148]. Another passivator used was *potassium molybdate* (K_2MoO_4), which is also a good AW additive due to the presence of Mo in the molecule [188]. Consequently, both wear and hydrogen permeation were reduced as compared to the base oil.

Steels treated with *black oxide* have a soft, thin layer (up to ~ 2 µm) of passivating oxides (mixed iron oxides) that offers corrosion protection and higher resistance to wear [203, 226]. This layer is soft and is slowly removed from the surface over time, but it has been shown to reduce HE and prolong RCF life.

Initially, it was suspected that a large amount of hydrogen is also absorbed outside the track during operation. However, AW additives (such as ZDDP) easily react in the contact due to the high pressures between asperities, producing characteristic tribofilms, and were found to increase RCF life, suggesting that the generation of atomic hydrogen at fresh catalytic sites on the wear track is the main cause for the onset of HE, while hydrogen absorption outside the track is negligible. The drawback of conventional AW additives resides in the fact that film generation usually requires elevated temperatures (at least 60ºC) and an initial running-in period (ZDDP films start growing immediately but depending on running conditions, they require 20-30 minutes to reach their average thickness) [8, 148, 188, 189].

The use of nanoparticle antiwear additives

NPs with AW/EP properties can be used as lubricant additives for the same effect. NPs can easily penetrate the contact due to their small size and react with the nascent metal surface on the wear track to generate a comparable tribofilm, capable of preventing the formation of hydrogen atoms and their permeation into the substrate [23]. From the myriad of potential nanoadditives, boron and molybdenum disulphide based NPs were shown to generate thick durable films and smooth tracks and have excellent wear and friction behaviour [92, 229]. Due to these favourable properties they have been proposed as promising candidate additives for wind turbine applications [230].

Amongst lubricant nanoadditives, WS_2 NPs have numerous advantageous properties [36, 92, 164, 166], but the most important for applications affected by hydrogen embrittlement is their recently discovered ability to react with the steel substrate in high-pressure, high-temperature contacts and form a protective chemical film, as discussed in the experimental sections. The complex structure and composition of this tribofilm provides them with an excellent ability to decrease friction in the boundary regime and great antiwear and extreme pressure properties. The former is due to the presence of a top layer of unreacted WS_2 NP sheets, while the latter is explained by the presence of elemental tungsten and tungsten oxide in the tribofilm, which enhance its hardness and elastic modulus values (Section 4.5.3). The presence of the complex WS_2 tribofilm has the potential to reduce the permeation of hydrogen in steel and reduce its detrimental effect on the properties of the material, similarly to other AW additives. As noted earlier, the diffusion coefficient of hydrogen through steel decreases with the increase of tungsten content [199] and therefore, the presence of tungsten compounds in the tribofilm offers an additional advantage. Furthermore, WS_2 NPs do not require a running-in period, because the NPs can cover the steel surface and prevent local contact. This process is responsible for their FM properties and is not temperature dependent.

2.4.6 Summary

Hydrogen damage is an important phenomenon in tribological components and is generally agreed to depend on three factors: material susceptibility to HD due to the microstructure, stress due to loading conditions and the presence of hydrogen in the material.

Hydrogen is introduced in steel during both production and operation and it is confined at low-energy locations known as traps. The bonding strength of the different traps affects the diffusion of hydrogen atoms towards regions of high stress, where it eventually initiates HD.

High-strength bearing steel is known to be susceptible to HE. Embrittlement is a most complex process which requires the presence of diffusible atomic hydrogen in the region of high stress. TDS is a useful technique to measure the hydrogen concentration in the material and many studies are currently trying to elucidate the mechanism of HE in order to provide practical solutions to hydrogen permeation and the initiation of HD.

In rolling element bearings, a large amount of hydrogen responsible for HE is generated by the decomposition of lubricant molecules on the catalytic metal surface. The use of AW/EP additives is an effective way of reducing hydrogen permeation by deactivating the ‘nascent surfaces’ generated during sliding. WS_2 nanoadditives show many beneficial properties that recommend them for use in rolling element lubrication.

In view of the facts presented above, a part of this study will investigate the ability of WS_2 nanoadditives to reduce the concentration of permeated hydrogen in rolling element bearings operating in high temperature and pressure conditions. Rolling contact tests were conducted using WS_2 nanoadditives in polyalphaolefin (PAO) base oil and the concentration of hydrogen in the samples at the end of tests was measured by TDS. The mechanism of action of WS_2 nanoadditives was investigated by performing surface analysis on the rolling tracks using optical profilometry, X-ray photoelectron spectroscopy (XPS) and Auger electron spectroscopy (AES).

2.5 NANOPARTICLE COLLOIDS

2.5.1 Introduction

Nanoparticles (NPs) are typically described as objects with a size range of 1 to 100 nm. As an exception, single molecules are generally not considered NPs [231]. At this small scale, the properties of NPs are very different in comparison to the corresponding bulk materials. NPs come in a great chemical diversity (metals, oxides, polymers, organic compounds etc.) and have various shapes (spheres, discs, cylinders etc.).

Although NPs have been studied in detail only recently, their properties have been observed and exploited for a very long time. Ancient Egyptians used lead salts in hair-dyeing recipes over 4000 years ago. During the process, lead sulphide NPs were formed and interacted with amino acids of hair keratin [232]. Metal NPs (gold and silver) have been used for centuries to imprint a metallic glitter to pottery [233]. In the Middle Ages craftsmen mastered the technique required to fabricate stained glass by using small amounts of metal and metal salt NPs and by controlling their size [234]. NPs also have an important role in influencing the climate. In the atmosphere, NPs are responsible for the formation of cloud drops and rain by acting as nucleation centres for water molecules (water is unlikely to form droplets without them) [230].

Solid particles form aerosols when dispersed in air (e.g. fog, smoke) and colloids when dispersed in a liquid (e.g. muds). In colloidal form, particles are prone to aggregation and sedimentation. In order to use solid NPs such as 2H-WS_2 as lubricant additives, they must form stable colloids. NPs have a high specific surface area and therefore very large surface energy. This makes them thermodynamically unstable in fluids. To avoid agglomeration, various approaches have been used to functionalize NPs and reduce their surface energy.

This section describes the factors involved in the stability of NPs in liquids and discusses the main stabilization methods suitable for 2H-WS_2. A variant of these methods was used to obtain stable dispersions of 2H-WS_2 NPs in PAO base oil in this study. However, these experimental results are not presented in the thesis, as they are currently being considered for patent submission.

2.5.2 Physical chemistry of NPs

The most distinctive feature of nanoscale materials is their very small size, which implies that a large proportion of the atoms are present on the surface layer as opposed to bulk materials, conferring on them a large surface area per unit volume [234]. This feature is responsible for many special physical and chemical properties displayed by NPs. The most important features related to the use of NP additives in oils are the particle size, mechanical properties, specific surface area and surface tension.

Particle size is correlated with the ability of NPs to infiltrate contact asperities. In practical applications, a powder will usually contain particles of various shapes and dimensions. Therefore, the most common measured properties are the mean particle size and particle size distribution. The size of the WS_2 NPs used in this study is characterized by dynamic light scattering and electron microscopy techniques, as discussed in Section 3.2.1.

Mechanical properties such as strength and hardness are notably higher for NPs, even reaching theoretical limits, which are one-two orders of magnitude higher than for crystals in bulk form. This can be explained by two factors: a) the higher compactness of the material, i.e. due to the forces acting inwardly on the surface, the bond length between surface and interior atoms is smaller. In a bulk particle, this difference is insignificant, but in a nanoparticle, where many atoms are part of the surface, this effect is important enough to influence the material properties [234]; b) the reduced probability of defects in the structure, i.e. dislocations and impurity precipitates are less likely to be found in a small NP [31]. Soft materials such as WS_2 NPs can benefit from increased mechanical properties when they are employed in tribological applications.

Specific surface area ($\boldsymbol{S_w}$) represents the surface area divided by the volume it encompasses. Surface atoms are obviously more active than those inside the bulk material, as they have at least one free side. As the $\boldsymbol{S_w}$ of a particle increases, so does the proportion of atoms present at the surface and thus the particles are more reactive [31, 234]). This is illustrated in Table 2.2, which shows how the fraction of surface atoms changes with the size of the particle. This implies that NPs are much more reactive than bulk materials and have a higher affinity for adsorption on substrates. Therefore, NPs used as lubricant additives are more likely to generate a tribofilm on steel as compared to other solid additives (e.g. micro sized powders).

Table 2.2 Fraction of surface atoms for differently sized particles [234]

Atoms in a side	Atoms at the surface	Total number of atoms	Fraction of surface atoms (%)
2	8	8	100
3	26	27	97
4	56	64	87.5
5	98	125	78.5
10	488	10^3	48.8
100	58,800	10^6	5.88
1,000	~6 x 10^6	10^9	~0.6
10,000	~6 x 10^8	10^{12}	~0.06
100,000	~6 x 10^{10}	10^{15}	~0.006

Surface tension is the free energy per unit of surface area (at constant temperature and pressure) [31, 235-237]. This energy is the result of the unbalanced action of the forces that act on surface and interior atoms. Figure 2.23 illustrates the interatomic forces that exist between atoms at different locations in a NP. Atoms present at the surface are subject to an inwardly directed force, which tends to minimize the surface area. As the surface area shrinks, the free energy decreases. Table 2.3 presents the surface tension for some materials in normal conditions (unless stated otherwise). WS_2 NPs have a large surface tension, which explains the difficulty of functionalizing and dispersing them in fluids.

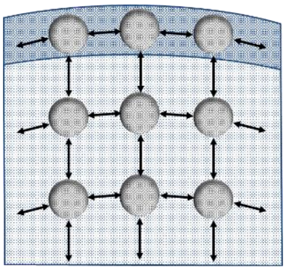

Figure 2.23 Forces acting on surface and interior atoms [adapted from 238]

Table 2.3 Surface tension of common materials in air [236, 239]

Substance	**Surface tension (mN/m)**
Glass (solid)	2000-4000
Ag (solid)	450
NaCl (solid)	300
PTFE (solid)	20
Water (liquid)	72
Acetone (liquid)	23.7
Neon (liquid, -247°C)	5
WS_2	~70 (estimated, [240, 241])
WS_2 NPs	>250 (estimated [242, 243])

2.5.3 Colloidal stability

2.5.3.1 Colloids

A ***colloid*** is a dispersion of particles in another material that does not settle under gravity [31-34]. Colloids consist of a dispersed phase (i.e. NPs) and a continuous phase (i.e. fluid). There are several types of colloids: sols, aerosols, emulsions and foams. Colloids are also classified according to their affinity towards the fluid as lyophilic (fluid attracting/wettable) and lyophobic (fluid repelling/non-wettable). Particularly, when the fluid is water, the terms used are *hydrophilic* and *hydrophobic*.

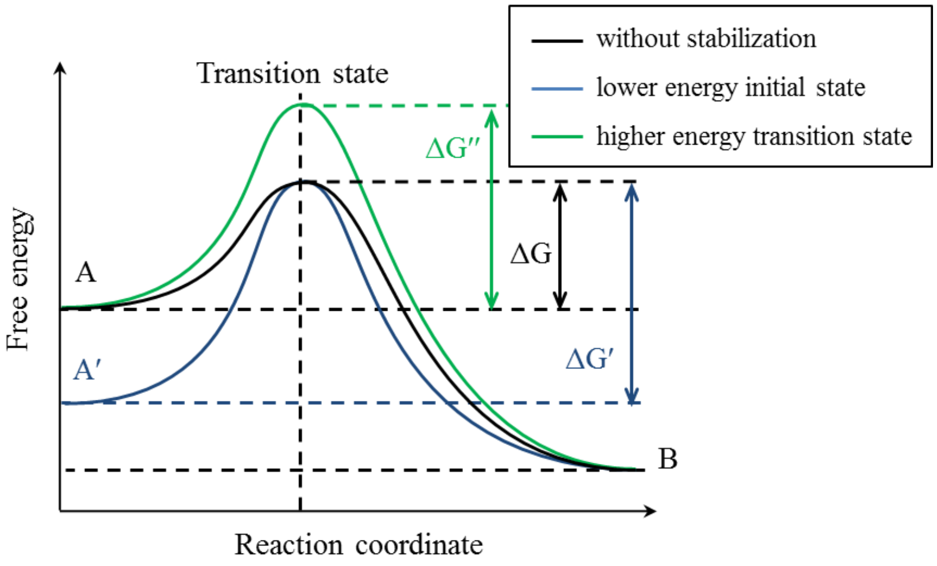

Figure 2.24 Energetic path of colloid collapse

As discussed in Section 2.5.2, nanoparticles have a large specific surface area and thus have higher surface free energy than the bulk material. A simple way of depicting the surface free energy is by looking at the energy state of individual atoms. Due to physical/chemical interactions, an atom in contact with a ‘neighbour’ is in a lower energy state. As a consequence, surface atoms (which have fewer ‘neighbours’) possess higher energy and any system will tend to minimize the overall energy by reducing the number of such high-energy atoms (i.e. decreasing the surface area). This makes nanoparticle colloids thermodynamically unstable and gives them a tendency to collapse (aggregate and sediment). The key to the survival of a colloid is in its collapse kinetics. Various interactions exist between the particles in a colloid and the sum of these interactions may render the colloid *kinetically non-labile*: Figure 2.24 shows a system in a temporary stable state A, which cannot undergo the change to the agglomerated state B without energetic interference (**Δ*G***) from outside the system (e.g. higher kinetic energy of particles due to higher temperatures) [33].

As can be seen in the figure, there are ways of altering the stability of the colloid, either by increasing the energy of the transition state (i.e. the activation energy required to overcome any repulsive forces and reach a transition state) or by changing the surface free energy (the initial energy state of the system). These methods are defined as electrostatic and steric stabilization and are discussed in detail in Section 2.5.3.4. They both rely on increasing the potential energy of particle interaction (**Δ*G***) and therefore, a basic description of the interactions between atoms and NPs in colloids is presented in Sections 2.5.3.2 and 2.5.3.3.

2.5.3.2 Interactions between atoms and NPs

There are two distinct types of interactions: strong chemical bonds (ionic, covalent and metallic) and intermolecular forces. Because NP colloids are dispersed in a liquid (i.e. the dispersion phase is composed of fluid molecules), this section will focus on ***intermolecular forces***: hydrogen bonds and Van der Waals interactions.

The ***hydrogen bond*** is an electrostatic attraction between the lone electron pair of a small-radius electronegative atom and a hydrogen atom bonded to another electronegative atom [236]. It is represented as **A–H···B** and is usually encountered for nitrogen-, oxygen- and fluorine-containing molecules. Group V oils such as PPGs have a large number of hydroxyl groups and can display hydrogen bonding with NPs containing polar atoms (e.g. oxygen) in their structure. Their strength is usually much weaker than chemical bonds.

Van der Waals interactions are weak, universal forces (i.e. they act between all molecules) manifested as various types of attractions or repulsions. The main contributions are the Keesom interaction, the Debye force, London forces and the Coulomb repulsions resulting from Pauli's exclusion principle. These interactions are based on the polarization of molecules by means of an external electric field or other induced dipoles. In a NP/oil colloid, all oil molecules will interact with the NPs via Van der Waals interactions.

Dipole-dipole interactions (also known as *Keesom interactions*) occur between pairs of polar molecules. They are attractive forces generated by the relative orientation of a molecule in the electric field generated by its pair. *Dipole-induced-dipole interactions* occur when a polar molecule induces polarization of a neighbouring nonpolar molecule. The dipoles then interact and are attracted to each other. This effect is also known as the *Debye force* and is much weaker than the Keesom interaction. *Induced-dipole-induced-dipole interactions* are the most general type of interactions and occur between all molecules, regardless of the dipole moment they possess. They are also called *London dispersion forces* and are usually the main contribution to Van der Waals interactions. Electrons constantly change their position around the nucleus and create small fluctuations in the electric dipole moment. This creates an electric field that polarizes other nearby molecules. Although weaker than chemical bonds, London forces are ubiquitous and grow in strength with the molecule size and polarizability (the ability of a molecule to suffer a redistribution of electrons) [235].

An important observation is that molecules tend to interact more strongly if they have similar electronic properties. Whether by hydrogen bonding, dipole-dipole interactions or London dispersion forces, the energy state of molecules is lower in like-environments. Therefore, nonpolar dispersion media such as oils prefer NPs covered in nonpolar surfaces [31, 244-246], and the interaction between them is represented by a larger $\mathbf{\Delta}\boldsymbol{G}$, which facilitates dispersion as described before in Figure 2.24.

Van der Waals interactions and the Brownian motion of NPs in the oil are responsible for agglomeration. However, the strength of the Van der Waals interactions between two NPs decreases very quickly with increasing distance and therefore, colloidal stability can still be induced.

2.5.3.3 Colloidal stability of NPs

The presence of NPs in a colloid is thermodynamically unfavoured compared to a bulk material due to their high specific surface area. Van der Waals interactions also act as attractive forces between particles. Therefore, NPs in colloids have a tendency to aggregate and sediment under gravity (Figure 2.25) [31, 33].

Aggregation is the process of clustering of NPs in the colloid, either spontaneously or induced intentionally by addition of clarifying agents. ***Sedimentation*** is the tendency of NPs to settle out of the colloid, usually under the influence of gravity, but can also be induced by external forces, such as centrifugal acceleration or electromagnetism. The size of the NPs is directly linked to the sedimentation process, as larger (heavier) NPs will sediment faster. Therefore, the formation of large aggregates facilitates sedimentation and the collapse of the colloid.

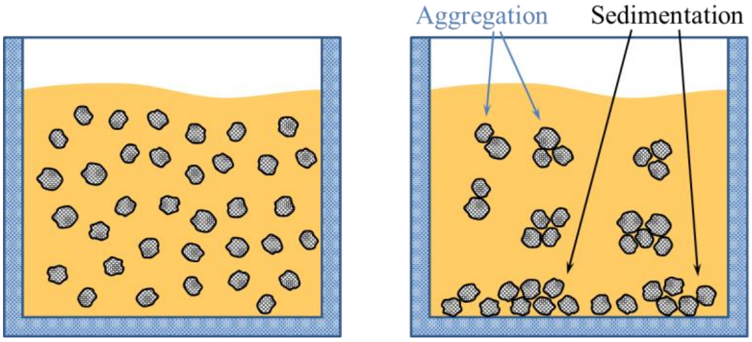

Figure 2.25 Aggregation and sedimentation of a colloid [adapted from 247]

The size of NPs may also be susceptible to change due to their high surface energy. ***Ostwald ripening*** is the spontaneous process of particle growth at the expense of the smallest particles in the colloid. This is thermodynamically-driven by the greater stability of larger particles. Small particles have a larger specific surface area and thus higher diffusion rates. This leads to the dissolution of material and redeposition on the larger particles (Figure 2.26). After sufficient time, only large crystals/NPs are obtained.

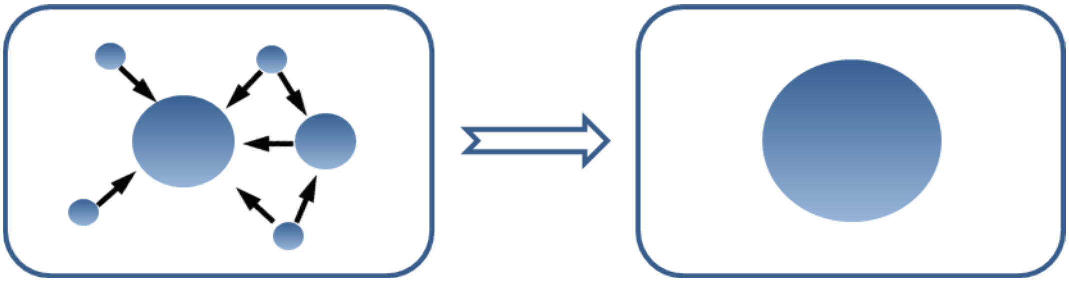

Figure 2.26 Ostwald ripening of NPs

As discussed above, there are many factors that contribute to the thermodynamic instability of a colloid. However, if the kinetics of these factors are unfavourable, the colloid can be kinetically non-labile (i.e. aggregation can be obstructed). One of the major reasons for this is the presence of an *electrical double layer* around charged particles.

Most surfaces have an electric charge which determines the clustering of oppositely charged ions (counterions) nearby. Figure 2.27 (b) shows a particle with an *ionic atmosphere* composed of two parallel layers. The first layer (the Stern layer) is fairly immobile and contains the closest ions to the particle. The slipping plane (still rich in ions compared to the bulk solution) is held by electrostatic forces and moves as part of the particle. The particle itself will thus interact with the environment through this encompassing double layer. The variation of the electric potential in the ionic atmosphere is shown in Figure 2.27 (a). The electric potential at the boundary of the electrical double layer relative to the bulk fluid is called the *zeta potential* (ζ).

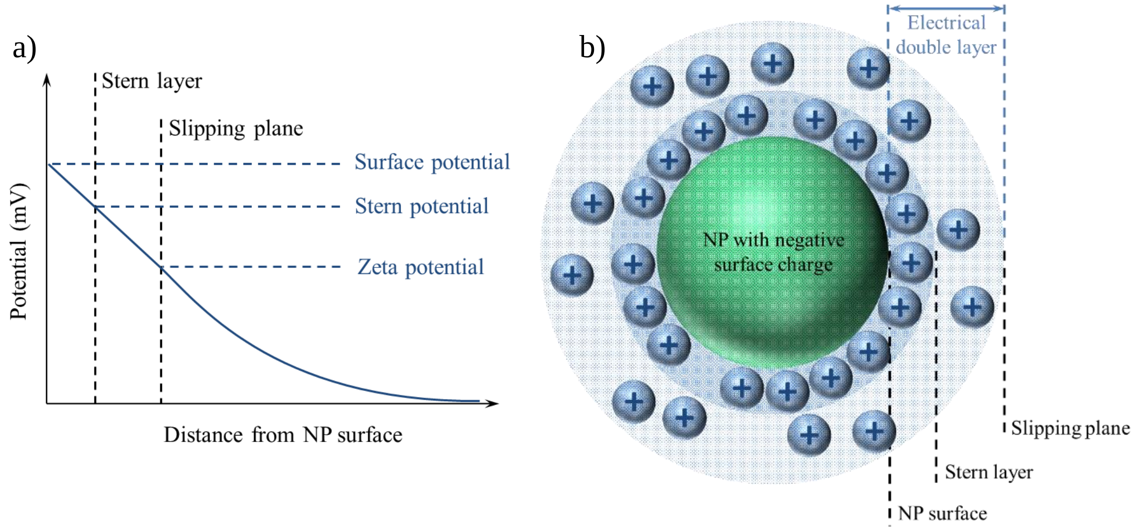

Figure 2.27 Electrical double layer around a NP in solution [adapted from 248]

The DLVO theory (developed by Derjaguin, Landau, Verwey and Overbeek) proposes that the stability of particles in a colloid is due to the balancing effect of the attractive Van der Waals interactions and the repulsive interaction between the charges of the electric double layers. Energetic barriers must be overcome by particles in order to approach sufficiently and to achieve a thermodynamically stable state (aggregation), as presented before in Figure 2.24. Figure 2.28 (a) shows the change in potential energy as two particles approach. A net potential is generated from the combination of Van der Waals and electrostatic forces, with a maximum **Δ*G*** energy required for agglomeration.

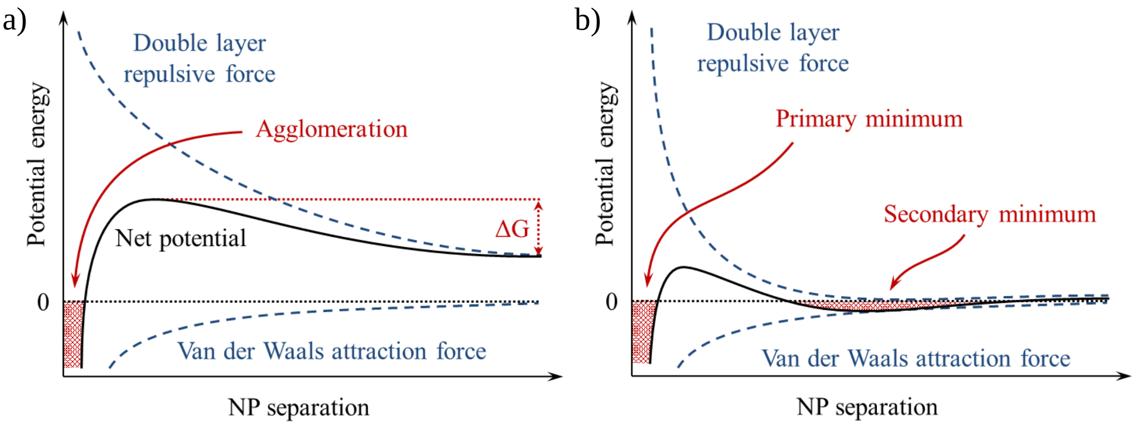

Figure 2.28 a) Potential energy of NP interaction, b) Potential energy of NP interaction at high ionic strengths [adapted from 249]

At high ionic strengths (many charged ions present in the solution), the electric interactions between particles are somewhat masked and the potential shows a *second minimum energy state* (Figure 2.28 (b)). This state is called ***flocculation*** and represents a weak form of particle aggregation. Flocculated particles can usually be dispersed by simple agitation.

The *primary minimum energy state* is called ***coagulation*** and it is the irreversible aggregation of particles in a colloid. When two particles collide with sufficient energy (particles are in constant motion in a fluid due to the Brownian motion), the repulsive force created by the double layer is surpassed and aggregation occurs. The ζ potential is a direct indication of the strength of the repulsive force between particles. Potentials of *over* ± *30 mV* are considered high and usually confer colloidal stability [250].

2.5.3.4 Stabilization of NP colloids

There are two main mechanisms by which the natural stability of a NP colloid in oil can be improved: ***electrostatic stabilization*** and ***steric stabilization***. Both methods involve the functionalization of the surface of the NPs, i.e. the chemical modification of the surface layer in order to obtain specific characteristics (in this case lower surface energy, higher zeta potential and compatibility with the base oil). Surfactants are often used in the process and in lubrication, it is paramount that their selection is achieved in such a way that they would also be compatible with the lubricated surfaces.

Surfactants are chemical compounds that can reduce the interfacial tension of fluids/surfaces. They are usually *amphiphilic* organic molecules capable of adsorbing at interfaces. An amphiphilic molecule has both a hydrophilic/oleophobic and a hydrophobic/oleophilic group. This allows them to interact with both polar and nonpolar fluids/NPs.

Surfactants are classified as ionic or non-ionic, depending on the presence of a charge in the polar group. Ionic surfactants are further divided into anionic (contain anions), cationic (contain cations) and amphoteric (contain both charges). The hydrophobic group is a long hydrocarbon chain and may be linear, branched or aromatic.

Good interactions between surfactant molecules and the dispersion medium are restricted to either hydrophobic or hydrophilic groups (depending on the polarity of the fluid). Surfactants therefore dissolve in a fluid in small amounts, but at a certain concentration (specific to each surfactant), the free energy of the system increases so much that surfactant molecules unite to form ***micelles*** (Figure 2.29).

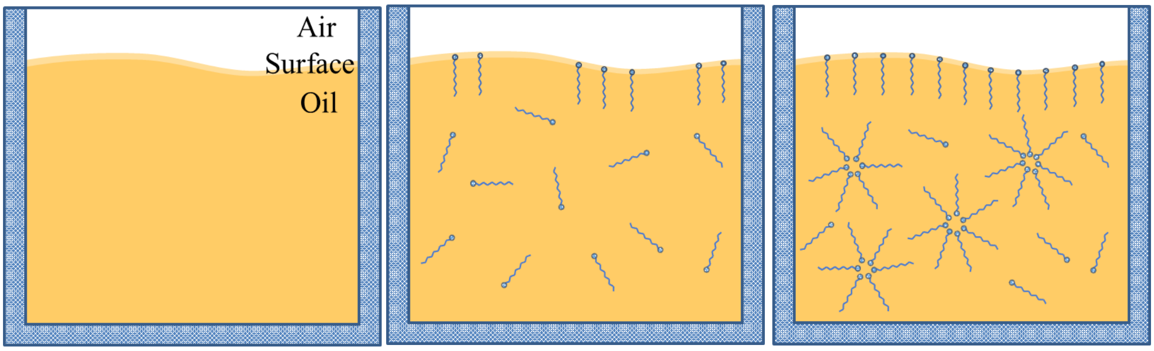

Figure 2.29 Formation of micelles by gradually increasing surfactant concentration [adapted from 251]

A micelle is a cluster of molecules formed by surfactants in order to reduce the overall free energy of the system. In a nonpolar solvent (e.g. oil) molecules will orientate with the nonpolar chains towards the solvent, while the polar groups are protected inside the micelle. This arrangement can loosely be used to imagine the functionalization of NPs, where surfactant molecules are attracted to the surface of NPs. An improvement of the stability of the colloid can be obtained if the adequate surfactant is chosen for the specific combination of NP surface charge and solvent.

Electrostatic stabilization

Electrostatic stabilization relies on increasing the Coulomb interactions between the electrical double layers of particles. This increases the amount of free energy (**ΔG**) required by two colliding particles in order to enter the well of minimum potential energy (aggregation), as presented in Figure 2.28 (a).

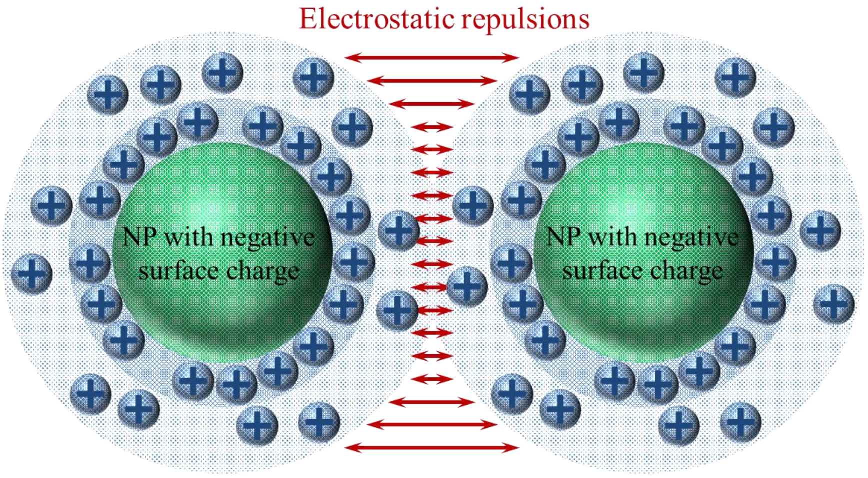

Figure 2.30 Electrostatic stabilization [adapted from 249]

This effect is obtained by increasing the ζ potential of the dispersed particles and therefore the strength of the ionic atmosphere (e.g. Figure 2.30 shows the interaction between two negatively charged NPs). Some compounds (usually metals) form oxide or hydroxide surface films in an oxygen rich atmosphere. This increases the polarity of the surface and may improve the stability of the colloid.

It should be noted though, that this mechanism relies on the kinetic properties of the process – if aggregation does occur, redispersion of particles is practically very difficult (as shown in Figure 2.28 (a), two aggregated particles must possess very large energy to exit the deep energy well associated with their state). Furthermore, the dispersed particles are sensitive to the addition of other ions to the colloidal system, i.e. NPs in high ionic strength solutions can undergo flocculation.

Electrostatic stabilization can also be employed in nonpolar fluids such as oils, as long as an adequate amphiphilic surfactant is used to shield the polar/charged surfaces from the oil molecules [31, 92, 252, 253].

Steric stabilization

Steric stabilization consists of the addition of surfactants (usually non-ionic) onto the particle surface. This is done to prevent the NPs from getting close enough for Van der Waals interactions to become dominant (as can be seen in Figure 2.31) [31].

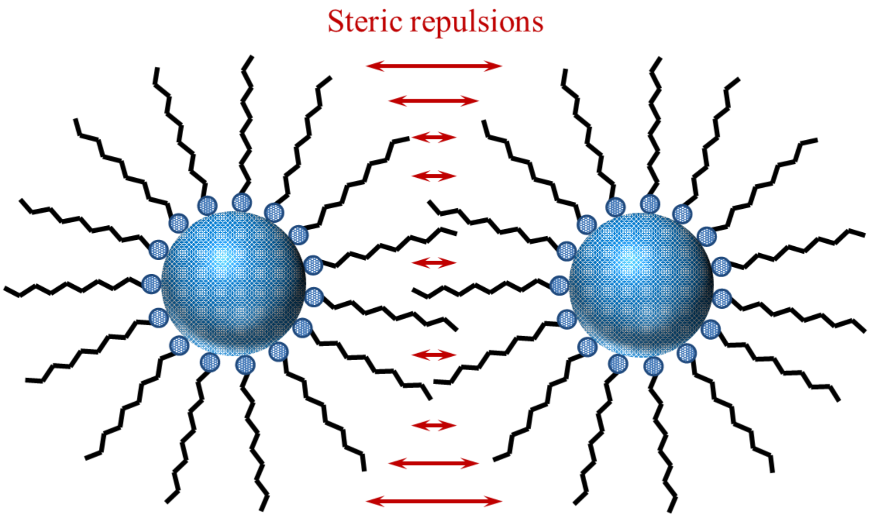

Figure 2.31 Steric stabilization [adapted from 249]

There are several requirements for good steric stabilization:

- The surfactant must be soluble in the dispersion medium
- The surfactant should adsorb or anchor itself (react) on the particle surface easily
- Adequate coverage of the particle must be obtained (little coverage leads to interpenetration of surfactant molecules on different particles and Van der Walls forces between the surfactant molecules will usually help aggregation)

Steric stabilization influences the thermodynamic parameters of aggregation, i.e. it decreases the free energy (**Δ*G***) associated with the particle surface (A' in Figure 2.24). If carried out correctly, it has several advantages: high concentrations can be achieved, the particles are redispersible and are not sensitive to ions in the colloid.

When a combination of both electrostatic and steric stabilization methods are used, the mechanism is referred to as ***electrosteric stabilization***. NPs are covered in a surfactant layer, but also possess an electric charge, and so may benefit from enhanced repulsive interactions (as shown schematically in Figure 2.32) [31, 253].

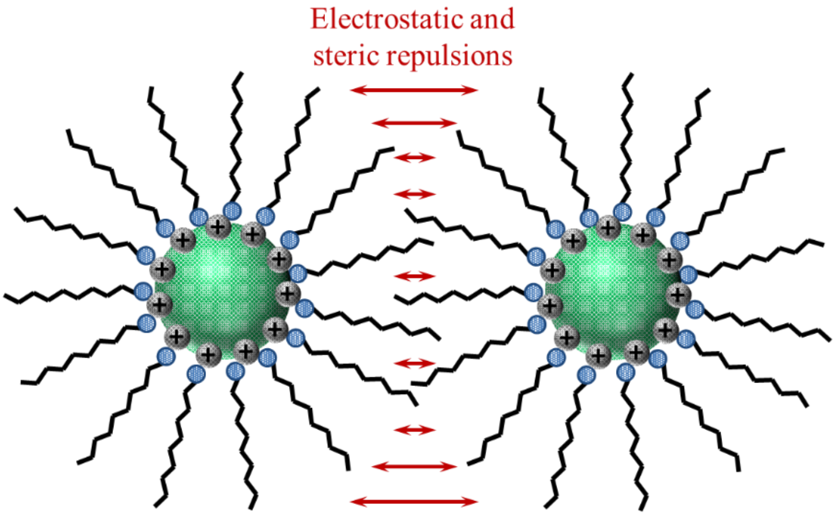

Figure 2.32 Electrosteric stabilization [adapted from 254]

These methods are the basis for the few literature studies that have attempted to functionalize WS_2 NPs in base oils.

2.5.4 Functionalization of WS_2 NPs

Functionalization requirements

Metal dichalcogenide NPs such as 2H-WS_2 and IF-WS_2 have already been shown to be very good dry lubricants [9, 29, 30, 83-88]. However, when used as lubricant nanoadditives, the NPs must simultaneously fulfil three main requirements:

- ✓ Reduce friction and wear in the contact (i.e. WS_2 NPs should be attracted to the lubricated surfaces)
- ✓ Show good dispersability and stability in oils to maintain a long-term tribological effectiveness. To achieve this, the WS_2 NP dispersions must have low mean particle

sizes, narrow size distributions and their surface must be functionalized to avoid agglomeration and sedimentation

- ✓ The functionalization process must not interfere with the ability of the WS_2 NPs to interact with the metal surface (i.e. to be attracted onto the wear track)

To achieve these requirements the surface chemistry of the nanoadditives must be carefully designed. This section discusses the methods used in the literature for the functionalization of WS_2 NPs, along with their main advantages and drawbacks.

Previous work on WS_2 functionalization

Nanoparticle colloids are mainly obtained by a) dispersing the NP powder in an appropriate fluid or by b) synthesizing the NPs directly in the solution.

a) The functionalization of NPs with a surfactant is usually required in the former case. Dispersion of NPs in the desired medium is then obtained by shaking, mixing or high shear mixing. The advantage of this method is that it can be applied to NPs in a powder form, but the dispersion of the functionalized NPs may be more difficult to achieve. In the case of WS_2, the surface of the NPs has proven to be particularly difficult to modify, as the intra-layer interactions between S and W atoms are very strong and the outer sulphide layer does not interact with surfactants.

b) The synthesis of functionalized NPs directly in the solvent is a more complex process. The surfactant must be selected prior to the synthesis in such a way that it does not interact with the reactants and must be able to adhere to the surface of the NPs being produced. On the other hand, once obtained, the NPs are already dispersed in the colloid. Some of the common ways of achieving this are by homogenous nucleation in a solvent (thermodynamic control) and microemulsion (kinetic control).

Very few methods have been employed in the literature to achieve the functionalization of WS_2 NPs and each has limitations. A brief review of these studies is presented below.

a) Coating with ***alkyl silanes*** has previously been a popular method for other types of NPs. Therefore, one study investigated the ability of C6-C18 alkyl silanes to disperse IF-WS_2 NPs in non-polar oils [255]. It was suggested that the silane molecules attach to the NPs at the structural defects present on the IF particles, where the full coordination between the S and W atoms is not achieved. The study used the average size of the agglomerates to calculate the number of IF-WS_2 NPs present in large particles, showing that it decreases from ~1600 particles for the uncoated NPs to ~340 and ~150 for C12- and C18-functionalized NPs. The sedimentation time of the dispersions was also increased, with the biggest improvement found to be for the C12 silane (by a factor of 5). The main disadvantage of this method is that the IF-WS_2 NPs are still agglomerated and have a large average size between 350 and 600 nm.

b) ***Trioctylamine*** – $[CH_3(CH_2)_7]_3N$ – is a popular surfactant and has also been used to coat IF-WS_2 NPs [37]. The NPs in this study were synthesized using a solvothermal process in pyridine and they were found to maintain their tribological properties after testing. However, the stability of the NP dispersions, which have an average size of ~200 nm, was not investigated with time. Furthermore, the quality of the product obtained is difficult to assess since the resolution of the XPS data presented is poor (the intensity of the signals presented in the spectra are masked by the background noise). This method also uses pyridine, which is a very toxic solvent.

c) ***Methyltrioctylammonium chloride*** – $[CH_3(CH_2)_7]_3N(CH_3)Cl$ – is another surfactant employed to functionalize IF-WS_2 NPs in the range of 200 nm, prepared through the same solvothermal process [38]. Dispersions in liquid paraffin were analysed and a positive effect was observed on the samples, but its magnitude was not quantified in the paper. Moreover, the XPS data retrieved is again inconclusive. The intensity of the signals in the spectra is similar to the background noise, making it difficult to draw conclusions as to the benefit of this surfactant.

d) A novel approach involved the docking of a transitional metal cation with high sulphur affinity (e.g. Ni^{2+}) to the outer sulphide layer of the NP and to a 'capping ligand'. The nickel ion was used as a binding agent between the NPs and a functionalized polymer matrix. Nitrilotriacetic acid (NTA) played the role of an anchor, with the carboxylic groups orientated around the Ni^{2+} ion, as portrayed schematically in Figure 2.33. The metal ion is able to form covalent coordinative bonds with the sulphur atoms on the NPs. As a result, the dispersed polymer matrix can attach the umbrella-type chelating agent NTA on different sites on the NPs, keeping them dispersed.

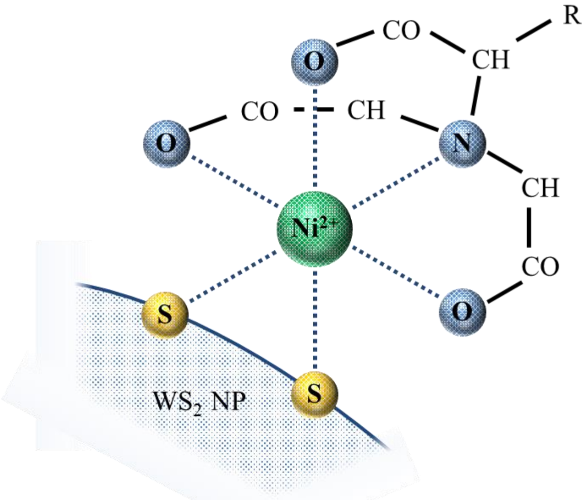

Figure 2.33 Ni^{2+} atom chelated by NTA [adapted from 256]

This method was used to functionalize WS_2 nanotubes for biological applications [257, 258]. Its drawbacks are the requirement of costly ligand molecules (involved in a multitude of elaborate steps) and the likelihood of the complex chelating agents and soluble polymer matrix suffering degradation in tribological applications, which normally involve high temperature and stress conditions.

2.5.5 Summary

NPs are small objects (1 – 100 nm) with different properties relative to the bulk material. These are a consequence of their small size, very large specific surface area and large proportion of higher-energy active atoms located at the surface.

Colloids are dispersions of particles in a fluid dispersion medium and applications using them rely on the stability of the system. However, when NPs are dispersed in a colloid, attractive Van der Waals forces act towards the agglomeration and subsequent sedimentation of the particles. The stabilization of colloids can usually be performed by increasing the ζ potential at the surface of the particles (electrostatic stabilization) or by coating NPs with surfactants that impede aggregation (steric stabilization).

The functionalization of WS_2 is particularly difficult to achieve due to the inactive nature of the outer sulphide layer of the NPs. There are few successful attempts described in the literature, with various disadvantages related to their application in tribological contacts, such as the toxicity of some reactants, the use of complex and expensive materials which may degrade in the contact, the scarcity of anchoring points for surfactants on the surface of NPs etc.

These observations indicate that the stable dispersion of WS_2 NPs in oils can only be achieved by using a combined approach that employs both steric and electrostatic stabilization principles, while using organic molecules compatible with the tribological application. However, the experimental results which describe the successful dispersion of 2H-WS_2 NPs in PAO base oil are currently being prepared for a patent application and are not described in the experimental sections of the thesis.

2.6 CONCLUSIONS

Increased interest has been shown for the development of new, efficient and affordable lubricants, in order to replace current available technologies, which have environmental shortfalls. In this context, WS_2 NPs have the potential to become successful nanoadditives in lubricants and tribological coatings, capable of delivering an improved performance with reduced cost to the environment.

WS_2 NPs have very good tribological properties and their use as nanoadditives in lubricants has been attempted by a large number of studies in the literature. However, their mechanism of action is not fully understood and a thorough study is necessary.

The nanoadditive has been mainly studied at low temperatures and the general view is that WS_2 NPs reduce friction in a tribological contact by rolling (IF-WS_2) or exfoliating under high stress (IF- and 2H-WS_2), producing a film of layered sheets which have low shear strength. However, their chemical nature indicates that WS_2 NPs could also display properties similar to EP/AW additives such as ZDDP. This behaviour involves a chemical reaction with the steel substrate and the generation of a sacrificial chemical film in high-temperature and high-pressure conditions.

The tribofilm generated by WS_2 NPs is similar to those generated by AW/EP additives, but can also have a positive effect on reducing the hydrogen permeation observed in bearing applications, which leads to hydrogen embrittlement. The action of WS_2 is similar to that of passivator molecules, which have been used in the past to generate a remarkably similar protective film on the steel surfaces. Therefore, the use of WS_2 NPs may reduce the amount of hydrogen in the material and the corresponding damage incurred.

The literature review has identified areas where further research is required. Thus the following studies were undertaken and are described in the experimental sections of the thesis as follows.

The first part of the experimental research (Chapter 4) concentrates on testing the tribological properties of WS_2 NPs and understanding their mechanism of action. The study focused on 2H-WS_2 rather than IF-WS_2 NPs because the layered structure enables them to exfoliate more easily under shear and react with the wear track. 2H-WS_2 NPs are also easier to functionalize and thus can form stable dispersions. Temperature is expected to play a major role in the chemical reactions with the steel surface and therefore, the tests are performed at both low and high temperatures (i.e. 40 and 100ºC). The effect of the polarity of the base oil is also investigated, as recent studies show lubricant components can compete for adsorption/reaction on the surface in the tribological contact. A comparison with IF-WS_2 and IF-WSe_2 NPs is also made.

The second part of the experimental research (Chapter 5) studies the ability of 2H-WS_2 NPs to compete with currently used oil additives. ZDDP is the most popular AW additive and is used together with a FM to reduce wear and friction in the contact. The tribofilms generated by these additives are investigated in order to enable a better understanding of the excellent properties displayed by 2H-WS_2 NPs.

The third part of the experimental research (Chapter 6) investigates the ability of the chemical tribofilm generated by 2H-WS_2 NPs to reduce the permeation of hydrogen in high-strength bearing steel. The amount of hydrogen in race/disc samples obtained in rolling contact tests has been quantified using thermal desorption spectroscopy. The tribofilms were analysed with XPS and Auger spectroscopy to determine the main factors responsible for the lower permeation of hydrogen in steel when using 2H-WS_2 additives.

The functionalization of the surface of the WS_2 NPs is required to generate stable dispersions which can be employed in tribological applications. The dispersion of 2H-WS_2 NPs has been successfully achieved and is currently being prepared for a patent application.

3. MATERIALS AND METHODOLOGY

In order to understand the mechanism of action of WS_2 nanoadditives in lubricants, it is necessary to characterize the NPs, the colloids and the wear tracks and tribofilms that may be generated when using them. A large variety of techniques were used to investigate the physical and chemical properties of the nanoadditives and the mechanical properties of the tribofilms. This chapter discusses the materials and techniques used throughout this study.

3.1 Materials

The 2H-WS_2 NPs were purchased from M K IMPEX Canada as a silvery-grey powder with a stated average size of 90 nm. The IF-WS_2 and IF-WSe_2 NPs were supplied by Dr Ekaterina Vasilyeva from the Saint-Petersburg State Polytechnical University and are black powders with a stated average size of 20-70 and <40 nm respectively.

Two types of base oils were used in this study. SpectraSyn Plus™ 6 is a polyalphaolefin (PAO) and was used as a nonpolar base oil. UCON™ LB-165 is polypropylene glycol-based (PPG) and is a polar base oil. The physical properties of the two base oils are presented in Table 3.1. The performance of WS_2 in steel contacts is expected to be superior in PAO, because the nonpolar nature of the base oil avoids any competition with the additive for adsorption/reaction on the lubricated metal surface.

Table 3.1 Base oil properties

	Density [kg/m3]	Viscosity (40ºC) [cSt]	Viscosity (100ºC) [cSt]
PPG	980	34	6.7
PAO	830	30.3	5.9

2H-WS_2 NP dispersions in base oil (PAO and PPG) with a concentration of 1 % w/w were prepared using a probe sonifier (Ultrasonic Probe ME/51). This concentration was recommended in published research as optimal for tribological applications (i.e. a study on the effect of 2H-WS_2 NP concentration on the friction coefficient in a pin-on-disc setup revealed an optimum concentration of 1% w/w NPs [164]). To avoid any competition for the additive to adhere/adsorb/react on the lubricated metal surface, no surfactant/dispersant was used to stabilize the dispersions.

IF-WS_2 and IF-WSe_2 NP dispersions in PAO (1 % w/w) were also prepared to investigate the differences between the tribological properties of the three types of NPs.

3.2 WS_2 characterization

The physical and chemical properties of 2H-WS_2 were characterized using X-ray powder diffractometry (XRD), Raman spectroscopy, Fourier transform infrared spectroscopy (FTIR), transmission electron microscopy (TEM), scanning transmission electron spectroscopy (STEM) and energy-dispersive X-ray spectroscopy (EDX). The particle size distribution of WS_2 and WSe_2 NP dispersions in oils was measured by dynamic light scattering (DLS).

3.2.1 Physical properties

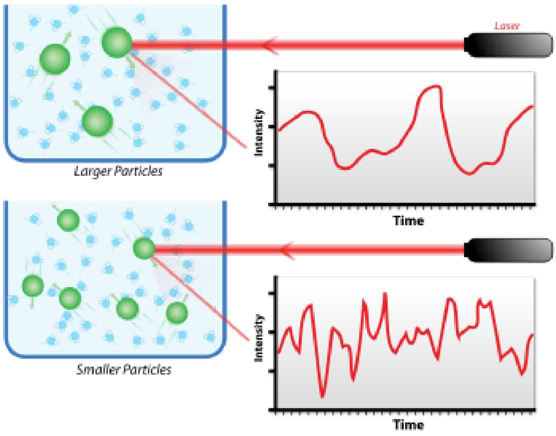

Figure 3.1 Dynamic light scattering [reproduced with permission from 261]

Dynamic light scattering (DLS) is used to measure the particle size distribution (PSD) profile of the dispersed NPs and the stability of a colloid [259, 260]. The PSD is the function that correlates the amount of particles (by mass) with their size. The DLS technique relies on the ability of NPs to scatter light of comparable wavelength with their size. As depicted in Figure 3.1, light is passed through the sample and a detector (usually placed at a 90 degrees angle) is used to observe and quantify the scattered light. However, due to the Brownian motion of particles suspended in the fluid, the signal fluctuates with time. The intensity of these fluctuations is directly related to the motion of the particles through the fluid and therefore, to the rate of diffusion (which is dependent on the size of the NPs). Measuring the PSD at various intervals of time gives information on the stability of the colloid.

The PSD of the WS_2 and WSe_2 NPs dispersed in PAO was characterized immediately after preparation and sonication in a Malvern ZetaSizer Nano ZS [262] using a 4 mW 633 nm He-Ne laser light source. The measurements were carried out in a standard cell at ambient temperature (23°C).

Transmission electron microscopy (TEM) is one of the most popular methods used to characterize NP size morphology [263, 264]. During the analysis, a beam of electrons is transmitted through the sample (which is mounted on a mesh grid) and focused on a screen or detected by a sensor. The technique is important in NP analysis because it offers very good resolution: high resolution transmission electron microscopy (HRTEM) allows imaging of individual atoms – under 10^{-10} m, well in the Angstrom range. In scanning TEM (STEM) the electron beam is focused onto a narrow spot and rastered across the sample to perform chemical analysis. However, all TEM samples must be very thin (~100 nm) and stable under the high voltage (up to 300 kV) and ultra-high vacuum (up to 10^{-9} Pa).

The shape and morphology of the NPs were investigated using a JEOL 3010 (University of Southampton) [265], a JEOL ARM 200cF 'MagTEM' (Glasgow University) [266], a FEI Titan G2 80 – 200 ChemiSTEM™ S/TEM (University of Manchester) [267], a Hitachi H-9000UHR (Toray Research Center, Japan), a JEOL JEM-ARM200F (Toray Research Center, Japan) and a JEOL ARM-200F (Oxford Materials, UK) [268]. The NPs were initially dispersed in solvents (acetone, acetone/hexane or dichloromethane), and added in drops onto TEM copper grids covered in a 'holey' amorphous carbon film.

TEM measurements on the JEOL 3010 were performed with the help of Dr Chao Ma, in Bright Field (BF) mode at an accelerating voltage of 300 kV. HRTEM measurements on the JEOL MagTEM were performed with the help of Dr Ian MacLaren, in both Bright-Field (BF) and High Angle Annular Dark-Field (HAADF) modes at 200 kV. The sample and holder were cleaned in an oxygen/argon plasma prior to insertion into the microscope in order to minimise carbon contamination. HRTEM and STEM measurements were performed on the FEI Titan G2 80 – 200 ChemiSTEM™ S/TEM with the help of Dr Fredrik Hage. The microscope was operated in STEM mode at an acceleration voltage of 200 kV and was equipped with a 3rd order aberration corrector allowing for sub 0.1 nm electron probe sizes. EDX maps were acquired using the SuperX EDX system, which allows for higher collection efficiency compared to conventional spectrometers. This is achieved by using a combination of 4 individual Silicon Drift Detectors (SDDs) arranged symmetrically around the microscope sample stage (more details are available in [269]). HRTEM and STEM measurements were also made on the Hitachi H-9000UHR (300 kV) and JEOL JEM-ARM200F by Toray Research Center in BF and HAADF modes. The JEOL JEM-ARM200F has a JEOL Centurio 100 mm^2 Silicon Drift Detector. STEM with EDX measurements were performed at 200 kV with a beam size of approximately 0.2 nm. HRTEM images of IF-WS_2 and IF-WSe_2 NPs were recorded on the JEOL ARM-200F at 200 kV in BF and HAADF modes.

3.2.2 Chemical properties

Raman spectroscopy gives information on the vibrational energies present in a molecule. It relies on the scattering of laser light passed through the sample, which leads to a shift in the energy of laser photons. By recording the amount of energy absorbed by the sample at every wavelength of the analysed spectrum, it is usually possible to determine the chemical structure of all the compounds present by reference to the specific vibrational energy bands given in the literature [270, 271]. Raman is commonly used because it requires a small quantity of sample and little sample preparation.

Raman spectroscopy was performed using a Renishaw RM1000 [272] with a HeNe laser, at a wavelength of 785 nm. The Raman is coupled with a Leica microscope and has a 1800 mm^{-1} grating and notch filter to prevent Rayleigh scattered photons reaching the detector.

X-ray diffraction (XRD or X-ray crystallography) is used to determine the atomic or molecular structure of a crystal. A beam of X-rays is diffracted off the atomic structure of the sample. The angle and intensity of each resulting beam are measured and used to generate a 3D picture of the electron density, which identifies the position of atoms in the crystal/lattice. XRD was used to observe the layered structure of WS_2.

XRD was performed at ambient temperature using two instruments with the help of Dr Mark Light at the University of Southampton. The Siemens D5000 θ/2θ powder X-Ray diffractometer [273] has a Bragg Brentano reflection geometry. It has a $K\alpha 1$ (λ=1.54056 Å) germanium primary monochromator and a point scintillation counter. The Bruker GADDS combinatorial X-ray instrument has Cu Kα radiation and is equipped with a XYZ stage and a multi-wire Hi-Star area detector. The calibration of the instrument was checked before each set of samples using the NIST Corundum Standard Reference Material SR1976 and found to be correct within 0.1 degree.

Energy-dispersive X-ray spectroscopy (EDX) can determine the elemental composition of a sample by ejecting electrons from the ground state of the component atoms and measuring the energy emitted as X-rays when the atoms return to a more stable state. The sample can be bombarded with high energy X-rays (the technique is called X-ray fluorescence) or a beam of electrons. The latter case is the most frequently used, because EDX is usually coupled with SEM or TEM. However, hydrogen, helium and lithium are not visible in EDX.

EDX measurements were performed using a FEI Titan G2 80 – 200 ChemiSTEM™ S/TEM (University of Manchester) and a JEOL JEM-ARM200F (Toray Research Center, Japan).

3.3 Tribological tests

Tribological tests using the WS_2 NP dispersions were carried out on a Mini Traction Machine (MTM2, PCS Instruments) in a sliding-rolling ball-on-disc setup (Figure 3.2). This features a 19 mm diameter ball and a 46 mm diameter disc, both made of AISI 52100 steel (hardness 750-770 HV). The root-mean-square roughness of both balls and discs is 11 ± 3 nm, resulting in a composite surface roughness of approximately 16 nm. New specimens (balls and discs) were used for each test and were cleaned with solvents (toluene followed by isopropanol) in an ultrasonic bath for 10 minutes prior to the test.

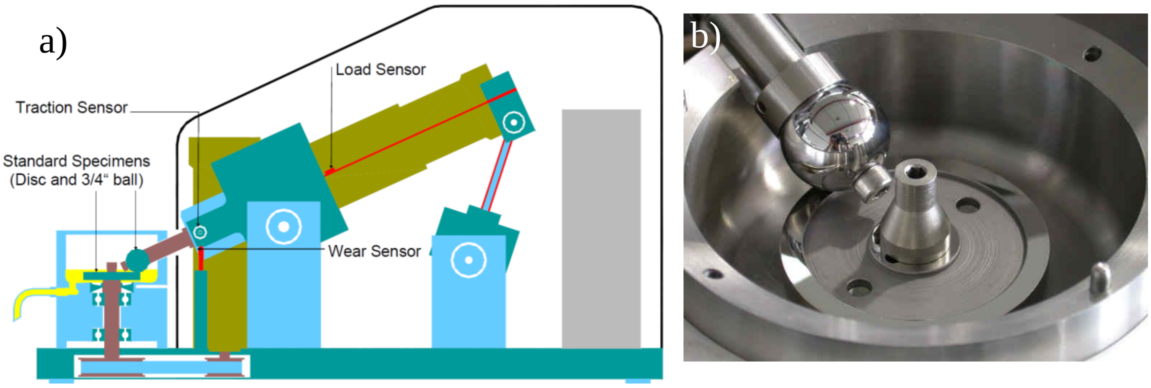

Figure 3.2 a) MTM2 rig and b) MTM2 pot [reproduced with permission from 274]

Throughout the test the temperature was kept constant at 40ºC or 100ºC and the applied load was 30 N, corresponding to an initial mean Hertzian pressure of 0.94 GPa. The slide-roll ratio (SRR), calculated as the ratio of the sliding speed (U_b-U_d) to the entrainment speed (U_b+U_d)/2 (where U_b and U_d are the speed of the ball and the disc respectively, with respect to the contact) was 150 %. This slide-roll ratio value was selected to be higher than in previously reported research [275] to accelerate the generation of the chemically reacted tribofilm, which is known to depend on the severity of the rubbing conditions [39]. During the test, the NP dispersion was maintained at constant temperature in the enclosed, temperature controlled insulated chamber, where it was stirred continuously and vigorously by the circular movements of the disc and ball. Therefore, even in the absence of a surfactant, the NPs were maintained well dispersed and only a small number sedimented to the bottom of the lubricant chamber at the end of the 3 hour test.

The MTM2 is fitted with the 3D Spacer Layer Imaging Method (SLIM) attachment, which enables *in situ* capture of optical interference images of the tribofilms on the steel ball using a high resolution RGB colour camera as shown in Figure 3.3 (a). The analysis software (a custom PCS Instruments 3D-SLIM software) matches colours in the image (Figure 3.3 (b)) to a calibration file in order to determine the film thickness of every point in the image [274]. Using the thickness map obtained (Figure 3.3 (c)), the thickness of the tribofilm in each image was calculated as the average value inside a circular area taken across the entire width of the wear track.

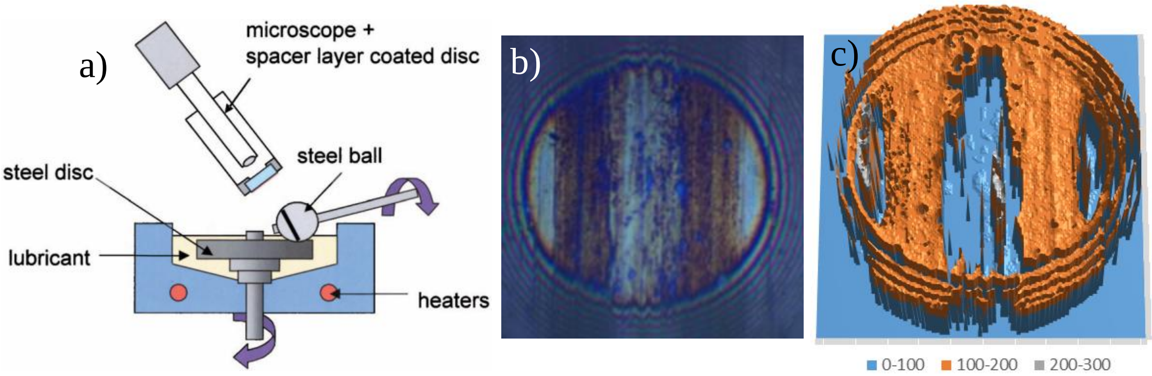

Figure 3.3 a) Diagram of MTM2-SLIM set up [274], b) SLIM image of the tribofilm generated by the WS_2 dispersion, c) 3D representation of the SLIM data (legend in nm)

The tribological tests followed a routine which can be divided in three alternative stages repeated at fixed time intervals. The first stage was the '*conditioning phase*', when the ball and disc were rubbed together at a fixed slow entrainment speed in mixed lubrication film conditions to generate a tribofilm on the ball and disc wear tracks. The following stage consisted of the '*Stribeck curve*' acquisition, in which friction was measured over a range of entrainment speeds at a fixed SRR. The acquisition of data for the Stribeck curve started at the highest speed (1.5 m/s) and continued towards the lowest speed (10 mm/s) value, to protect the tribofilm formed by avoiding its damage at low speeds in the boundary regime. This stage is automated and lasts about 1 minute. The third stage was the '*tribofilm measurement*', when the motion was halted, the spacer layer-coated window was loaded against the ball track and an image was captured. This stage is also automated and lasts 5-10 s. Table 3.2 summarizes the conditions used for the MTM2-SLIM tests in this study.

Table 3.2 MTM2 – SLIM test conditions

Conditioning phase	
Temperature	40°C, 100°C
Load	30 N
Mean Hertzian pressure	0.94 GPa
Entrainment speed	0.1 m/s
Slide-roll ratio	150 %
Stribeck curve phase	
Temperature	40°C, 100°C
Load	30 N
Mean Hertzian pressure	0.94 GPa
Entrainment speed	1.5 to 0.01 m/s
Slide-roll ratio	150 %

Rolling contact fatigue (RCF) tests were performed in a ball-on-disc setup test rig at the Hydrogenius Center, Kyushu University, Japan. Figure 3.4 shows a schematic illustration of the apparatus [276]. Although the rig is modified to allow testing in hydrogen atmosphere conditions, the experiments in this study were performed in atmospheric conditions. Six 6.35 mm diameter balls are placed on a guide disc with raceway grooves and separated by a retainer. A normal load (2650 N, equivalent to a Hertzian pressure of 4.8 GPa) is applied to the chamber by a lever and the disc/ball contact undergoes rolling through the rotation of the upper shaft. The contact pressure used in this study is higher than the calculated pressure encountered during normal operation in bearings, in order to accelerate the formation of hydrogen (from the decomposition of the lubricant) and initiation of embrittlement and is in line with recommendations from other publications [64, 190, 194, 213, 214]. The Hertzian pressure is slightly higher than the shakedown limit (the maximum contact pressure which the material can support in the elastic range under steady state conditions). Theoretically this means that plastic deformation below the surface continues to occur repeatedly. In practice however, the pressure reduces due to the change in surface geometry (to become more conformal) by initial deformation and wear, and virtually elastic contact occurs in the rest of the cycles.

The Hertzian contact pressure for the dynamic load rating (load for a rating life of 10^8 load cycles) of this steel is 4.2 GPa. The ball and disc steel is JIS SUJ2, equivalent to AISI 52100. The disc specimens were polished with abrasive paper followed by buff polishing with 3-µm diamond slurry to an R_a (arithmetic average roughness) of 0.05 µm. The contact is subjected to mixed lubrication conditions. The specimens were ultrasonically cleaned with hexane and acetone prior to the rolling contact tests. Table 3.3 summarizes the testing conditions.

Table 3.3 Rolling contact test conditions

Test duration	2, 5 and 10 h
Number of cycles	~595,000/h (ball) ~270,000/h (race)
Temperature	120ºC
Load	2650 N
Mean Hertzian pressure	4.8 GPa
Entrainment speed	1500 rpm (3.4 m/s)
Film parameter λ	2

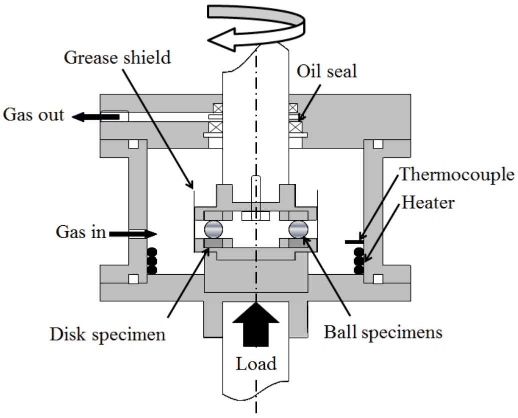

Figure 3.4 Diagram of the rolling contact test rig [reproduced with permission from 277]

3.4 Tribofilm analysis

The steel wear tracks and tribofilms were analysed using optical microscopy, Alicona profilometry, focused ion-beam coupled with secondary ion mass spectroscopy (FIB/SIMS), X-ray photoelectron spectroscopy (XPS), Auger electron spectroscopy (AES) and nanoindentation. The techniques described below provide valuable information about the morphology, thickness, chemistry and hardness of the tribofilms generated in the contact.

3.4.1 Structural properties

Optical microscopy on the wear tracks was performed on an Olympus BH2-UMA optical microscope connected to a Prosilica GC camera (at 20x magnification).

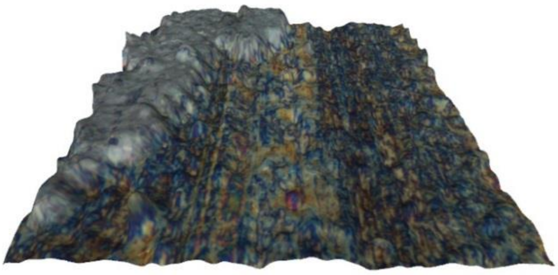

Figure 3.5 Alicona profile of WS_2 NPs deposited on the steel wear track (their height is approximately 200 nm)

Profilometry measurements are usually made across solid surfaces in contact or non-contact modes. Contact profilometers (such as the Taylor Hobson Talysurf) move a sharp stylus across the measured surface, achieving resolutions of around 10 nm. A drawback of this technique is that the surface can be damaged during this measurement. Non-contact profilometers (e.g. Alicona Infinite Focus, Bruker ContourGT) use light to obtain the same information. The resolution is similar but the samples are not damaged, enabling the use of the technique to measure nanomaterial structures (Figure 3.5).

Alicona Infinite Focus profilometry was used to study the thickness and morphology of the tribofilms generated by the additives across the wear track on the disc specimen after the 3 h MTM tests. The equipment generates a 3-D surface profile of the wear track that can be analysed with the Alicona IFM software supplied [278]. Multiple surface profiles were measured for each tribofilm image and the average height values were calculated. The measurements were conducted only on the disc specimens due to their flat geometry. The contact specimens (ball and disc) were made of the same material (AISI 52100) and have similar roughness values. Therefore, it is expected that both contact surfaces form tribofilms of very similar composition and thickness values.

Optical profilometry was also performed on the Bruker ContourGT [279] to investigate the depth and morphology of the wear tracks on the disc specimens after the RCF test. The equipment generates a 3D surface profile of the wear track that can be analysed with the Vision64 Analysis Software supplied. For each image multiple surface profiles were measured and used to calculate average depth values.

Scanning electron microscopy (SEM) is a powerful technique that produces images of a sample by scanning it with a beam of focused electrons (e.g. Figure 3.6 shows an SEM image of the tribofilm generated by WS_2 NPs on a steel substrate at 100ºC, revealing the thick but patchy nature of the film). SEM can provide accurate information on particle morphology and NP size. Modern SEMs have a wide range of magnification (from 10x to ~500,000x – sub nanometre) but they operate at high beam voltages (up to ~40 kV) and under vacuum (10^{-4} Pa in the sample chamber and 10^{-7} Pa in the column). Samples must therefore be very clean, dry and electrically conductive. A thin layer of metal or carbon can be deposited on the sample if it is not conductive.

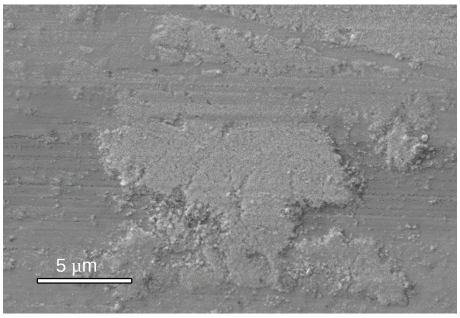

Figure 3.6 SEM image of the tribofilm generated by WS_2 NPs

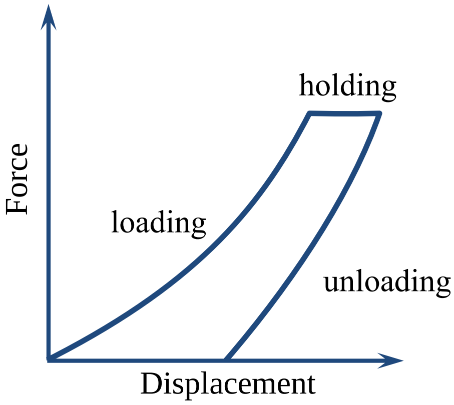

Figure 3.7 Typical nanoindentation force-distance curve

In this study, SEM imaging of the wear tracks was performed during the FIB, XPS and Auger analysis and details of these techniques are presented in Section 3.4.2.

Nanoindentation is a depth sensing technique capable of providing measurements of elastic and plastic properties, where the indentation process is continually monitored with respect to force, displacement and time. It is performed by pressing a hard tip (frequently diamond) into the sample and most commonly measures hardness and reduced Young's modulus (E'). The loading conditions can be maintained for a period of time to see whether the tip continues to penetrate the substrate. The elastic behaviour of the material (i.e. E') can also be studied from the unloading curve. Figure 3.7 presents a schematic of typical nanoindentation results.

Nanoindentation of tribofilms was performed using a NanoTest Platform 3 instrument (Micro Materials, Wrexham, UK) [280] with the help of Dr Jurgita Zekonyte. This pendulum based nanoindentation system is extensively explained in the literature [281]. Indents were made using a Berkovich diamond indenter in a depth-controlled mode. The maximum penetration depth depended on the tribofilm thickness and was set to 20 or 30 nm. The maximum loading force was 1 mN and the loading and unloading rates were kept constant at 0.1 mN/s. The loading and unloading times were set to 20 s and a dwell time of 10 s was selected at maximum load to reduce the influence of creep. A matrix of 100 or 200 indents was imprinted onto the sample surface (15 µm apart, over an area of 150x150/300x300 μm^2) to map the distribution of mechanical properties. The data was analysed using the Oliver and Pharr method with the custom analytical software provided by the instrument manufacturers. The hardness and reduced elastic modulus were determined [282].

3.4.2 Chemical properties

Auger electron spectroscopy (AES) is a common technique for characterizing the chemistry of surfaces. Excitation of an atom can lead to the expulsion of a core electron and the formation of a high energy state 'hole'. An outer shell electron is likely to fill this orbital by losing a certain amount of energy. Part of this energy can be used to emit a second electron from an outer shell (called an Auger electron). The energy of this second electron contains information about the specific energy states of the atom and allows the detection of elements and their oxidation state. Limitations of Auger spectroscopy include the accumulation of charge on nonconductive samples and the presence of *plasmons* (variations in the energy of electrons due to scattering effects, making the spectra difficult to interpret in some cases) [270, 271].

An Auger electron spectrometer (JEOL JAMP 9500 F) [276] with a 10 keV electron beam was used to investigate the elemental distribution across the wear track generated by the WS_2 nanoadditive during the RCF tests. Ion sputtering for 10 seconds was also performed before the analysis in order to remove the contamination layer from the surface. This 10 second sputtering time removed material to an estimated depth of 3 nm. Auger mapping was performed on a 2x2 μm^2 area inside the track in order to investigate the atomic distribution of the main components of the tribofilm, i.e. tungsten, oxygen, iron and sulphur. These measurements were performed at Kyushu University, Japan, with the help of Dr Hiroyoshi Tanaka.

X-ray photoelectron spectroscopy (XPS) is one of the most important chemical analysis techniques. It can measure the composition, chemical state and electronic state of samples containing any element except hydrogen and helium. This is performed by bombarding the sample with X-rays and measuring the number and kinetic energy of all the electrons emitted. Samples must be cleaned and dried before analysis, as ultra-high vacuum conditions are needed for XPS (pressures lower than 10^{-7} – 10^{-8} Pa). Modern systems have very good detection limits and are capable of line profiling (they measure the composition across the surface) and depth profiling (an ion beam is used to sputter atoms from the sample and therefore allows sequential analysis of deep layers) [270].

XPS analysis of the MTM discs was performed at Newcastle University with the help of Dr Naoko Sano. The instrument is a Thermo Scientific K-Alpha spectrometer (East Grinstead, UK) [283] with a 1486.6 eV microfocused monochromatic Al ($K\alpha$) X-ray source. The spot size was 200x400 μm^2 (ellipse shape). The pass energy was 200 eV for the wide (survey) spectra and 40 eV for the high resolution regions (narrow spectra). The instrument features an argon gun, which was used to clean the samples by sputtering. The raster size for the sputtering was 1x2 mm^2, using the Ar gas cluster ion beam (GCIB) mode at 6KeV with 1000 atoms for 60 s.

XPS analysis was also performed at Cardiff University with the help of Dr David Morgan. Measurements were conducted using a Kratos Axis Ultra-DLD photoelectron spectrometer [284], utilising monochromatic Al (Kα) radiation. Samples were mounted using conductive carbon tape on to a standard sample bar. The analysis area was 110x110 μm^2. The pass energy was 80 eV for high resolution scans and 140 eV for survey scans. Depth profiling analysis was performed using a Kratos minibeam-I ion source operating at 4 kV with an argon pressure of 10^{-6} torr and rastered over a 4 mm^2 area. The choice of the 110 micron wide analysis area ensured that edge effects in the etch crater were minimised during analysis. The research that employed this equipment is described in Section 4.4.2.

XPS measurements were also conducted at the University of Leeds with the help of Dr Benjamin Johnson. The results are presented in Section 4.4.2. The instrument used was a VG Escalab 250 XPS with monochromated aluminium K-alpha X-ray source [285]. The spot size was 500 μm^2 with a power of 150 W. Detailed spectra of individual peaks were taken with a pass energy of 20 eV, 0.1 eV step size and dwell time of 50 millisecond whilst the survey scan was taken with a pass energy of 150 eV, step size of 1 eV and dwell time of 50 msec. Sputtering was performed using an argon ion gun with parameters specific to the sample, in this case with energy of 1 keV and a current of 0.1 μA/mm^2. Binding energy was calibrated by setting the carbon 1s peak to 285 eV. Core level spectra were normalized to Shirley background and the peaks were fitted using mixed Gaussian-Lorentzian fits (using the CasaXPS^{TM} software).

XPS combined with Argon ion sputtering for depth profile analysis (JEOL JPS 9200 X-ray Microprobe) [276] was performed on the tribofilms at the end of the RCF tests to study the elemental composition and chemical state of the elements. These results are presented in Section 6.2. The excitation source was a monochromatized Al Ka (1476.6 eV) X-ray beam of 100 μm diameter. The instrument spectral resolution was 1.1 eV (path energy). Points *on* and *off* the wear track were selected by optical micrograph imaging. During depth profiling, measurements were alternated with rastered Ar$^+$ beam milling. The milling rate was calibrated using a SiO_2/Si substrate with known oxide thickness, in accordance with standard techniques. Sputtering was performed for 30 seconds, which removed an estimated 2 nm of material. These measurements were performed at Kyushu University, Japan with the help of Dr Hiroyoshi Tanaka.

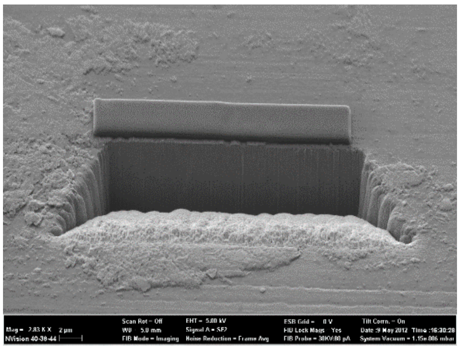

Figure 3.8 SEM image showing FIB milling and the protective layer deposited on the wear track

Focused ion beam (FIB) is a useful way of imaging solid surfaces. The technique is similar to SEM, but a beam of ions (usually gallium) is used instead. Gallium atoms are much larger than electrons, so a FIB beam is capable of sputtering the sample. Secondary electrons are emitted in the process and can be used for imaging purposes, but most of the time FIB is coupled with a SEM for better resolution. However, the advantages of FIB come with the sputtering capabilities of the beam. This makes subsurface features visible and depth profiling (analysis of the surface as the beam sputters sample atoms) is a commonly used technique (Figure 3.8). These capabilities make the technique valuable for studying tribofilm features. When imaging thin layers, a metal or carbon coating is deposited on the surface to protect the analysis area.

Secondary ion mass spectrometry (SIMS) is a very sensitive surface analysis method, capable of detection limits of up to parts per billion. Although mainly a *qualitative* technique, determining the chemical composition is possible with the use of standards. An ion beam is used to eject secondary ions from the sample surface, which are then analysed in a mass spectrometer. Here, the molecular mass of chemical species is detected and plotted against their relative intensity (linked to composition). Positive or negative charge detectors can be used to identify ions of respective charges. SIMS is usually coupled with FIB/SEM in order to provide information about different layers of the sample. The analysis can produce spectra of elemental composition in a single layer or map the distribution of an element across the sample depth.

FIB and SIMS analysis were carried out on the MTM discs using a dual beam Zeiss NVision40 SEM-FIB [286]. After depositing a layer of carbon to protect the surface, FIB cross-sections were conducted through the surface of the tribofilm to measure the thickness. The gallium ion beam was used in conjunction with a Hiden Analytical EQS quadruple detector to perform dynamic SIMS depth profiles of the WS_2 tribolayers. Areas of 30x30 μm^2 were sputtered using a 5 kV acceleration voltage operating at 3 nA beam current, with positive/negative ion masses being recorded as a function of sputter time for carbon, sulphur, iron and tungsten. Although important for this study, oxygen was not monitored during the SIMS analysis because it is an element with *background-limited sensitivity* (i.e. the sensitivity is limited by an undesired background, such as residual oxygen gas in the vacuum systems). The measurements were performed with the help of Dr John Walker at the University of Southampton.

Thermal desorption spectroscopy (TDS) is a very useful technique capable of determining and quantifying the gaseous components absorbed in a sample. The analysis is performed by heating the sample under a constant heating rate in order to induce the desorption of all gaseous species from the test samples, which are then measured by a mass spectrometer.

The hydrogen content in the steel samples after the RCF tests was measured using TDS (Denshi-Kagaku TDS1200) [276]. Immediately after the tribological tests, the specimens were cooled, cleaned in an ultrasonic bath with hexane and acetone and small pieces (7x3.5x1 mm, weighting approximately 0.2 g) were cut from the rolling contact area. During the TDS analysis, the cut disc and ball pieces were heated from room temperature to 800ºC at a rate of 60ºC/min and 10ºC/min respectively. A lower rate of heating was used for the ball due to its larger mass and subsequent greater thermal inertia. The TDS rig is equipped with a quadrupole mass spectrometer that can measure and analyse the hydrogen species released from the disc and ball specimens. The measurements were performed with the help of Dr Hiroyoshi Tanaka at Kyushu University, Japan.

4. EXPERIMENTAL INVESTIGATION OF THE TRIBOLOGICAL PROPERTIES OF WS$_2$ NPs

4.1 Introduction

The first part of the experimental research focuses on testing the tribological properties of ***2H-WS$_2$ NPs*** and understanding their mechanism of action. To avoid any competition for the additive to adhere/adsorb/react on the lubricated metal surface, no surfactant/dispersant was used to stabilize the dispersions.

As discussed in Section 2.3.5, the behaviour of WS$_2$ NPs has been previously studied in the published literature only in nonpolar base fluids (e.g. PAO and mineral oils) and at low temperatures, with no justification given for the parameters chosen. This approach did not offer a comprehensive view on the mechanism of action of these nanoparticles and a thorough, more detailed study is necessary. This chapter aims to elucidate the mechanism of action of 2H-WS$_2$ NPs in high pressure contacts by investigating the tribofilm generated on the wear track in a ball-on-disc setup over a range of testing temperatures and lubrication regimes.

NPs were studied at two temperatures, namely 40 and 100ºC, to verify if high-temperature applications promote a different lubrication mechanism, and in two base oils of different polarity – PAO and PPG, to investigate the affinity of the NPs for the steel substrate. The concentration of the 2H-WS$_2$ NPs in the oil was 1 % w/w.

The physical and chemical properties of the NPs were characterized using a variety of techniques such as dynamic light scattering, X-ray powder diffractometry, Raman spectroscopy, transmission electron microscopy and energy-dispersive X-ray spectroscopy. The steel wear tracks were analysed using optical microscopy, Alicona profilometry, focused ion-beam coupled with secondary ion mass spectroscopy, X-ray photoelectron spectroscopy and nanoindentation. The tribological properties of the NPs were tested in a Mini Traction Machine. A thorough characterization of the NPs is crucial to understand their tribological properties and identify their mechanism of action.

This chapter is mainly based on a published paper [287], with some additional discussions on the importance of oil polarity. The tribological properties of ***IF-WS$_2$*** and ***IF-WSe$_2$ NPs*** were also investigated in PAO base oil at 100ºC and a comparison was made between the efficiency of the three types of tungsten dichalcogenide NPs.

4.2 Characterization of 2H-WS$_2$ NPs

The physical and chemical characterization of the 2H-WS$_2$ NPs was carried out in order to investigate their chemical composition, structure, purity and size distribution.

The XRD pattern (Figure 4.1) shows that all the diffraction peaks can be indexed to hexagonal WS$_2$. All the peaks are sharp, as reported by other studies in the literature and in accordance with JCPDS data (Joint Committee on Powder Diffraction Standards). The (hk0) peaks give information on the arrangement of atoms in the basal plane, while the (00l) peaks show the structural organisation along the z axis [92]. The (002), (004) and (006) peaks have the highest intensity and are much stronger than expected from standards, due to the preferential orientation of the flat sheets in 2H-WS$_2$, as highlighted in Figure 4.2. In contrast to this, IF-WS$_2$ NPs were reported to have very broad peaks, especially (002) and (101), as a result of the nanometre size of the individual crystals in the NP structure and the imperfection of the layer stacking [92, 288].

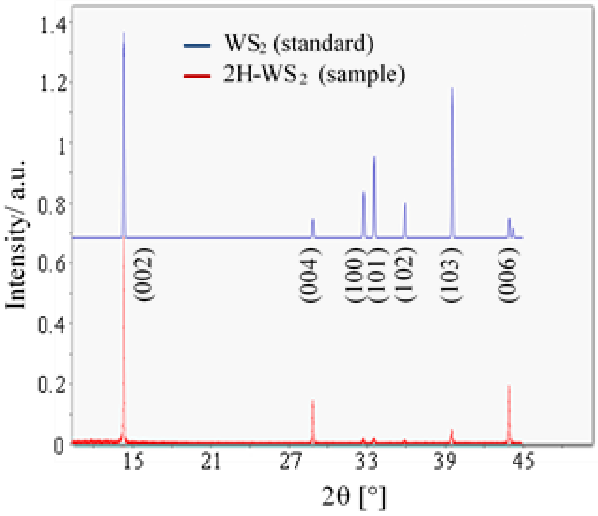

Figure 4.1 XRD diffraction pattern of 2H-WS$_2$ NPs [adapted from 287]

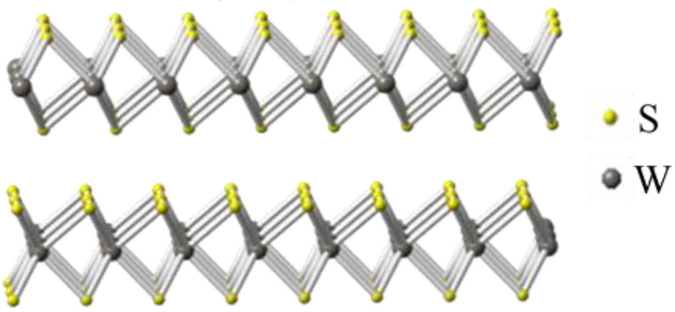

Figure 4.2 Structure and orientation of 2H-WS$_2$ layers [reproduced with permission from 287]

The Raman scattering spectrum for 2H-WS_2 is shown in Figure 4.3. Two signals are present at 355 and 419 cm^{-1}, consistent with other published values for the E^1_{2g} and A_{1g} bands [92, 162, 166, 288-290]. The A_{1g} peak represents the axial S–S vibration between two different layers (inset in Figure 4.3). The relative intensity of the A_{1g} peak suggests that this vibration energy is small and that the NPs therefore contain only a few stacked layers [289]. This can also be seen in the TEM images presented below.

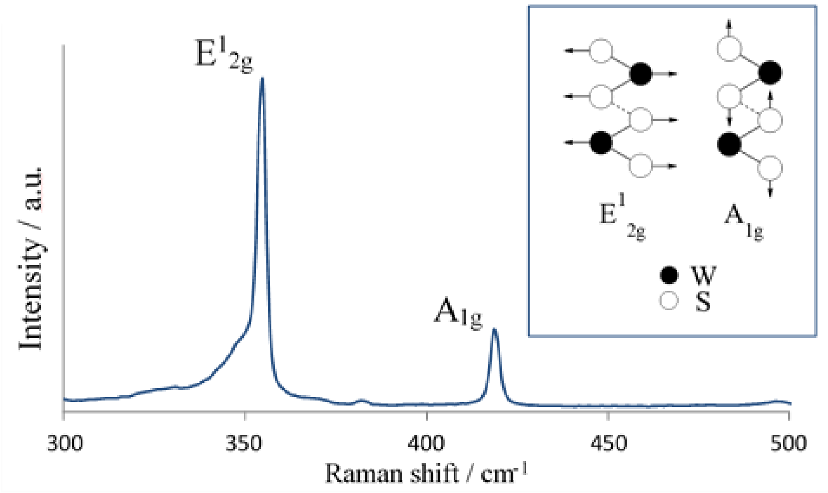

Figure 4.3 Raman spectrum of 2H-WS_2 NPs [adapted from 287]

The shape and morphology of the NPs were investigated using transmission electron microscopy. The low-magnification TEM images shown in Figure 4.4 (a) and (b) suggest the presence of two populations of 2H-WS_2 NPs of distinct morphologies: large, regular structures and small, irregular particles. The 90 nm size of the 2H-WS_2 given by the manufacturer is therefore an average of the two populations. This particular size distribution could be beneficial for tribological applications, conferring the nanoadditive the ability to penetrate contacts and fill asperity gaps of different sizes in order to limit the adhesion of contact surfaces and ultimately reduce friction.

The trigonal prismatic geometry of the 2H-WS_2 crystal structure is reflected in the triangular and hexagonal shapes of the large NPs (Figure 4.4 (c), (e) and (f)). Smaller NPs are irregular in shape, probably the result of fracture during the fabrication process (Figure 4.4 (g)). The layered structure can be seen in Figures 4.4 (d) and (h). The 2H-WS_2 NPs consist of a small number of individual sheets (7 layers can be seen in Figure 4.4 (h) and ~25 layers in Figure 4.4 (d)). The images are consistent with the results obtained from XRD and Raman analysis. The average interlayer spacing is ~0.63 nm, as noted in the literature [37, 38, 49, 169, 171, 255, 291]. Figure 4.4 (i) shows a HRTEM image of the hexagonal arrangement of atoms in a 2H-WS_2 individual sheet.

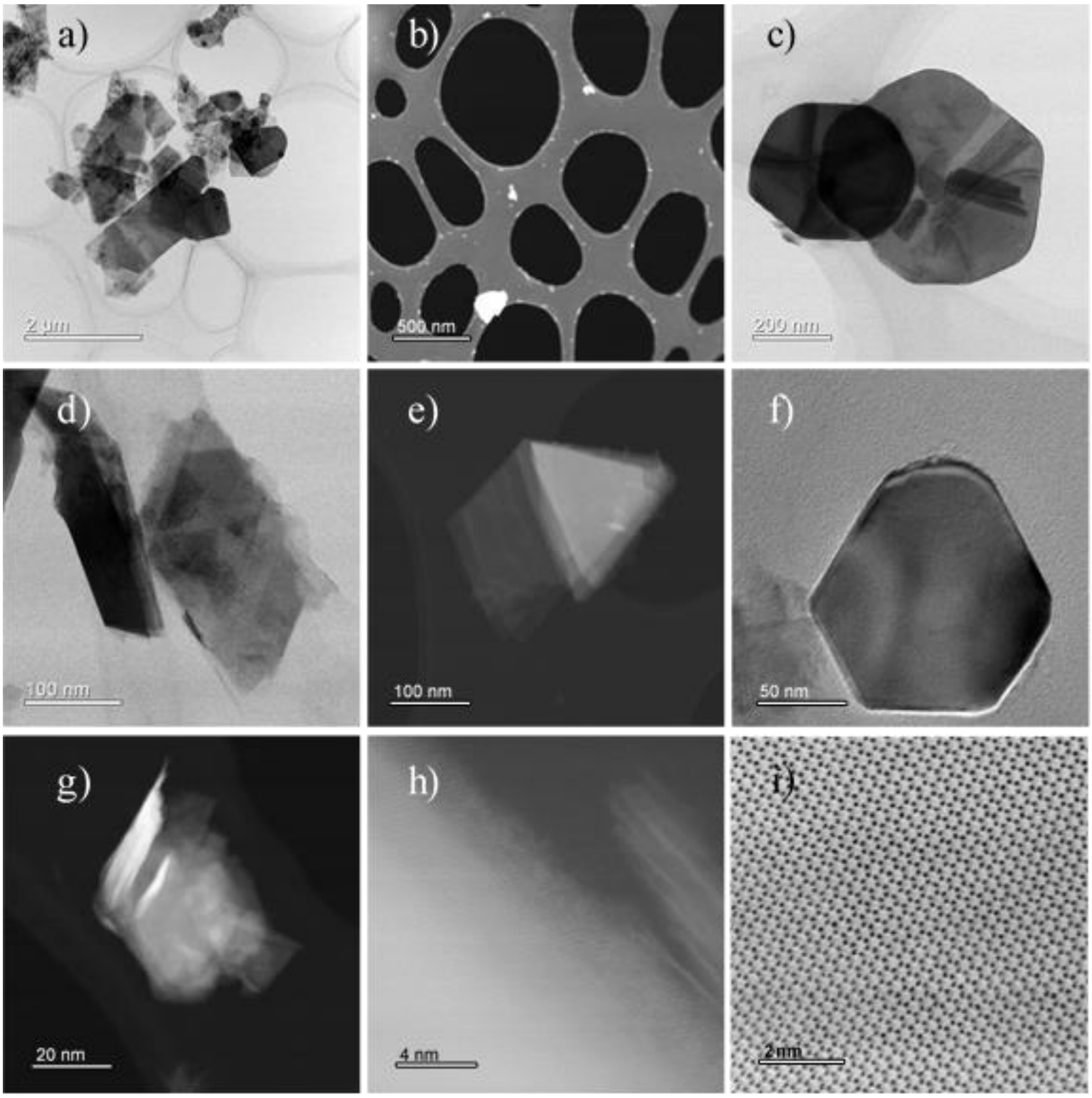

Figure 4.4 TEM images showing: a) and b) a general view of the two different 2H-WS_2 NP populations; c), d), e) and f) large 2H-WS_2 plate-like NPs; g) a small, irregular 2H-WS_2 NP; h) atomic structure of the 2H-WS_2 sheet and profile of a thin WS_2 NP with 7 layers and i) hexagonal arrangement of atoms in a 2H-WS_2 sheet

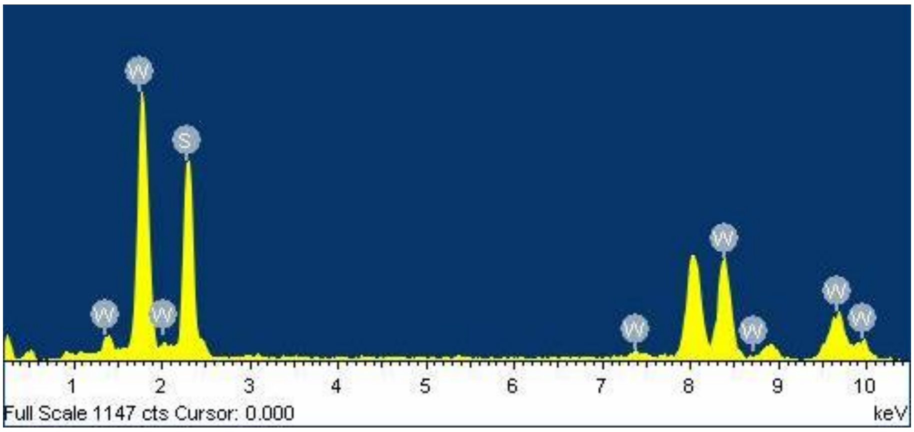

Figure 4.5 EDX analysis of 2H-WS_2 NPs [reproduced with permission from 287]

The EDX analysis of the 2H-WS_2 NP powder showed peaks corresponding to W and S (Figure 4.5), confirming the high purity of the sample. The unmarked peak at 0.28 keV is C, while the peaks at 0.93, 8.04 and 8.9 keV are Cu, both present in the TEM carbon copper grids.

The size distribution of the 2H-WS_2 NPs dispersed in PAO was measured with the Malvern Zetasizer immediately after preparation. The intensity distribution shows two narrow peaks, which confirms the presence of two distinct NP size populations: one with an average size of 30-40 nm and the other of approximately 250 nm (Figure 4.6 shows two separate experiments). These results are in agreement with the TEM images discussed above.

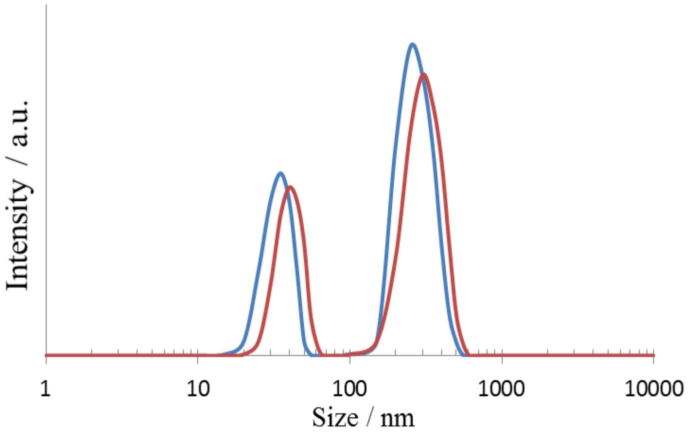

Figure 4.6 Size distribution of the 2H-WS_2 NPs showing the two distinct populations [reproduced with permission from 287]

4.3 The tribological properties of 2H-WS_2 NP dispersions in PAO base oil

The tribological tests were performed in the MTM2-SLIM rig in three alternative stages repeated at fixed intervals: '*conditioning phase*', '*Stribeck curve acquisition*' and '*tribofilm measurement*', as described in Section 3.3. Table 4.1 summarizes the conditions used for the MTM2-SLIM tests presented in this chapter.

Figures 4.7 and 4.8 present the Stribeck curves for 2H-WS_2 NP dispersions in PAO. The experiments were carried out under similar conditions, at 40 and 100ºC and three hours in the '*conditioning phase*' at 100 mm/s. The curves illustrate the dynamics of tribofilm growth/removal with time (following various conditioning periods) throughout the mixed and boundary lubrication regimes.

Table 4.1 MTM2 – SLIM test conditions

Conditioning phase	
Temperature	40°C, 100°C
Load	30 N
Hertzian pressure	0.94 GPa
Entrainment speed	0.1 m/s
Slide-roll ratio	150 %
Stribeck curve phase	
Temperature	40°C, 100°C
Load	30 N
Hertzian pressure	0.94 GPa
Entrainment speed	1.5 to 0.01 m/s
Slide-roll ratio	150 %

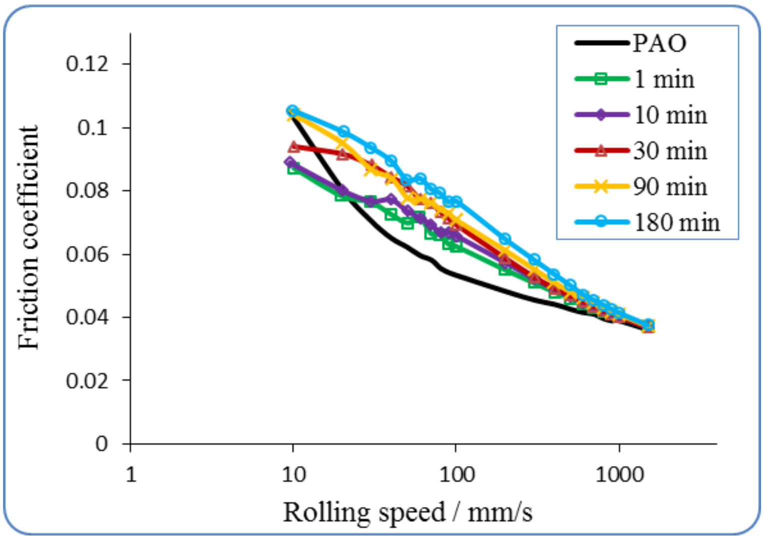

Figure 4.7 Stribeck curves for 1 % w/w 2H-WS_2 NPs in PAO at 40ºC [adapted from 287]

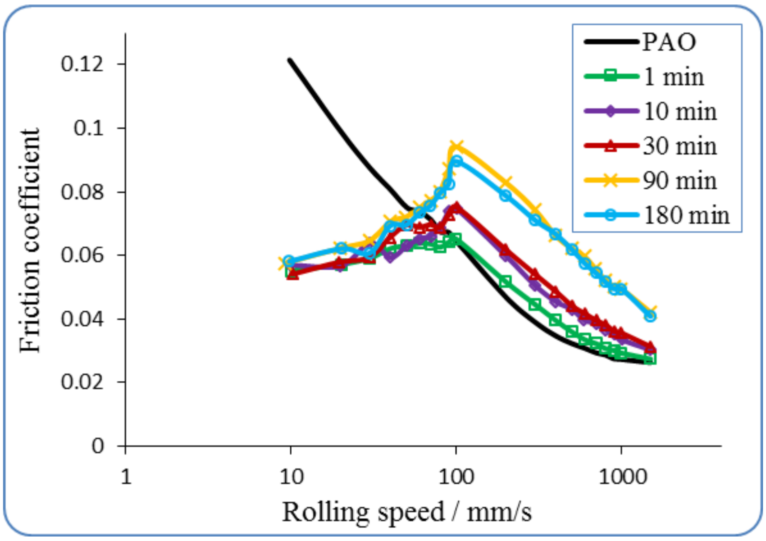

Figure 4.8 Stribeck curves for 1 % w/w 2H-WS_2 NPs in PAO at 100ºC [adapted from 287]

The Stribeck curves at 40ºC (Figure 4.7) show a linear increase in friction with decreasing speed. The boundary COF increased constantly from 0.09 (1 minute) to 0.11 (180 minutes). The Stribeck curves are also relatively stable with time.

At 100ºC (Figure 4.8) all the Stribeck curves show a similar pattern throughout the test: they reach a peak COF value at the onset of the mixed lubrication regime (~100 mm/s), followed by a sharp and constant decrease all the way into the boundary regime. However, as the test progressed, the Stribeck curves shifted upward towards higher values of COF. The highest COF value (0.09) was reached after 90 minutes and remained constant until the end of the test. This type of behaviour has been previously reported for ZDDP antiwear additives tested under similar conditions, when a rough, high-friction tribofilm of considerable thickness formed on the wear track [275]. However, the sharp decrease in the COF values to 0.05-0.06 at low rolling speeds early in the experiment and the persistence at this value for the rest of the test is reminiscent of the behaviour of some of the most efficient friction modifiers [22].

The experiments showed that 2H-WS_2 NP dispersions were most efficient at higher temperatures (100ºC), giving large differences in friction compared to the base oil.

The specific film thickness (**λ**) values calculated for the conditions in the present experiment are ~2 for a speed of 1200 mm/s, ~1 for 400 mm/s and ~0.1 for 10 mm/s. These values should show the Stribeck curve from the onset of mixed lubrication (for the highest speed) and well into the boundary regime (for the lowest speeds). However, the shape of the Stribeck curve for the base oil indicates that the rig operates mostly in mixed lubrication conditions, reaching boundary lubrication only for the lowest speeds (below 10 mm/s).

The relationship between **λ** and the lubrication regimes is empirical and is determined by experimental data. Recent studies suggest that the limit for the boundary regime for counter-formal contacts is difficult to define and depends on surface roughness and the rheological properties of the lubricant. This can be explained by the micro-EHL theory, which also considers the possibility of the elastic deformation of individual asperities [1, 2, 46-48].

4.4 Characterization of tribofilms generated by 2H-WS$_2$ nanoadditives in PAO

4.4.1 Physical properties

The striking difference shown by the Stribeck curves of the 2H-WS$_2$ NP dispersions at the two test temperatures suggests that their mechanism of action is different in each case and that temperature plays a key role. The tribofilms generated by the 2H-WS$_2$ NP dispersions in PAO (which grow unhindered by the base oil) were therefore further analysed in order to understand the influence of temperature on the tribofilm generation. The physical characteristics of the wear tracks were observed using optical microscopy, Alicona profilometry and 3D SLIM interference.

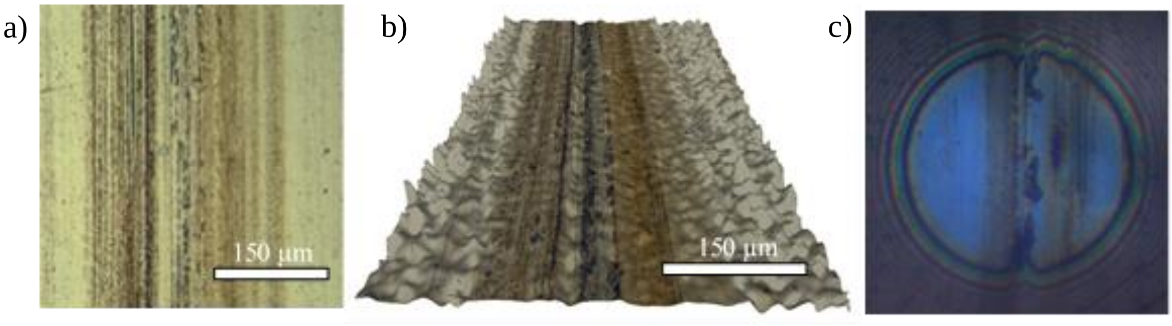

Figure 4.9 Images of the tribofilm generated at 40ºC after the 3 h conditioning time. (a) Optical image of the wear track on the disc. (b) Alicona 3D optical image of the tribofilm on the disc. (c) 3D SLIM interference image of the tribofilm on the ball [reproduced with permission from 287]

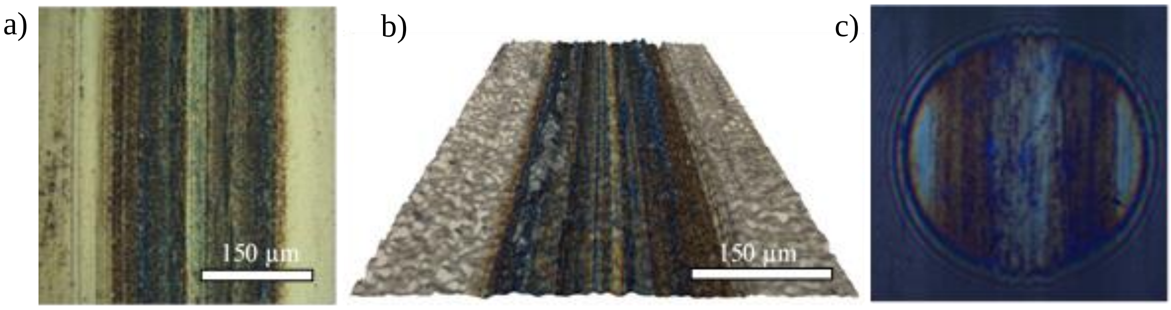

Figure 4.10 Images of the tribofilm generated at 100ºC after the 3 h conditioning time. (a) Optical image of the wear track on the disc. (b) Alicona 3D optical image of the tribofilm on the disc. (c) 3D SLIM interference image of the tribofilm on the ball [reproduced with permission from 287]

Figures 4.9 and 4.10 show images of the ball and disc wear tracks obtained with the 2H-WS$_2$ NP dispersions in PAO at 40 and 100ºC. Thickness profiles of the wear tracks were measured after the tests with the Alicona Infinite Focus profilometer, at 20x magnification. The SLIM images are shown only after the entire duration of the tribological tests and after washing with solvent, as the 2H-WS_2 NPs agglomerate and adhere onto the glass window, obstructing the imaging of the contact during the test.

As seen in Figure 4.11, the variation of the tribofilm thickness is significant across the wear track due to the patchy nature of the film. However, the film thickness was calculated as an average of profiles measured at different positions on the disc and on separate samples and the results are shown in Table 4.2.

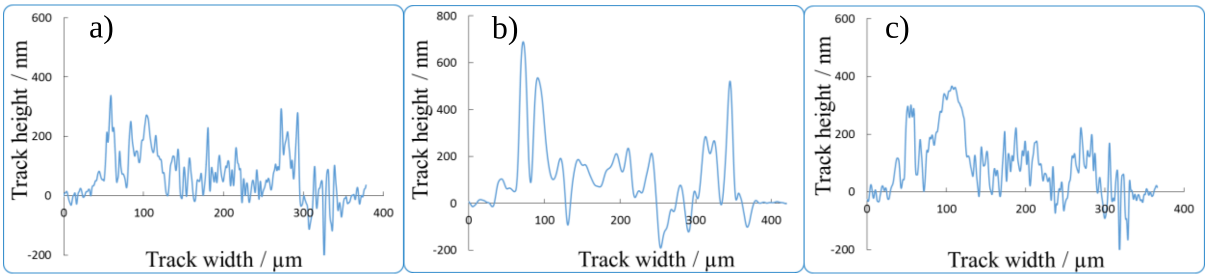

Figure 4.11 Examples of profiles across the tribofilm generated by 2H-WS_2 NPs in PAO at 100°C, measured with the Alicona after the 3 h test

Table 4.2 Average film thickness measured using Alicona profilometry and SLIM

	Measured values of tribofilm thickness and standard error (nm)	
	40°C	100°C
Alicona	37 ± 12	109 ± 10
SLIM	26 ± 10	98 ± 7

The wear track generated at 40ºC (Figure 4.13) showed a thin, patchy tribofilm (with an average height of ~30 nm), which displayed many local NP agglomerations. A more consistent tribofilm with an average film thickness of ~100 nm was generated at 100ºC. The calculated average height of the tribofilms measured with SLIM on the MTM balls and Alicona on the MTM discs were similar. The slightly lower thickness values measured *in situ* with the SLIM system can be a result of the tip asperities being flattened under the high contact pressure.

4.4.2 Chemical composition

Wide XPS spectra were recorded on the samples (from 0 to 1500 eV), along with high-resolution narrow spectra on regions where each element has a characteristic signal (i.e. the 4f orbital for W at 25-45 eV etc.). On the wear track generated at 40°C, the XPS analysis was performed on an area with fewer NP agglomerations. The results (Table 4.3) show small quantities of tungsten and sulphur on the surface of the wear track (before ion sputtering). The position of the signals indicates that W is in the form of W^{6+} (in WO_3, tungsten trioxide), and that S is found as iron sulphide. These indicate that a reaction has started to take place between the steel substrate and the NPs, but the temperature was unfavourable. After ion sputtering, only iron, oxygen and carbon were detected (most likely from iron oxides and oxidized residues of oil molecules) in all of the recorded spectra. Therefore, the film thickness must be very small, as confirmed by Alicona and SLIM results. XPS analysis was also performed outside of the wear track, but only Fe, O and C were detected.

Table 4.3 XPS results: composition of the tribofilm (40°C) before ion sputtering

	W 4f	**S 2p**	**Fe 2p**	**O 1s**	**C 1s**
Composition (%)	0.1	1.1	26	37.1	35.7

Figure 4.12 shows the XPS wide spectrum of the thick tribofilm formed by 2H-WS_2 at 100°C. As expected, tungsten and sulphur are present, as they compose the NPs. Iron, copper, manganese, chromium (masked by Cu at 574 eV) and carbon are found as part of the steel substrate and oxygen is present as metal oxides. The carbon and oxygen signals can also be due to the oxidation of the oil. The energy of the signals was compared to literature data [292].

The chemical composition of the tribofilm is presented in Figure 4.13, as detected by XPS – this analysis is *quantitative* and represents the real chemical composition of the tribofilm. Comparing the abundance of tungsten from the XPS analysis with profilometry thickness measurements, the sputtering process can be related to the tribofilm thickness: the final depth was 3500 s, equivalent to approximately 200 nm. However, the rate of the sputtering process is expected to be nonlinear due to the varying chemical composition of the film and the thickness of different layers cannot be accurately determined and thus can only be approximated.

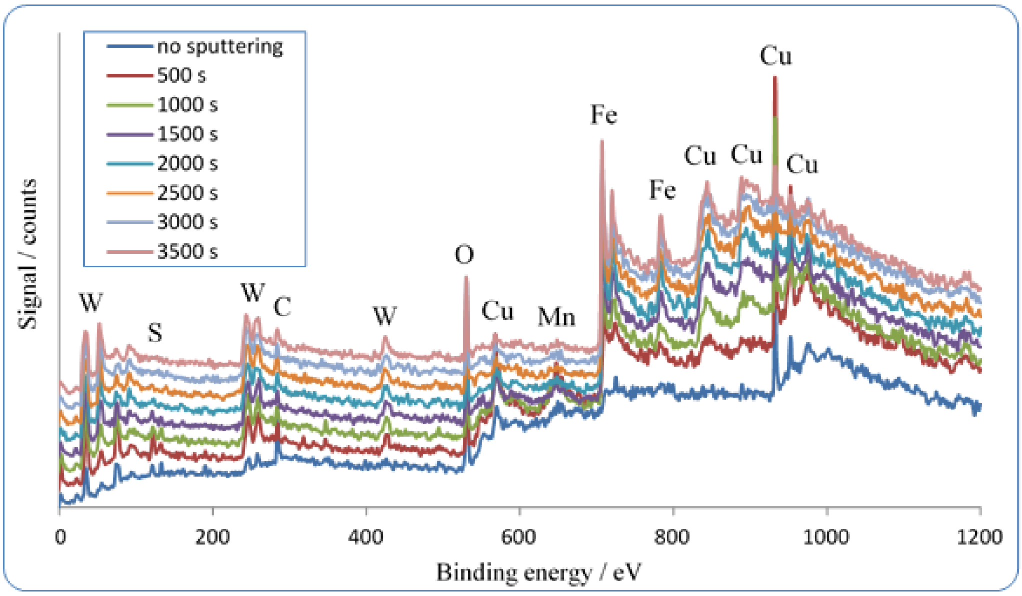

Figure 4.12 XPS spectra of the tribofilm formed at 100ºC

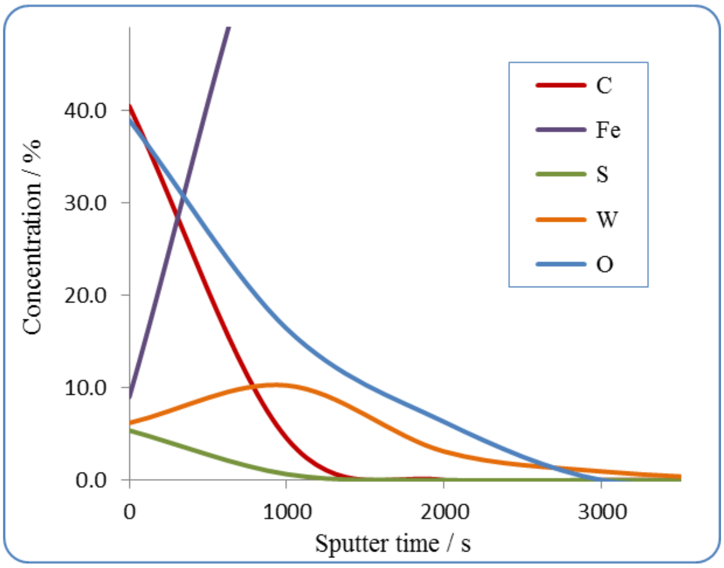

Figure 4.13 XPS results: composition of the tribofilm formed at 100°C [adapted from 287]

A large amount of W is present throughout the depth of the tribofilm. Sulphur is also present in the top layer (an estimated top 50 nm, if the sputtering process is considered linear), as part of unreacted 2H-WS_2 NPs and iron sulphides. Iron is in the form of iron sulphides and oxides (near the surface) and elemental iron. The oxidation state of the elements can be verified by analysing the narrow XPS spectra.

The narrow spectra for W are shown in Figure 4.14 (a). The W 4f signal appears as a doublet (i.e. two separate peaks with proportional intensities: 4f 7/2 and 4f 5/2) with an energy gap of ~2.15 eV. The position of the signal is a direct indication of the chemical state of the element. For tungsten, W^0 (elemental W) is expected at ~31 eV, W^{4+} (in WS_2) at ~33 eV and W^{6+} (in WO_3) at ~35.5 eV [67, 92, 292, 293].

The main signals recorded in the sample are for W^{6+}, specific to WO_3 (35.6 eV), and for W^0 (31.2 eV). The only exception was in the top layer (before sputtering), where W^0 was found at 31.5 eV. The shift of ~0.3 eV between the non-sputtered and sputtered layers is generally due to a slight energy loss of the electrons coming through the carbon contamination layer on top. The consistent presence of WO_3 in the various layers of the tribofilm is an indication of the chemical reaction between the 2H-WS_2 NPs with the steel substrate, with the generation of WO_3 and various iron oxides and sulphides. The quantification of the XPS narrow spectra is performed by fitting the recorded signals with theoretical curves and integrating the area under the fitted curves, as shown in the example in Figure 4.14 (b). The atomic W^0/W^{6+} ratio at the top of the tribofilm (before sputtering) is ~ 2, and increases to ~4.5 at the interface with the steel substrate, indicating an increasing relative concentration of elemental tungsten in the deeper layers of the tribofilm.

Figure 4.14 (c) shows the XPS signal measured for iron. The Fe 2p signal appears as a doublet, 2p 3/2 and 2p 1/2, with an area ratio of 2:1 and 13.1 eV energy gap. Fe^0 is expected at ~707 eV and Fe^{2+}/Fe^{3+} species (oxides, sulphides etc.) are normally found at higher values. In the present sample signals were recorded for Fe^0 at 707.3 and 720.4 eV at the top of the tribofilm and at 706.9 and 720 eV after sputtering. The presence of oxides/sulphides was only observed at the top of the wear track.

Aside from Fe^0, iron has a complex signal and the spectra are usually difficult to fit. As shown in Figure 4.14 (d), fitting was performed for Fe 2p 3/2 by considering all Fe^{2+}/Fe^{3+} contributions into a single signal at 709.9 eV. An additional signal was added at 715 eV. This ‘Fe(II) satellite’ is a specific signal due to a degree of covalence in Fe^{2+} compounds. A ‘Fe(III) satellite’ could also be present at ~720 eV, but this is difficult to state due to the overlapping with the Fe^0 2p 1/2 signal. The spectrum indicates that the surface of the tribofilm contains little elemental iron compared to the oxide/sulphide species (~1:11). However, the deeper parts of the tribofilm contain iron exclusively in its elemental form (Fe^0).

Figures 4.14 (e) and (f) show the S 2p signal, which appears as a doublet at 161.9 and 163.1 ($\Delta E = 1.2$ eV). Sulphur is found in relatively large amounts in the top layer of the tribofilm (~13 %) and in very small quantities (~2 %) at a depth of an estimated ~50 nm. In the lower levels of the tribofilm sulphur was not detected. The position of the signal indicates that S is in the form of sulphides, while the lack of a visible W^{4+} signal corresponding to WS_2 in Figures (a) and (b) implies that they must be iron sulphides (as shown by the Fe 2p signal in Figures 4.14 (c) and (d)). Such compounds should be formed by the chemical reaction of 2H-WS_2 NPs with the metal substrate.

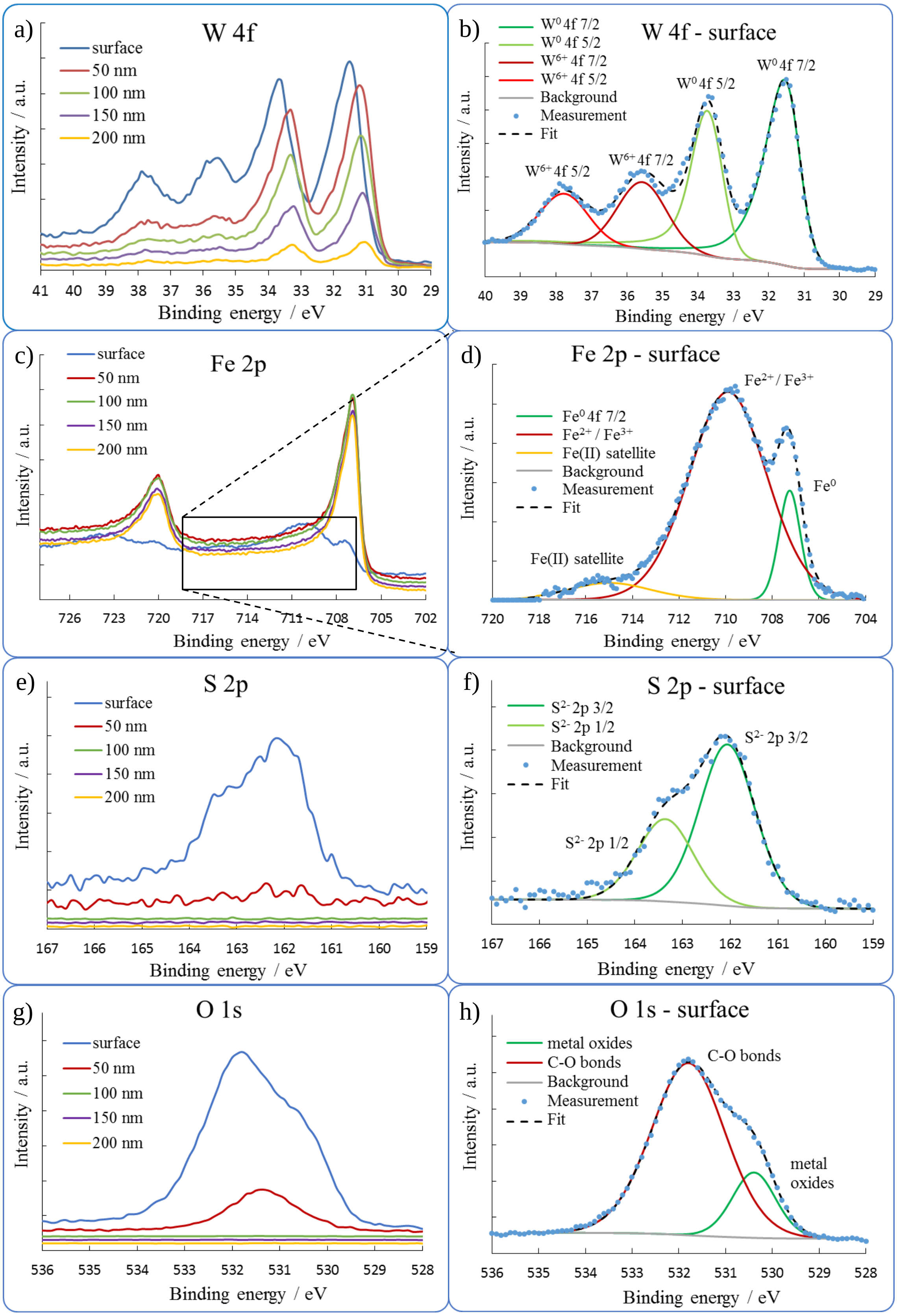

Figure 4.14 a) XPS depth profiling narrow spectra and CasaXPS fitting for the signal measured at the surface of the tribofilm for a)/ b) W 4f [adapted from 287], c)/d) Fe 2p, e)/f) S 2p and g)/h) O 1s energy regions

Oxygen was found in the top ~100 nm of the films, as seen in Figure 4.14 (g). The signals recorded at the surface (Figure 4.14 (h)) were assigned to metal oxides (530.5 eV) and a large contribution from C-O bonds from oxidized oil molecules (531.7 eV).

From the XPS results of the tribofilms generated at the two temperatures (but otherwise under similar testing conditions), it is again evident that the temperature plays a major role in the mechanism of action of the 2H-WS_2 NPs, with higher temperatures promoting the chemical reaction with the steel substrate and generation of larger quantities of reaction products, which form the tribofilm.

XPS was performed outside of the wear track but only Fe, O and C were found. This demonstrates that the tribofilm is only generated on the wear track and that apart from temperature, it requires high pressure and shear (high SRR) to form.

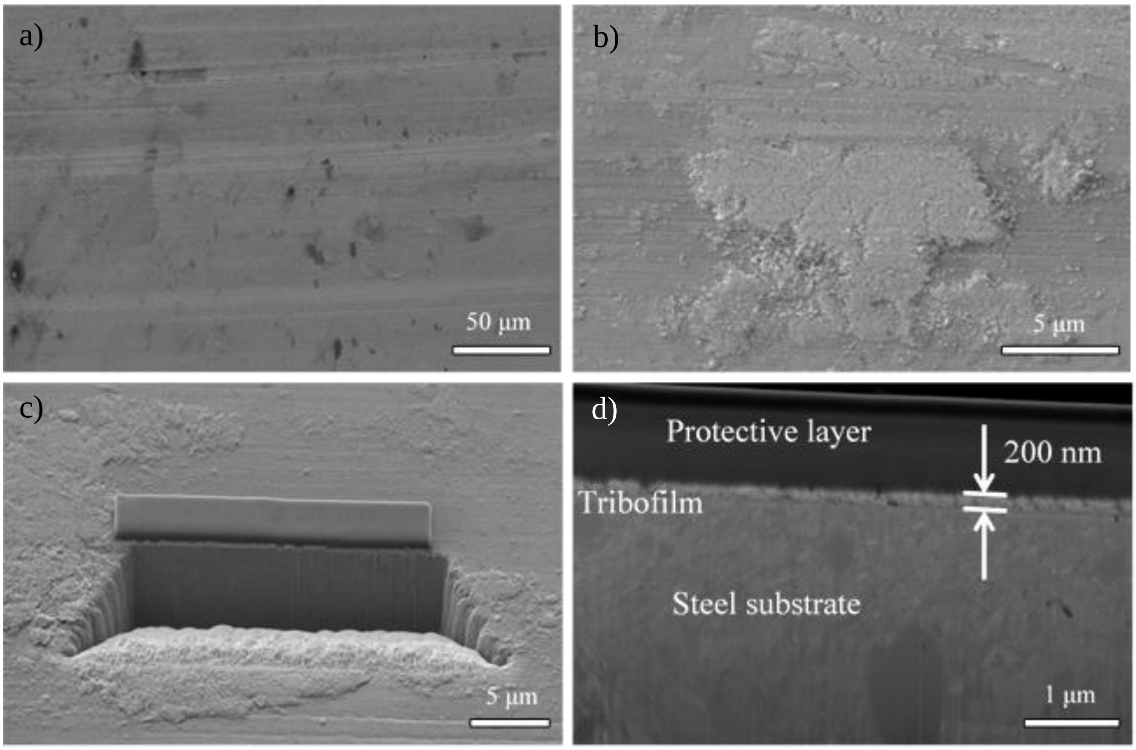

Figure 4.15 (a) SEM image of the wear track generated at 40ºC, displaying a few NP agglomerations; (b) SEM image of the wear track generated at 100ºC, covered by a tribofilm; (c) SEM image during the analysis of wear track generated at 100ºC; (d) Profile view of the tribofilm formed by the NP dispersion on the track at 100ºC [reproduced with permission from 287]

Additional information about the thickness, morphology and chemistry of the tribofilms generated under the two temperature conditions were obtained using FIB/SIMS analysis (Figure 4.15). The wear track generated at 40ºC showed many non-uniformly distributed deposits of NPs (Figure 4.15 (a)). The wear track generated at 100ºC was imaged in a thicker region than average and Figure 4.15 (b) shows large typical patches on the wear track. In this specific position, the track was uniformly covered by a chemically formed tribofilm 200 nm thick, as highlighted in Figure 4.15 (d). A layer of carbon was deposited on the wear track to protect the surface of the film during the sputtering process (Figure 4.15 (c)).

Secondary ion mass spectroscopy (SIMS) was also employed to reveal the chemical composition of the tribofilms and to map its layers. Figure 4.16 presents the mass spectra recorded on the surface of the tribofilm.

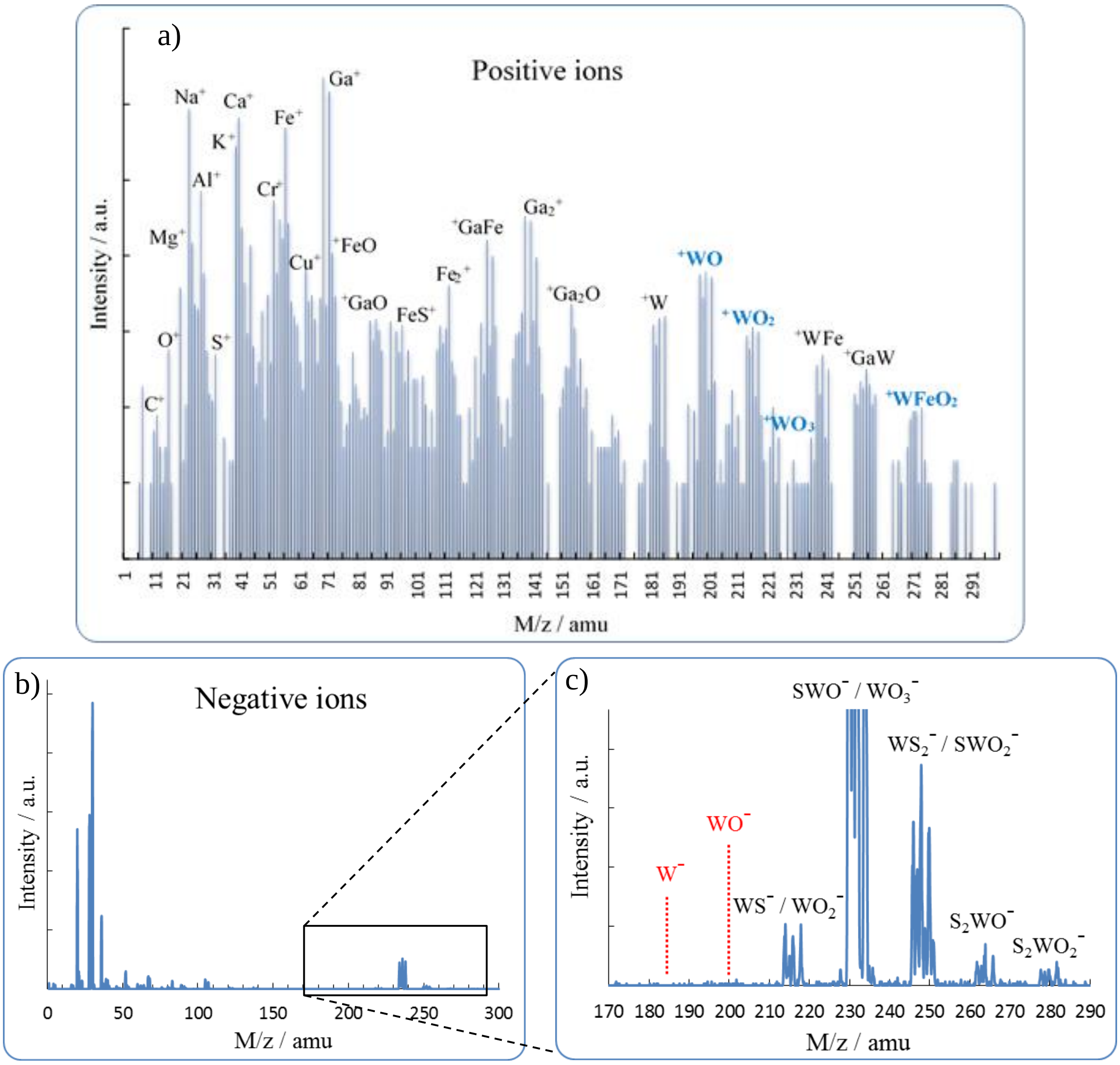

Figure 4.16 SIMS spectra of the tribofilm generated by 2H-WS₂ NPs in PAO at 100ºC, showing a) positive, b) and c) negative ions/fragments sputtered from the disc sample

The positive ions recorded during the analysis are shown in Figure 4.16 (a). Aside from Ga (from the ion beam), O, Na, Mg, Al, K, Ca, Cu and Zn (from impurities, most likely as contaminating salts on the surface), the metal substrate and the tribofilm contain Fe, C, Cr, Mn, Si, S, P (elements in the steel) and W (from the NPs). Most of the other signals result from the combinations of two or more metallic atoms and are not labelled.

Some elements have more than one signal due to their isotopic composition. The atomic mass of elemental isotopes can be found in literature databases [294, 295]. The most interesting features to observe are the signals for tungsten oxides, visible at 198-202 (^{+}WO), 214-218 ($^{+}WO_2$), 230-234 ($^{+}WO_3$) and 270-274 ($^{+}WFeO_2$) m/z, attesting the reaction of 2H-WS_2 NPs with the substrate and the generation of oxide species in the contact. The relatively low intensity of $^{+}WO_3$ is probably due to the fact that such fragments are less likely to have a positive charge.

Figures 4.16 (b) and (c) show the negative ions sputtered from the sample. W^- and WO^- are not visible because these fragments are likely to carry a positive charge. However, there are signals at regular atomic mass unit (amu) intervals corresponding to W atoms bound to various numbers of S and O atoms (the most likely fragments are displayed in the figure). These are indicating a chemical reaction in the contact.

The SIMS depth profiling of the tribofilm generated at 100ºC (Figure 4.17) monitored the variation in the chemical composition of different layers as the ion beam removes material from the sample. Due to the fact that the analysis has varying sensitivity to different chemical elements and that only a part of the ejected material is analysed (only the positive/negative ions in each case), the technique is considered to be *qualitative*. Therefore, a direct correlation between the sputtering time and the tribofilm thickness cannot be made.

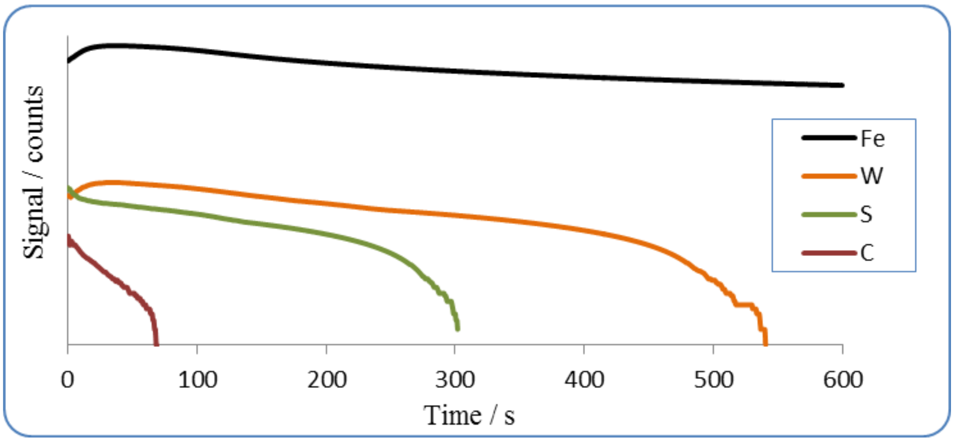

Figure 4.17 SIMS depth profile of the tribofilm generated at 100ºC [reproduced with permission from 287]

Similar to the XPS results, the most important information offered by the SIMS data is the layer arrangement. The tribofilm was found to contain tungsten below a sulphur rich layer. This arrangement suggests that the upper part of the tribofilm can contain tungsten and iron sulphides, while the interface with the steel is only composed of tungsten and iron, in their oxide and elemental states. However, due to the qualitative nature of the technique, it is difficult to assess the thickness of the different layers.

The chemical analysis of the tribofilm generated at 100ºC confirms the mechanism of action initially indicated by the imaging and the tribological tests. The tribofilm was generated through a chemical reaction between the 2H-WS_2 NPs and the steel substrate at high temperatures. A similar mechanism of action is also known to occur in the case of antiwear (e.g. ZDDP) or extreme pressure additives [275].

The XPS and SIMS results of the tribofilm generated at 100ºC indicate that it is likely to be formed of several layers as illustrated in Figure 4.18:

- carbon impurities and unreacted sheets of 2H-WS_2 on the top surface
- a layer of WO_3, iron oxides and sulphides, elemental Fe and W
- a layer WO_3, elemental Fe and W
- a layer of elemental Fe and W

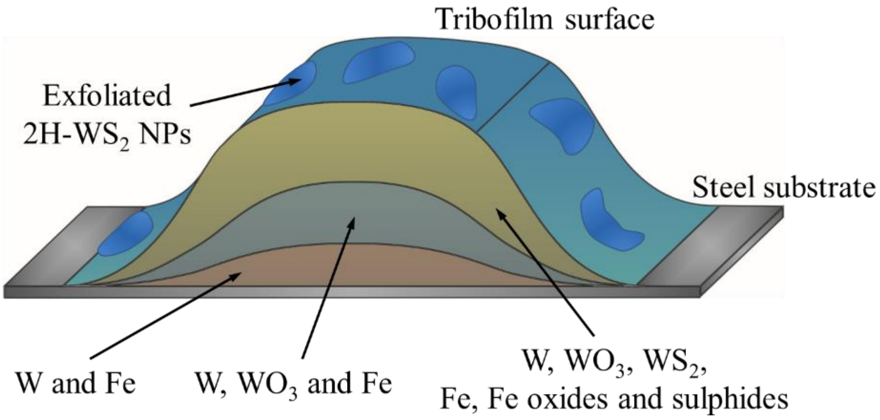

Figure 4.18 Likely composition of the tribofilm generated at 100ºC
[adapted from 287]

4.4.3 Mechanical properties

To investigate the mechanical properties of the tribofilm, nanoindentation tests were performed inside and outside the wear track for comparative purposes. As shown in Figure 4.19, the analysis was started from outside the tribofilm (wear track), moving towards its centre as follows:

- ✓ section (1) – steel
- ✓ section (2) – chemically formed tribofilm

- ✓ section (3) – chemically formed tribofilm covered in a thick layer of unreacted, squashed 2H-WS_2 NPs
- ✓ section (4) – chemically formed tribofilm with a few NPs

The Berkovich hardness (H) and reduced Young's modulus (E') results with their respective standard deviation (SD) for the measurements are presented in Table 4.4. According to data from published literature, to avoid the effects of the substrate on the determination of thin film mechanical properties, the depth of nanoindentation should be a maximum of 10 % of its thickness when measuring the reduced Young modulus and 20 % when measuring hardness [296]. The depth of the indentations in this experiment was 20 nm and the measurements were performed on the thickest part of the tribofilm (~ 200 nm thick). Therefore, the depth of indentation in this study is ~10 % of the measured tribofilm thickness, which indicates that the results should not be affected by the substrate.

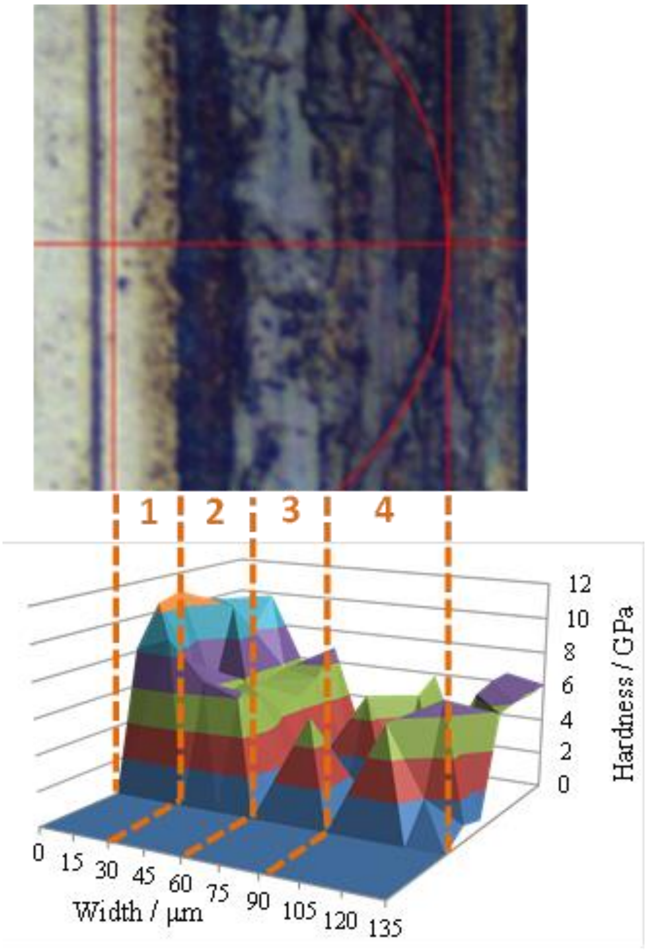

Figure 4.19 Map of nanoindented sections of the tribofilm (points are 15 µm apart) [reproduced with permission from 287]

Table 4.4 Measured values for H and E' in the four sections of the tribofilm

Section		Parameters measured (GPa)			
		H	SD	E'	SD
1	Steel	8.9	1.6	192.5	17.3
2	Tribofilm	5.7	0.7	165.5	17.1
3	Tribofilm fully covered with NPs	1.9	1.9	92.4	45.8
4	Tribofilm with a few NPs	4.5	2.5	132	50

Sections 2, 3 and 4 of the tribofilm show different parameter values. In section 3 and 4 they also have a high standard deviation because, as shown in Figure 4.19, the tests were performed on the chemically reacted layers covered with NPs.

Results indicate that the mechanical properties of the tribofilm are inferior to those exhibited by the steel substrate (i.e. it is softer). This behaviour is typical for an AW/EP additive, whose role is to generate a sacrificial film with a low shear strength that is worn away slowly over time in a tribological contact, protecting the metal surface and inducing a controlled wear rate.

Nanoindentation was performed on the thickest part of the tribofilm, where the measured chemical tribofilm was approximately 200 nm, in order to reduce the influence of the steel substrate. The average thickness of the unreacted NP layer found on top of the chemical tribofilm was measured with the Alicona Infinite Focus to be ~250 nm. Therefore, the indentation in section 3 is carried out only through the NPs layer and was not influenced by the chemically formed tribofilm. Figure 4.20 shows an Alicona 3D profile across the track, measured at 100x magnification (the height axis is magnified 20 times for better viewing).

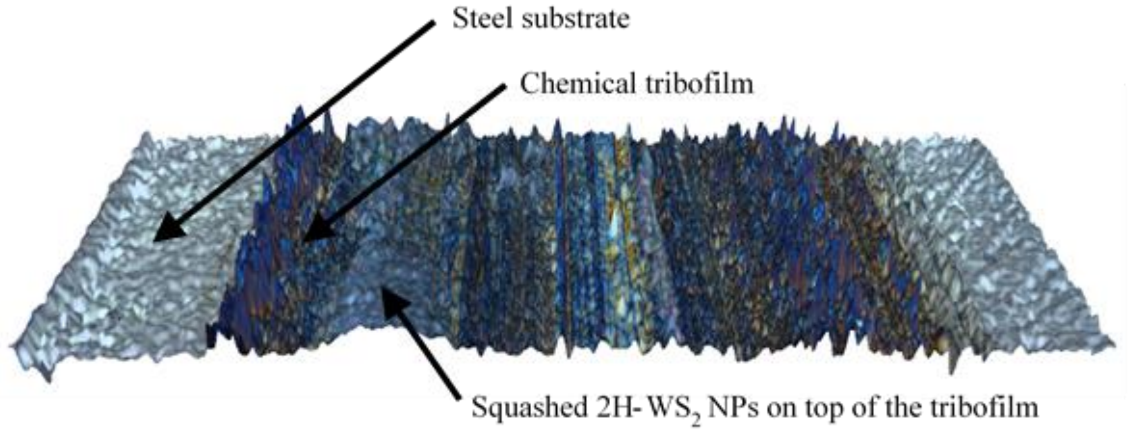

Figure 4.20 Alicona profile view across the tribofilm
[reproduced with permission from 287]

The measured hardness of the steel substrate is higher than the expected 750-770 HV, which is equivalent to ~7.5 GPa. Several factors may be responsible for these H values, such as the difference between the Vickers and Berkovich indenter geometries, the indenter size versus the surface roughness, possible work hardening of the substrate or the fact that nanoindentation is a surface technique, as opposed to the Vickers hardness test, which measures bulk hardness.

The chemical tribofilm and the squashed NPs have very characteristic mechanical properties (i.e. very small H and E' for WS_2 NPs and larger for the tribofilm). Although the values for H and E' were initially presented as averages for the four sections, they can also be separated based on their distinctive values. Table 4.5 shows the individual mechanical properties of the tribofilm and NP agglomerations on the wear track.

Table 4.5 H and E' values for the chemical tribofilm and squashed 2H-WS_2 NPs

	H (GPa)	E' (GPa)
Tribofilm	5.8 ± 0.6	165.7 ± 19.4
Squashed NPs	1 ± 0.4	72.7 ± 24.8

Representative force-distance curves measured during manoindentation are shown in Figure 4.21. The behaviour of the squashed layer of 2H-WS_2 NPs under loading is markedly different. During the 10 s dwell time at the maximum load, the soft NPs structure was penetrated to a large depth (i.e. exhibited creep).

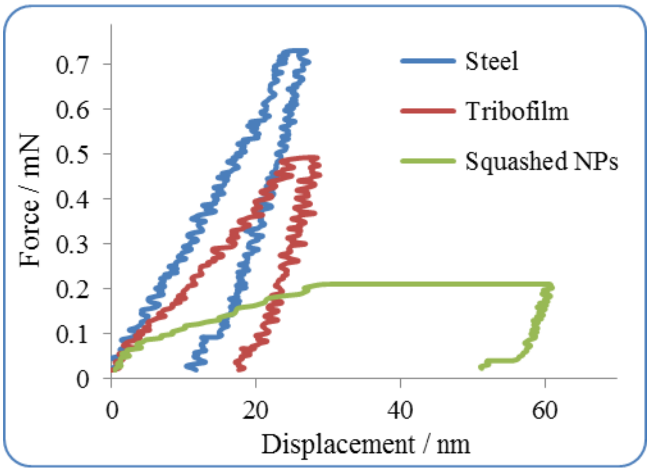

Figure 4.21 Loading/unloading hysteresis on the three different types of substrate [reproduced with permission from 287]

The hardness and reduced Young's modulus of the 2H-WS_2 tribofilm are higher than other reported values for tribofilms generated by other oil additives (H = 5 GPa and E' = 110 GPa for the AW ZDDP [297], H = 0.4 GPa and E' = 10 GPa for the FM MoDTC

[106]). These values indicate that the presence of tungsten in tribofilms improves their mechanical properties, which is expected to improve the antiwear behaviour. The antiwear properties of the 2H-WS_2 NP dispersions are compared to those of ZDDP additized oils in Chapter 5.

4.5 Influence of base oil on the tribological performance of 2H-WS_2 NPs

The chemistry of the base oil is an important factor that influences the behaviour (adsorption/reaction) of the additives in the lubricated contact. Boundary additives such as 2H-WS_2 are attracted to the polar steel surfaces, where they adhere and react on the wear track to form a tribofilm.

Base oils as carriers of boundary additives can be of a variety of polarities, ranging from nonpolar (PAOs), to oils with some polarity (mineral oils) and very polar oils (PPGs, esters etc.). Oils of high polarity can also be attracted to the lubricated contact and in this way compete with the boundary additives for adsorption/reaction. To test how the polarity of the base oil can influence the ability of nanoadditives to interact (adhere/react) with the wear track and build a tribofilm, 2H-WS_2 NPs were also dispersed in a polar base oil (PPG) and their friction performance was measured at 40 ºC and 100ºC.

Figures 4.22 and 4.24 show the variation of the COF with speed (Stribeck curves) for 2H-WS_2 NP dispersions in PPG at 40 and 100ºC, during three hours of running in the '*conditioning phase*' at 100 mm/s (in the mixed lubrication regime).

The Stribeck curves for the dispersion tested at 40ºC (Figure 4.22) show a similar pattern to the base oil. An almost linear increase in friction with decreasing speed in all the lubrication regimes is recorded throughout the 3 h conditioning. The boundary COF varied between 0.11 and 0.12. The values are only slightly higher than those for pure PPG (0.11), indicating that 2H-WS_2 NPs have little efficiency at 40ºC. A small increase in friction is seen with conditioning over longer periods (90 and 180 minutes). This can be explained by tribofilm formation.

Figure 4.23 shows an optical image of the disc wear track and an interferometry image of the ball wear track, obtained after the test conducted in PPG at 40ºC. Many 2H-WS_2 NP agglomerates can be seen on the thin tribofilm formed on the disc wear track. A similar situation was expected to take place on the ball wear track, but acquiring the SLIM images required the cleaning of both the ball and glass window prior to the measurement.

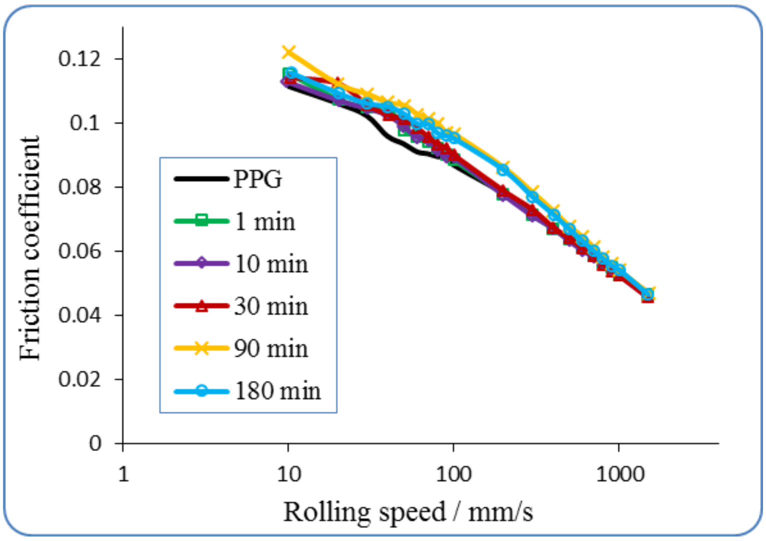

Figure 4.22 Stribeck curves for 2H-WS$_2$ NPs in PPG at 40ºC

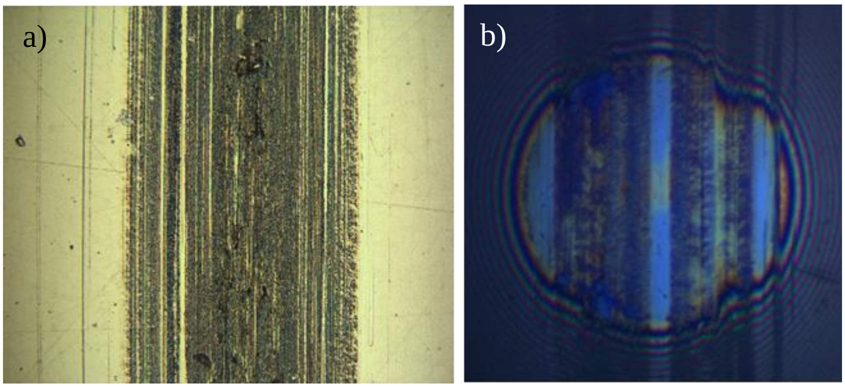

Figure 4.23 Images of the tribofilm generated at 40ºC after the 3 h conditioning time. (a) Optical image of the wear track on the disc, (b) 3D SLIM interference image of the tribofilm on the ball

At 100ºC (Figure 4.24), 2H-WS$_2$ dispersions in PPG show a similar pattern to the PAO dispersions. The COF generated by 2H-WS$_2$ fluctuates between 0.07 and 0.09 in the boundary regime, as opposed to 0.07 for pure PPG. In the mixed regime, the Stribeck curves gradually move towards a higher COF in the first 30 minutes, a behaviour reminiscent of EP additives, which react with the metal substrate to form a sacrificial antiwear tribofilm with high friction characteristics. For the rest of the test (30-180 min) the COF decreases, an indication that the film is becoming smoother/thinner and that the chemical reaction with the steel may not be fast enough to sustain a thick, stable tribofilm.

The irregular tribofilm patches created during the test can be seen in Figure 4.25, which shows an optical image on the disc wear track and an interferometry image of the ball wear track. The tribofilm thickness measured on the ball with the SLIM software was 36 ± 15 nm.

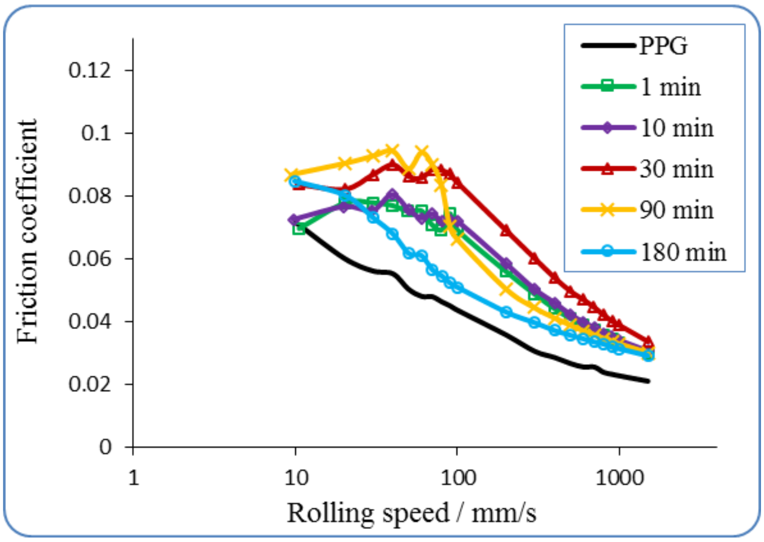

Figure 4.24 Stribeck curves for 2H-WS_2 NPs in PPG at 100ºC

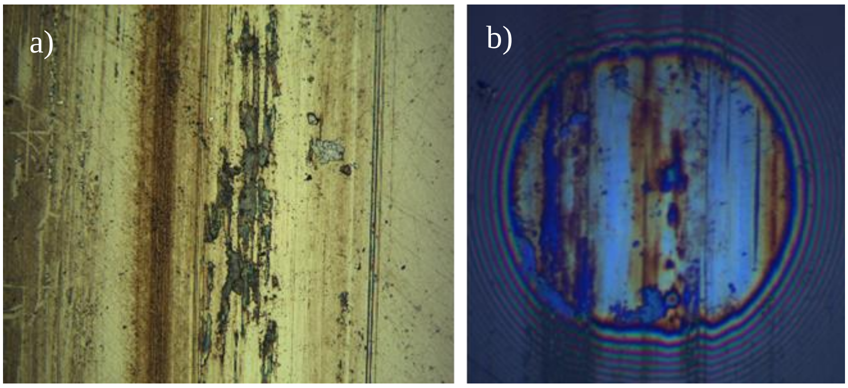

Figure 4.25 Images of the tribofilm generated at 100ºC after 3 h of rubbing. (a) Optical image of the wear track on the disc, (b) 3D SLIM interference image of the tribofilm on the ball

Similar to the PAO dispersions, the experiments show that temperature plays an important role in the mechanism of these NPs. The different shape of the Stribeck curves at the two temperatures also suggests that the mechanism of action of 2H-WS_2 is very different.

Figure 4.26 shows a comparison of the Stribeck curves generated in PPG and PAO at 100ºC at the end of the 3 h tests. The lowest values for the COF in the boundary regime were obtained in PAO and therefore, it can be concluded that 2H-WS_2 NPs are more efficient friction modifiers when dispersed in nonpolar oils. The higher friction in the case of PPG can be explained by the ability of this polar oil to adsorb on the wear track and impede the interaction between 2H-WS_2 and the metal substrate (the generation of a tribofilm).

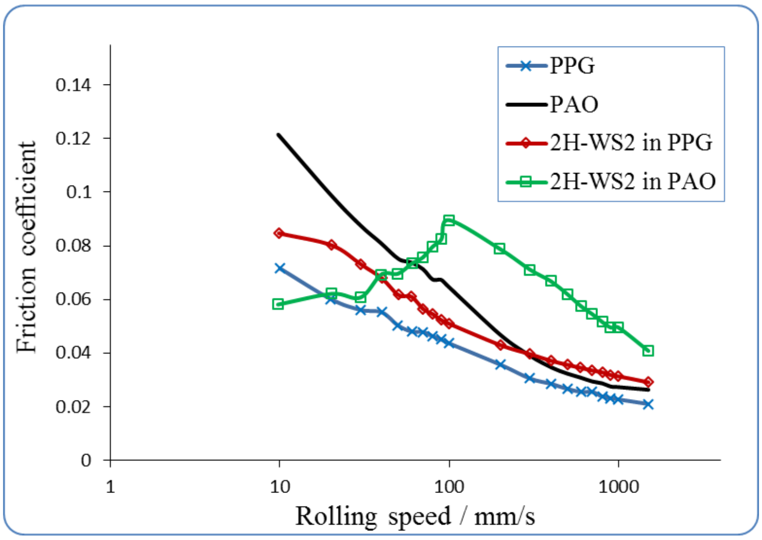

Figure 4.26 Stribeck curves after 3 h of rubbing for 2H-WS_2 NPs in PPG and PAO at 100ºC

4.6 The tribological properties of IF-WS_2 and IF-WSe_2 NPs

The tribological properties of IF-WS_2 and IF-WSe_2 NPs were investigated in the MTM2 rig. The inertness of the IF structures implies a delay in the formation of a tribofilm in the contact. Moreover, for the same reasoning it is also expected that the chemical film generated by IF-WS_2 and IF-WSe_2 NPs is thinner than for 2H-WS_2.

TEM images of the IF-WS_2 NPs were acquired with the JEOL ARM-200F (Oxford Materials) and are shown in Figure 4.27. Low-magnification images (Figures 4.27 (a), (b) and (c)) show that the IF-WS_2 NPs generally have a spherical shape and an average size between 15-20 and 70-80 nm, in agreement with their stated size. Most IF particles have a closed structure, as shown in Figures 4.27 (d), (e) and (f), but some are only partially closed (Figures 4.27 (g) and (i)). This may be due to the manufacturing process, as temperature has been reported to influence the formation of the closed IF structures [10, 169, 171, 298]. The layered structure visible in the high-resolution images has an interlayer spacing of 0.65 nm, in accordance with other values previously reported in the literature [10, 49, 162, 171, 174, 298-300].

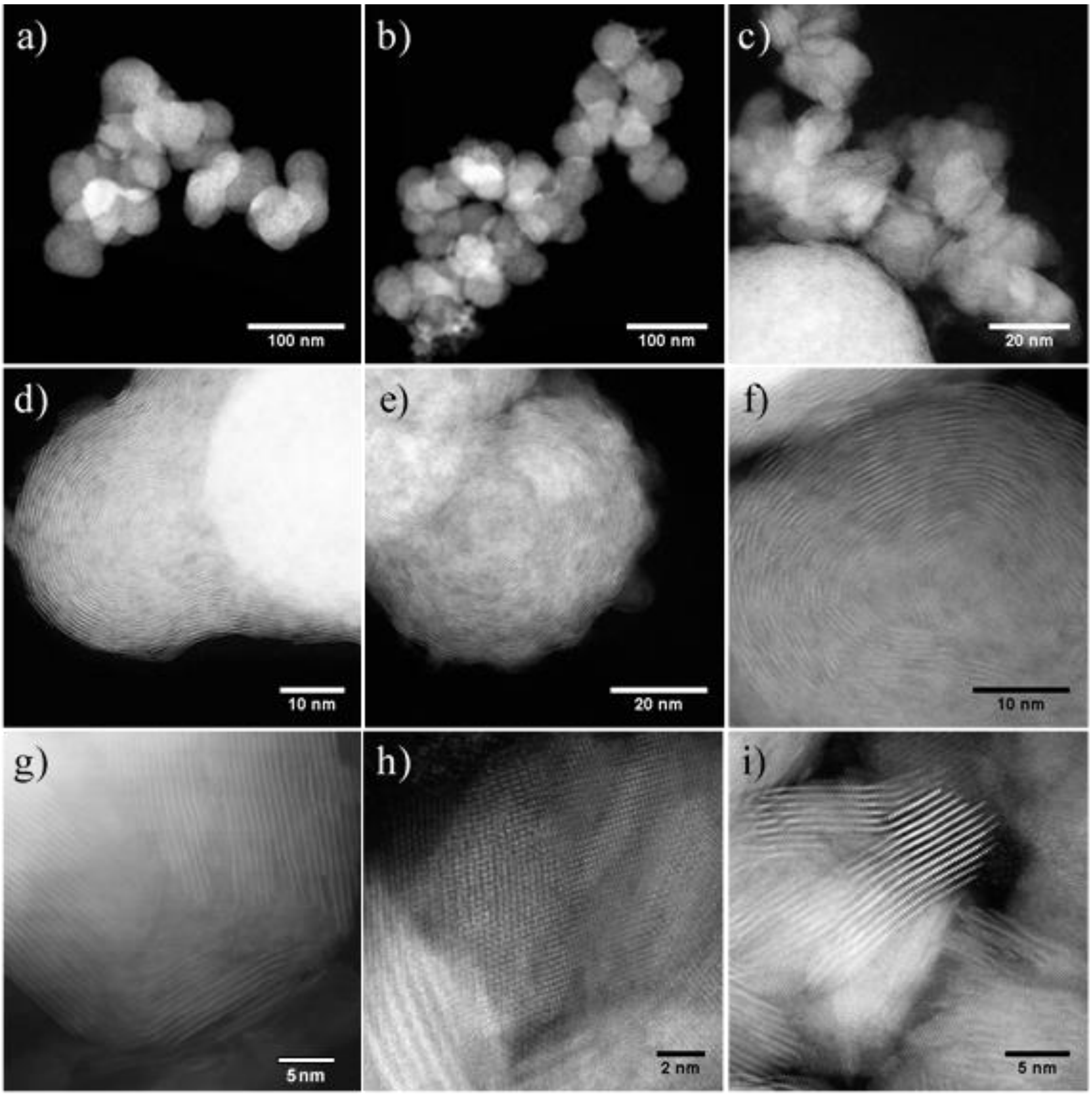

Figure 4.27 TEM images of IF-WS_2 NPs: a), b) and c) low-magnification images showing the size, size distribution and morphology, d), e) and f) HRTEM images showing single spherical NPs with a very high percentage of multi-layered structure g), h) and i) WS_2 nonspherical multilayer structures

Figure 4.28 shows TEM and HRTEM images of the IF-WSe_2 NPs taken with the JEOL ARM-200F (Oxford Materials). The low magnification images (Figures 4.28 (a) and (b)) show a very narrow size distribution, with most of the particles displaying a fairly spherical shape and an average size of 20-30 nm. However, the high resolution images (Figures 4.28 (c) and (d)) indicate that most of the IF structures are only partially closed. This may be again ascribed to the effect of temperature during the manufacturing process or due to the larger size of the Se atom, which induces higher strain in the layers and flattens the structure [180]. The interlayer spacing for the IF-WSe_2 NPs was measured to be 0.65 nm, similar to other findings in the literature [180, 181].

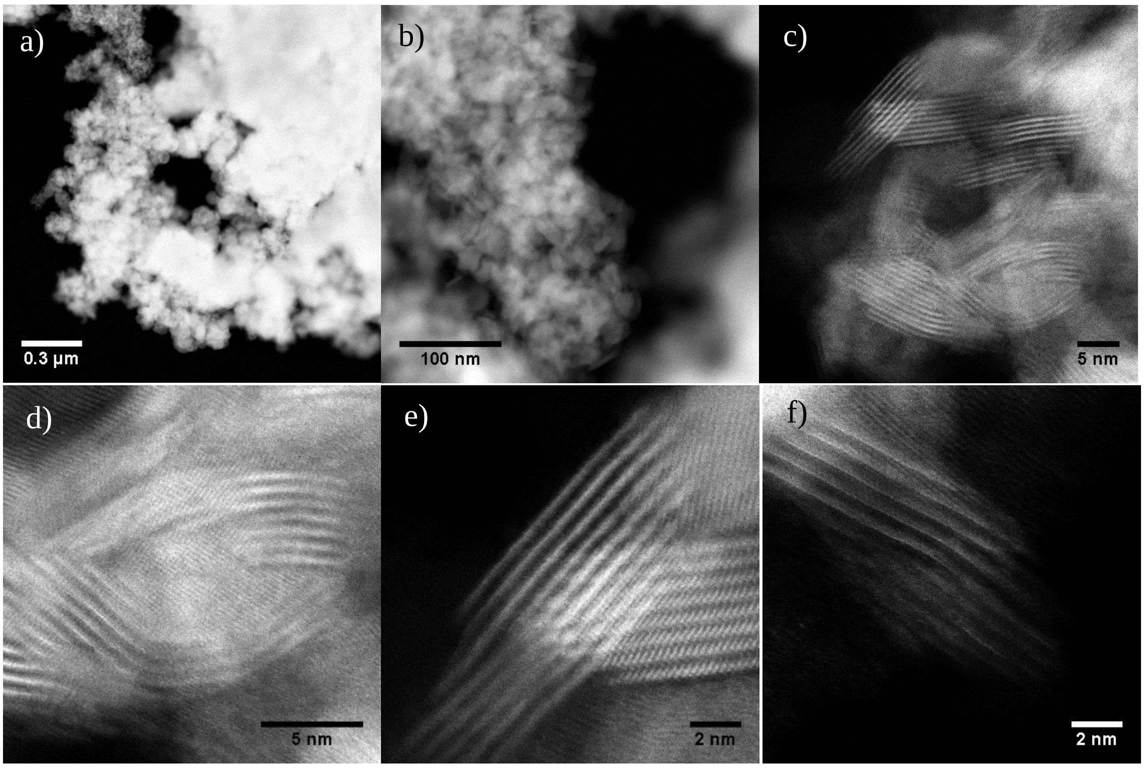

Figure 4.28 TEM images of IF-WSe_2 NPs: a) and b) low-magnification images showing the size, size distribution and morphology, c) HRTEM image showing their partially closed structure, d), e) and f) HRTEM images of single IF-WSe_2 NPs showing their nonspherical multilayer structure

Figures 4.29 (a) and (b) show the particle size distribution of the IF-WS_2 and IF-WSe_2 NPs measured in PAO at room temperature immediately after dispersion. The intensity distribution in Figure 4.29 (a) indicates that the IF-WS_2 NPs are agglomerated due to their large surface energy and form solid particles with an average diameter of ~315 nm. The colloid contains particles in the 250-600 nm range, as opposed to the small individual size of the NPs shown in the TEM images in Figure 4.27.

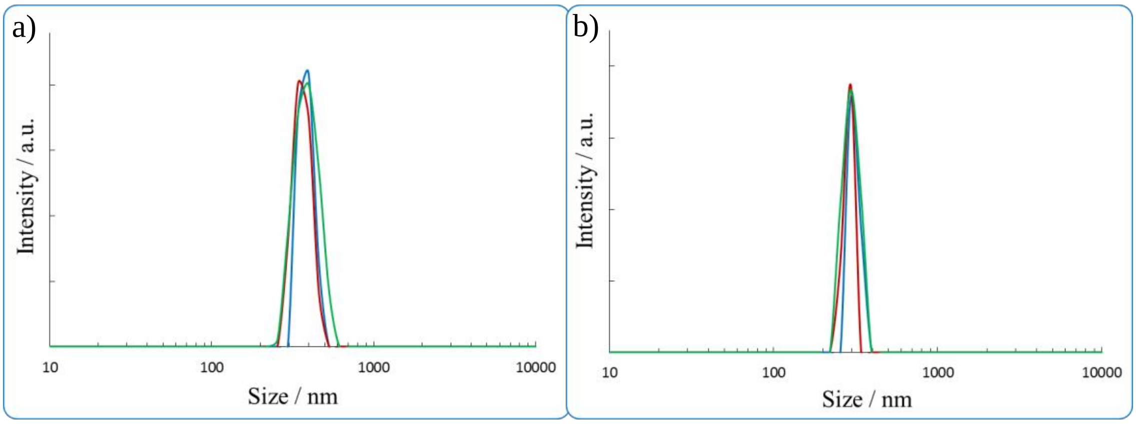

Figure 4.29 NP size distribution for a) IF-WS_2 and b) IF-WSe_2

Similar findings are shown in Figure 4.29 (b). The IF-WSe_2 NP colloids in PAO have an average size of ~ 355 nm, much larger than the individual particles seen in Figure 4.28. The size of the agglomerates is in the range of 220-400 nm.

Figure 4.30 presents the Stribeck curves measured in the MTM2 rig using the IF-WS_2 NP dispersion at 100ºC. In the boundary regime, the NPs display superior tribological properties compared to the PAO base oil, reducing the COF to 0.08-0.1. In the mixed regime, the Stribeck curves are shifted to higher values during the first 30 min, indicating the formation of a rough tribofilm on the wear track. The COF decreased in the second part of the test (90-180 min). This may be because the generated tribofilm is rubbed off and becomes smoother and eventually thinner. It also indicates that the tribofilm growth rate is smaller than for 2H-WS_2 NPs, due to the higher inertness of the IF structures and the lower affinity for the steel surface. Nevertheless, this mechanism of action has similarities to the behaviour of 2H-WS_2 NPs at 100ºC.

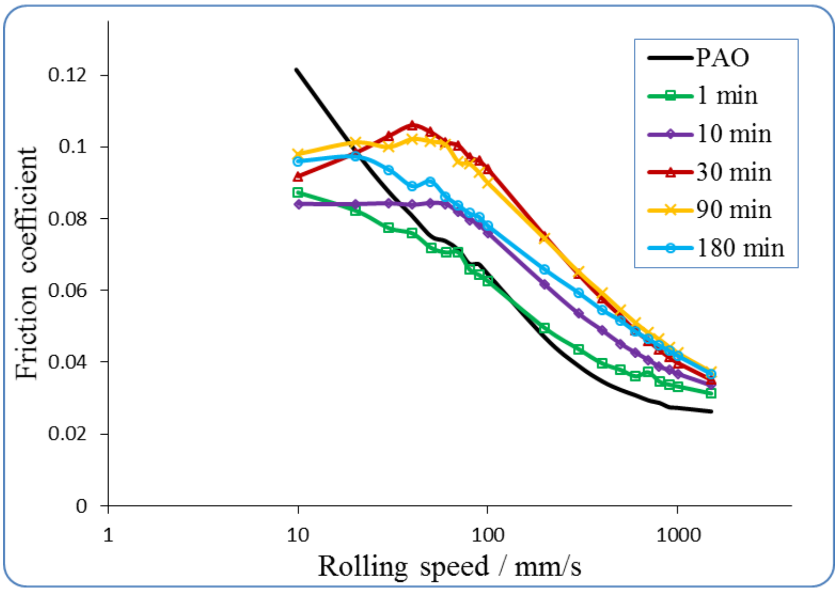

Figure 4.30 Stribeck curves for IF-WS_2 NPs in PAO at 100ºC

Figure 4.31 shows the Stribeck curves measured for the IF-WSe_2 NP colloid at 100ºC in PAO. In the first 10 min of the test, the NPs are efficient at reducing the COF in the boundary regime to ~0.09. However, for the remainder of the test friction increases significantly with time to values similar to those of the PAO base oil (0.12), indicating inferior FM properties compared to 2H- and IF-WS_2 NPs. In the mixed regime, friction increases slowly in the first 30 min, and rapidly towards the end of the test. This indicates that the decreased reactivity of the NPs delays the formation of the tribofilm in the contact. The high COF at the end of the test indicates the generation of a very patchy tribofilm.

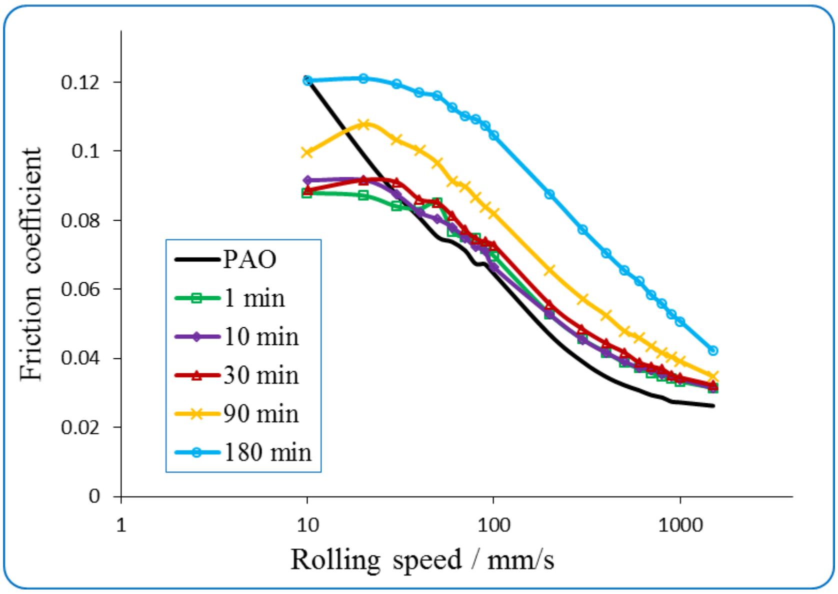

Figure 4.31 Stribeck curves for IF-WSe_2 NPs in PAO at 100°C

Figure 4.32 shows a comparison between 2H-WS_2, IF-WS_2 and IF-WSe_2 NPs. The variation of the COF with time during the conditioning phases of the tests shown in Figure 4.32 (a) gives important information regarding the difference between the mechanisms of action of the two nanoadditives. 2H-WS_2 is a superior FM in the first half of the test, while in the second part friction increases due to its ability to build a chemical tribofilm. A distinctive feature of the 2H-WS_2 COF consists of pronounced dips, which correspond to the moments when the conditioning phase was resumed after the measurement of the Stribeck curves. The higher reactivity of the 2H-WS_2 NPs can be also inferred from the presence of these dips. During the Stribeck curve phase, the speed was reduced until mixed and boundary conditions were achieved. When the conditioning phase resumes in the mixed regime (i.e. at 100 mm/s) the tribofilm offers extra protection for the first few minutes, before the COF returns to its normal value. However, the IF-WS_2 and IF-WSe_2 NPs do not show this type of behaviour to the same extent. As shown in Figures 4.8, 4.30 and 4.31, 2H-WS_2 is a better FM in these regimes and the COF is much lower.

A comparison between the Stribeck curves of the base oil and the two nanoadditive dispersions after three hours in the conditioning phase is shown in Figure 4.32 (b). The tribofilms generated by 2H-WS_2 and IF-WS_2 on the wear track have a markedly different behaviour. The 2H-WS_2-generated film displays a high COF in the mixed regime (i.e. above 100 mm/s), but friction decreases sharply at lower speeds to values much smaller than for IF-WS_2 and IF-WSe_2.

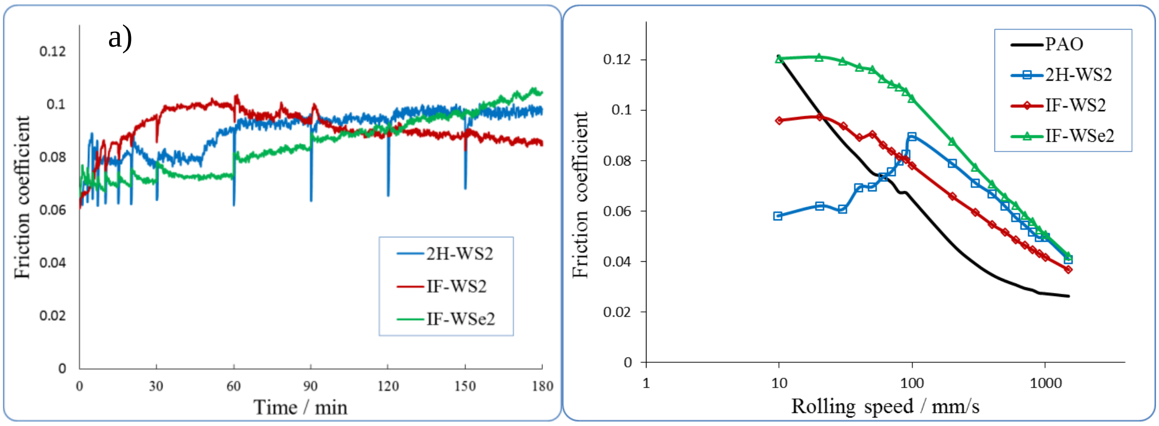

Figure 4.32 Comparison between 2H-WS_2, IF-WS_2 and IF-WSe_2 NPs in PAO at 100ºC: a) the variation of the COF with time during the conditioning phases; b) Stribeck curves measured after 3h

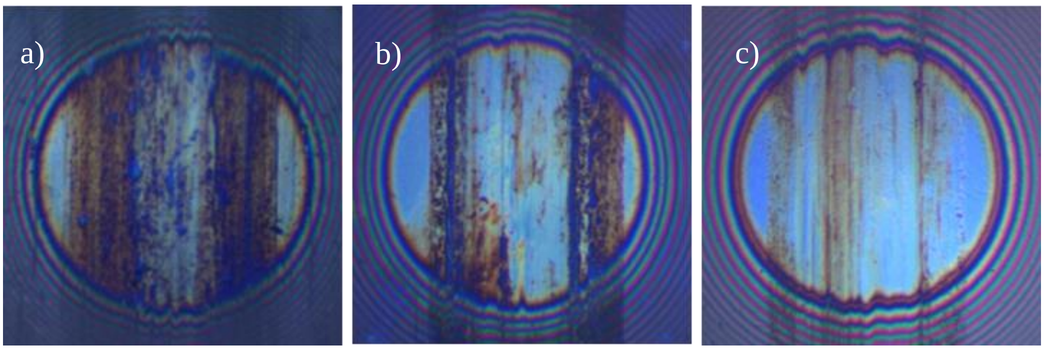

Figure 4.33 3D SLIM images of the tribofilm on the ball generated by a) 2H-WS_2 NPs, b) IF-WS_2 NPs and c) IF-WSe_2 NPs

Analysis of the SLIM interferometry images recorded at the end of the tests (Figure 4.33) confirms that the tribofilm generated by the IF-WS_2 and IF-WSe_2 NPs on the ball are thinner and less uniform compared to the 2H-WS_2 NPs. These results are a consequence of the 2H-WS_2 NPs being more reactive. The thickness values of the two tribofilms calculated by the SLIM software are 98 nm for 2H-WS_2, 61 nm for IF-WS_2 and 46 nm for IF-WSe_2 (as shown in Table 4.6). The standard error for these values are large for individual measurements due to the patchy, rough nature of the tribofilms.

Table 4.6 Average film thickness measured using Alicona profilometry and SLIM

	Measured values of tribofilm thickness and standard error (nm)		
	2H-WS_2	IF-WS_2	IF-WSe_2
Alicona	109 ± 10	121 ± 12	72 ± 15
SLIM	98 ± 7	61 ± 5	46 ± 8

The results suggest that the tribofilm generated by the IF-WS_2 NPs is thicker than for the 2H-WS_2 NPs, but lower according to the SLIM measurement. However, it should be noted that the Alicona measured the thickness of the film on the disc without previous cleaning, while the SLIM system measures the thickness on the ball after cleaning.

Therefore, the difference is probably due to a large number of IF-WS_2 NPs adhered to the contact, but which can be removed during gentle cleaning with solvents. However, 2H-WS_2 generates a chemically reacted film which is not removed by cleaning with solvents. Indeed, the tribofilm thickness measured with the Alicona after cleaning the surface of the discs is 73 ± 16 nm for IF-WS_2 and 42 ± 11 nm for IF-WSe_2, which are similar to the values measured with the SLIM system (Table 4.6).

XPS analysis was performed on the tribofilm generated by the IF-WS_2 NP dispersion at 100ºC. The surface of the wear track was cleaned prior to the analysis using Ar gas sputtering for 60 s (a few nm), in order to remove some of the C and O due to oxidized oil molecules. The composition of the tribofilm is presented in Table 4.7. Carbon is still present, although in a smaller quantity. Tungsten and iron are found in similar concentrations, but sulphur is only detected as traces. As seen in the 2H-WS_2-generated tribofilm in Figure 4.14 (e), sulphur is predominantly present on the surface and therefore most of it was probably removed during sputtering.

Table 4.7 Composition of the IF-WS_2 NP-generated tribofilm (100°C)

	W 4f	**S 2p**	**Fe 2p**	**O 1s**	**C 1s**
Composition (%)	15.81	2.95	11.68	53.73	15.84

The narrow spectra for W, S and O are presented in Figure 4.34. Signals were found at 32.5 eV for W^{4+} in WS_2 and at 35.4 eV for W^{6+} in WO_3 (Figure 4.34 (a)). The samples were cleaned with solvents before the XPS analysis and it was expected that there would be a very small amount of IF-WS_2 NPs on the tribofilm (the W^{4+}/W^{6+} ratio is ~1:11.5). However, unlike the 2H-WS_2 tribofilm, signals for elemental tungsten were not found. This suggests that the tribofilm may have inferior mechanical properties.

The sulphur signal is shown in Figure 4.34 (b). In addition to the sulphide doublet at 162 eV, there is an additional signal corresponding to sulphur oxides (168.8 eV). These are likely due to the oxidation of the exterior surface of the IF-WS_2 NPs or exfoliated WS_2 sheets (i.e. in relation to the entire composition of the tribofilm, the W^{4+} and S_{oxides} signals amount for ~1.4 % and 0.9 % respectively).

Figure 4.34 (c) shows that a large quantity of the C and O impurities have been removed from the surface of the tribofilm by the initial sputtering process. This is indicated by the smaller amount of C-O bonds present relative to the entire O 1s signal. The remaining signal (530.6 eV) is assigned to iron and tungsten oxides.

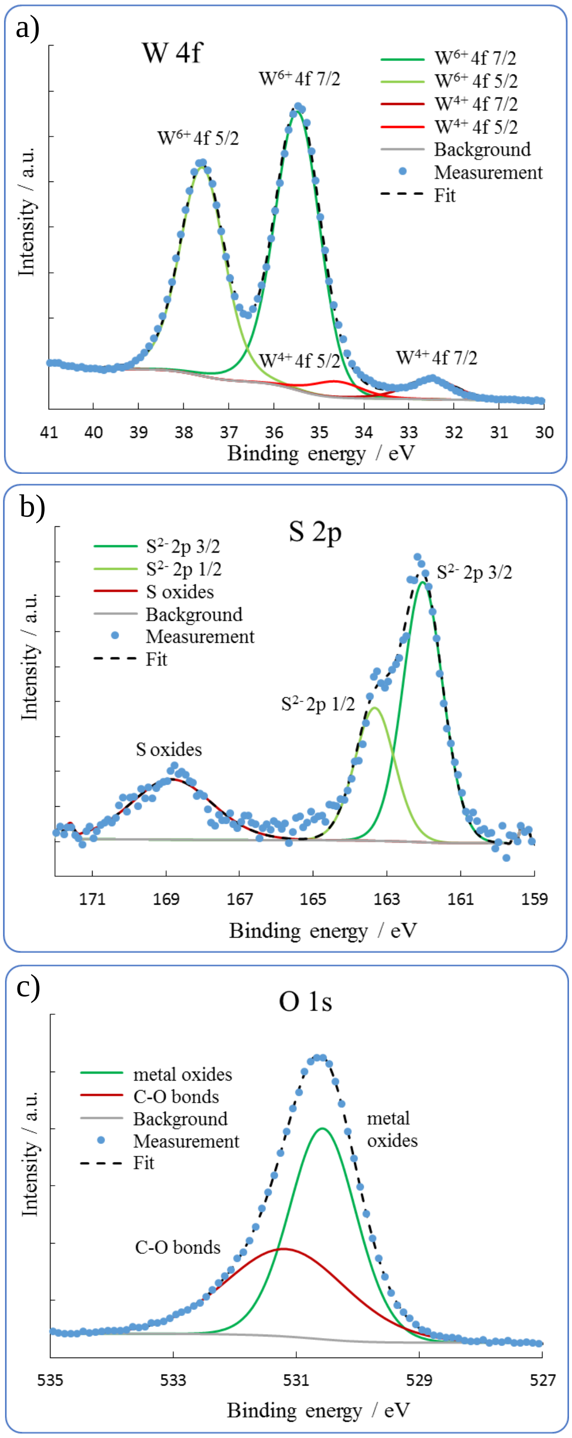

Figure 4.34 XPS narrow spectra recorded on the tribofilm generated by IF-WS_2 at 100°C, showing a) W 4f, b) S 2p and c) O 1s signals

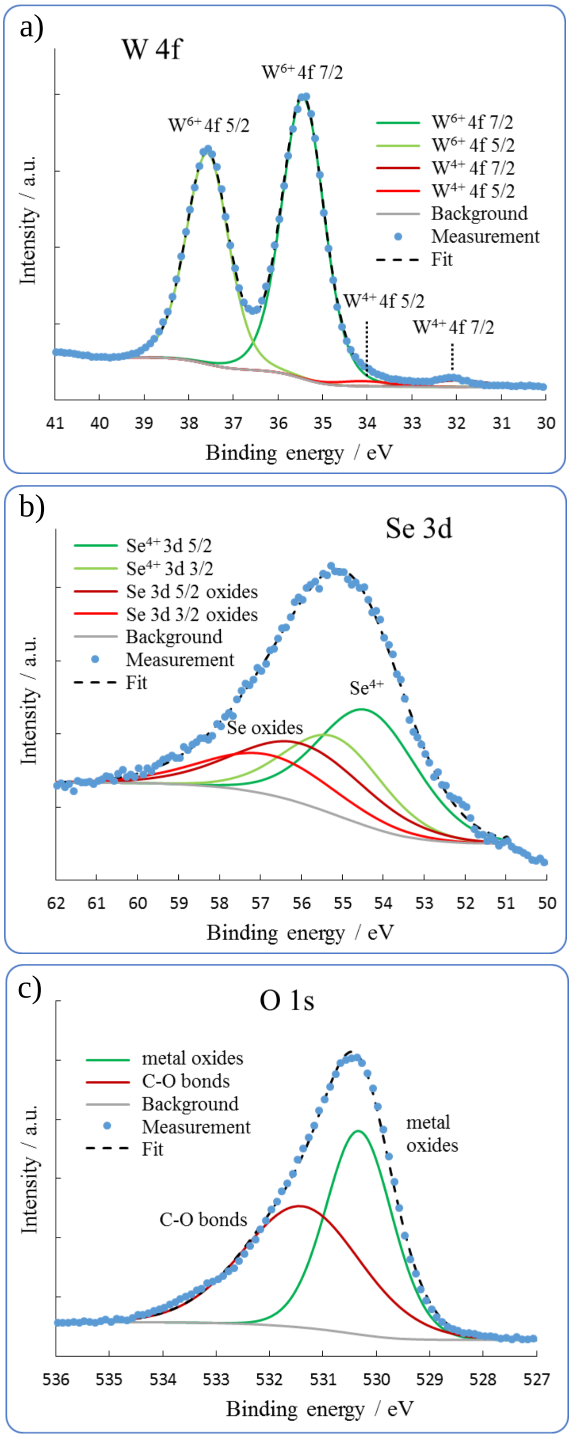

Figure 4.35 XPS narrow spectra recorded on the tribofilm generated by IF-WSe_2 at 100°C, showing a) W 4f, b) Se 3d and c) O 1s signals

Table 4.8 shows the composition of the tribofilm generated by the IF-WSe_2 NPs on the wear track as revealed by XPS. The analysis was performed in identical conditions to the IF-WS_2 tribofilm (i.e. the sample was sputtered for 60 s prior to the analysis to remove surface impurities, although small amounts of C are still present). The W:Se ratio is ~1:2, corresponding to the WSe_2 structure. As opposed to the 2H- and IF-WS_2 tribofilms, which have a larger amount of S at the surface but larger amounts of W in the deeper layers of the tribofilm, XPS analysis suggests that the W-Se composition in the film is linear, an indication that the tribofilm does not display the same complex layered structure and that the WSe_2 NPs are less reactive.

Table 4.8 Composition of the IF-WSe_2 NP-generated tribofilm (100°C)

	W 4f	**Se 2p**	**Fe 2p**	**O 1s**	**C 1s**
Composition (%)	7.56	14.89	15.18	51.85	10.51

The narrow XPS spectra recorded on the IF-WSe_2 tribofilm are presented in Figure 4.35. Signals for W^{4+} and W^{6+} were found at 31.9 and 35.5 eV (Figure 4.35 (a)). The ratio of the two chemical species is ~1:30, as any WSe_2 NPs (W^{4+}) adhered to the track are washed off prior to the analysis.

Figure 4.35 (b) shows the narrow spectra for Se 3d. The doublet signals at 54.4 and 56 eV are assigned to Se^{4+} and Se oxides. The formation of Se oxides is likely determined by the oxidation of the NPs. However, the Se^{4+} signal is probably given by iron selenides rather than WSe_2. This is supported by the very small amount of W^{4+} on the wear track.

The narrow spectra for O 1s are shown in Figure 4.35 (c). The two signals are assigned to metal oxides (530.3 eV) and C-O bonds from impurities (531.4 eV).

The presence of tungsten trioxide and iron selenides in the film are evidence of a similar mechanism of action of IF-WSe_2 NPs, although the reactions leading to the tribofilm generation are inhibited by the lower reactivity of the NPs.

The width of the tribofilms on the disc was measured from the Alicona profiles and it was found that the three nanoadditives appear to have similar antiwear behaviour: 300 μm for IF-WS_2 and IF-WSe_2 NPs and 290 μm for 2H-WS_2 NPs. Wear loss measurements were not possible because during the tests, the tribofilms were formed on the surface of the substrate, essentially implying negative loss. In order to obtain a deep wear track and to measure the wear loss, the tests would need to be much longer. Therefore, the hardness of the film is probably an important factor in the generation of wear and the better mechanical properties of the 2H-WS_2-generated tribofilm may ultimately confer better antiwear resistance. However, nanoindentation of the chemical tribofilms generated by the IF-WS_2 and IF-WSe_2 NPs was not performed because their thickness is very small and results would be largely influenced by the steel substrate.

4.7 Conclusions

Previous published work has shown that 2H- and IF-WS_2 NPs are strong candidates to replace environmentally harmful lubricant additives due to their potential to reduce friction and wear in high pressure contacts. This research was mainly carried out at room temperature and the mechanism of action proposed was the delamination of NPs under pressure and adherence of WS_2 sheets to the wear track to generate a tribofilm. The present study has investigated the behaviour of WS_2 NPs in both low- and high-temperature, high-pressure sliding contacts and found that the tribological performance of the NPs significantly depends on the testing temperature.

- The physical and chemical properties of the 2H-WS_2 NPs were investigated using XRD, Raman, TEM and EDX analysis. The 2H-WS_2 NPs show two size populations with averages of 20-30 nm and ~250 nm. Such a PSD can be beneficial in tribological contacts, which have asperities of various shapes and sizes, because the NPs can fill the gaps and reduce roughness and friction. WS_2 NPs have a layered structure and display low interlayer shear strength, a typical structure for very good FMs. The high purity of the sample was confirmed with XRD, Raman and EDX.
- The 2H-WS_2 NP dispersions tested at 40ºC displayed a modest reduction in the COF (0.11-0.12 in PPG and 0.09-0.11 in PAO) compared to the base oil (0.11 for PPG and 0.11 For PAO). The optical and XPS analysis on the wear track formed by 2H-WS_2 NPs in PAO revealed a thin and patchy tribofilm ~30 nm thick, which consisted mainly of agglomerated or flattened 2H-WS_2 NPs. Small quantities of WO_3 and iron sulphides were also found, indicating that a chemical reaction has started to take place between the steel substrate and the NPs, but the process was not favoured by temperature.
- At 100ºC, the NP dispersions immediately showed a very small value of the COF in the boundary lubrication regime (~0.08 in PPG and ~0.06 in PAO) and a gradually increasing COF in the mixed regime. Chemical analysis of the wear tracks showed the presence of tribofilms with distinct properties and composition. The 2H-WS_2 nanoadditive reacts with the metal substrate and in PAO forms a thick chemical tribofilm (100-200 nm) on the wear track. The chemical composition of the tribofilm was investigated with XPS and SIMS and

was found to have a layered structure. The upper part of the tribofilm is formed of unreacted 2H-WS_2 sheets and/or squashed NPs, WO_3, iron oxides and sulphides. The deeper layers consist of WO_3 and elemental W and Fe, while the film at the interface with the steel substrate is composed of only elemental W and Fe. The chemical composition of the tribofilm explains the high values of hardness (5.8 ± 0.6 GPa) and reduced Young's modulus (166 ± 19 GPa) measured by nanoindentation.

- The influence of oil polarity on the efficiency of the 2H-WS_2 NPs was also investigated. The tribological results showed that NPs are more efficient when used in a nonpolar oil (PAO), which does not compete for the polar sites of the tribological contact and therefore favours the generation of the tribofilm.
- IF-WS_2 and IF-WSe_2 NPs are more chemically inert and exhibit inferior tribofilm generating properties, although a film of adhered NPs was observed on top of the chemical tribofilm. The COF in the boundary regime at the end of the test is much higher (0.095 and 0.12 respectively) than the COF generated by the 2H-WS_2 NP dispersion (0.06). The AW properties of the chemical tribofilms generated by IF-WS_2 and IF-WSe_2 are also expected to be inferior due to their smaller thickness and different chemical structure. A preliminary assessment of the AW behaviour of the NPs was done by measuring the width of the wear tracks at the end of the tests. 2H-WS_2 NPs generated a slightly smaller wear track (290 µm) compared to IF-WS_2 and IF-WSe_2 NPs (300 µm).

5. COMPARISON BETWEEN 2H-WS_2 NPs AND CONVENTIONAL ADDITIVES

5.1 Introduction

The previous chapter studied the mechanism of action of WS_2 NPs as additives in PAO base oil. It was found that in high-temperature, high-pressure sliding contacts 2H-WS_2 reacts with the metal substrate to generate 100+ nm chemical tribofilms with a layered structure and excellent tribological properties.

The second part of the experimental research focuses on comparing the tribological properties of 2H-WS_2 NP dispersions with formulations containing popular conventional additives such as antiwear ZDDP and organic friction modifier (OFM) additives. The OFM is required to reduce the higher values of friction of the rough ZDDP tribofilm.

2H-WS_2 NPs display better tribological properties than IF-WS_2 and IF-WSe_2 NPs and therefore, the tests discussed in this chapter were performed only with 2H-WS_2 NPs. Apart from their excellent antiwear action, 2H-WS_2 tribofilms are capable of reducing friction in mixed and boundary lubrication conditions. For this reason, 2H-WS_2 NP dispersions do not require the use of a FM.

Tribological tests were conducted at 100ºC in the MTM2 rig in the conditions described in Chapter 3. The high temperature promotes the reaction of both 2H-WS_2 and ZDDP with the substrate and the formation of a chemical tribofilm. The properties of the tribofilms were investigated using SLIM interferometry, Alicona profilometry and nanoindentation. As in previous tests, 1 % w/w 2H-WS_2 NP colloids in base oil were prepared and no surfactant/dispersant was used to stabilize the dispersions.

The antiwear additive was a mixed primary/secondary alkyl ZDDP used in 0.4 % w/w (1351 ppm phosphorous) in the base oil. The OFM is a straight chain polyamidoalcohol added at a 0.5 % w/w treat rate. These concentrations of ZDDP and OFM are typical for commercial formulated lubricants.

This chapter is mainly based on two published papers [56] and [301], with an additional discussion on the importance of oil polarity on ZDDP tribofilm formation, i.e. the behaviour of ZDDP was investigated in both PAO and PPG base oils.

5.2 Characterization of tribofilms generated by ZDDP in PAO

The MTM tribological tests followed the same routine repeated at fixed time intervals – the ‘*conditioning phase*’, the ‘*Stribeck curve*’ acquisition, and the ‘*tribofilm measurement*’, as described in Section 3.3. The test temperature was 100ºC, because ZDDP additives require temperatures higher than 60ºC to generate an AW tribofilm in the contact.

Figures 5.1 (a) and (b) show the Stribeck curves for the ZDDP dispersion in PAO at 100ºC and the corresponding SLIM images. As ZDDP is soluble in the base oil, it was possible to record SLIM images throughout the test. The first image was taken before the test started. The sliding direction in all images is from left to right.

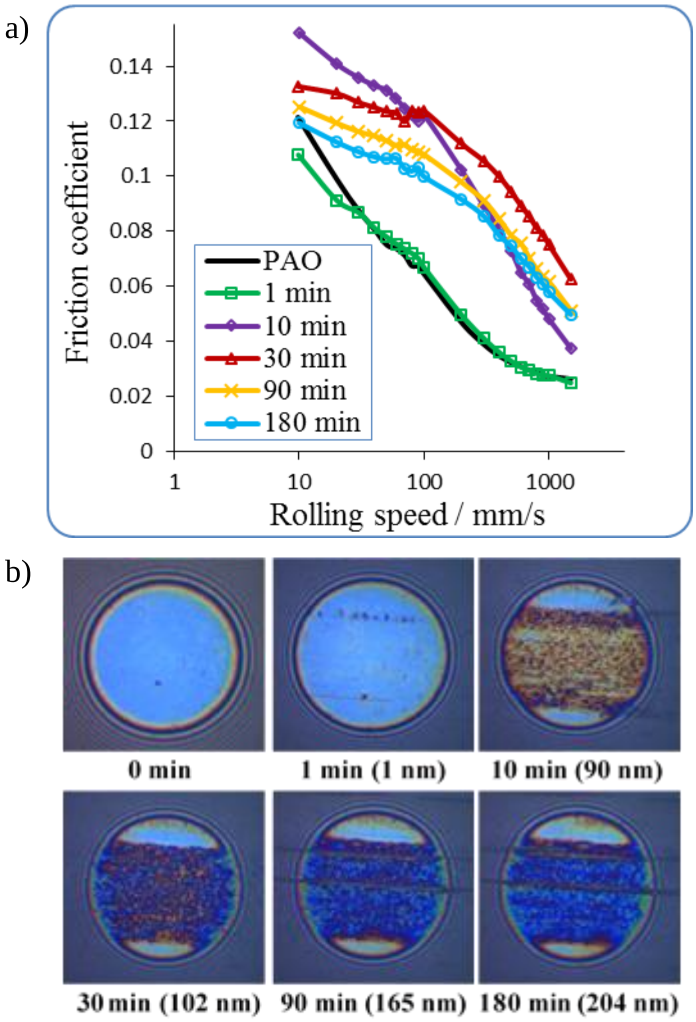

Figure 5.1 a) Stribeck curves for 0.4 % w/w ZDDP in PAO after 1, 10, 30, 90 and 180 minutes of rubbing at 100ºC, b) SLIM interferometry images of the ball track during rubbing with ZDDP in PAO [reproduced with permission from 301]

Results show that ZDDP develops a pad-like structure in the nonpolar base oil. The film starts to form after approximately 5 minutes of rubbing and during the first 30 minutes, the increase in film thickness can be correlated with the increase in friction. As the test progressed with time, the tribofilms continued to increase in thickness but their associated COF decreased (as shown by the Stribeck curves measured after 90 and 180 minutes of rubbing). These results are explained by the evolution of the morphology of ZDDP-generated tribofilms with rubbing time, towards smoother and more uniformly distributed films [39, 40]. The value of the COF in the boundary regime after 3 h was 0.12, similar to that of the base oil.

Tribofilms generated by ZDDP in PAO grow to a thickness of 204 ± 9 nm. The current study employed a high SRR (150 %). This resulted in the formation of thicker ZDDP tribofilms than reported in other published work, which used a SRR of 50 % but otherwise similar testing conditions [124, 275]. The SRR was reported to influence tribofilm formation and its characteristics and the final tribofilm thickness values are the result of the balance between its formation rate (determined by the kinetics of the chemical reactions) and its removal rate (determined by wear) [57, 58].

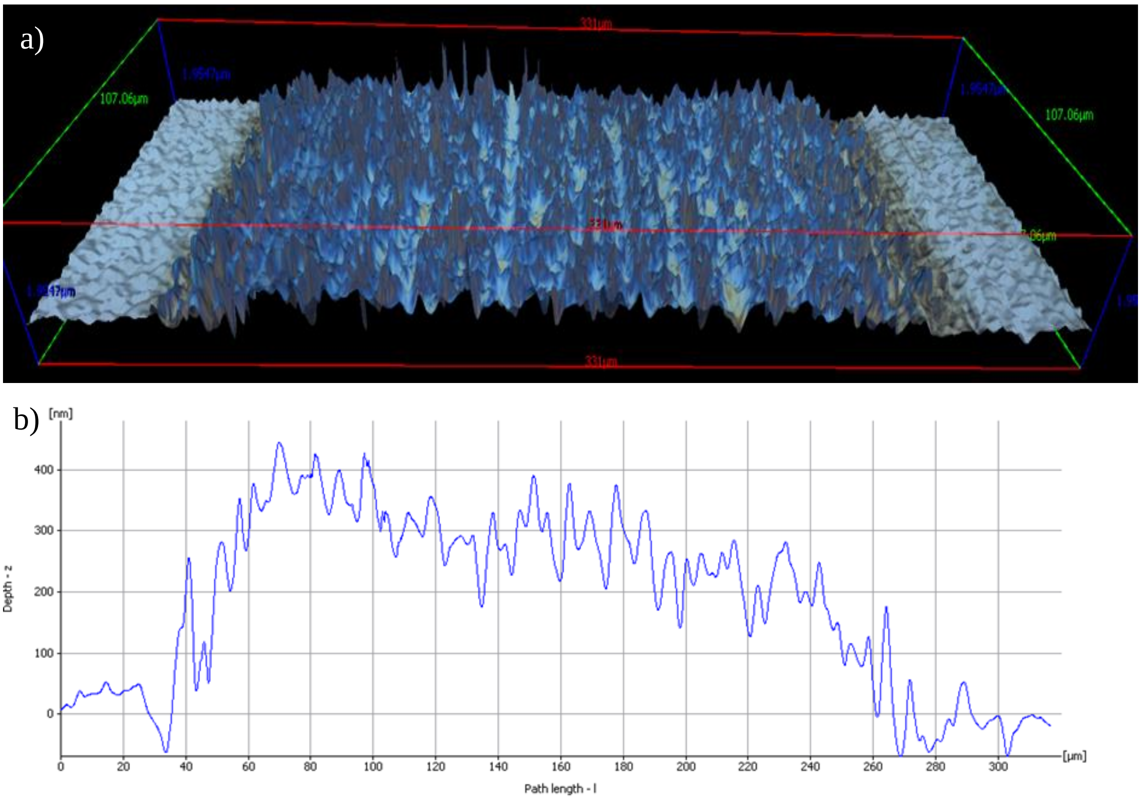

Figure 5.2 a) Typical 3D Alicona image of the tribofilm generated by ZDDP and b) profile view across the wear track [reproduced with permission from 301]

Figure 5.2 (a) shows an Alicona profilometry image at 100x magnification, which reveals the rough and patchy nature of the ZDDP tribofilm. As in the previous Alicona images shown, the height axis was increased 20 times for a clearer view of the structure. A typical profile across the wear track is shown in Figure 5.2 (b). The average height of the tribofilm has been calculated from multiple profiles to be 220 ± 25 nm, which is higher than the calculated value using SLIM interferometry. As discussed in Chapter 4, Alicona profilometry is performed on the disc specimens after the tribological tests, while SLIM interferometry is performed on the ball specimen during the MTM tests, under high pressure and thus gives a smaller film thickness when the asperity tips are flattened.

FIB analysis was performed inside the ZDDP-generated wear track to investigate the morphology of the tribofilm. Figure 5.3 (a) shows the deposited protective layer and a low-magnification view of the patchy tribofilm. As described in Section 2.3.3.2, the structure of the ZDDP tribofilm displays a pad-like distribution (typically 5-20 µm in size) separated by deep fissures.

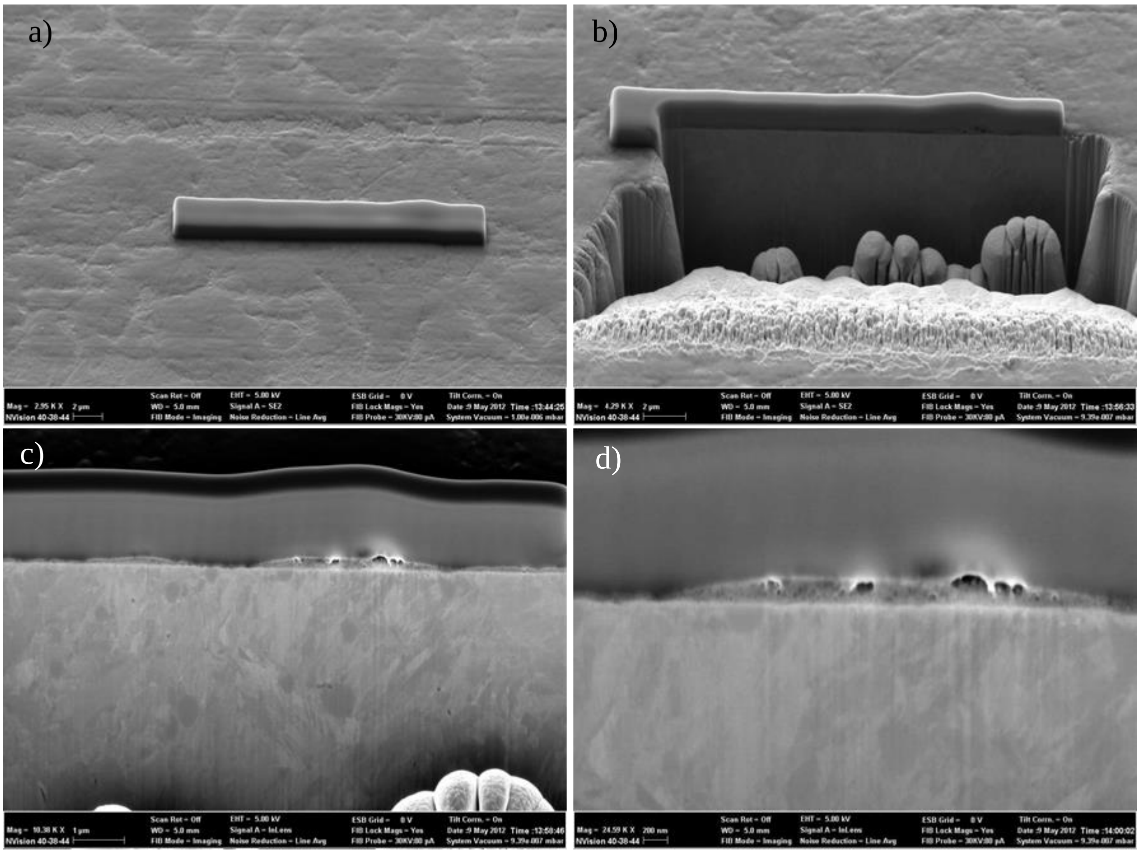

Figure 5.3 a) low-magnification SEM image of the ZDDP tribofilm, b) analysis area as produced with Ga^+ sputtering, c) and d) high magnification images of the ZDDP tribofilm

Figure 5.3 (b) shows the analysis area created by gallium ion sputtering. Due to the presence of the carbon protective layer, the cross-section of the film can be investigated without damaging the surface of the tribofilm. Cross-section images of the ZDDP tribofilm confirmed that it takes the form of islands (or pads) (Figure 5.3 (c) and (d)). The thickness of the pads is determined by the tribological conditions in the contact. In the present sample, the average film thickness is ~200 nm (the thickest pads are approximately 250 nm, as showen in Figure 5.3 (d)), consistent with results from the SLIM system (204 ± 9 nm), Alicona profilometry (220 ± 25 nm) and results from published research [8]. The SEM images also show the presence of dark particles inside the individual pads. Many studies have identified these as metal oxide particles generated during the formation of the ZDDP tribofilm [8, 302, 303].

The chemistry of the surface of the tribofilm was investigated using XPS. The wide spectrum is shown in Figure 5.4 (a) and the corresponding measured composition of the tribofilm is presented in Table 5.1, indicating a large amount of oxygen, which is due to the presence of oxides and phosphates. Carbon contamination was also present and was attributed to the C-O bonds in decomposed oil molecules.

Table 5.1 Composition of the ZDDP-generated tribofilm at 100°C

	Zn 2p	**Fe 2p**	**P 2p**	**O 1s**	**C 1s**
Composition (%)	1.09	13.61	12.59	49.55	23.16

The narrow spectrum for O 1s in Figure 5.4 (b) reveals the presence of metal oxides in the tribofilm at 530 eV, which can be seen in the FIB images presented in Figures 5.3 (c) and (d) as dark particles. However, the majority of oxygen atoms are bound to C and P (the signal at 531.5 eV), as organic oxide impurities (the C-O bonds) and phosphates generated due to the AW activity of ZDDP (the P-O bonds).

Small amounts of Zn^{2+} ions have been identified at 1022 eV (Figure 5.4 (c)), corresponding to zinc oxide and phosphate/polyphosphate compounds present at the top of the chemical tribofilm.

Phosphorous gives weak signals at 133.2 and 190.5 eV as shown in Figure 5.4 (d), attributed to the various phosphates generated in the ZDDP film.

The narrow spectrum for Fe 2p and the signal fittings are presented in Figures 5.4 (e) and (f). Significant amounts of elemental iron (43 % of the Fe signal) at 706.5 eV are an indication of the chemical reactions involved in the tribofilm formation. Fe oxides and phosphates were also detected, and these are fitted into a single peak at 708.4 eV due to the number and complexity of the individual signals.

The energy of all recorded signals was compared to literature data [292]. The chemical composition of the ZDDP tribofilm is similar to other findings in the literature, containing metal oxides and large amounts of phosphates. The presence of significant amounts of elemental Fe attests the dynamic nature of the tribofilm formation.

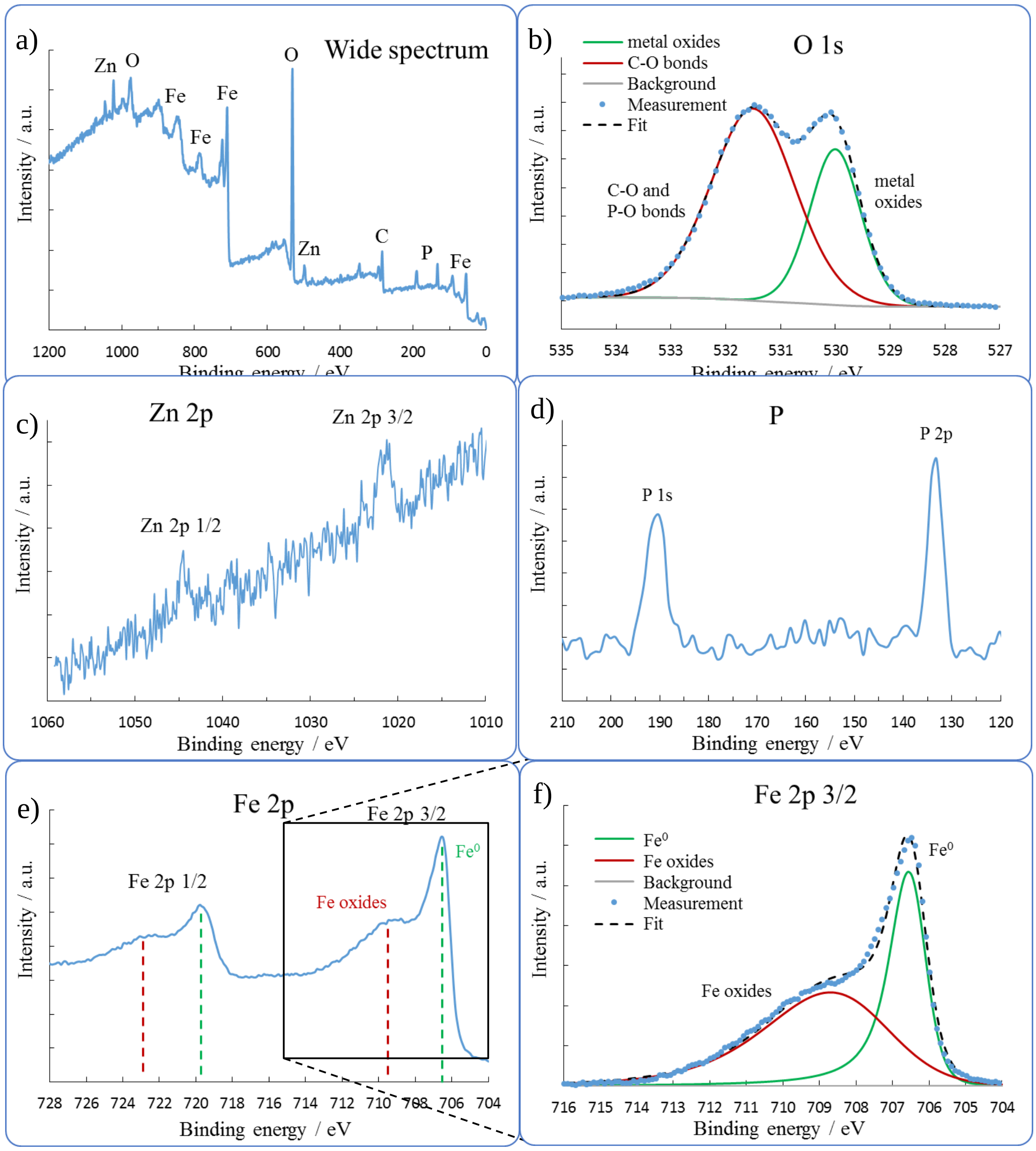

Figure 5.4 XPS spectra on the surface of the tribofilm generated by ZDDP: a) wide spectrum, b), c) Zn 2p, d) P 1s and 2p, e) narrow spectrum and CasaXPS fitting for the Fe 2p signal

ZDDP + OFM in PAO

Figure 5.5 (a) shows the Stribeck curves for ZDDP+OFM in PAO at 100ºC. In line with expectations, the addition of OFM to ZDDP resulted in decreased friction during the tests. The COF measured in the boundary regime was ~0.1, about 20 % lower than for the PAO base oil. In the mixed regime, the small increase in the COF is an indication of the formation of a tribofilm in the contact. This is also observed in the SLIM interferometry images in Figure 5.5 (b). The formation of the tribofilm is delayed in the first 30 min of the test, and the final thickness value is much smaller in the presence of the OFM. This is due to the ability of the OFM to compete with the ZDDP additive for adsorption/reaction with the steel substrate.

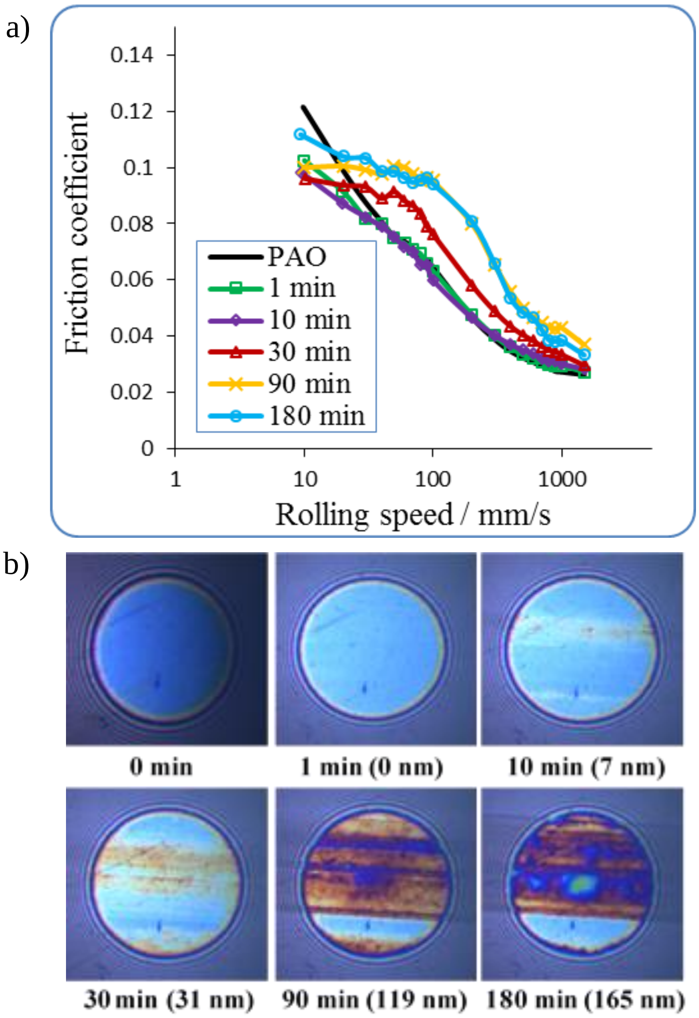

Figure 5.5 a) Stribeck curves for 0.4 % w/w ZDDP+OFM in PAO after 1, 10, 30, 90 and 180 minutes of rubbing at 100ºC, b) SLIM interferometry images of the ball track during rubbing with ZDDP in PAO [reproduced with permission from 301]

Figure 5.6 shows the evolution of the ZDDP and ZDDP+OFM tribofilms with time. The OFM has a negative impact on the ability of ZDDP additives to generate a thick AW film (~204 nm for ZDDP and only ~165 nm for ZDDP+OFM, as measured using SLIM interferometry on the ball specimens during the tests) and significantly delayed its formation (ZDDP+OFM only started to generate a tribofilm after approximately 30 minutes of rubbing). These findings are in agreement with other previously published work, in which a mineral oil was used as base oil [56].

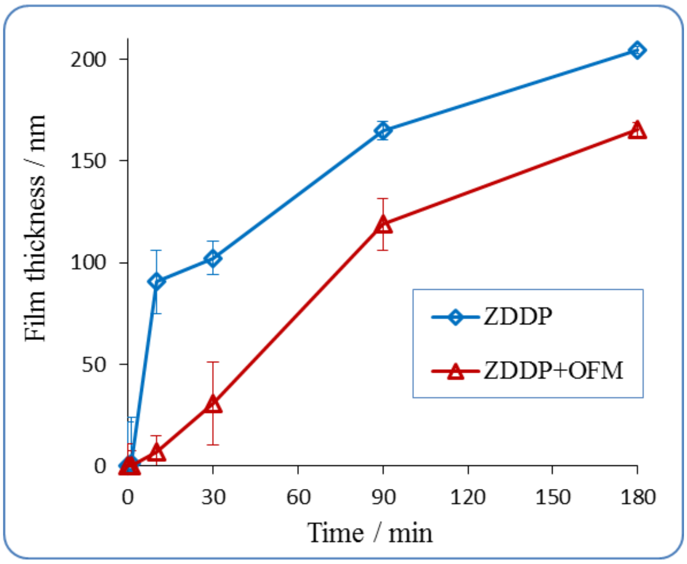

Figure 5.6 Growth kinetics of the ZDDP and ZDDP+OFM tribofilms [reproduced with permission from 301]

5.3 Comparison between the tribological behaviour of 2H-WS$_2$ NPs and conventional additives

Figure 5.7 shows a comparison of the Stribeck curves obtained for 2H-WS$_2$ NPs, the AW ZDDP and the combination of AW ZDDP and an OFM (ZDDP+OFM) in PAO. In all cases, the COF values in the mixed regime increase with time, indicating the generation of rough tribofilms that grow in thickness. The increase in friction is greatest for ZDDP, which also shows the highest film thickness. The friction levels of 2H-WS$_2$ are similar to the ZDDP+OFM lubricant for speeds higher than 100 mm/s.

A significant difference between the three lubricants is seen below 100 mm/s. As the speed is reduced, the COF for 2H-WS$_2$ drops to 0.55 (at 10 mm/s), but continues to increase for ZDDP to values similar to that of the base oil. The addition of the OFM to ZDDP reduces the COF, especially during the formation of the tribofilm, in the first 90 min of the test. Figure 5.7 (d) shows the Stribeck curves at the end of the tests for the PAO base oil and its blends with the three additives.

The COF measured for the ZDDP+OFM dispersion is smaller at the beginning of the test, but progressively increases during the test. This behaviour is attributed to the delayed formation of a tribofilm in the contact and is revealed by the shape of Stribeck curves in Figure 5.7 (c).

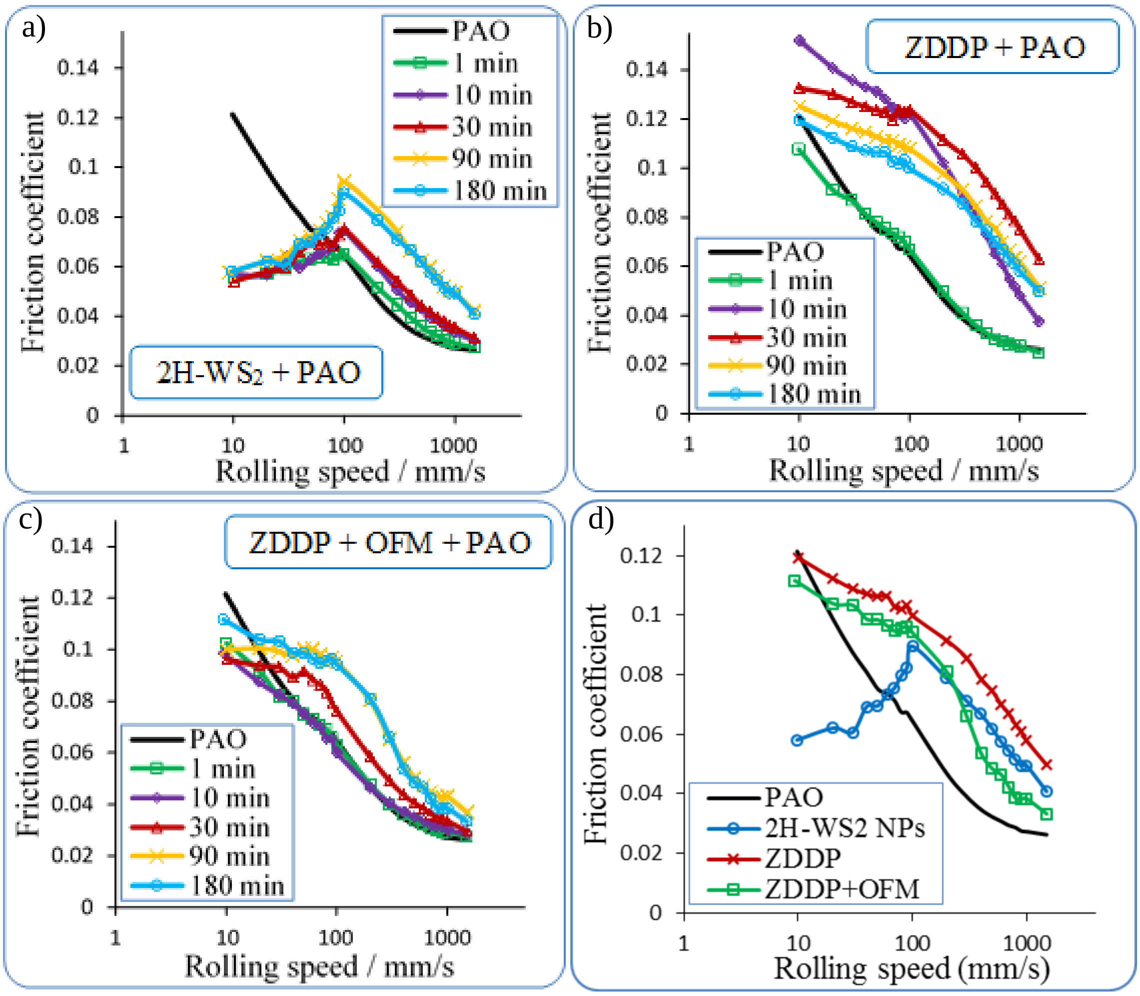

Figure 5.7 Stribeck curves after 1, 10, 30, 90 and 180 min of rubbing at 100ºC for: a) 2H-WS$_2$ NPs, b) ZDDP and c) ZDDP+OFM; d) comparison at the end of the tests [reproduced with permission from 301]

Figure 5.8 shows interference images of the ball wear tracks acquired at the end of the 3 h MTM tests for the PAO lubricants containing the three additives. The average tribofilm thickness values were 204 nm for ZDDP, 165 nm for ZDDP+OFM and 98 nm for the 2H-WS$_2$ NPs lubricant. Table 5.2 summarizes these results.

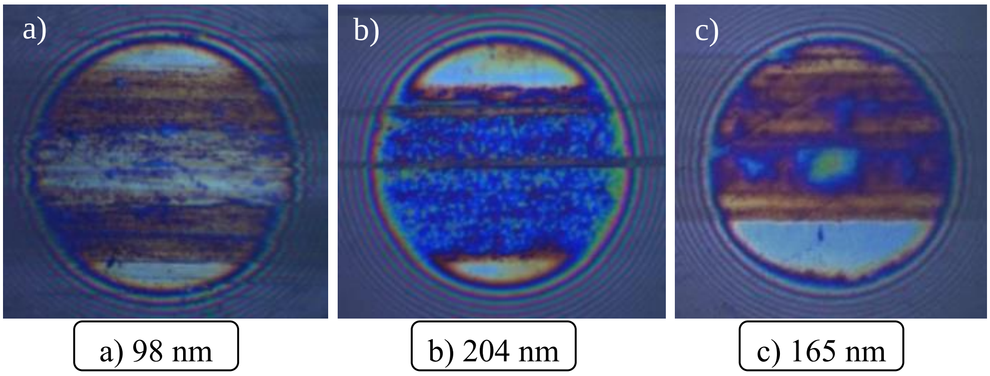

Figure 5.8 Interference images of the ball track after 3 h rubbing with a) 2H-WS$_2$ NPs, b) ZDDP and c) ZDDP+OFM [reproduced with permission from 301]

The thickness of the chemical tribofilm generated by the 2H-WS_2 lubricant was measured with the SLIM system only at the end of the 3 h test. During the test, the 2H-WS_2 NPs adhered to the spacer layer-coated window and impeded the imaging of the tribofilm. At the end of the test the window and the wear track were cleaned with solvents and the image of the tribofilm was acquired (Figure 5.8 (a)). Therefore, the 2H-WS_2 NPs physically adsorbed onto the wear track were removed before the image was taken.

Alicona images and profiles of the tribofilms formed on the MTM discs reveal their specific morphology (Figure 5.9 shows 3D Alicona profiles for the tribofilms generated by 2H-WS_2 NP, ZDDP and ZDDP+OFM). The height axis was increased 20 times for a clearer view. The calculated average height of the tribofilms measured with SLIM on the MTM balls and Alicona on the MTM discs were similar (Table 5.2). The slightly lower thickness values measured *in situ* with the SLIM system are the result of the tip asperities being flattened under the high contact pressure (0.94 GPa).

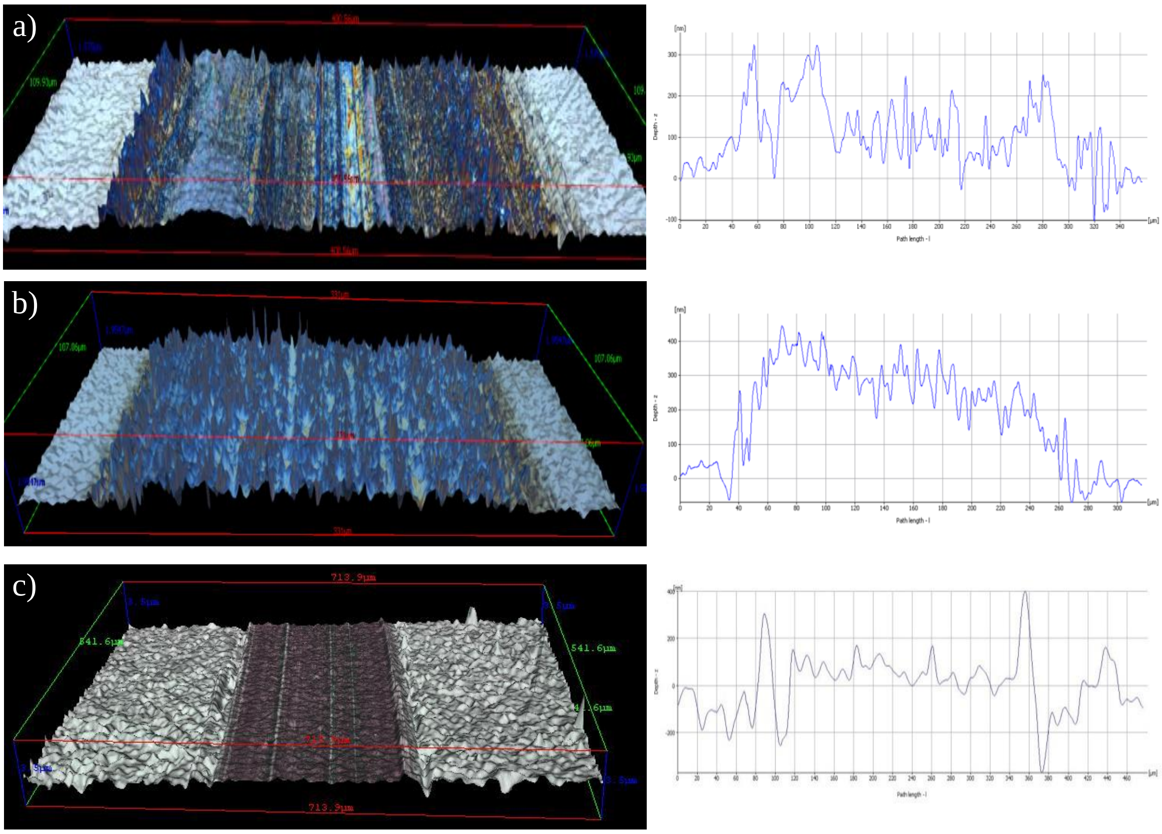

Figure 5.9 3D Alicona image of the tribofilms and profile views across the track for: a) 2H-WS_2 NPs, b) ZDDP and c) ZDDP+OFM [reproduced with permission from 301]

The antiwear properties of the additive can usually be assessed by determining the wear volume lost during the test. However, in all cases the additives formed thick tribofilms which rise above the steel surface. Some indications about the antiwear behaviour of the lubricants can be obtained by using Alicona to measure the wear track width on the discs at the end of the tests.

Table 5.2 Average film thickness measured using Alicona profilometry and SLIM

	Measured values of tribofilm thickness and standard error (nm)		
	$2H\text{-}WS_2$	ZDDP	ZDDP+OFM
Alicona	109 ± 10	220 ± 25	180 ± 31
SLIM	98 ± 7	204 ± 9	165 ± 12

The average width of the ZDDP wear track on the disc after the tests was approximately 280 ± 10 μm. The average width value for the $2H\text{-}WS_2$ NP and ZDDP+OFM dispersions was slightly larger – 290 ± 10 μm. This may seem to indicate that the antiwear properties of the $2H\text{-}WS_2$ NPs are somewhat similar to the ZDDP and ZDDP+OFM additives. However, the mechanical properties of the films determine their wear rate and need to be investigated.

Micromechanical properties (hardness, H, and reduced Young modulus, E') of the tribofilms generated by $2H\text{-}WS_2$, ZDDP and ZDDP+OFM lubricants were measured using nanoindentation. As discussed in Chapter 3, the depth of nanoindentation was 20-30 nm, depending on the tribofilm thickness. Measurements were performed on the thickest part of the tribofilm (film approximately 200-250 nm thick) to reduce the influence of the steel substrate. The depth of indentation in this study is 12–17% of the measured tribofilm thickness, which indicates that the hardness results determined during the analysis are correct, but the reduced Young's modulus results may be affected to some degree by the substrate. Nanoindentation tests of the steel substrate were also performed outside the wear track for comparison. The analysis started outside the tribofilm and continued towards the centre.

Figure 5.10 shows hardness maps and the corresponding location of the analysis on the Alicona images recorded on the disc samples. As discussed in Chapter 4, the $2H\text{-}WS_2$ tribofilm presents four distinctive sections: section 1 (0-30 μm)—steel; section 2 (30-60 μm)—chemically formed tribofilm; section 3 (60-90 μm)—chemically formed tribofilm covered with a thick layer of unreacted sheets of $2H\text{-}WS_2$ NPs and section 4 (90+ μm) – chemically formed tribofilm with a few NPs. The tribofilm (section 2) is characterized by high H (5.8 ± 0.6 GPa) and E' (166 ± 19 GPa) values, as a result of its unique chemical composition.

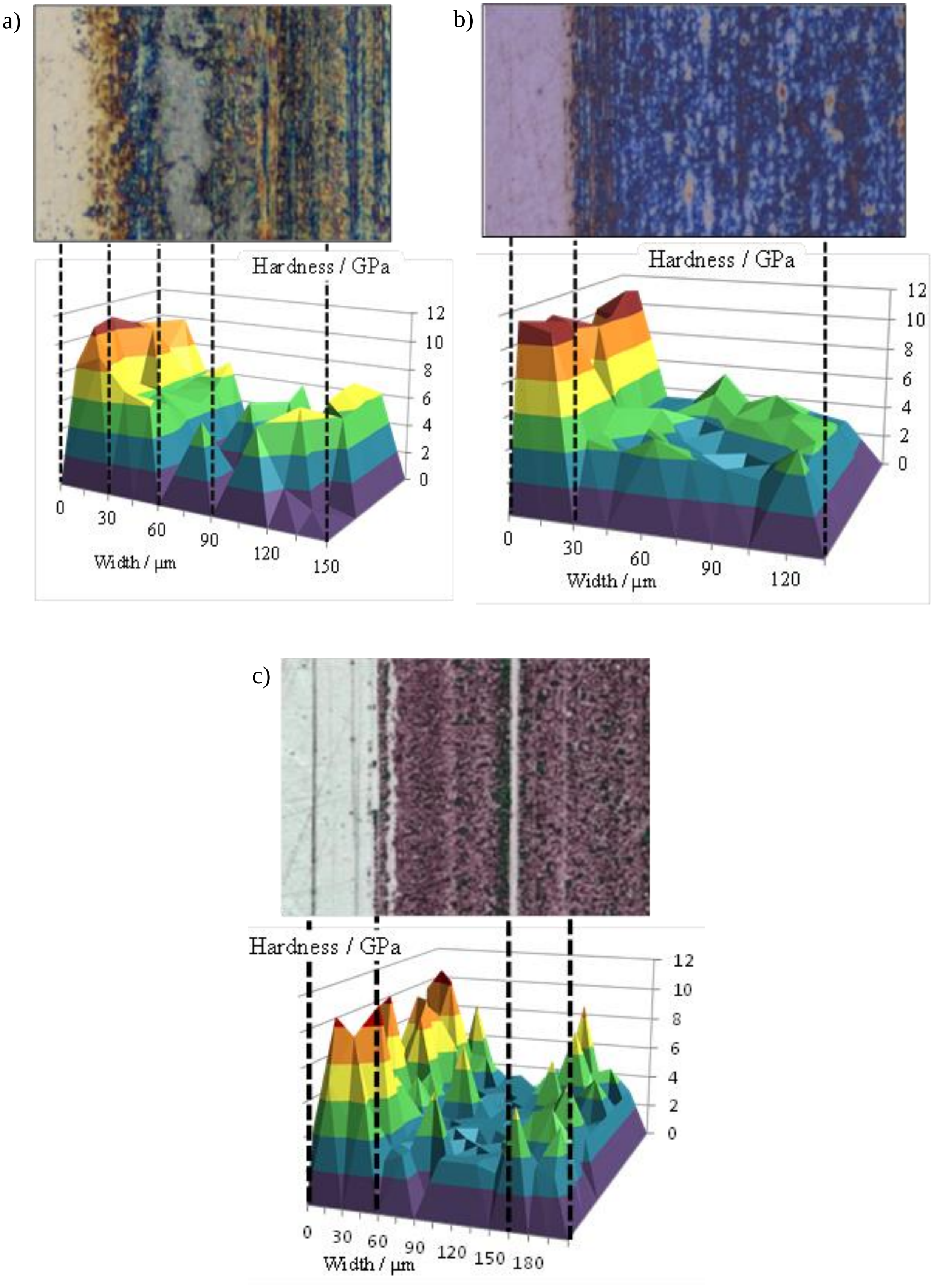

Figure 5.10 Hardness maps of nanoindented sections of steel and tribofilm for: a) 2H-WS$_2$ NPs, b) ZDDP and c) ZDDP+OFM [reproduced with permission from 301]

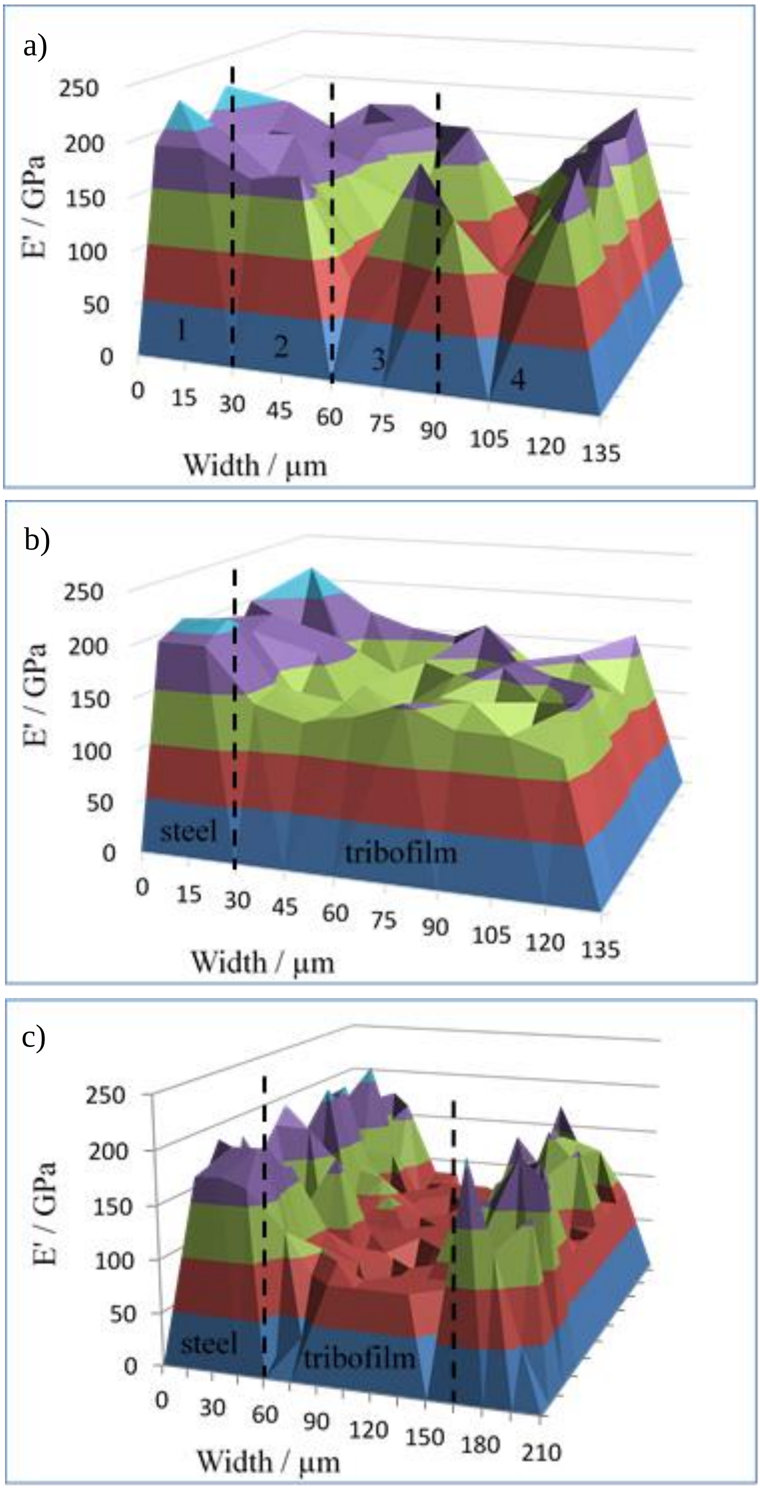

Figure 5.11 E' maps of nanoindented sections of steel and tribofilm for: a) 2H-WS_2 NPs, b) ZDDP and c) ZDDP+OFM

The ZDDP and ZDDP+OFM tribofilms have uniform hardness and the analysis only shows two sections: the steel substrate and the chemical film. This observation is in agreement with Alicona images and profiles (Figure 5.10), which indicate a more uniform film thickness. There is only one exception for the ZDDP+OFM film at 165 µm from the starting position of the analysis, where values are high due to a large scratch in the chemical tribofilm.

Young's modulus maps of the tribofilms are shown in Figure 5.11. These are in agreement with the hardness results described earlier, with high values for the steel sections and the scratch observed on the ZDDP+OFM tribofilm, and lower values for the different types of chemical films. The lowest E' values are measured on the squashed 2H-WS_2 NP agglomerations.

Figure 5.12 shows force-displacement curves measured during the nanoindentation analysis. During the dwell time at maximum load, creep was observed on the squashed WS_2 NPs.

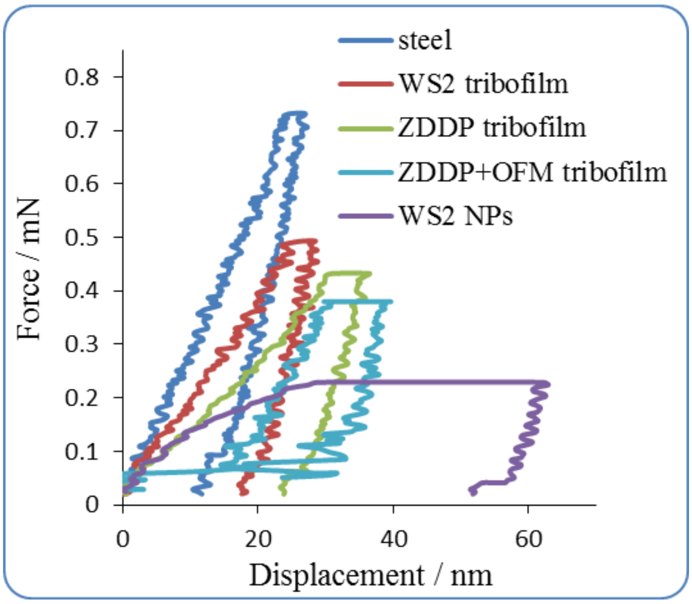

Figure 5.12 Loading/unloading hysteresis on the tribofilms

Table 5.3 shows hardness and reduced Young's modulus values measured for the steel substrate and the ZDDP, ZDDP+OFM and 2H-WS_2 (section 2) chemical tribofilms.

Table 5.3 Measured values for H and E' for the three tribofilms

Tribofilm	Parameters measured (GPa)			
	H	**SD**	**E'**	**SD**
Steel	9.5	0.9	197	10
2H-WS_2 tribofilm	5.8	0.6	166	19
ZDDP tribofilm	4.3	1.0	140	24
ZDDP+OFM tribofilm	3.2	1.8	85	57

As discussed in Chapter 4, the hardness of the steel substrate measured during the analysis is higher than expected. The main factors considered responsible are the difference between the Vickers and Berkovich tests, work hardening of the substrate and the nature of the nanoindentation technique, which measures surface properties.

The H and E' values of the ZDDP tribofilms are comparable with those reported by other research studies [297] and are higher than for ZDDP+OFM tribofilms. The OFM therefore influenced not only the thickness and generation kinetics of the ZDDP tribofilm (as shown in Figure 5.6), but also reduced the mechanical properties of the chemical tribofilm. These findings prove that the OFM has interfered with the ZDDP tribofilm formation. The H and E' values of the 2H-WS_2 tribofilm are higher than those of the ZDDP and ZDDP+OFM tribofilms and much larger than the reported values of MoDTC tribofilms (H = 0.4 GPa and E' = 10 GPa [106]), a typical Mo-based antiwear additive. These values imply that the presence of tungsten in the chemical composition of the 2H-WS_2 tribofilms enhances its mechanical properties and grants the excellent antiwear and extreme pressure behaviour reported by many studies.

The antiwear properties of the 2H-WS_2 NPs are therefore expected to be very competitive due to the excellent mechanical properties of the tribofilms generated in the contact. The inferior hardness of the ZDDP and ZDDP+OFM films can result in a higher wear rate. For example, the ZDDP+OFM tribofilm was the only one to show a large scratch (Figures 5.10 (c) and 5.11 (c)).

ZDDP in PPG

As discussed in Chapter 4, the chemistry of the base oil is an important factor that can influence the adsorption/reaction of additives in the lubricated contact. Tribological experiments confirmed that 2H-WS_2 NPs are more efficient friction modifiers when dispersed in nonpolar oils (PAO). The higher values of the COF obtained when using PPG dispersions can be explained by the ability of this polar oil to adsorb on the wear track and impede the interaction between 2H-WS_2 and the metal substrate. To study the influence of base oil polarity on the performance of ZDDP, tests were also performed in PPG base oil.

Figure 5.13 shows the variation of the Stribeck curves for ZDDP dispersions in PPG at 100ºC and the SLIM interferometry images recorded on the ball.

The Stribeck curves in Figure 5.13 (a) show a steady increase in friction in the mixed lubrication regime during the first 90 minutes, indicating a constant increase in the film thickness and roughness with time, after which the friction remains constant throughout the test. The increase in film thickness is also seen in the SLIM interferometry images on the ball wear tracks in Figure 5.13 (b). The development of the tribofilm is indicated by the darker areas. The maximum film thickness achieved after the first 90 minutes is 93 ± 7 nm. For the rest of the test, both friction and the film thickness remained constant.

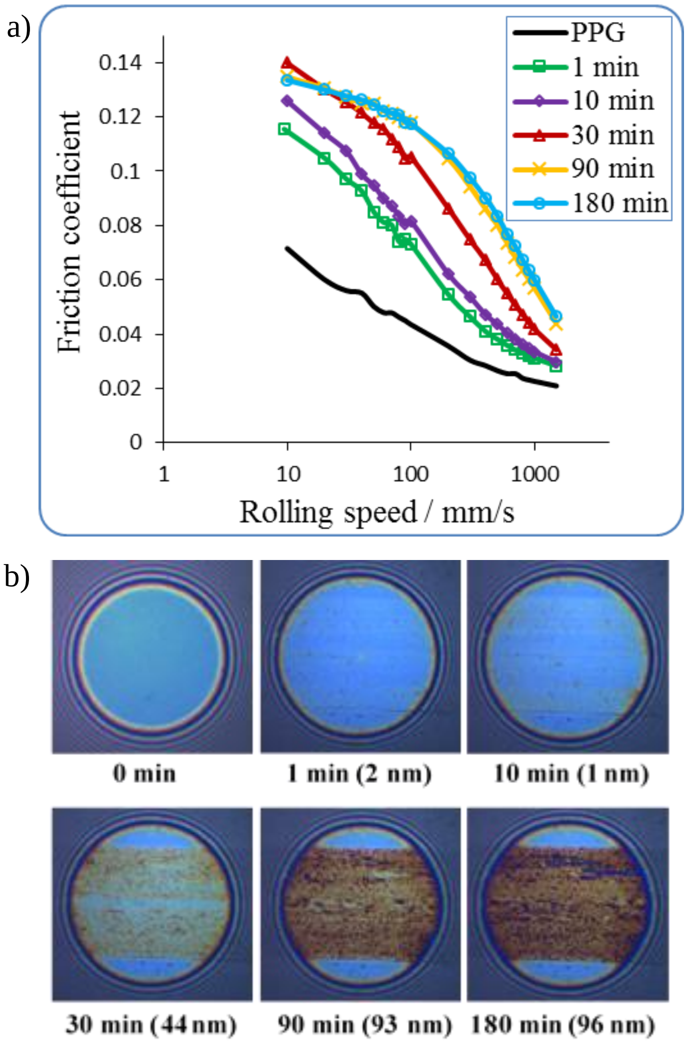

Figure 5.13 a) Stribeck curves for 0.4 % w/w ZDDP in PPG after 1, 10, 30, 90 and 180 minutes of rubbing at 100ºC, b) SLIM interferometry images of the ball track during rubbing with ZDDP in PPG

The boundary COF increased in the first 30 minutes, an indication of the rough nature of the developing tribofilm. It can be seen in Figure 5.13 (b) that the ZDDP lubricant develops a pad-like structure during prolonged rubbing. As the test progressed in time, the tribofilm thickness increased (SLIM images) but the boundary COF generated in the contact decreased (as shown by the Stribeck curves measured after 90 and 180 minutes of rubbing). These results can be explained by considering other published results, which showed that the morphology of ZDDP derived tribofilms evolves with rubbing time to become smoother and more uniformly distributed [39, 40].

As observed with WS_2 NP dispersions, the performance of ZDDP in PAO is superior compared to PPG. The polar nature of PPG interferes with the ability of ZDDP to adsorb/react with the metal substrate.

5.4 Conclusions

This chapter has focused on comparing the tribological properties of 2H-WS_2 NPs with lubricants containing popular conventional additives, such as ZDDP and OFMs.

- The generation of a tribofilm by a mixed primary/secondary alkyl ZDDP has been studied in PAO and PPG base oils. Similar to results described in Chapter 4, it was demonstrated that the AW activity of ZDDP additives is hindered by polar molecules, such as those composing the PPG base oil. This effect is due to the competition between molecules for adsorption/reaction with the steel substrate. The thickness of the tribofilm was dramatically reduced from ~204 nm in PAO to ~95 nm in PPG (measured using SLIM interferometry).
- OFMs are also capable of adsorption onto the steel surface and can reduce the COF in a tribological contact by forming thin boundary films. However, this mechanism interferes with the formation of the AW sacrificial film by ZDDP additives. Experiments described in this chapter have shown that the addition of an OFM (a straight chain polyamidoalcohol) was able to reduce the ZDDP tribofilm thickness from ~204 nm to ~165 nm (SLIM interferometry), while also greatly delaying its formation (by ~30 minutes under current testing conditions).
- The ZDDP tribofilm has a pad-like morphology, as revealed by FIB analysis and consistent with published studies in the literature. The size of the pads is around 5-20 µm and their height is ~200 nm, although larger/thicker pads were found in the tribofilm (~250 nm thick). However, the generation and morphology of the tribofilm is known to be dependent on the testing conditions. Dark particles were observed in the pads, likely to be oxide particles formed during the tribofilm build-up.

- The COF of the ZDDP tribofilm in the boundary regime after 3 hours was similar to that of the base oil (0.12). The OFM was able to reduce the boundary COF to ~0.1, but also interfered with the formation of the ZDDP tribofilm. By comparison, the tribofilm formed by the 2H-WS_2 NPs is thinner (~98 nm), but is covered in unreacted 2H-WS_2 sheets, which exert a levelling and smoothing effect of the rough areas of the chemical tribofilm and thus significantly lower the boundary friction to ~0.06. Therefore, the 2H-WS_2 NP dispersion exhibited a much lower boundary COF than ZDDP+OFM mixtures commonly used in tribological applications.
- Nanoindentation measurements showed that 2H-WS_2 NPs generate tribofilms with higher values of hardness and Young's modulus than ZDDP and ZDDP+OFM. As described in Chapter 4, 2H-WS_2 tribofilms have a layered structure, with the upper part composed of unreacted WS_2 sheets and/or squashed WS_2 NPs, WO_3, iron oxides and sulphides, while the deeper layers and the interface with the steel substrate consist of WO_3 and elemental W and Fe. The presence of elemental tungsten and tungsten trioxide in the WS_2 chemically reacted tribofilm enhances its mechanical properties, as evidenced by the hardness and reduced elastic modulus values ($H = 5.8 \pm 0.6$ GPa and $E' = 166 \pm 19$ GPa) and may explain the excellent antiwear and extreme pressure behaviour reported by numerous published studies.
- The mechanical properties of the ZDDP tribofilm ($H = 4.3 \pm 1$ GPa and $E' = 140 \pm 24$ GPa) are inferior to those of the WS_2 tribofilm. The OFM further decreases the properties of the ZDDP tribofilm to values of $H = 3.2 \pm 1.8$ GPa and $E' = 85 \pm 57$ GPa. This implies that the wear resistance (and therefore AW performance) of the 2H-WS_2 NP tribofilm is superior compared to lubricants containing conventional additives.

In view of these results, 2H-WS_2 nanoadditives are a suitable candidate for the replacement of conventional lubricant additives. 2H-WS_2 NPs have the advantage of reducing both friction and wear in sliding contacts and show great potential for the replacement of some of the most popular but problematic additives in use.

6. 2H-WS$_2$ NANOPARTICLES IN APPLICATIONS AFFECTED BY HYDROGEN EMBRITTLEMENT

6.1 Introduction

The previous chapters have studied the growth of the 2H-WS$_2$ NP-generated tribofilm on steel substrates in high-pressure, high-temperature contacts. The complex structure and composition of this tribofilm has provided the NPs with an excellent ability to decrease friction in the boundary regime and excellent antiwear and extreme pressure properties. The tribofilm also has the potential to reduce the permeation of hydrogen in steel and reduce its detrimental effect on the properties of the material.

In hydrogen applications, the rolling contact fatigue (RCF) life of rolling element bearings was reported to decrease with increasing concentration of hydrogen permeated into the bulk material [212-214]. The source of hydrogen is still debated, but the decomposition of water and/or oil molecules catalysed by the fresh metal surface locally generated in severe friction contacts is usually considered responsible [64, 182, 188-194].

The protective 2H-WS$_2$ tribofilm can prevent the formation of catalytic nascent surfaces in the contact and the ensuing generation of atomic hydrogen. This chapter presents the experimental investigations on the ability of 2H-WS$_2$ NP dispersions to reduce hydrogen permeation during RCF tests, such as those designed to simulate wind turbine gearbox failures.

Tribological tests were performed using 1 % w/w 2H-WS$_2$ NP dispersions in PAO. As in previous tests, no surfactant/dispersant was used to stabilize the dispersions. Thermal desorption spectroscopy (TDS) measurements were performed to measure the concentration of hydrogen species in the race samples at the end of the tests. The mechanism of action of 2H-WS$_2$ nanoadditives was investigated by performing surface analysis on the rolling tracks using optical profilometry, X-ray photoelectron spectroscopy (XPS) and Auger electron spectroscopy (AES).

The chapter is based on a published paper [277], with additional discussions on the TDS analysis. The experimental work was done at Kyushu University, Japan, courtesy of a JSPS (Japan Society for the Promotion of Science) Fellowship.

6.2 The performance of 2H-WS_2 NPs in hydrogen environments

Tribological tests employing 2H-WS_2 NP oil dispersions and the PAO base oil were performed in the conditions described in Table 6.1. To compare the different lubricants, the total amount of hydrogen released from the specimens during heating was measured using TDS, which monitors the rate of hydrogen release from samples by an applied temperature ramp.

Table 6.1 Rolling contact test conditions

Test duration	2, 5 and 10 hours
Number of cycles	~595,000/h (ball) and ~270,000/h (race)
Temperature	120ºC
Load	2650 N
Mean Hertzian pressure	4.8 GPa
Entrainment speed	1500 rpm (3.4 m/s)
Film parameter λ	2

In the high-stress, high-temperature conditions encountered in systems for supplying hydrogen such as compressors, both hydrogen gas and oil molecules can decompose on the fresh metal sites generated on the wear track and create atomic hydrogen [62, 64]. The passage of the hydrogen atoms through steel is hindered by lattice imperfections that tend to attract and bind them, thus rendering atoms immobile at temperatures where they should be able to diffuse readily. This phenomenon is known as ‘trapping’. The hydrogen atoms that permeate the steel substrate can be trapped in the bulk material, at dislocations, grain boundary interfaces, or they can be confined by their chemical reaction with other atoms (e. g. oxygen atoms from oxide particles). During the TDS analysis, the hydrogen desorption process must be preceded by the breakage of the physical/chemical bonds formed by the hydrogen atoms inside the specimen. The bonding energy between hydrogen and different atoms varies, and therefore, as the sample is heated during the desorption process, the mass spectrometer records complex signals. Furthermore, as hydrogen desorbs from the steel sample, it can combine with other gas atoms (especially oxygen) to generate hydrogen-containing species (most commonly water). Therefore, when quantifying the hydrogen permeation into the substrate, all hydrogen containing species must be taken into account [304].

As shown in Figure 6.1, the total amount of hydrogen (in ppm) permeated in the disc specimen was reduced by approximately 30% when lubrication was carried out with 2H-WS_2-additized PAO as compared to the PAO oil. These values were obtained by integrating the desorption spectra recorded during the TDS analysis and are corrected for the mass of each specimen. The signals recorded for the disc and ball samples have a similar profile and therefore, only analysis performed on the disc samples is shown.

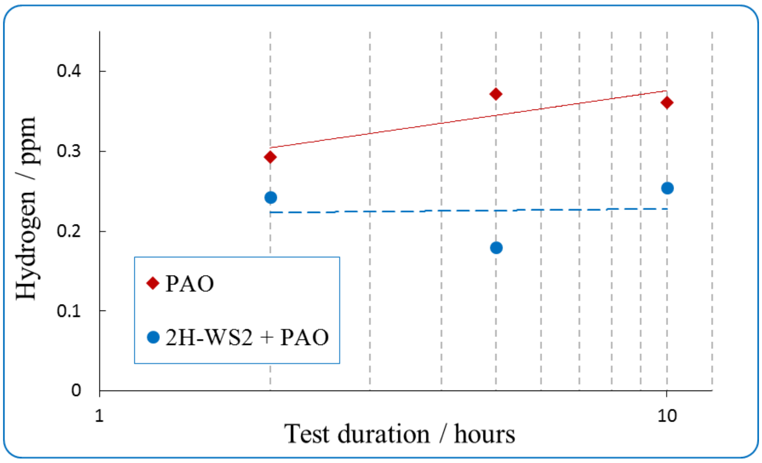

Figure 6.1 Concentration of hydrogen in the disc specimen after 2, 5 and 10 h of lubrication with WS_2 additized and non-additized PAO oil [reproduced with permission from 277]

Figure 6.2 shows the desorption curve for hydrogen (m/z=2) and water (m/z=18) from samples lubricated with the PAO base oil. Other hydrogen containing species were also monitored but their concentration was very low. The small discrepancies in the position and size of peaks may be due to the difference between the real temperature of the specimens and the temperature determined by the thermocouple, the small variations in the thermal capacity of the samples or any surface films formed on the wear tracks. The similar intensity of the signal at 200ºC after 5 and 10 hours may be an indication of diffusion after prolonged rolling.

Previous research shows that the position of the desorption peaks depends on the tribological testing conditions (material properties, temperature) and TDS analysis heating rate [216-219, 305].

In this study, the first hydrogen peak is at around 150-200ºC (Figure 6.2 (a)) and is attributed to atoms trapped at the interface with metal oxide particles, although previous research does not explain the nature of the bonds [306, 307]. The concentration of these species increases with the length of the experiment. This can be explained by the accumulation of larger amounts of hydrogen atoms in the sample, which are then more likely to react with the oxide species in the material.

The peak at 350-400ºC corresponds to hydrogen atoms trapped in the bulk material, at dislocations, microvoids and grain boundary interfaces, and is the main signal recorded during the analysis [215, 217, 218, 305, 308, 309]. The hydrogen bound to undissolved metal carbides and highly disorientated grain boundary interfaces has higher binding energies and is therefore released at very high temperatures (the signal above 400ºC) [215, 217, 218, 308, 309].

Apart from hydrogen, water desorption kinetics were also measured using the TDS apparatus (Figure 6.2 (b)). As observed from the spectra, water can be adsorbed at the surface and then desorbed when the sample is heated (the signal occurring at 100ºC). There are also additional peaks, corresponding to hydrogen trapped in the steel, which has reacted with oxygen to form water molecules during the desorption process from the material (signals at ~200ºC and ~350ºC). The sources for this hydrogen can be from metal oxide grain boundaries, as well as hydrogen atoms trapped in the bulk material. Hydrogen trapped at the interface with oxide species is more likely to form water molecules and therefore in this case, the intensity of the signal at ~200ºC is relatively higher compared to the signal at ~350ºC corresponding to the bulk hydrogen.

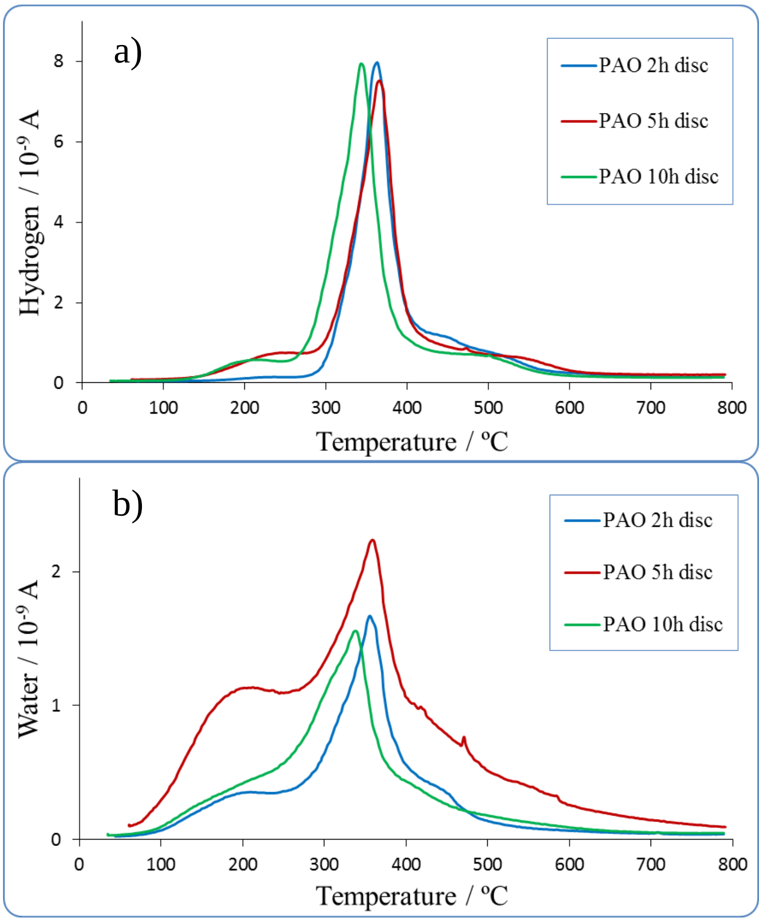

Figure 6.2 Desorption spectra of hydrogen (a) and water (b) from the sample tested with PAO [reproduced with permission from 277]

Figure 6.3 (a) compares the hydrogen signals from the tests lubricated with PAO and PAO+2H-WS$_2$ for 10 hours. The shape of the curves is similar, but the amount of hydrogen bound to metal oxide species (the signal at 150-200ºC) is larger for the 2H-WS$_2$ sample. These results are compatible with previous findings, which showed that 2H-WS$_2$ NPs react with the wear track and generate a tribofilm rich in metal oxides. The metal oxides interact with hydrogen atoms and trap them at the interface.

Figure 6.3 (b) shows the water desorption spectra of the disc samples for both lubricants. The results reveal that 2H-WS$_2$ reduces the amount of water in the substrate, compared to the base oil.

The amount of water detected consists of the molecules adsorbed on the surface and/or inside the steel substrate, and water formed from the reaction of hydrogen atoms with oxides. The presence of water in the substrate is detrimental to the life of the steel, as it can initiate oxidation in the substrate, interact with the scale interior to affect its microstructure and properties [310] and promote the growth of any cracks present in the material [311]. By reducing the water content through tribofilm generation, 2H-WS$_2$ additives can exert a beneficial effect on the lubricated steels.

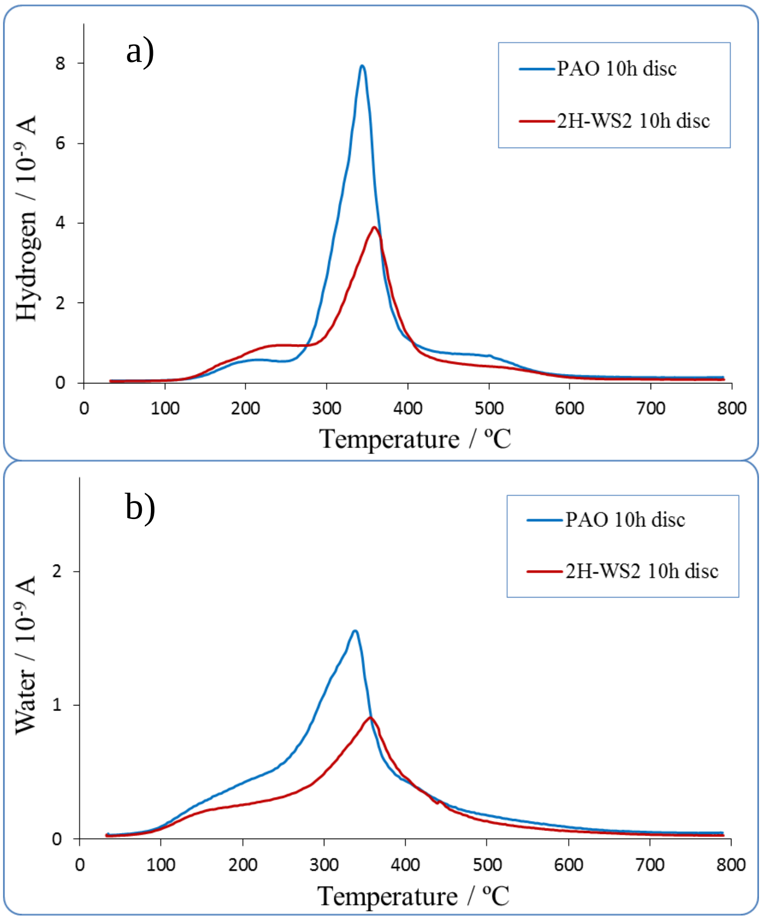

Figure 6.3 Desorption spectra of hydrogen (a) and water (b) for PAO and PAO+2H-WS$_2$ samples [reproduced with permission from 277]

Other hydrogen containing chemical species were also monitored during the TDS analysis. As an example, Figure 6.4 shows the main signals recorded by the mass spectrometer from the disc specimen tested with the 2H-WS_2 NP dispersion in PAO for 2 hours. The main gaseous components desorbed from the sample are molecular hydrogen (M/z 2) and water (M/z 18). There are also small amounts of HO^-, atomic oxygen, molecular oxygen and atomic hydrogen. Although these signals are not shown in Figures 6.2 and 6.3, they are accounted for in calculating the concentration of hydrogen present in the samples (i.e. the values in Figure 6.1).

The low intensity of the atomic/ionic species is due to the nature of the TDS analysis, which involves high temperatures and allows the formation and desorption of molecular species. By contrast, in SIMS atoms/fragments are sputtered by Ga^+ ions and can be detected immediately, as shown in Chapter 4.

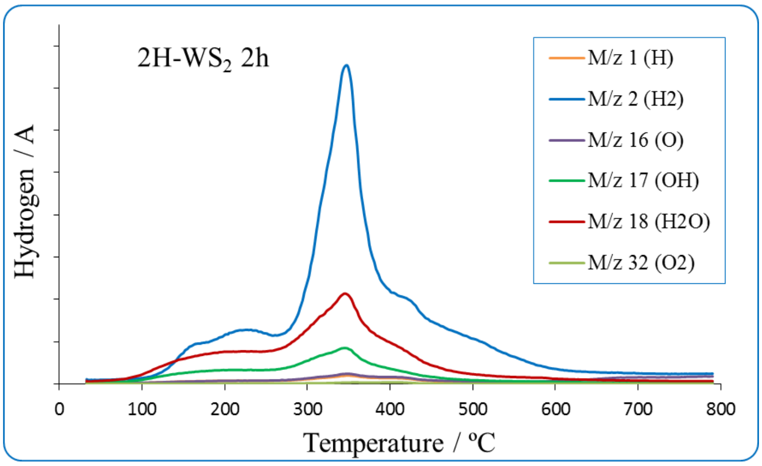

Figure 6.4 TDS spectra of the PAO+2H-WS_2 sample subjected to the 2 h RCF test

To investigate why the 2H-WS_2-additized PAO significantly reduced the total amount of hydrogen permeated in the disc specimen (by 30 %) as compared to the PAO oil, the wear tracks were physically and chemically characterized. 3D profilometry images of the wear tracks at the end of the tests (2, 5 and 10 hours) and the corresponding track profiles are shown in Figure 6.5. In all tests, the 2H-WS_2 NP lubricant generated slightly wider, but smoother tracks than the base oil.

As reported in numerous publications, during testing involving high loads the edges of the wear track become slightly raised. The height of the side ridges or furrows due to plastic deformation of the track may not change unless there are additional piles due to wear. This situation was seen in an almost similar degree in all our tests shown in Figure 6.5 (a) – (f).

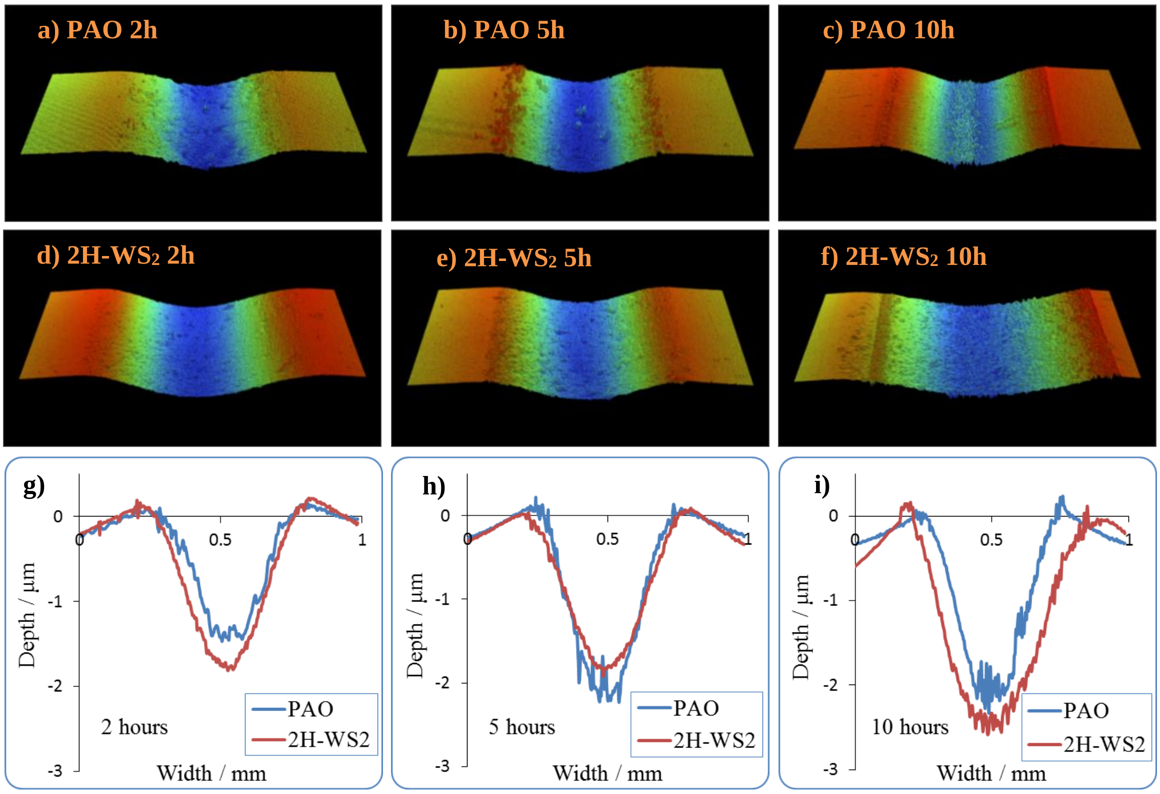

Figure 6.5 Profilometry images (a) – (f) and wear track profiles (g) – (i) for pure PAO and PAO + 2H-WS_2 dispersions [reproduced with permission from 277]

Chemical analysis (XPS) was performed on the wear tracks in order to investigate the presence of a tribofilm generated during the 10 hour tests and to measure the elemental composition and chemical state of elements in the tribofilm. Figure 6.6 shows the wide spectra for the 2H-WS_2-additized lubricant, recorded at the surface of the wear track and after sputtering of the top contamination layer. At the surface, only carbon and oxygen were detected (from the degradation of the oil). Below the surface layer, the tribofilm contains mainly iron, oxygen and tungsten. Sulphur only gave a very weak signal, while the other small signals are given by the other constituents of the steel substrate.

XPS was also performed on the pure PAO sample tested for 10 h. The comparative core level spectra for Fe 2p and W 4f of the wear tracks lubricated with 2H-WS_2-additized and pure PAO lubricants are shown in Figure 6.7.

The XPS analysis was performed after sputtering of the top 2 nm (30 s) to remove impurities and carbon species from decomposed oil molecules. For the PAO lubricated specimen, iron is found mostly in its oxide form. The wear track of the PAO+2H-WS_2 lubricated sample exhibited mainly signals for tungsten in the form of W^0 (31.4 eV) and W^{6+} (35.6 eV, specific for WO_3) and iron in both oxide (708.9 eV) and elemental state (706.6 eV). The rest of the signals recorded are attributed to sulphur (S_{2p}, 162 eV), carbon (C_{1s}, 285 eV), oxygen (O_{1s}, 530 eV), iron (Fe_{3p}, 53 eV; Fe_{3s}, 92 eV; Fe_{2p}, 707 and 720 eV;

Fe_{LMM}, 784 eV; Fe_{2s}, 845 eV) and other elements present in the steel: manganese (Mn_{2p}, 641 eV; Mn_{LMM}, 852 and 900 eV), nickel (Ni_{2p}, 853 and 870 eV) and copper (Cu_{2p}, 933 eV). The values have been verified against literature data [292, 312].

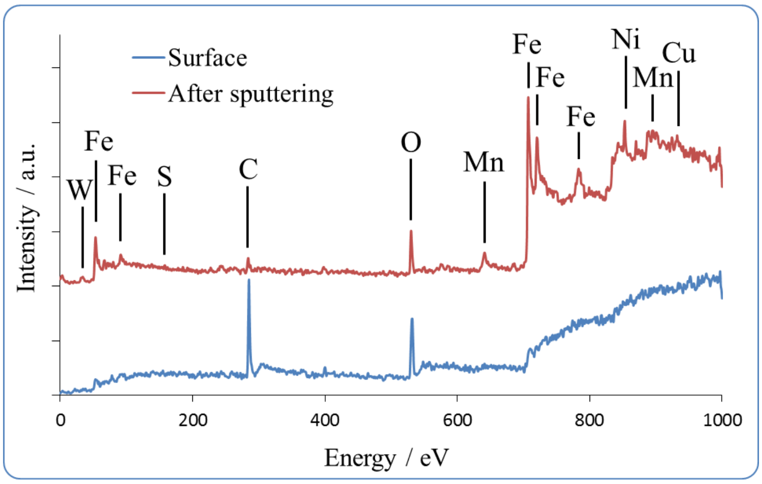

Figure 6.6 XPS spectra for the PAO+WS_2 lubricated specimen, before and after ion sputtering [reproduced with permission from 277]

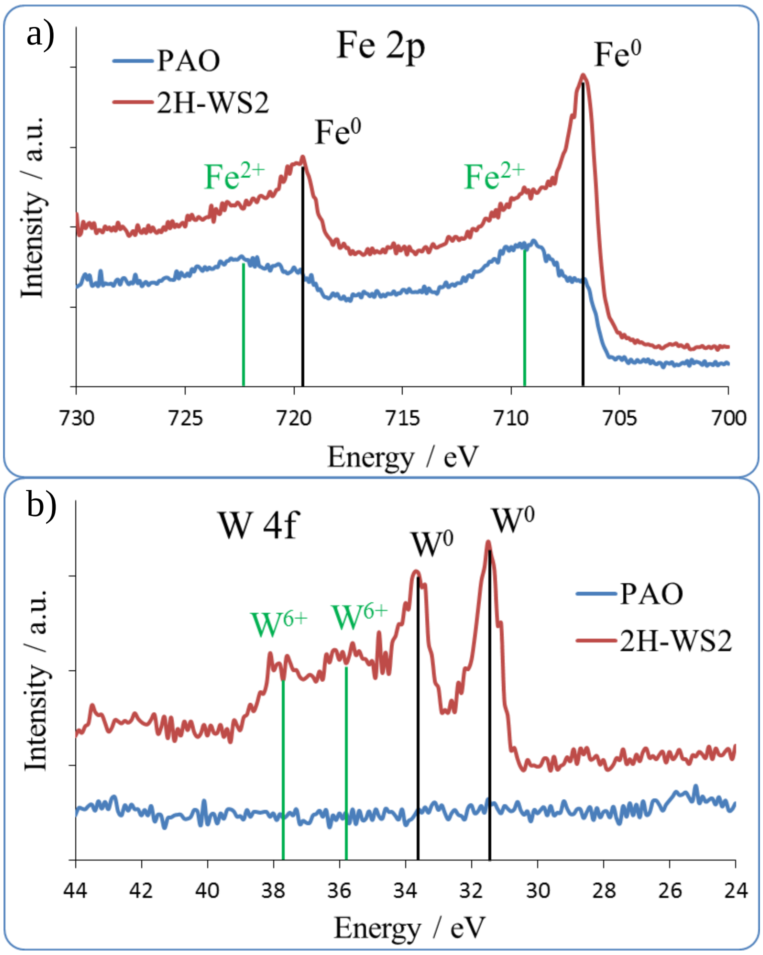

Figure 6.7 XPS spectra of Fe 2p and W 4f for PAO and PAO+WS_2 lubricated specimens [reproduced with permission from 277]

These findings are in agreement with previous reported results [287] and indicate a reaction between the 2H-WS$_2$ nanoadditive and the steel wear track, with the formation of iron sulphides, tungsten trioxide and elemental iron and tungsten. This type of chemical reaction that generates a tribofilm is characteristic of antiwear additives and explains the morphology of the wear tracks showing wider and smoother profiles. The XPS analysis of C$_{1s}$ also revealed a small amount of carbides present on the tribofilm, which may also help increase the mechanical properties of the tribofilm.

To achieve a better understanding of the mechanism of the NP reaction with the steel substrate, the wear track of the 10 hour 2H-WS$_2$ lubricated specimen was subjected to further analysis employing Auger spectroscopy.

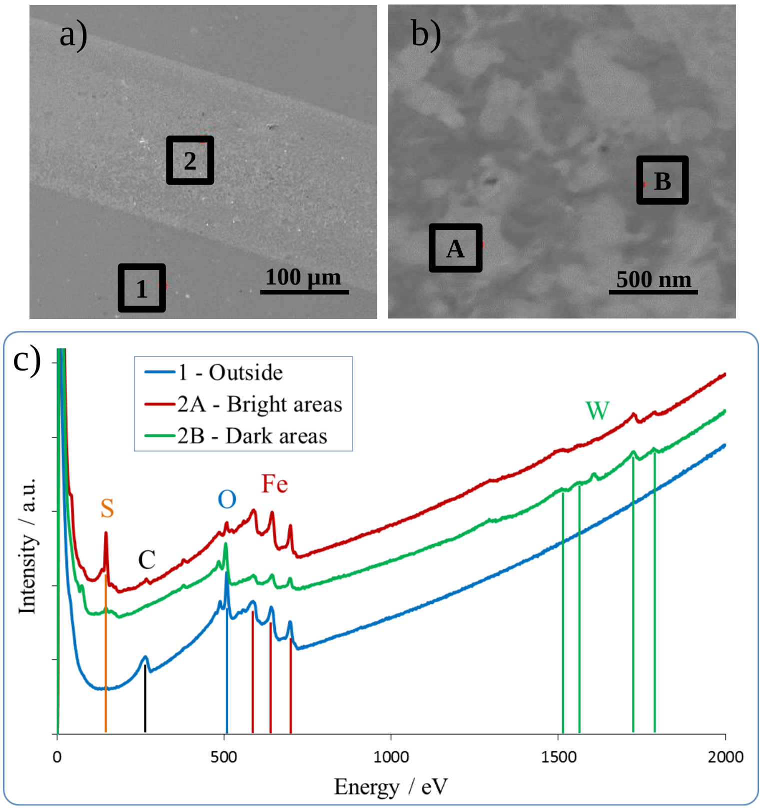

Figure 6.8 Auger spectra for the PAO+WS$_2$ sample and location of the analysis [reproduced with permission from 277]

Figure 6.8 shows the location of the analysis and the corresponding Auger spectra. Outside the wear track (position 1), only carbon (from decomposed oil), oxygen and iron were detected. Inside the track (position 2), two separate regions were found with SEM imaging, bright (A) and dark (B), and chemical analysis was performed on each of these sections. The spectra indicate that the bright regions (A) are rich in iron and sulphur compounds, but also contain some amounts of tungsten species. The dark regions display mostly oxygen and tungsten species and small amounts of iron. The results indicate the predominant presence of iron sulphides in the bright areas and tungsten oxides in the dark areas. The signals identified were carbon (C_{KLL}, 269 eV), oxygen (O_{KLL}, 509 eV), iron (Fe_{LMM}, 592 eV, 645 eV and 700 eV), sulphur (S_{LMM}, 148 eV) and tungsten (W_{MNN}, 1512 eV, 1565 eV, 1726 eV and 1787 eV). The values have been verified against literature data [313].

Auger elemental mapping was performed on the wear track of the 2H-WS_2-lubricated specimen to visualize the distribution of the main constituents of the tribofilm. As seen in Figure 6.9, the distributions of iron and sulphur are similar and indicate the presence of iron sulphides. The rest of the investigated area is covered by oxygen compounds. Tungsten is found more uniformly distributed across the track, as also seen in the Auger spectra recorded in both dark and bright areas.

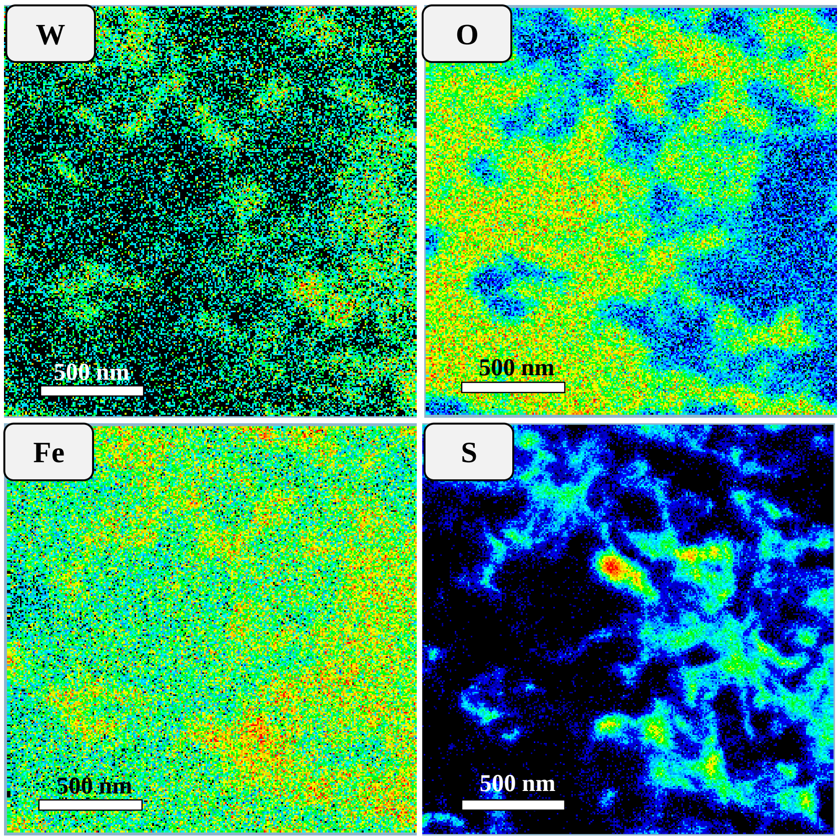

Figure 6.9 Auger elemental mapping for the PAO+2H-WS_2 specimen [reproduced with permission from 277]

The results of the XPS and Auger analysis are in good agreement and indicate the generation of a thin tribofilm on the wear track. The formation of the chemical film can explain the controlled wear seen during the testing (2, 5 and 10 hours) and the smoother wear tracks produced by the 2H-WS_2 lubricant. The properties of the tribofilm reported in previous studies account for the reduced hydrogen permeated in the bearing steel.

These effects are achieved through a number of mechanisms. The continuous generation of film through the reaction of 2H-WS_2 with the wear track impedes the formation of fresh, catalytic surfaces during rubbing and thus prevents the decomposition of oil/water molecules and generation of atomic hydrogen.

The tribofilm can also act as a physical barrier for hydrogen permeating through the wear track. Previous research showed that a thin layer of nickel electrodeposited on the steel substrate can effectively reduce hydrogen permeation due to its very small coefficient of hydrogen diffusion as compared to the coefficient of diffusion through steel [64]. It was also reported that the diffusion coefficient of hydrogen through steel decreases with the increase of tungsten content [199].

Therefore, the chemical composition of the 2H-WS_2 generated tribofilm, comprising of tungsten in elemental and oxide form, could be an effective obstacle to the permeation of hydrogen atoms in steel.

The presence of tungsten in the tribofilm also increases its hardness and results in less wear. This delays the formation of active catalytic surfaces on the metal substrate and prevents the generation of atomic hydrogen.

Furthermore, hydrogen may play an active role in the generation of the tribofilm i.e. tungsten and iron are also found in their elemental states in the film and some amounts of hydrogen could be used up for the chemical reduction of these metal species to their elemental form instead of permeating the steel.

All the above mentioned discussed benefits offered by the 2H-WS_2 additized oil in reducing hydrogen embrittlement have been summarized in Figure 6.10.

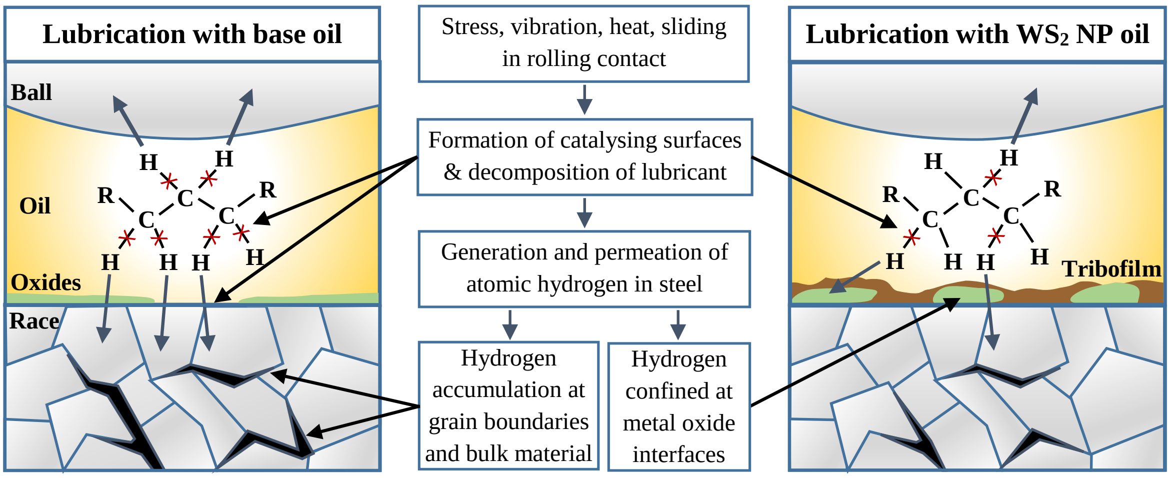

Figure 6.10 Lubrication with PAO base oil and 2H-WS_2 NP additized oil [reproduced with permission from 277]

Previous studies of the 2H-WS_2 nanoadditive, which employed milder loading conditions (1 GPa), resulted in a tribofilm formed only on the wear track, above the surface level. The thickness of the tribofilm could be measured with optical interferometry (SLIM) and profilometry (Alicona) and it was found to be approximately 100 nm. The tribofilm showed a uniform chemical composition across the track and had a layered structure. The upper part was composed of unreacted 2H-WS_2 NP sheets, WO_3, iron oxides and sulphides, while the deeper layers and the interface with the steel substrate consisted of WO_3 and elemental tungsten and iron [287, 301].

The severe contact conditions employed in the current study, with contact pressures of 4.8 GPa specifically used to accelerate the wear process, generated wear scars below the surface level which did not allow the measurement of the tribofilm thickness. Figures 6.8 (c) and 6.9 show the presence of a tribofilm and its chemical composition varies across the scanned area. The elemental mapping of the tribofilm revealed the presence of two chemically different regions. This indicates that the tribofilm is either partly formed or partly worn off. In a tribological contact, the film growth is controlled by its generation (chemical reaction kinetics) and removal (wear) rates, which depend on the operating conditions, such as temperature, time, load, slide-roll ratio etc. [56-58]. In practical applications the contact pressures in bearings are much lower than those used in this study, which favours the generation of thicker and more uniform films. These properties of the tribofilm have the potential to increase their efficiency to impede permeation of hydrogen into bearing steel.

6.3 Conclusions

In Chapters 4 and 5 it was shown that 2H-WS_2 NPs react with the steel substrate at high temperatures and pressures to form a protective tribofilm. This study has investigated the ability of this tribofilm to reduce the permeation of hydrogen into rolling element bearings and thus prevent hydrogen embrittlement.

- Rolling contact tests were conducted in a ball-on-disc setup using 2H-WS_2 NP additized and plain PAO oil as lubricants. The concentration of hydrogen in the specimens, measured with TDS at the end of the tests, was significantly reduced for the 2H-WS_2-additized oil (by ~30%). The results were attributed to the chemical tribofilm generated on the wear track during the test and its specific properties.

- Chemical analysis performed on the tribofilm generated by the 2H-WS_2 NPs revealed the presence of two different regions: one rich in iron sulphides, while the other is mostly composed of tungsten trioxide. This composition suggests an intermediary state during the formation of a full chemical tribofilm.
- The tribofilm accounts for the controlled wear recorded during the testing (2, 5 and 10 hours), smoother wear tracks and the reduced hydrogen concentration permeated in the bearing steel. These effects are achieved through: 1) the continuous generation of film through the reaction of the 2H-WS_2 NPs with the wear track, which impedes the formation of fresh, catalytic surfaces during rubbing and thus prevents the decomposition of oil/water molecules and generation of atomic hydrogen; 2) the tribofilm acting as a physical barrier for hydrogen permeation through the wear track; 3) the lower coefficients of hydrogen diffusion in tungsten compounds, which impede hydrogen permeation; 4) the contribution of hydrogen to the generation of the tribofilm by redox reactions (i.e. reducing the chemical state of tungsten and iron).
- 2H-WS_2 NP tribofilms reduce the total amount of water in the steel, entailing both surface and bulk-adsorbed molecules and water formed from the reaction of hydrogen atoms with oxides. By reducing the water content, 2H-WS_2 NP additives can exert a beneficial effect on lubricated steels, such as extending the life of the steel, inhibiting oxidation in the substrate and decelerating the growth of any cracks present in the material.

The results of the study indicate that 2H-WS_2 nanoadditives can reduce hydrogen embrittlement of bearing steel and extend RCF life. 2H-WS_2 NPs are a promising candidate for applications affected by hydrogen embrittlement, but further work must be carried out to determine optimal operating conditions for the formation of a thick tribofilm in the contact.

7. CONCLUSIONS

This study focused on investigating the tribological properties of WS_2 NPs and their potential to become novel lubricant nanoadditives, which can replace the problematic AW/EP additives currently available. WS_2 NPs have received increased interest in the past years, but a consensus on their mechanism of action in high-pressure lubricated contacts has not been achieved.

To address these aspects, tungsten dichalcogenide (2H-WS_2, IF-WS_2 and IF-WSe_2) dispersions in synthetic base oils were tested in an MTM2 rig at high pressures (1 GPa) and a range of temperatures (40ºC and 100ºC). The physical, chemical and mechanical properties of the chemical tribofilms generated on the wear tracks were analysed using a wide range of techniques (including optical microscopy, Alicona profilometry, 3D SLIM, FIB/SIMS, XPS and nanoindentation) to reveal their structure and to determine the mechanism of action. The influence of several factors that are known to affect tribological performance, such as time, temperature (40 ºC vs 100 ºC), oil polarity (PPG vs PAO) and NP structure (2H-WS_2 vs IF-WS_2) were also investigated.

The FM/AW properties of 2H-WS_2 NP dispersions were compared to those of popular conventional additives, such as ZDDPs and OFMs.

This is the first study that investigates the ability of 2H-WS_2 NPs to inhibit hydrogen permeation related to hydrogen embrittlement. RCF tests were performed in high-pressure high-temperature conditions to induce the accelerated permeation of hydrogen into bearing steel.

The main conclusions of this study are presented below.

The mechanism of action of WS_2 NPs

The 2H-WS_2 NPs investigated in this study show two particle size distributions, i.e. 20-30 nm and ~250 nm. This particular PSD may be an advantage in tribological contacts, which contain asperities of various shapes and sizes. The NPs have a layered structure and possess low interlayer shear strength, which allows them to exfoliate under the high shear/pressure conditions encountered in tribological contacts and imparts their FM properties. The AW behaviour of the NPs is given by their ability to react with the steel substrate and generate a chemical tribofilm.

1 % w/w 2H-WS_2 NPs were dispersed in two base oils of different polarities (PAO and PPG) to test the influence of oil polarity on the performance of the nanoadditives.

At 40ºC the 2H-WS_2 NP dispersions only showed a modest reduction in the COF compared to the PPG and PAO base oils. A thin and patchy tribofilm was generated on the wear track (~30 nm thick), consisting mainly of agglomerated or flattened 2H-WS_2 NPs. XPS analysis found small quantities of WO_3 and iron sulphides, indicating that a chemical reaction has started to take place on the steel substrate, but the reaction rate was slow due to the low temperature.

The 2H-WS_2 NP dispersions in both oils showed a remarkably different behaviour at higher temperatures. At 100ºC, the dispersions induced a very small value of the COF in the boundary lubrication regime (~0.08 in PPG and ~0.06 in PAO) and an increasing COF with time in the mixed regime, indicating the formation of a rough tribofilm. Chemical analysis of the wear tracks investigated the structure of the thick chemical tribofilms (100-200 nm). A layered structure was proposed, in which the upper part of the tribofilm is covered with unreacted 2H-WS_2 NP sheets, WO_3, iron oxides and sulphides. The deeper layers contain WO_3 and elemental W and Fe, while the film at the interface with the steel substrate is composed of only elemental W and Fe.

The presence of W compounds throughout the tribofilm improves its mechanical properties, as confirmed by nanoindentation, which measured high hardness (5.8 ± 0.6 GPa) and reduced Young's modulus (166 ± 19 GPa) values. The excellent AW tribological properties of 2H-WS_2 NPs were attributed to the formation of this tribofilm.

Tests also showed that 2H-WS_2 NPs are more efficient when used in nonpolar oils such as PAO, which does not compete for adsorption on the polar sites of the tribological contact and therefore allows the generation of the chemical tribofilm.

Comparison between tungsten dichalcogenide NPs

SLIM interferometry analysis on the ball wear tracks indicated that the chemical tribofilms generated by IF-WS_2 (61 ± 5) and IF-WSe_2 (46 ± 8) have a smaller thickness compared to 2H-WS_2 (98 ± 7). Alicona measurements on the disc wear track showed that the IF-WS_2 and IF-WSe_2 NPs also adhere onto the chemical films and form a physical layer, which can be removed by washing with solvents.

The COF in the boundary regime after 3 h of rubbing was much higher for IF-WS_2 (0.095) and IF-WSe_2 (0.12) than for the 2H-WS_2 NP dispersion (0.06).

A comparison between the AW properties of the NPs was made by measuring the width of the wear track after the tribological tests. It was found that 2H-WS_2 NPs (290 µm) appear to have superior AW behaviour compared to IF-WS_2 (300 µm) and IF-WSe_2 (300 µm).

The results indicate that 2H-WS_2 nanoadditives have the best FM and AW properties of the three dicalcogenides tested and that they are a potential candidate to obtain a novel lubricant.

Comparison between 2H-WS_2 NPs and conventional lubricant additives

This study compared the performance of 2H-WS_2 NPs with popular conventional additives such as AW ZDDPs and organic FMs, which are frequently used together in oil formulations.

The efficiency of OFMs relies on their ability to adsorb onto the steel surfaces and generate thin boundary films, but this mechanism can interfere with the formation of the ZDDP-generated tribofilm. A straight chain polyamidoalcohol was able to reduce the ZDDP tribofilm thickness from ~204 nm to ~165 nm, while also delaying its formation by ~30 minutes under the testing conditions used in this study.

FIB analysis was used to observe the morphology of the ZDDP tribofilm. Consistent with results reported in the literature, the film shows a pad-like structure, with individual pads measuring 5-20 µm in size and 200-250 nm in thickness. The tribofilm also contains dark particles, which are attributed to the embedded metal oxide particles. However, the thickness and morphology of the ZDDP tribofilm may change in different test conditions.

ZDDP-based lubricants induce large values of the COF in the boundary regime. The OFM was able to decrease the COF to ~0.1, but also interfered with the formation of the ZDDP tribofilm, leading to films ~165 nm thick. By contrast, the 2H-WS_2 NP-generated tribofilm is thinner (~98 nm), but it is covered with unreacted 2H-WS_2 sheets, which exert a levelling and smoothing effect of the rough areas of the chemical tribofilm and thus significantly lower the boundary friction to ~0.06. Compared to ZDDP+OFM, 2H-WS_2 tribofilms are generated much faster and show a superior ability to decrease friction in the boundary regime.

The tribofilms generated by 2H-WS_2 NPs have superior mechanical properties compared to those generated by ZDDP and ZDDP+OFM, due to the layered structure rich in elemental tungsten and tungsten trioxide. Lower values of hardness and reduced

Young's modulus were found for ZDDP (H = 4.3 ± 1 GPa and E' = 140 ± 24 GPa) and ZDDP+OFM (H = 3.2 ± 1.8 GPa and E' = 85 ± 57 GPa). Therefore, the OFM also affected the mechanical properties of the ZDDP tribofilm. These results suggest that the AW performance of the 2H-WS_2 NPs is superior to lubricants containing common additives such as ZDDP and OFMs.

The experiments conducted in this study showed that in high-pressure high-temperature conditions 2H-WS_2 NPs have the advantage of reducing both friction and wear and show great potential for the replacement of some of the most popular but problematic additives in use.

ZDDP generates thick tribofilms in nonpolar oils such as PAO, but its AW activity is hindered by polar base oils such as PPG. Polar molecules can compete for adsorption/reaction with the steel substrate. In the testing conditions employed in this study the thickness of the tribofilm was dramatically reduced from ~204 nm in PAO to ~95 nm in PPG.

Prior to this study, other researchers attempted to functionalize and disperse WS_2 NPs in base oils using toxic reagents or elaborate syntheses involving complex molecules. Functionalization with dispersants containing highly hydrophobic chains such as silanes may achieve a stable oil dispersion, but the NPs will not be attracted to the polar steel contact and therefore will not be ideal AW and FM additives. During this project, 2H-WS_2 NPs were functionalized and stable dispersions in base oil were prepared while considering their affinity for the steel substrate. The method is currently being prepared for a patent application.

The influence of 2H-WS_2 NPs on hydrogen permeation into bearing steel

2H-WS_2 NP dispersions are capable of reducing the concentration of hydrogen in the specimens by ~30 % compared to the PAO base oil, due to the generation of a chemical tribofilm on the wear track during the RCF tests.

The chemical properties of the tribofilm were investigated using XPS and AES, revealing the presence of two different regions: one rich in iron sulphides, while the other is mainly composed of tungsten trioxide. The presence of these regions suggests that the chemical tribofilm is in an intermediary state during its formation. Nevertheless, the wear tracks generated by the 2H-WS_2 NPs are smoother than for PAO, which indicates that the AW properties of the NPs induce a controlled wear rate during the tests.

A number of reasons were proposed for the reduced amount of hydrogen measured in the steel samples lubricated with the nanoadditive. They are all related to the continuous formation of the chemical tribofilm on the wear track:

- The smaller amount of fresh catalytic surfaces formed during rubbing, which are responsible for the decomposition of oil/water molecules and generation of atomic hydrogen.
- The formation of a physical barrier for hydrogen permeation.
- The lower coefficients of hydrogen diffusion through the tungsten compounds present in the tribofilm.
- The involvement of hydrogen in the chemical reactions that occur during the generation of the tribofilm (i.e. reducing the chemical state of tungsten and iron).

The tribofilm generated by 2H-WS_2 can also reduce the total amount of water in the steel, which is due to both surface and bulk-adsorbed molecules and water formed from the reaction of atomic hydrogen with oxides in the film. Water molecules promote oxidation in the substrate and the growth of any cracks present in the material and therefore, by reducing the water content, 2H-WS_2 nanoadditives can exert a beneficial effect and extend the service life of the steel.

This study shows that 2H-WS_2 nanoadditives can reduce hydrogen generation and permeation into high-strength bearing steels and extend their RCF life. Although they are a promising candidate for applications affected by hydrogen embrittlement, the efficiency of 2H-WS_2 NPs depends on the formation of a thick tribofilm on the wear track and therefore, further work must be carried out to determine optimal operating conditions.

8. FUTURE WORK

Tribological performance of 2H-WS$_2$ NPs after functionalization

Stable dispersions of 2H-WS$_2$ in base oil have been obtained by functionalizing the surface of the NPs. However, it is possible that this process affects the affinity of the NPs for the steel surface and may delay/inhibit the growth of a chemical tribofilm in the contact. In order to verify the effect of the surfactant molecules on the tribological properties of 2H-WS$_2$, further tests should be performed and compared with those presented in the current study.

Investigation of the AW properties of WS$_2$ NPs

Preliminary investigations of the AW properties of 2H-WS$_2$ NPs have been performed by measuring the width of the wear track on the steel disc samples at the end of the three hour tests and by considering the mechanical properties of the tribofilms generated in the contact. Although wear volume measurements are a more accurate way of determining the AW properties of additives, such measurements were not possible in the current study because the tribofilms generated in the contact were above the surface level, essentially yielding negative wear volumes. A different testing technique must be employed to generate measurable wear scars (e.g four-ball test).

Interaction with oil additives

This study has investigated the tribological properties of 2H- and IF-WS$_2$ NP dispersions in base oils, without the use of any surfactants/dispersants, in order to understand their basic mechanism of action. However, lubricants often contain a large number of additives and a number of studies in the literature have demonstrated an interaction between them. Therefore, the efficiency of the WS$_2$ NPs in fully formulated oils must be investigated.

Identifying optimum conditions for use of WS_2 NPs in applications affected by HE

The RCF tests that investigated the ability of the tribofilm generated by 2H-WS_2 NPs to reduce hydrogen permeation were conducted under different operating conditions compared to the tests which investigated the mechanism of tribofilm formation. Operating parameters such as temperature and contact pressure play an important role in the growth of the chemical tribofilm. The film generated in the RCF tests was only in an intermediary formation phase due to the testing conditions employed. It is likely that under milder conditions the 2H-WS_2 NPs can generate a fully formed, thick tribofilm that can further reduce hydrogen generation and permeation in the steel. Additional tests should be conducted to find the optimum conditions for the 2H-WS_2 nanoadditive.

Development of a responsive and recyclable WS_2 nanoadditive

With a correct choice of parameters and surfactants it is possible to obtain a functional nanoadditive that is not only stable to aggregation and separation from the oil, but is also responsive to certain conditions and recyclable. The functionalization process which allows the use of 2H-WS_2 NPs in base oils is currently being prepared for a patent application.

REFERENCES

[1] G. Stachowiak, A. W. Batchlor, *Engineering tribology*, 3rd Edition, Butterworth-Heinemann, **2006**.

[2] J. Williams, *Engineering tribology*, Cambridge University Press, **2005**.

[3] E. Salek, *Handbook of lubrication and tribology: theory and design*, Volume 2 of Handbook of lubrication and tribology, CRC Press, **2012**.

[4] B. Bhushan, *Principles and applications of tribology*, John Wiley & Sons, **1999**.

[5] J. Persson, *Sliding friction: physical principles and applications*, Volume 1 of NanoScience and Technology, Springer, **2000**, 9-16.

[6] B. Tower, First report on friction experiments, *Proc. Inst. Mech. Eng.*, 1883, **34**, 632.

[7] D. Dowson, *History of Tribology*, 2nd Edition, Professional Engineering Publishing, **1998**.

[8] H. Spikes, The history and mechanisms of ZDDP, *Tribol. Lett.*, 2004, **17**(3), 469-489.

[9] V. N. Bakunin, A. Y. Suslov, G. N. Kuzmina, O. P. Parenago, Synthesis and application of inorganic nanoparticles as lubricant components – a review, *J. Nanopart. Res.*, 2004, **6**(2), 273-284.

[10] O. Tevet, P. Von-Huth, R. Popovitz-Biro, R. Rosentsveig, H. D. Wagner, R. Tenne, Friction mechanism of individual multi-layered nanoparticles, *Proc. Natl. Acad. Sci. U. S. A., Early Ed.*, 2011, **108**(50), 19901-19906.

[11] Y. Y. Wu, W. C. Tsui, T. C. Liu, Experimental analysis of tribological properties of lubricating oils with nanoparticle additives, *Wear*, 2007, **262**(7-8), 819-825.

[12] R. Tenne, M. Redlich, Recent progress in the research of inorganic fullerene-like nanoparticles and inorganic nanotubes, *Chem. Soc. Rev.*, 2010, **39**(5), 1423-1434.

[13] B. A. Rozenberg, R. Tenne, Polymer-assisted fabrication of nanoparticles and nanocomposites, *Prog. Polym. Sci.*, 2008, **33**, 40-112.

[14] J. Persson, *Sliding friction: physical principles and applications,* Volume 1 of NanoScience and Technology, Springer, **2000**, 1-8.

[15] A. Pytel, J. Kiusalaas, *Engineering mechanics: statics*, 3rd Edition, Cengage Learning, **2010**, 341-400.

[16] R. Lu, I. Minami, H. Nanao, S. Mori, Investigation of decomposition of hydrocarbon oil on the nascent surface of steel, *Tribol. Lett.*, 2007, **27**(1), 25-30.

[17] E. A. Gulbrasen, The role of minor elements in the oxidation of metals, *Corrosion*, 1956, **12**, 61-67.

[18] M. Eriksson, F. Bergman, S. Jacobson, On the nature of tribological contact in automotive brakes, *Wear*, 2002, **252**, 26-36.

[19] L. R. Rudnick, *Lubricant additives: chemistry and applications*, 2nd Edition, CRC Press, **2010**.

[20] R. M. Mortier, M. Fox, S. T. Orszulik, *Chemistry and technology of lubricants*, 3rd Edition, Springer, **2010**.

[21] M. Ratoi, V. Anghel, C. Bovington, H. A. Spikes, Mechanism of oiliness additives, *Tribol. Int.*, 2000, **33**, 241-247.

[22] M. Ratoi, C. H. Bovington, H. A. Spikes, In situ study of metal oleate friction modifier additives, *Tribol. Lett.*, 2003, **14**(1), 33-40.

[23] M. Ratoi, WS_2 Fullerene-like Lubricant Nano-Additives – A Review, *2nd UK-China Summer School of Tribology & Surface Engineering*, 2010.

[24] B. J. Hamrock, S. R. Schmid, B. O. Jacobson, *Fundamentals of fluid film lubrication*, 2nd Edition, Volume 169 of Mechanical Engineering, CRC Press, **2004**.

[25] P. Studt, The influence of the structure of isomeric octadecanols on their adsorption from solution on iron and their lubricating properties, *Wear*, 1981, **70**, 329-334.

[26] D. W. Morecroft, Reactions of octadecane and decoic acid with clean iron surfaces, *Wear*, 1971, **18**, 333-339.

[27] C. F. Prutton, D. R. Frey, D. Turnbull, G. Dlouhy, Corrosion of metals by organic acids in hydrocarbon solvents, *Ind. Eng. Chem.*, 1945, **37**(1), 90-100.

[28] S. V. Prasad, B. D. McConnell, Tribology of aluminum metal-matrix composites: lubrication by graphite, *Wear*, 1991, **149**, 241-253.

[29] L. Rapoport, Yu. Bilik, Y. Feldman, M. Homyonfer, S. B. Cohen, R. Tenne, Hollow nanoparticles of WS_2 as potential solid-state lubricants, *Nature*, 1997, **387**, 791-793.

[30] L. Rapoport, M. Lvovsky, I. Lapsker, V. Leshinsky, Y. Volovik, Y. Feldman, A. Zak, R. Tenne, Slow release of fullerene-like WS_2 nanoparticles as a superior solid lubrication mechanism in composite matrices, *Adv. Eng. Mater.*, 2001, **3**(1-2), 71-75.

[31] G. Cao, Y. Wang, *Nanostructures and nanomaterials: synthesis, properties and applications*, Volume 2, 2nd Edition, World Scientific Publishing, **2011**.

[32] M. S. Johal, *Understanding nanomaterials*, CRC Press, **2011**.

[33] P. Atkins, J. de Paula, Macromolecules and self-assembly, In *Atkins' Physical Chemistry*, 9th Edition, OUP Oxford, **2010**, 659-677.

[34] F. Caruso, *Colloids and colloid assemblies: synthesis, modification, organization and utilization of colloid particles*, Wiley-VCH Verlag GmbH & Co. KGaA, **2004**.

[35] A. Masuko, M. Hirata, H. Watanabe, Electron probe microanalysis of wear scars of Timken test blocks on sulfur-phosphorous type industrial gear oils, *ASLE Trans.*, 1977, **20**(4), 304-308.

[36] L. Rapoport, V. Leshchinsky, I. Lapsker, Yu. Volovik, O. Nepomnyashchy, M. Lvovsky, R. Popovitz-Biro, Y. Feldman, R. Tenne, Tribological properties of WS_2 nanoparticles under mixed lubrication, *Wear*, 2003, **255**(7-12), 785-793.

[37] J. F. Wu, W. S. Zhai, G. F. Jie, Preparation and tribological properties of WS_2 nanoparticles modified by trioctylamine, *Proc. Inst. Mech. Eng., Part J*, 2009, **223**(4), 695-703.

[38] W. Jifen, Z. Wensheng, J. Guifen, Preparation and tribological properties of tungsten disulfide hollow spheres assisted by methyltrioctylammonium chloride, *Tribol. Int.*, 2010, **43**(9), 1650-1658.

[39] M. Aktary, M. T. McDermott, G. A. McAlpine, Morphology and nanomechanical properties of ZDDP antiwear films as a function of tribological contact time, *Tribol. Lett.*, 2001, **12**(3), 155–162.

[40] Z. Zhang, E. S. Yamaguchi, M. Kasrai, G. M. Bancroft, Tribofilms generated from ZDDP and DDP on steel surfaces: part 1, growth, wear and morphology, *Tribol. Lett.*, 2005, **19**(3), 211–220.

[41] D. E. Jones, G. A. Schott, *Miscellaneous papers by Heinrich Hertz*, London: Macmillan, **1896**.

[42] K. L. Johnson, *Contact Mechanics*, Cambridge University Press, **1987**, 84-106.

[43] PCS Instruments, *EHL Ultra thin film measurement system*, Retrieved: April 2013, http://www.pcs-instruments.com/ehd/applications/ehd-thin-measurement-system.shtml.

[44] D. Dowson, The relationship between steady-state wear rate and theoretical film thickness in metal-on-metal total replacement hip joints, *Tribological Research and Design for Engineering Systems*, Tribology Series, 2003, **41**, 273-280.

[45] D. Dowson, Thin Films in Tribology, *Tribol. Ser.*, 1993, **25**, 3-12.

[46] D. Zhu, Effect of surface roughness on mixed EHD lubrication characteristics, *Tribol. Trans.*, 2003, **46**(1), 44-48.

[47] D. Zhu, Y. Z. Hu, Effects of rough surface topography and orientation on the characteristics of EHD and mixed lubrication in both circular and elliptical contacts, *Tribol. Trans.*, 2001, **44**(3), 391-398.

[48] Y. Z. Hu, D. Zhu, A full numerical solution to the mixed lubrication in point contacts, *J. Tribol.*, 1999, **122**(1), 1-9.

[49] L. Chang, H. Yang, W. Fu, N. Yang, J. Chen, M. Li, G. Zou, J. Li, Synthesis and thermal stability of W/WS_2 inorganic fullerene-like nanoparticles with core-shell structure, *Mater. Res. Bull.*, 2006, **41**, 1242-1248.

[50] M. Ratoi Salagean, The design of lubricating oil-in-water emulsions, PhD Thesis, University of London, July 1996.

[51] T. Sasada, M. Oike, N. Emori, The effect of abrasive grain size on the transition between abrasive and adhesive wear, *Wear*, 1984, **97**(3), 291-302.

[52] R. W. Johnson, The use of the scanning electron microscope to study the deterioration of abrasive papers, *Wear*, 1968, **12**(3), 213-216.

[53] N. Canter, Special report: additive challenges in meeting new automotive engine specifications, *Tribol. Lubr. Technol.*, 2006, 10–19.

[54] H. A. Spikes, Low- and zero-sulphated ash, phosphorous and sulphur anti-wear additives for engine oils, *Lubr. Sci.*, 2008, **20**(2), 103–136.

[55] F. P. Bowden, G. W. Rowe, The adhesion of clean metals, *Proc. R. Soc. London, Ser. A*, 1956, **233**, 429-442.

[56] M. Ratoi, V. B. Niste, H. Alghawel, A. Suen, K. Nelson, The impact of organic friction modifiers on engine oil tribofilms, *RSC Adv.*, 2014, **4**, 4278-4285.

[57] J. M. Palacios, Films formed by antiwear additives and their incidence in wear and scuffing, *Wear*, 1987, **114**(1), 41-49.

[58] J. M. Palacios, Thickness and chemical composition of films formed by antimony dithiocarbamate and zinc dithiophosphate, *Tribol. Int.*, 1986, **19**(1), 35-39.

[59] H. K. D. H. Bhadeshia, Steels for bearings, *Prog. Mater. Sci.*, 2012, **57**, 268-435.

[60] W. H. Johnson, On some remarkable changes produced in iron and steel by the action of hydrogen and acids, *Proc. R. Soc. London*, 1874, **23**, 168-179.

[61] H. Harada, T. Mikami, M. Shibata, D. Sokai, A. Yamamoto, H. Tsubakino, Microstructural changes and crack initiation with white etching area formation under rolling/sliding contact in bearing steel, *ISIJ Int.*, 2005, **45**(12), 1897-1902.

[62] S. Brahimi, *Fundamentals of hydrogen embrittlement in steel fasteners*, 2014. http://www.boltcouncil.org/files/HydrogenEmbrittlementInSteelFasteners-Brahimi.pdf. Retrieved: March 2015.

[63] A. Barnoush, *Hydrogen embrittlement*, 2011. http://www.uni-saarland.de/fak8/wwm/research/phd_barnoush/hydrogen.pdf. Retrieved: March 2015.

[64] N. Kino, K. Otani, The influence of hydrogen on rolling contact fatigue life and its improvement, *JSAE Rev.*, 2003, **24**, 289-294.

[65] Y. R. Li, G. Pereira, M. Kasrai, P. R. Norton, The effect of steel hardness on the performance of ZDDP antiwear films: a multi-technique approach, *Tribol. Lett.*, 2008, **29**, 201–211.

[66] A. Erdemir, *Large-scale manufacturing of nanoparticulate-based lubrication additives for improved energy efficiency and reduced emissions*, United States, 2013. Retrieved: April 2013. http://www.osti.gov/scitech/servlets/purl/1097780.

[67] B. Spath, F. Kopnov, H. Cohen, A. Zak, A. Moshkovich, L. Rapoport, W. Jagermann, R. Tenne, X-ray photoelectron spectroscopy and tribology studies of annealed fullerene-like WS_2 nanoparticles, *Phys. Status Solidi B*, 2008, **245**(9), 1779-1784.

[68] L. R. Rudnick, *Lubricant additives: chemistry and applications*, 2nd Edition, CRC Press, **2010**.

[69] R. M. Mortier, M. Fox, S. T. Orszulik, *Chemistry and technology of lubricants,* 3rd Edition, Springer, **2010**.

[70] R. F. Haycock, A. J. Caines, *Automotive lubricants reference book*, 2nd Edition, John Wiley & Sons, **2004**.

[71] T. Mang, W. Dresel, *Lubricants and lubrication*, 2nd Edition, Wiley, **2007**.

[72] A. R. Lansdown, *Lubrication and lubricant selection*, Third Edition, Professional Engineering Publishing, **2004**.

[73] L. A. Toms, A. M. Toms, *Machinery oil analysis*, Third Edition, STLE, **2008**.

[74] L. R. Rudnick, *Synthetics, mineral oils, and bio-based lubricants, Chemistry and Technology*, Taylor & Francis Group, **2006**.

[75] M. Ratoi, H. A. Spikes, Langmuir-Blodgett films in high pressure rolling contacts, *Tribol. Trans.*, 2003, **46**, 24–30.

[76] F. P. Bowden, D. Tabor, *The friction and lubrication of solids, Volume 1*, Clarendon Press, Oxford, **1950**.

[77] E. P. Kingsbury, Some aspects of the thermal desorption of a boundary lubricant, *J. Appl. Phys.*, 1958, **29**, 888-891.

[78] D. Li, B. Hong, W. Fang, Y. Guo, R. Lin, Preparation of well-dispersed silver nanoparticles for oil-based nanofluids, *Ind. Eng. Chem. Res.*, 2010, **49**(4), 1697-1702.

[79] Z. Li, Y. Zhu, Surface-modification of SiO_2 nanoparticles with oleic acid, *Appl. Surf. Sci.*, 2003, **211**, 315-320.

[80] T. Arita, Y. Ueda, K. Minami, T. Naka, T. Adschiri, Dispersion of fatty acid surface modified ceria nanocrystals in various organic solvents, *Ind. Eng. Chem. Res.*, 2010, **49**(4), 1947-1952.

[81] X. Kang, B. Wang, L. Zhu, H. Zhu, Synthesis and tribological property study of oleic acid-modified copper sulphide nanoparticles, *Wear*, 2008, **265**, 150-154.

[82] S. Chen, W. Liu, Oleic acid capped PbS nanoparticles: synthesis, characterization and tribological properties, *Mater. Chem. Phys.*, 2006, **98**(1), 183-189.

[83] L. Cizaire, B. Vacher, T. Le Mogne, J. M. Martin, L. Rapoport, A. Margolin, R. Tenne, Mechanisms of ultra-low friction by hollow inorganic fullerene-like MoS_2 nanoparticles, *Surf. Coat. Technol.*, 2002, **160**(2-3), 282-287.

[84] O. P. Parenago, Molybdenum compounds as efficient additives to lubricants, In *Molybdenum: Characteristics, Production and Applications*, ed. M. Ortiz, T. Herrera, Nova Science Publishers, New York, **2012**.

[85] T. W. Scharf, S. V. Prasad, Solid lubricants: a review, *J. Mater. Sci.*, 2013, **48**(2), 511-531.

[86] J. P. G. Farr, Molybdenum disulphide in lubrication. A review, *Wear*, 1975, **35**(1), 1-22.

[87] H. E. Sliney, Solid lubricant materials for high temperatures – a review, *Tribol. Int.*, 1982, **15**(5), 303-315.

[88] W. O. Winer, Molybdenum disulfide as a lubricant: A review of the fundamental knowledge, *Wear*, 1967, **10**(6), 422-452.

[89] A. Erdemir, Solid lubricants and self-lubricating films, In *Modern Tribology Handbook, Two Volume Set*, ed. B. Bhushan, CRC Press, **2000**.

[90] G. A. Tsigdinos, Inorganic sulfur compounds of molybdenum and tungsten, In *Topics in Current Chemistry, Volume 76, Aspects of molybdenum and related chemistry*, ed. F. L. Boschke, Springer Berlin Heidelberg, **1978**.

[91] S. Huang, Y. Feng, H. Liu, K. Ding, G. Qian, Electrical sliding friction and wear properties of Cu-MoS_2-graphite-WS_2 nanotubes composites in air and vacuum conditions, *Mater. Sci. Eng., A*, 2013, **560**, 685-692.

[92] J. M. Martin, N. Ohmae, Nanoparticles made of metal dichalcogenides, In *Nanolubricants; Volume 13 of Tribology in Practice Series*, John Wiley & Sons, Chichester, **2008**.

[93] L. Yu, P. Zhang, Z. Du, Tribological behavior and structural change of the LB film of MoS_2 nanoparticles coated with dialkyldithiophosphate, *Surf. Coat Technol.*, 2000, **130**(1), 110-115.

[94] M. I. Barros'Bouchet, J. M. Martin, T. Le-Mogne, B. Vacher, Boundary lubrication mechanisms of carbon coatings by MoDTC and ZDDP additives, *Tribol. Int.*, 2005, **38**, 257-264.

[95] E. S. Yamaguchi, S. H. Roby, Time-dependent film formation from ZnDTPs and nonphosphorous antiwear agents, *Tribol. Trans.*, 2005, **48**, 57–68.

[96] K. Topolovec Miklozic, J. Graham, H. Spikes, Chemical and physical analysis of reaction films formed by molybdenum dialkyl-dithiocarbamate friction modifier additive using Raman and atomic force microscopy, *Tribol. Lett.*, 2001, **11**(2), 71-81.

[97] P. C. H. Mitchell, Oil-soluble Mo-S compounds as lubricant additives, *Wear*, 1984, **100**(1-3), 281-300.

[98] J. Graham, H. Spikes, S. Korcek, The friction reducing properties of molybdenum dialkyldithiocarbamate additives: part I – factors influencing friction reduction, *Tribol. Trans.*, 2001, **44**(4), 626-636.

[99] J. Graham, H. Spikes, R. Jensen, The friction reducing properties of molybdenum dialkyldithiocarbamate additives: part II – durability of friction reducing capability, *Tribol. Trans.*, 2001, **44**(4), 637-647.

[100] C. Grossiord, K. Varlot, J. M. Martin, Th. Le Mogne, C. Esnouf, K. Inoue, MoS_2 single sheet lubrication by molybdenum dithiocarbamate, *Tribol. Int.*, 1998, **31**(12), 737-743.

[101] M. I. De Barros, J. Bouchet, I. Raoult, Th. Le Mogne, J. M. Martin, M. Kasrai, Y. Yamada, Friction reduction by metal sulfides in boundary lubrication studied by XPS and XANES analyses, *Wear*, 2003, **254**(9), 863-870.

[102] A. Morina, A. Nevile, M. Priest, J. H. Green, ZDDP and MoDTC interactions in boundary lubrication – the effect of temperature and ZDDP/MoDTC ratio, *Tribol. Int.*, 2006, **39**(12), 1545-1557.

[103] J. M. Martin, C. Grossiord, K. Varlot, B. Vacher, J. Igarashi, Synergistic effects in binary systems of lubricant additives: a chemical hardness approach, *Tribol. Lett.*, 2000, **8**(4), 193-201.

[104] A. Morina, A. Nevile, M. Priest, J. H. Green, ZDDP and MoDTC interactions and their effect on tribological performance – tribofilm characteristics and its evolution, *Tribol. Lett.*, 2006, **24**(3), 243-256.

[105] M. Kasrai, J. N. Cutler, K. Gore, G. Canning, G. M. Bancroft, K. H. Tan, The chemistry of antiwear films generated by the combination of ZDDP and MoDTC examined by X-ray absorption spectroscopy, *Tribol. Trans.*, 1998, **41**(1), 69-77.

[106] S. Bec, A. Tonck, J. M. Georges, G. W. Roper, Synergistic effects of MoDTC and ZDTP on frictional behaviour of tribofilms at the nanometer scale, *Tribol. Lett.*, 2004, **17**(4), 797-809.

[107] M. Muraki, Y. Yanagi, K. Sakaguchi, Synergistic effect on frictional characteristics under rolling-sliding conditions due to a combination of molybdenum dialkyldithiocarbamate and zinc dialkyldithiophosphate, *Tribol. Int.*, 1997, **30**(1), 69-75.

[108] J. M. Martin, Th. Le Mogne, C. Grossiord, Th. Palermo, Tribochemistry of ZDDP and MoDDP chemisorbed films, *Tribol. Lett.*, 1996, **2**(3), 313-326.

[109] R. Unnikrishnan, M. C. Jain, A. K. Harinarayan, A. K. Mehta, Additive-additive interaction: an XPS study of the effect of ZDDP on the AW/EP characteristics of molybdenum based additives, *Wear*, 2002, **252**, 240-249.

[110] K. Komvopoulos, S. A. Pernama, P. R. Ryason, Friction reduction and antiwear capacity of engine oil blends containing zinc dialkyl dithiophosphate and molybdenum-complex additives, *Tribol. Trans.*, 2006, **49**, 151–165.

[111] A. Morina, A. Neville, Understanding the composition and low friction tribofilm formation/removal in boundary lubrication, *Tribol. Int.*, 2007, **40**, 1696–1704.

[112] C. Grossiord, J. M. Martin, K. Varlot, B. Vacher, T. Le Mogne, Y. Yamada, Tribochemical interactions between ZnDTP, MoDTC and calcium borate, *Tribol. Lett.*, 2000, **8**(4), 203–212.

[113] F. A. Davis, T. S. Eyre, The effect of a friction modifier on piston ring and cylinder bore friction and wear, *Tribol. Int.*, 1990, **23**(3), 163-171.

[114] T. Reeswinkel, D. Music, J. M Schneider, Coulomb-potential-dependent decohesion of Magnéli phases, *J. Phys.: Condens. Matter*, 2010, **22**, 292203.

[115] T. Reeswinkel, Self-lubricious tool coatings for ecological metal cutting, EngD Thesis, RWTH Aachen University, 2012.

[116] Ansong Omari et al., Tungsten dithiocarbamate compositions and lubricating compositions containing the same, US Patent WO2004043910 A2, 2004.

[117] Robert J. Tynik, Organoammonium tungstate and molybate compounds, and process for preparing such compounds, US Patent US7335625 B2, 2008.

[118] L. Yu, P. Zhang, Z. Du, Tribological behavior and structural change of the LB film of MoS_2 nanoparticles coated with dialkyldithiophosphate, *Surf. Coat. Technol.*, 2000, **130**(1), 110-115.

[119] J. Q. Hu, X. Y. Wei, G. L. Dai, Y. W. Fei, F. Xie, Z. M. Zong, Tribological behaviors and mechanism of sulfur- and phosphorus-free organic molybdate ester with zinc dialkyldithiophosphate, *Tribol. Int.*, 2008, **41**, 549-555.

[120] D. A. Bokarev, V. N. Bakunin, G. N. Kuz'mina, O. P. Parenago, Highly effective friction modifiers from nano-sized materials, *Chem. Technol. Fuels Oils*, 2007, **43**(4), 305-310.

[121] S. Yangming, J. Sijuan, Y. Jinyin, Z. Linqing, T. Kalue, W. Dedong, Friction behaviour and structure of boundary lubrication film for a molybdenum dithiolate anti-wear additive, *Tribol. Int.*, 1991, **24**(6), 357-364.

[122] D. W. Johnson, J. E. Hils, Phosphate esters, thiophosphate esters and metal thiophosphates as lubricant additives, *Lubricants*, 2013, **1**(4), 132-148.

[123] M. L. Suominen Fuller, M. Kasrai, G. M. Bancroft, K. Fyfe, K. H. Tan, Solution decomposition of zinc dialkyl dithiophosphate and its effect on antiwear and thermal film formation studied by X-ray absorption spectroscopy, *Tribol. Int.*, 1998, **31**(10), 627-644.

[124] L. Taylor, H. A. Spikes, Friction-enhancing properties of ZDDP antiwear additive: part I – friction and morphology of ZDDP reaction films, *Tribol. Trans.*, 2003, **46**, 303-309.

[125] M. Muraki, H. Wada, Frictional properties of organomolybdenum compounds in the presence of ZnDTP under sliding conditions, *Tribol. Ser.*, 1995, **30**, 409-422.

[126] K. Topolovec Miklozic, T. Reg Forbus, H. A. Spikes, Performance of friction modifiers on ZDDP-generated surfaces, *Tribol. Trans.*, 2007, **50**(3), 328–335.

[127] P. U. Aldana, B. Vacher, Th. Le Mogne, M. Belin, B. Thiebaut, F. Dassenoy, Action mechanism of WS_2 nanoparticles with ZDDP additive in boundary lubrication regime, *Tribol. Lett.*, 2014, **56**(2), 249-258.

[128] J. J. McCarroll, R. W. Mould, H. B. Silver, M. L. Sims, Auger electron spectroscopy of wear surfaces, *Nature*, 1977, **266**, 518-519.

[129] R. Schumacher, E. Gegner, A. Schmidt, H. J. Mathieu, D. Landolt, Auger electron spectroscopy study on reaction layers formed under Reichert wear test conditions in the presence of extreme pressure additives, *Tribol. Int.*, 1980, **13**(6), 311-317.

[130] A. Mammen, V. K. Verma, C. V. Agarwal, Mechanism of ep additive-metal interaction: assessment of certain S-benzylisothiocarbamides, *Tribol. Int.*, 1983, **16**(6), 291-296.

[131] R. J. Bird, G. D. Galvin, The application of photoelectron spectroscopy to the study of e. p. films on lubricated surfaces, *Wear*, 1976, **37**(1), 143-167.

[132] K. Arai, Y. Yamamoto, Effect of molybdenum dithiocarbamate on friction and wear properties between aluminum alloy and steel, *Tribol. Trans.*, 2000, **43**(1), 45-50.

[133] W. J. Bartz, K. Muller, Investigations on the lubricating effectiveness of molybdenum disulfide, *Wear*, 1972, **20**(3), 371-379.

[134] A. Knappwost, Physikalisch-chemische Reaktionseffekte bei der Feststoffschmierung mit Molybdändisulfid und mit Graphit-Einlagerungsverbindungen, *Naturwissenschaften*, 1965, **52**(16), 474.

[135] A. Knappwost, F. D. Grigutsch, Graphit-eisen(III)-chlorid-Einlagerungsverbindungen als Festschmierstoffe mit Reaktionseffekt, *Wear*, 1966, **9**(3), 189-198.

[136] H. Isoyama, T. Sakurai, The lubricating mechanism of di-*u*-thio-dithio-bis (diethyldithiocarbamate) dimolybdenum during extreme pressure lubrication, *Tribology*, 1974, **7**(4), 151-160.

[137] M. Hosokawa, K. Nogi, M. Naito, T. Yokoyama, *Nanoparticle technology handbook*, Elsevier, **2007**.

[138] Z. J. Zhang, D. Simionesie, C. Schaschke, Graphite and hybrid nanomaterials as lubricant additives, *Lubricants*, 2014, **2**(2), 44-65.

[139] K. Stadler, A Stubenrauch, Premature bearing failure in industrial gearboxes, *Antriebstechnisches Kolloquium (ATK)*, 2013, Aachen, Germany.

[140] Y. Feng, P. Tavner, Introduction to wind turbines and their reliability & availability, *Durham side event at the EWEC conference*, 2010, Warsaw.

[141] Advanced extreme pressure nano lubricants, APNano, Retrieved: June 2015, http://www.apnano.com/product/.

[142] NIS Nanotech Industrial Solutions, Retrieved: June 2015, http://nisusacorp.com/product/.

[143] Archoil Europe, Retrieved: June 2015, http://archoil.eu/tech/.

[144] Nano Extreme WS_2, Retrieved: June 2015, http://nanoextremews2.com/products/.

[145] M. Nosonovsky, B. Bhushan, Green tribology: principles, research areas and challenges, *Phil. Trans. R. Soc. A*, 2010, **368**, 4677-4694.

[146] L. Klebanoff, *Hydrogen storage technology: materials and applications*, CRC Press, **2012**.

[147] M. Hirscher, *Handbook of hydrogen storage*, John Wiley & Sons, **2010**.

[148] T. Endo, D. Dong, Y. Imai, Y. Yamamoto, Study on rolling contact fatigue in hydrogen atmosphere – Improvement of rolling contact fatigue life by formation of surface film, *Life Cycle Tribology, Tribol. Interface Eng. Ser.*, 2005, Ed. Dowson et al., Elsevier B.V., **48**, 343-350.

[149] National Institute for Occupational Safety and Health, *Approaches to safe nanotechnology: managing the health and safety concerns associated with engineered nanomaterials*, 2009, http://www.cdc.gov/niosh/docs/2009-125/pdfs/2009-125.pdf, Retrieved: March 2015.

[150] Nanosafe 2 Dissemination reports, Safe production and use of nanomaterials, 2008, http://www.nanosafe.org/home/liblocal/docs/Press%20Room/Nanosafe_newsletter_Issue%203.pdf, Retrieved: March 2015.

[151] L. Sun, Z. J. Zhang, Z. S. Wu, H. X. Dang, Synthesis and characterization of DDP coated Ag nanoparticles, *Mater. Sci. Eng. A*, 2004, **379**, 378-383.

[152] M. Zhang, X. Wang, X. Fu, Y. Xia, Performance and anti-wear mechanism of CaCO3 nanoparticles as a green additive in poly-alpha-olefin, *Tribol. Int.*, 2009, **42**, 1029-1039.

[153] A. Hernandez Battez, R. Gonzalez, J. L. Viesca, J. E. Fernandez, J. M. Diaz Fernandez, A. Machado, R. Chou, J. Riba, CuO, ZrO2 and ZnO nanoparticles as antiwear additive in oil lubricants, *Wear*, 2008, **265**, 422-428.

[154] Y. Y. Wu, W. C. Tsui, T. C. Liu, Experimental analysis of tribological properties of lubricating oils with nanoparticle additives, *Wear*, 2007, **262**, 819-825.

[155] W. Liu, S. Chen, An investigation of the tribological behaviour of surface-modified ZnS nanoparticles in liquid paraffin, *Wear*, 2000, **238**, 120-124.

[156] S. Chen, W. Liu, Characterization and antiwear ability of non-coated ZnS nanoparticles and DDP-coated ZnS nanoparticles, *Mater. Res. Bull.*, 2001, **36**, 137-143.

[157] X. Kang, B. Wang, L. Zhu, H. Zhu, Synthesis and tribological property study of oleic acid-modified copper sulphide nanoparticles, *Wear*, 2008, **265**, 150-154.

[158] S. Chen, W. Liu, L. Yu, Preparation of DDP-coated PbS nanoparticles and investigation of the antiwear ability of the prepared nanoparticles as additive in liquid paraffin, *Wear*, 1998, **218**, 153-158.

[159] A. Yu. Suslov, V. N. Bakunin, L. M. Kuz’mina, O. P. Parenago, Surface-capped molybdenum sulphide nanoparticles – a novel type of lubricant additives, *ROTRIB ’03 National Tribology Conference*, 2003.

[160] R. Greenberg, G. Halperin, I. Etsion, R. Tenne, The effect of WS2 nanoparticles on friction reduction in various lubrication regimes, *Tribol. Lett.*, 2004, **17**(2), 179-186.

[161] O. Eidelman, H. Friedman, R. Rosentveig, A. Moshkovith, V. Perfiliev, S. R. Cohen, Y. Feldman, L. Rapoport, R. Tenne, Chromium-rich coatings with WS2 nanoparticles containing fullerene-like structure, *NANO*, 2011, **6**(4), 313-324.

[162] M. Redlich, A. Katz, L. Rapoport, H. D. Wagner, Y. Feldman, R. Tenne, Improved orthodontic stainless steel wires coated with inorganic fullerene-like nanoparticles of WS2 impregnated in electroless nickel-phosphorous film, *Dent. Mater.*, 2008, **24**(12), 1640-1646.

[163] T. Hubert, H. Hattermann, M. Griepentrog, Sol-gel-derived nanocomposite coatings filled with inorganic fullerene-like WS2, *J. Sol-Gel Sci. Technol.*, 2009, **51**(3), 295-300.

[164] F. Abate, V. D'Agostino, R. Di Giuda, A. Senatore, Tribological behaviour of MoS2 and inorganic fullerene-like WS2 nanoparticles under boundary and mixed lubrication regimes, *Tribology*, 2010, **4**(2), 91-98.

[165] L. Rapoport, Y. Feldman, M. Homyonfer, H. Cohen, J. Sloan, J. L. Hutchinson, R. Tenne, Inorganic fullerene-like material as additives to lubricants: structure-function relationship, *Wear*, 1999, **225-229**(2), 975-982.

[166] L. Joly-Pottuz, F. Dassenoy, M. Belin, B. Vacher, J. M. Martin, N. Fleischer, Ultralow-friction and wear properties of IF-WS2 under boundary lubrication, *Tribol. Lett.*, 2005, **18**(4), 477-484.

[167] L. Yadgarov, V. Petrone, R. Rosentsveig, Y. Feldman, R. Tenne, A. Senatore, Tribological studies of rhenium doped fullerene-like MoS2 nanoparticles in boundary, mixed and elasto-hydrodynamic lubrication conditions, *Wear*, 2013, **297**, 1103-1110.

[168] L. Chang, H. Yang, W. Fu, J. Zhang, Q. Yu, H. Zhu, J. Chen, R. Wie, Y. Sui, X. Pang, G. Zou, Simple synthesis of MoS2 inorganic fullerene-like nanomaterials from MoS2 amorphous nanoparticles, *Mater. Res. Bull.*, 2008, **43**, 2427-2433.

[169] D. Vollath, D. V. Szabo, Synthesis of nanocrystalline MoS2 and WS2 in a microwave plasma, *Mater. Lett.*, 1998, **35**, 236-244.

[170] Y. Feldman, E. Wasserman, D. J. Srolovitz, R. Tenne, High-rate, gas-phase growth of MoS2 nested inorganic fullerenes and nanotubes, *Science*, 1995, **267**(5195), 222-225.

[171] E. S. Vasilyeva, O. V. Tolochko, B. K. Kim, D. W. Lee, D. S. Kim, Synthesis of tungsten disulphide nanoparticles by the chemical vapor condensation method, *Microelectron. J.*, 2009, **40**, 687-691.

[172] Y. Feldman, G. L. Frey, M. Homyonfer, V. Lyakhovitskaya, L. Margulis, H. Cohen, G. Hodes, J. L. Hutchison, R. Tenne, Bulk synthesis of inorganic fullerene-like MS2 (M = Mo, W) from the respective trioxides and the reaction mechanism, *J. Am. Chem. Soc.*, 1996, **118**(23), 5362-5367.

[173] Y. Feldman, A. Zak, R. Popovitz-Biro, R. Tenne, New reactor for production of tungsten disulfide hollow onion-like (inorganic fullerene-like) nanoparticles, *Solid State Sci.*, 2000, **6**(1), 663-672.

[174] S. M. Ghoreishi, S. S. Meshkat, A. A. Dadkhah, IF-WS_2 nanoparticles size design and synthesis via chemical reduction, *Mater. Res. Bull.*, 2010, **45**, 584-588.

[175] W. Jifen, F. Xun, A low-temperature solvothermal method to prepare hollow spherical WS_2 nanoparticles modified by TOA, *Mater. Lett.*, 2007, **61**, 4332-4335.

[176] L. Rapoport, N. Fleischer, R. Tenne, Fullerene-like WS_2 nanoparticles: superior lubricants for harsh conditions, *Adv. Mater.*, 2003, **15**(7-8), 651-655.

[177] L. Rapoport, O. Nepomnyashchy, I. Lapsker, A. Verdyan, A. Moshkovich, Y. Feldman, R. Tenne, Behaviour of fullerene-like WS_2 nanoparticles under severe contact conditions, *Wear*, 2005, **259**(1-6), 703-707.

[178] I. Lahouij, F. Dassenoy, L. de Knoop, J. M. Martin, B. Vacher, In situ TEM observation of the behavior of an individual fullerene-like MoS2 nanoparticle in a dynamic contact, *Tribol. Lett.*, 2011, **42**(2), 133-140.

[179] Y. Golan, C. Drummond, J. Israelachvili, R. Tenne, In situ imaging of shearing contacts in the surface forces apparatus, *Wear*, 2000, **245**(1-2), 190-195.

[180] T. Tsirlina, Y. Feldman, M. Homyonfer, J. Sloan, J. L. Hutchinson, R. Tenne, Synthesis and characterization of inorganic fullerene-like WSe_2 material, *Fullerene Sci. Technol.*, 1998, **6**(1), 157-165.

[181] E. Vasilyeva, A. G. Nasibulin, M. Maximov, O. Tolochko, A. Sachdev, X. Xiao, Synthesis of tungsten diselenide nanoparticles by chemical vapor condensation method, *Materials Science*, 2015, **21**(3), 339-342.

[182] M. R. Louthan, Hydrogen embrittlement of metals: a primer for the failure analyst, *J. Fail. Anal. And Preven.*, 2008, **8**, 289-307.

[183] K. Mills, J. R. Davis, Modes of fracture, In *ASM Handbook, Volume 12 Fractography*, ASM International, 1992, 12.

[184] S. D. Cramer, B. S. Covino Jr., Evaluating hydrogen embrittlement, In *ASM Handbook, Volume 13A Corrosion: Fundamentals, Testing, and Protection*, ASM International, 2003, 617.

[185] S. D. Cramer, B. S. Covino Jr., Hydrogen damage, In *ASM Handbook, Volume 13A Corrosion: Fundamentals, Testing, and Protection*, ASM International, 2003, 367.

[186] R. K. Dayal, N. Parvathavarthini, Hydrogen embrittlement in power plant steels, *Sadhana*, 2003, **28**(3-4), 431-451.

[187] A. Pundt, R. Kirchheim, Hydrogen in metals: microstructural aspects, *Annu. Rev. Mater. Res.*, 2006, **36**, 555-608.

[188] M. Kohara, T. Kawamura, M. Egami, Study on mechanism of hydrogen generation from lubricants, *Tribol. Trans.*, 2006, **49**(1), 53-60.

[189] R. Lu, H. Nanao, K. Kobayashi, T. Kubo, S. Mori, Effect of lubricant additives on tribochemical decomposition of hydrocarbon oil on nascent steel surfaces, *J. Jpn. Pet. Inst.*, 2010, **53**(1), 55-60.

[190] H. Uyama, H. Yamada, H. Hidaka, N. Mitamura, The effects of hydrogen on microstructural change and surface originated flaking in rolling contact fatigue, *Tribology Online*, 2011, **6**(2), 123-132.

[191] D. Ray, L. Vincent, B. Coquillet, P. Guirandenq, Hydrogen embrittlement of a stainless ball bearing steel, *Wear*, 1980, **65**(1), 103-111.

[192] S. Fujita, N. Mitamura, Y. Murakami, Research of new factors affecting rolling contact fatigue life, World Tribology Congress III, 2005.

[193] K. Mizuhara, T. Taki, K. Yamanaka, Anomalous cracking of bearing balls under a liquid-butane environment, *Tribol. Int.*, 1993, **26**(2), 135-142.

[194] J. A. Ciruna, H. J. Szieleit, The effect of hydrogen on the rolling contact fatigue life of AISI 52100 and 440C steel balls, *Wear*, 1973, **24**(1), 107-118.

[195] D. J. Figueroa Gordon, Hydrogen re-embrittlement susceptibility of ultra high strength steels, PhD Thesis, Cranfield University, 2005.

[196] G. Chalaftris, Evaluation of aluminium-based coatings for cadmium replacement, PhD Thesis, Cranfield University, 2003.

[197] H. Wipf, Solubility and diffusion of hydrogen in pure metals and alloys, *Phys. Scr.*, 2001, **T94**, 43-51.

[198] A. Pundt, Hydrogen in nano-sized metals, *Adv. Eng. Mater.*, 2004, **6**(1-2), 11-21.

[199] J. K. Wu, C. W. Su, Hydrogen permeability and diffusivity in low tungsten steels, *J. Mater. Sci. Lett.*, 1988, **7**, 347-349.

[200] Z. Shirband, M. R. Shishesaz, A. Ashrafi, Hydrogen degradation of steels and its related parameters, a review, *Phase Transitions*, 2011, **11-12**, 924-943.

[201] W. T. Becker, R. J. Shipley, Rolling contact fatigue, In *ASM Handbook, Volume 11 Failure analysis and prevention*, ASM International, 2005, 941.

[202] J. Gegner, Tribological aspects of rolling bearing failures, In *Tribology – Lubricants and Lubrication*, ed. C. H. Kuo, InTech, Croatia, 2011, 33-94.

[203] M. H. Evans, White structure flaking failure in bearings under rolling contact fatigue, PhD Thesis, University of Southampton, 2013.

[204] M. Shibata, M. Goto, N. Oguma, T. Mikami, A new type of micro-structural change due to rolling contact fatigue on bearings for the engine auxiliary devices, *Proc. Int. Tribol. Conf.*, 1995, **3**, 1351.

[205] N. Mitamura, H. Hidaka, S. Takaki, Microstructural development in bearing steel during rolling contact fatigue, *Mater. Sci. Forum*, 2007, **539-543**, 4255-4260.

[206] H. K. Birnbaum, P. Sofronis, Hydrogen-enhanced localized plasticity-a mechanism for hydrogen-related fracture, *Mater. Sci. Eng.*, 1994, **A176**, 191-202.

[207] A. Grabulov, Fundamentals of rolling contact fatigue, PhD Thesis, University of Belgrade, 2010.

[208] M.-H. Evans, A. D. Richardson, L. Wang, R. J. K. Wood, Effect of hydrogen on butterfly and white etching crack (WEC) formation under rolling contact fatigue (RCF), *Wear*, 2013, **306**(1-2), 226-241.

[209] A. Ruellan, F. Ville, X. Kleber, A. Arnaudon, D. Girodin, Understanding white etching cracks in rolling element bearings: The effect of hydrogen charging on the formation mechanisms, *Proc. Inst. Mech. Eng., Part J*, 2014, **228**(11), 1252-1265.

[210] H. Uyama, H. Yamada, White structure flaking in rolling bearings for wind turbine gearboxes, *Wind systems*, 2014. http://www.windsystemsmag.com/article/detail/619/ white-structure-flaking-in-rolling-bearings-for-wind-turbine-gearboxes. Retrieved: October 2014.

[211] H. Hamada, Y. Matsubara, The influence of hydrogen on tension-compression and rolling contact fatigue properties of bearing steel, *NTN Technical Review*, 2006, **74**, 54-61.

[212] H. Tanaka, M. Hashimoto, J. Sugimura, Y. Yamamoto, Rolling contact fatigue of bearing steel in hydrogen environment, *World Tribology Congress III*, 2005, **1**, 155-156.

[213] T. Otsu, H. Tanaka, K. Ohnishi, J. Sugimura, Simple experiment on permeation of hydrogen into steel in cyclic contact, *Tribology Online*, 2011, **6**(7), 311-316.

[214] H. Tanaka, T. Morofuji, K. Enami, M. Hashimoto, J. Sugimura, Effect of environmental gas on surface initiated rolling contact fatigue, *Tribology Online*, 2013, **8**(1), 90-96.

[215] A. H. M. Krom, A. D. Bakker, Hydrogen trapping models in steel, *Metall. Mater. Trans. B*, 2000, **31**(6), 1475-1482.

[216] S. Frappart, A. Oudriss, X. Feaugas, J. Creus, J. Bouhattate, F. Thebault, L. Delattre, H. Marchebois, Hydrogen trapping in martensitic steel investigated using electrochemical permeation and thermal desorption spectroscopy, *Scr. Mater.*, 2011, **65**, 859-862.

[217] B. A. Szost, R. H. Vegter, P. E. J. Rivera-Diaz-del-Castillo, Hydrogen trapping mechanisms in nanostructured steels, *Metall. Mater. Trans. A*, 2013, **44**(10), 4542-4550.

[218] F. G. Wei, T. Hara, K. Tsuzaki, Precise determination of the activation energy for desorption of hydrogen in two Ti-added steels by a single thermal-desorption spectrum, *Metall. Mater. Trans. B*, 2004, **35**(3), 587-597.

[219] D. Perez Escobar, E. Wallaert, L. Duprez, A. Atrens, K. Verbeken, Thermal desorption spectroscopy study of the interaction of hydrogen with TiC precipitates, *Met. Mater. Int.*, 2013, **19**(4), 741-748.

[220] E. J. Song, D. W. Suh, H. K. D. H. Bhadeshia, Theory for hydrogen desorption in ferritic steel, *Comput. Mater. Sci.*, 2013, **79**, 36-44.

[221] Johan et al., Method for increasing the fatigue strength of a predominantly steel mechanical part of a wind turbine and/or for reducing the tendancy to form what are called ‘white etching cracks’ or ‘brittle flakes’ in such steel mechanical parts, US Patent 0288742 A1, 2009.

[222] Takata et al., Bearing steel, US Patent 5403545, 1995.

[223] Takashi et al., Steel part having long rolling contact fatigue life and method for producing the same, E Patent 1826286 A2, 2007.

[224] K. Tamada, H. Tanaka, Occurrence of brittle flaking on bearings used for automotive electrical instruments and auxiliary devices, *Wear*, 1996, **199**, 245-252.

[225] Takemura et al., Rolling bearing, US Patent 6602360 B2, 2003.

[226] J. Luyckx, Hammering wear impact fatigue hypothesis WEC/irWEA failure mode on roller bearings, *Wind turbine tribology seminar*, Broomfield, USA, 2011.

[227] N. Mitamura, Rolling contact element steel and rolling bearing made thereof, US Patent 5084116, 1992.

[228] C. Newlands, A. Olver, N. Brandon, Gaseous evolution of hydrogen from hydrocarbon oil and grease lubricated contacts, *Tribol. Ser.*, 2003, **41**, 719-726.

[229] A. Verma, W. Jiang, H. H. Abu Safe, W. D. Brown, A. P. Malshe, Tribological behavior of deagglomerated active inorganic nanoparticles for advanced lubrication, *Tribol. Trans.*, 2008, **51**(5), 673-678.

[230] R. Errichello, S. Sheng, J. Keller, A. Greco, *Wind turbine tribology seminar- A recap*, 2011. www.nrel.gov/docs/fy12osti/53754.pdf Retrieved: October 2014.

[231] C. Binns, *Introduction to nanoscience and nanotechnology, Volume 14 of Wiley Survival Guides in Engineering and Science*, John Wiley & Sons, 96-175, **2010**.

[232] P. Walter, E. Welcomme, P. Hallegot, N. J. Zaluzec, C. Deeb, J. Castaing, P. Veyssiere, R. Breniaux, J.-L. Leveque, G. Tsoucaris, Early use of PbS nanotechnology for an ancient hair dyeing formula, *Nano Lett.*, 2006, **6**(10), 2215-2219.

[233] A. Ruivo, C. Gomes, A. Lima, L. Botelho, R. Melo, A. Belchior, A. Pires de Matos, Gold nanoparticles in ancient and contemporary ruby glass, *J. Cult. Heritage*, 2008, **9**, 134-137.

[234] M. Hosokawa, K. Nogi, M. Naito, T. Yokoyama, In *Nanoparticle technology handbook, Chemical, petrochemical & process*, Elsevier, **2007**, 1-50.

[235] P. Atkins, J. de Paula, Molecular interactions, In *Atkins' Physical Chemistry, 9th Edition*, OUP Oxford, **2010**, 622-653.

[236] I. Tinoco, K. Sauer, J. Wang, J. Puglisi, Free energy and physical equilibria – Membranes, In *Physical chemistry: principles and applications in biological sciences, 4th Edition*, Prentice Hall, **2002**, 213-227.

[237] G. Carboni, Experiments on surface phenomena and colloids, Retrieved: April 2013, http://www.funsci.com/fun3_en/exper2/exper2.htm.

[238] Surface tension, Retrieved: April 2013, http://en.wikipedia.org/wiki/Surface_tension.

[239] A. I. Bailey, Surface and interfacial tension, Retrieved: April 2013, http://www.thermopedia.com/content/30/?tid=104&sn=1312.

[240] X. Chen, R. A. Boulos, P. K. Eggers, C. L. Raston, *p*-Phosphonic acid calix[8]arene assisted exfoliation and stabilization of 2D materials in water – Supporting Information, *Chem. Commun.*, 2012, **48**, 11407-11409.

[241] J. N. Coleman et al., Two-dimensional nanosheets produced by liquid exfoliation of layered materials – Supporting Online Material, *Science*, 2011, **331**(6017), 568-571.

[242] Q. H. Wang, K. Kalantar-Zadeh, A. Kis, J. N. Coleman, M. Strano, Electronics and optoelectronics of two-dimensional transition metal dichalcogenides, *Nat. Nanotechnol.*, 2012, **7**, 699-712.

[243] G. Cunningham, M. Lotya, C. S. Cucinotta, S. Sanvito, S. D. Bergin, R. Menzel, M. S. P. Shaffer, N. Coleman, Solvent exfoliation of transition metal dichalcogenides: dispersability of exfoliated nanosheets varies only weakly between compounds, *ACS Nano*, 2012, **6**(4), 3468-3480.

[244] J. McMurry, *Organic chemistry*, Cengage Learning, **2010**.

[245] T. N. Sorrell, *Organic chemistry*, 2nd Edition, University Science Books, **2006**.

[246] W. H. Brown, B. L. Iverson, *Organic chemistry*, 5th Edition, Cengage Learning, **2009**.

[247] Colloid, Retrieved: April 2013, http://en.wikipedia.org/wiki/Colloid.

[248] Spectroscopic analysis (UV-visible spectroscopy) – Zeta potential, Retrieved: April 2013, http://nanocomposix.com/kb/general/characterization-techniques.

[249] Derjaguin, Landau, Verwey and Overbeek theory (DLVO theory), Retrieved: April 2013, http://www.malvern.com/labeng/industry/colloids/dlvo_theory.htm.

[250] Zeta potential measurement using laser Doppler electrophoresis (LDE), http://www.malvern.com/labeng/technology/zeta_potential/zeta_potential_LDE.htm, Retrieved: April 2013.

[251] Critical micelle concentration, Retrieved: April 2013, http://en.wikipedia.org/wiki/Critical_micelle_concentration.

[252] I. D. Morrison, Criterion for electrostatic stability of dispersions at low ionic strength, *Langmuir*, 1991, **7**, 1920-1922.

[253] M. F. Hsu, E. R. Dufresne, D. A. Weitz, Charge stabilization in nonpolar solvents, *Langmuir*, 2005, **21**, 4881-4887.

[254] Electrosteric stabilization, *MSE 502 – Sol-gel processing*, Retrieved: April 2013, http://depts.washington.edu/solgel/images/courses/MSE_502/Ch_2/figure_2.22.JPG.

[255] C. Shahar, D. Zbaida, L. Rapoport, H. Cohen, T. Bendikov, J. Tannous, F. Dassenoy, R. Tenne, Surface functionalization of WS_2 fullerene-like nanoparticles, *Langmuir*, 2010, **26**(6), 4409-4414.

[256] IBA GmbH, "Ni-NTA Resins", Retrieved: April 2013, http://www.iba-lifesciences.com/tl_files/uploads/bilder/produkte/double-tag/Ni-NTA.jpg.

[257] M. N. Tahir, N. Zink, M. Eberhardt, H. A. Therese, S. Faiss, A. Janshoff, U. Kolb, P. Theato, W. Tremel, Hierarchical assembly of TiO_2 nanoparticles on WS_2 nanotubes achieved through multifunctional polymeric ligands, *Small*, 2007, **3**(5), 829-834.

[258] M. N. Tahir, F. Natalio, H. A. Therese, A. Yella, N. Metz, M. R. Shah, E. Mugnaioli, R. Berger, P. Theato, H. C. Schroder, W. E. G. Muller, W. Tremel, Enzyme-mediated deposition of a TiO_2 coating onto biofunctionalized WS_2 chalcogenide nanotubes, *Adv. Funct. Mater.*, 2009, **19**, 285-291.

[259] P. Atkins, J. de Paula, *Determination of size and shape*, In *Atkins' Physical Chemistry, 9th Edition*, OUP Oxford, 677-686, **2010**.

[260] B. J. Berne, R. Pecora, *Dynamic light scattering: with applications to chemistry, biology and physics*, Courier Dover Publications, **2000**.

[261] Dynamic light scattering, Retrieved: April 2013, http://en.wikipedia.org/wiki/Dynamic_light_scattering.

[262] Malvern Zetasizer, Retrieved: April 2013, http://www.malvern.com/en/products/product-range/zetasizer-range/zetasizer-nano-range/zetasizer-nano-z/.

[263] B. Fultz, J. M. Howe, *Transmission electron microscopy and diffractometry of materials*, 3rd Edition, Springer, **2008**.

[264] D. B. Williams, B. Carter, *Transmission electron microscopy: a textbook for materials science: basics, diffraction, imaging, spectrometry*, Springer, **1996**.

[265] The Science and Engineering Electron Microscopy Centre, University of Southampton, Retrieved: April 2013, http://www.micro.soton.ac.uk/JEM3010.php.

[266] Kelvin Nanocharacterisation Centre, University of Glasgow, Retrieved: June 2015, http://www.gla.ac.uk/schools/physics/research/groups/mcmp/knc/facilities/arm200fcs-magtem/.

[267] School of Materials, University of Manchester, Retrieved: June 2015, http://www.materials.manchester.ac.uk/our-research/facilities/electron-microscopy/transmissionelectronmicroscopes/.

[268] David Cockayne Centre for Electron Microscopy, University of Oxford, Retrieved: June 2015, http://www-em.materials.ox.ac.uk/instruments/transmission/jeol-arm-200.html.

[269] T. J. A. Slater, P. H. C. Camargo, M. G. Burke, N. J. Zaluzec, S. J. Haigh, Understanding the limitations of the Super-X energy dispersive x-ray spectrometer as a function of specimen tilt angle for tomographic data acquisition in the S/TEM, *J. Phys.: Conf. Ser.*, 2014, **522**, 012025.

[270] G. Gauglitz, T. Vo-Dihn, *Handbook of spectroscopy*, John Wiley & Sons, **2006**.

[271] J. M. Hollas, *Modern spectroscopy*, John Wiley & Sons, **2004**.

[272] The Tony Davies High Voltage Laboratory, University of Southampton, Retrieved: April 2013, http://www.highvoltage.ecs.soton.ac.uk/commercialTesting/facilitiesAndTestingCapabilities.php.

[273] UK National Crystallography Service, University of Southampton, Retrieved: April 2013, http://www.ncs.ac.uk/equipment/diffractometers/.

[274] PCS Instruments. *MTM2 Mini-Traction Machine*, Retrieved: April 2013, http://www.pcs-instruments.com/brochures/brochures.shtml.

[275] M. Ratoi, R. C. Castle, C. H. Bovington, H. A. Spikes, The influence of soot and dispersant on ZDDP film thickness and friction, *Lubr. Sci.*, 2004, **17**(1), 25–43.

[276] International Research Center for Hydrogen Energy, Kyushu University, Retrieved: June 2015, http://h2.kyushu-u.ac.jp/english/05facilities/index.html.

[277] V. B. Niste, H. Tanaka, M. Ratoi, J. Sugimura, WS_2 nanoadditized lubricant for applications affected by hydrogen embrittlement, *RSC Adv.*, 2015, **5**(51), 40678-40687.

[278] Alicona Infinite Focus® IFM Manual, IFM 2.1.5 EN 16.06.2008.

[279] Contour Elite 3D Optical Microscopes, Bruker, Retrieved: June 2015, https://www.bruker.com/products/surface-analysis/3d-industrial-optical-microscopy/3d-surface-metrology.html.

[280] Nano Test Vantage, Micro Materials, Retrieved: June 2015, http://www.micromaterials.co.uk/the-nano-test/nanotest-vantage/.

[281] B. D. Beake, S. Zheng, M. R. Alexander, Nanoindentation testing of plasma-polymerised hexane films, *J. Mater. Sci.*, 2002, **37**(18), 3821-3826.

[282] W. C. Oliver, G. M. Pharr, An improved technique for determining hardness and elastic-modulus using load and displacement sensing indentation experiments, *J. Mater. Res.*, 1992, **7**(6), 1564–1583.

[283] NEXUS XPS Facilities, K-alpha, Retrieved: June 2015. http://www.ncl.ac.uk/nexus/xps/instruments/kalpha.htm.

[284] XPS Analysis Services, Cardiff University, Retrieved: June 2015, http://sites.cardiff.ac.uk/xpsaccess/services/.

[285] Leeds EPSRC Nanoscience and Nanotechnology Research Equipment Facility, University of Leeds, Retrieved: June 2015, http://www.engineering.leeds.ac.uk/lennf/ facilities/x-ray-photoelectron-spectroscopy.shtml.

[286] Southampton Nanofabrication Centre, University of Southampton, Retrieved: June 2015, http://www.southampton-nanofab.com/characterisation/fib.php.

[287] M. Ratoi, V. B. Niste, J. Walker, J. Zekonyte, Mechanism of action of WS2 lubricant nanoadditives in high-pressure contacts, *Tribol. Lett.*, 2013, **52**(1), 81–91.

[288] D. O. Dumcenco, K. Y. Chen, Y. P. Wang, Y. S. Huang, K. K. Tiong, Raman study of 2H-$Mo_{1-x}W_xS_2$ layered mixed crystals, *J. Alloys Compd.*, 2010, **506**(12), 940-943.

[289] X. Fang, C. Hua, C. Wu, X. Wang, L. Shen, Q. Kong, J. Wang, Y. Hu, Z. Wang, L. Chen, Synthesis and electrochemical performance of graphene-like WS2, *Chem. - Eur. J.*, 2013, **19**(18), 5694–5700.

[290] L. Joly-Pottuz, J. M. Martin, M. Belin, F. Dassenoy, G. Montagnac, B. Reynard, Study of inorganic fullerenes and carbon nanotubes by *in situ* Raman tribometry, *Appl. Phys. Lett.*, 2007, **91**, 153107.

[291] H. A. Therese, J. Li, U. Kolb, W. Tremel, Facile large scale synthesis of WS_2 nanotubes from WO_3 nanorods prepared by a hydrothermal route, *Solid State Sci.*, 2005, **7**(1), 67-72.

[292] NIST X-ray Photoelectron Spectroscopy Database, Version 4.1 (National Institute of Standards and Technology, Gaithersburg, 2012), http://srdata.nist.gov/xps/.

[293] F. Y. Xie, L. Gong, X. Liu, Y. T. Tao, W. H. Zhang, S. H. Chen, H. Meng, J. Chen, XPS studies on surface reduction of tungsten oxide nanowire film by Ar^+ bombardment, *J. Electron Spectrosc. Relat. Phenom.*, 2012, **185**(3-4), 112-118.

[294] Isotopic abundances, Commission on isotopic abundances and atomic weights, Retrieved: April 2013, http://www.ciaaw.org/isotopic-abundances.htm.

[295] M. Berglund, E. Wieser, Isotopic compositions of the elements 2009 (IUPAC Technical Report), *Pure Appl. Chem.*, 2011, **83**(2), 397-410.

[296] R. Saha, W. D. Nix, Effects of the substrate on the determination of thin film mechanical properties by nanoindentation, *Acta Mater.*, 2002, **50**, 23-38.

[297] G. Pereira, A. Lachenwitzer, M. Kasrai, G. M. Bancroft, P. R. Norton, M. Abrecht, P. U. P. A. Gilbert, T. Regier, R. I. R. Blyth, J. Thompson, Chemical and mechanical analysis of tribofilms from fully formulated oils Part 1 – films on 52100 steel, *Tribol.-Mater., Surf. Interfaces*, 2007, **1**(1), 48–61.

[298] A. Margolin, F. L. Deepak, R. Popovitz-Biro, M. Bar-Sadan, Y. Feldman, R. Tenne, Fullerene-like WS_2 nanoparticles and nanotubes by vapor-phase synthesis of WCl_n and H_2S, *Nanotechnology*, 2008, **19**(9), 095601.

[299] Y. Q. Zhu, T. Sekine, Y. H. Li, W. X. Wang, M. W. Fay, H. Edwards, P. D. Brown, N. Fleischer, R. Tenne, WS_2 and MoS_2 inorganic fullerenes – super shock absorbers at very high pressures, *Adv. Mater.*, 2005, **17**(12), 1500-1503.

[300] O. Tevet, O. Goldbart, S. R. Cohen, R. Rosentsveig, R. Popovitz-Biro, H. D. Wagner, R. Tenne, Nanocompression of individual multilayered polyhedral nanoparticles, Nanotechnology, 2010, **21**(36), 365705.

[301] M. Ratoi, V. B. Niste, J. Zekonyte, WS2 nanoparticles – potential replacement for ZDDP and friction modifier additives, *RSC Adv.*, 2014, **4**(41), 21238-21245.

[302] J. M. Martin, Antiwear mechanisms of zinc dithiophosphate: a chemical hardness approach, *Tribol. Lett.*, 1999, **6**(1), 1-8.

[303] J. M. Martin, T. Onodera, C. Minfray, F. Dassenoy, A. Miyamoto, The origin of anti-wear chemistry of ZDDP, *Faraday Discuss.*, 2012, **156**, 311-323.

[304] H. Tanimoto, H. Tanaka, J. Sugimura, Observation of hydrogen permeation into fresh bearing steel surface by thermal desorption spectroscopy, *Tribology Online*, 2011, **6**(7), 291-296.

[305] J. H. Ryu, Hydrogen embrittlement in TRIP and TWIP steels, PhD Thesis, Pohang University of Science and Technology, 2012.

[306] A. Yamauchi, Y. Yamauchi, Y. Hirohata, T. Hino, K. Kurokawa, TDS measurement of hydrogen released from stainless steel oxidized in H_2O-containing atmospheres, *Mater Sci. Forum*, 2006, **522**(523), 163-170.

[307] L. Begrambekov, O. Dvoychenkova, A. Evsin, A. Kaplevsky, Ya. Sadovskiy, N. Schitov, S. Vergasov, D. Yurkov, Hydrogen transport through metal oxide surface under atom and ion irradiation, *J. Phys.: Conf. Ser.*, 2014, **567**, 012003.

[308] J. P. Hirth, Effects of hydrogen on the properties of iron and steel, *Metall. Trans. A*, 1980, **11**(6), 861-890.

[309] J. R. Scully, H. Dogan, D. Li, R. Gangloff, Controlling hydrogen embrittlement in ultra-high strength steels, *Corrosion 2004*, New Orleans, 2004.

[310] D. J. Young, Effects of water vapour on oxidation, *High Temperature Oxidation and Corrosion of Metals*, Elsevier, **2008**, 455-496.

[311] M. Kamaya, Environmental effect on fatigue strength of stainless steel in PWR primary water – Role of crack growth acceleration in fatigue life reduction, *Int. J. Fatigue*, 2013, **55**, 102-111.

[312] J. F. Moulder, W. F. Stickle, P. E. Sobol, K. D. Bomben, *Handbook of X-ray Photoelectron Spectroscopy: A Reference Book of Standard Spectra for Identification and Interpretation of XPS Data*, Physical Electronics Inc, **1995**.

[313] L. E. Davis, N. C. MacDonald, P. W. Palmberg, G. E. Riach, R. E. Weber, *Handbook of Auger Electron Spectroscopy: A Reference Book of Standard Data for Identification and Interpretation of Auger Electron Spectroscopy Data*, Physical Electronics Division, **1976**.

PERMISSIONS

[43] **Figure 2.5 c)** Interferometry image of an EHL contact.
Reproduced with permission from PCS Instruments.
http://www.pcs-instruments.com/ehd/applications/ehd-thin-measurement-system.shtml.

[1] **Figure 2.10** Structure of MoS_2.
Reprinted from G. Stachowiak, A. W. Batchlor, *Engineering Tribology, 3rd Ed*, **2006**, Chapter 9, Solid lubrication and surface treatments, page 433, with permission from Elsevier. http://www.sciencedirect.com/science/book/9780750678360.

[8] **Figure 2.13** Diagram of a ZDDP pad structure and composition.
Reprinted from H. Spikes, The history and mechanisms of ZDDP, *Tribol. Lett.*, 2004, **17**(3), 469-489, with kind permission from Springer Science and Business Media. Warranties: None.
http://link.springer.com/article/10.1023%2FB%3ATRIL.0000044495.26882.b5.

[198] **Figure 2.19** Hydrogen trapping at different trap sites.
Reprinted from A. Pundt, Hydrogen in nano-sized metals, *Adv. Eng. Mater.*, 2004, **6**(1-2), 11-21, with permission from John Wiley and Sons.
http://onlinelibrary.wiley.com/doi/10.1002/adem.200300557/abstract.

[64] **Figure 2.22** Section through a SCM420 JIS (4118 ASTM) wear track which shows: a) typical damage in a sample with a long RCF life, b) typical damage in a sample subjected to HE with a short RCF life.
Reprinted from N. Kino, K. Otani, The influence of hydrogen on rolling contact fatigue life and its improvement, *JSAE Rev.*, 2003, **24**, 289-294, with permission from Elsevier.
http://www.sciencedirect.com/science/article/pii/S0389430403000353.

[261] **Figure 3.1** Dynamic light scattering.
Reproduced with permission from Wikipedia, original work by Mike Jones, 2010, DLS.svg.
http://en.wikipedia.org/wiki/Dynamic_light_scattering.

[274] **Figure 3.2** a) MTM2 rig and b) MTM2 pot.
[274] **Figure 3.3 a)** Diagram of MTM2-SLIM set up.
Reproduced with permission from PCS Instruments.
http://www.pcs instruments.com/brochures/brochures.shtml.

[56] M. Ratoi, V. B. Niste, H. Alghawel, A. Suen, K. Nelson, The impact of organic friction modifiers on engine oil tribofilms, *RSC Adv.*, 2014, **4**, 4278-4285, reproduced by permission of the Royal Society of Chemistry.

[277] V. B. Niste, H. Tanaka, M. Ratoi, J. Sugimura, WS_2 nanoadditized lubricant for applications affected by hydrogen embrittlement, *RSC Adv.*, 2015, **5**(51), 40678-40687, reproduced by permission of the Royal Society of Chemistry.

[287] M. Ratoi, V. B. Niste, J. Walker, J. Zekonyte, Mechanism of action of WS2 lubricant nanoadditives in high-pressure contacts, *Tribol. Lett.*, 2013, **52**(1), 81–91, reproduced with kind permission from Springer Science and Business Media.

[301] M. Ratoi, V. B. Niste, J. Zekonyte, WS2 nanoparticles – potential replacement for ZDDP and friction modifier additives, *RSC Adv.*, 2014, **4**(41), 21238-21245, reproduced by permission of the Royal Society of Chemistry.